Université de Montréal
et
Université de Provence

Cinématique et dynamique des galaxies spirales barrées

par

Olivier Hernandez

Thèse effectuée en cotutelle
au
Département de Physique
Faculté des arts et des sciences
Université de Montréal
et au
Laboratoire d'Astrophysique de Marseille
Université de Provence

Thèse présentée à la Faculté des études supérieures de l'Université de Montréal en vue de l'obtention du grade de Philosophiæ Doctor (Ph.D.) en Physique
et à
l'Université de Provence en vue de l'obtention du grade de Docteur de l'Université de Provence

Décembre, 2004

Université de Montréal
Faculté des études supérieures
et
Laboratoire d'Astrophysique de Marseille
Université de Provence

Cette thèse intitulée :

Cinématique et dynamique des galaxies spirales barrées

présentée et soutenue à l'Université de Montréal par :

Olivier Hernandez

a été évaluée par un jury composé des personnes suivantes :

Anthony Moffat, (Université de Montréal)	**Président-rapporteur et membre du jury**
Claude Carignan, (Université de Montréal)	**Directeur de recherche**
Philippe Amram, (Université de Provence)	**Directeur de recherche**
Jacques Boulesteix, (Université de Provence)	**Membre du jury**
Françoise Combes, (Observatoire de Paris)	**Examinateur externe**
Paul Arminjon,	**Représentant du Doyen de la FES**

Thèse acceptée le : 21 février 2005

Résumé

La masse totale (lumineuse et non lumineuse) des galaxies est déduite de la vitesse circulaire de rotation des galaxies. L'observation spectroscopique de type Fabry-Perot du gaz ionisé des galaxies spirales permet d'obtenir leur cinématique. Dans le cas de champs de vitesses parfaitement axisymétriques - c'est à dire pour des galaxies spirales non barrées et non actives - ces champs de vitesses donnent directement accès à la composante circulaire de la vitesse de rotation. Les champs de vitesses des galaxies barrées sont plus complexes et ont besoin d'une analyse plus poussée pour en déduire leur vitesse circulaire. Or, les galaxies spirales barrées constituent plus des deux tiers des galaxies spirales. Une étude à grande échelle sur un échantillon de spirales barrées est donc nécessaire pour comprendre les mouvements non circulaires dans les galaxies.

Cette thèse propose les moyens nécessaires pour rechercher la composante axisymétrique des galaxies spirales. L'accent a d'abord été mis sur une instrumentation de haute qualité, en développant FANTOMM, la caméra à comptage de photons la plus sensible au monde couplée à un interféromètre de Fabry-Perot. Dans un premier temps, l'analyse des données d'observation d'un échantillon rigoureusement choisi de spirales barrées - *BHαBAR* - a permis d'obtenir des champs de vitesses de grande qualité. Par la suite, la méthode de Tremaine-Weinberg, surtout utilisée jusqu'à maintenant avec la composante stellaire et qui permet de déterminer la fréquence de rotation de la barre dans une galaxie, a été utilisée sur ces données Hα et s'est révélée également efficace avec la composante de gaz ionisé. Enfin tous les éléments précédents ont permis d'étudier, parmi les galaxies de l'échantillon *BHαBAR*, des éléments clés de leur évolution - résonances des orbites, fréquences de rotation des barres, ondes stationnaires multiples,... - qui permettront, grâce aux modèles N-corps+SPH développés en parallèle, de déterminer beaucoup plus précisément la masse de galaxies spirales barrées.

Mots clés : Instrumentation astronomique - Caméra à comptage de photons -

Spectroscopie 3D - Interférométrie Fabry-Perot - Évolution des galaxies spirales barrées - Cinématique - Dynamique - Modélisation N-coprs+SPH.

Summary

The total mass (luminous and dark) of galaxies is derived from their circular velocities. Spectroscopic Fabry-Perot observations of the ionized gas component of spiral galaxies allow one to derive their kinematics. In the case of purely axisymmetric velocity fields - as in non-active and unbarred spirals galaxies - the circular velocities can be derived directly. However, the velocity fields of barred galaxies (which constitute two thirds of the spirals) exhibit strong non-circular motions and need a careful analysis to retrieve the circular component.

This thesis proposes the necessary steps to recover the axisymmetric component of barred spiral galaxies. The first step was to develop the best instrumentation possible for this work. FANTOMM, which is the most sensitive photon counting camera ever developed, was coupled to a Fabry-Perot interferometer. The observations of a sample of barred spiral galaxies - the *BHαBAR* sample - was assembled in order to obtain the most rigourous velocity fields. Then, the Tremaine-Weinberg method, which can determine the bar pattern speed and is usually used with the observations of stellar component, has been tested on the ionised gas and gave satisfactory results. Finally, all the above techniques have been applied to the *BHαBAR* sample in order to study the key parameters of the galaxies' evolution - bar pattern speeds, multiple stationary waves, resonances etc... - which will allow one to use N-body+SPH simulations to model properly the non-circular motions and determine the true total mass of barred spiral galaxies.

Keywords : Astronomical instrumentation - Photon counting system - 3D Spectroscopy - Fabry-Perot Interferometer - Evolution of bar spiral galaxies - Kinematics - Dynamics - N-coprs+SPH modelling.

Remerciements

Mes premiers remerciements vont tout naturellement à mes deux directeurs de thèse Claude Carignan et Philippe Amram, qui ont toujours été présents au cours de ce doctorat et m'ont sincèrement soutenu sur divers plans (universitaire, moral, financiers, ...). Merci beaucoup, j'espère vivement que nous auront encore beaucoup de projets en commun.

Je voudrais aussi profiter de cette occasion pour remercier les personnes avec qui j'ai travaillé et qui ont contribué à la qualité de ce travail. D'abord, ceux de Montréal, Olivier II et Laurent, votre aide et savoir précieux nous ont permis d'aller plus loin et de mieux comprendre la physique des Galaxies. Marie-Maude et Damien, merci pour votre disponibilité et vos savoir-faire respectifs. Enfin, merci à Sébastien pour les longues discussions et les perspectives de carrière... Ensuite, je ne voudrais pas oublier le soutien et la collaboration avec l'équipe de l'Observatoire de Marseille. Jean-Luc et Jacques, c'est un plaisir de travailler avec vous, même à 2500 m d'altitude. Michel, Philippe B., Olivier B. et Olivia, je vous remercie aussi pour votre expérience utilisée à juste profit dans ce travail. Hervé, de l'Observatoire de Lyon, je tiens aussi à te remercier pour m'avoir reçu plusieurs fois et partager tes expériences théoriques et multiprocesseurs. Enfin, une mention spéciale pour Chantal B., de l'Observatoire de Paris, pour ton enthousiasme inégalable même à 4500 m d'altitude !

Table des matières

Liste des tableaux

Liste des figures

Abréviations

ADHOC	Analyse et Dépouillement Homogène des Observations Cigale
AT	Australia Telescope
BHαBAR	Big H-Alpha kinematics sample of BARred spiral galaxies
CCD	Charge Coupling Device
CDM	Cold Dark Matter
DAO	Dominion Astrophysical Observatory
DDO	David Dunlap Observatory
FQRNT	Fond Québécois de la Recherche sur la Nature et les Technologies
FANTOMM	Fabry-Perot de Nouvelle Technologie pour l'Observatoire du mont Mégantic
FP	Fabry-Perot
FSR	Free Spectral Range
GHASP	Gassendi observations of Hα in SPiral galaxies
GIPSY	Groningen Image Processing SYstem
IDL	Interactive Data Language
IR	Infra-rouge
ISL	Intervalle Spectral Libre
LAE	Laboratoire d'Astrophysique Expérimentale de Montrèal
LAM	Laboratoire d'Astrophysique de Marseille
MACHO	MAssive Compact Halo Objects
$(\mathcal{M}/\mathrm{L}_B)_\star$	Rapport Masse-Luminosité stellaire dans la bande Bleue
MOND	MOdified Newtonian Dynamics

MOS	Multi-Object Spectrograph
MOSFP	Multi-Object Spectrograph Fabry-Perot
NGC	New General Catalog
NSERC	Natural Sciences and Engineering Research Council of Canada
PA	Position Angle
pc	Parsec
pixel	Picture Element
TCFH	Télescope Canada-France-Hawaï
UGC	Uppsala General Catalog
VLA	Very Large Array
WIMPS	Weakly Interactive Massive Particles
WHISP	Westerbork observations of neutral Hydrogen in Irregular and SPiral galaxies
WRST	Westerbork Radio Synthesis Telescope

"J'essaie de ne pas vivre en contradiction avec les idées que je ne défends pas."

Pierre Desproges

Introduction

En 1933, Zwicky est le premier à évoquer le concept de matière non lumineuse (dite "matière sombre") en remarquant la différence existant entre la masse dynamique et la masse lumineuse d'un amas de galaxies. Plus tard, Freeman (1970) a démontré, grâce à des observations radio de la raie à 21 cm de l'hydrogène neutre, que les courbes de rotation des galaxies ne suivaient pas la décroissance képlerienne attendue des disques exponentiels qui servent à les modéliser. De plus, les simulations numériques (Ostriker & Peebles, 1973) démontrèrent que les disques des galaxies ne sont pas stables - selon le critère de Toomre (1964) - et qu'ils pouvaient être stabilisés par l'ajout d'un halo de matière non lumineuse de distribution en densité sphérique et isotherme.

Par la suite, des observations du gaz neutre ont démontré clairement, que pour la majorité des galaxies spirales, les vitesses de rotation demeurent constantes à de très grands rayons galactocentriques, ce qui montre, hors de tout doute, que la matière lumineuse ne représente qu'une petite proportion de la distribution de masse totale d'une galaxie spirale. Les galaxies de type précoce et massive semblent être dominées par la composante stellaire dans leurs parties internes alors qu'à l'opposée du diapason de Hubble, les naines irrégulières semblent être dominées par la matière non lumineuse même au centre (Carignan & Freeman, 1988). Dans ce dernier cas, les courbes de rotation conduisent à des profils de densité centrale quasi constants du halo de matière non lumineuse, dans les parties centrales du disque galactique, en contradiction avec les profils piqués prédits par les simulations numériques du processus d'évolution cosmologique de l'Univers (Navarro et al., 1997). Malheureusement, la faible résolution spatiale des observations radio-astronomiques n'est pas suffisante pour déterminer avec assurance la cinématique des parties internes et ainsi contraindre les modèles de masse des galaxies. En effet, la vitesse de rotation circulaire permet de déduire le potentiel axisymétrique d'une galaxie et de remonter directement à sa masse. Les travaux de Blais-Ouellette et al. (1999, 2001 et 2004) ont montré l'importance de la pente interne

des courbes de rotation dans la détermination des paramètres des modèles de masse. Une erreur sur la pente interne, donc de la courbe de rotation, conduirait directement à une mauvaise détermination de la masse totale d'une galaxie. Les observations spectroscopiques de type Fabry-Perot, à grande résolution spatiale et spectrale, permettent d'accéder à des champs de vitesses d'une grande précision desquels les courbes de rotation sont calculées. Cependant, seule la composante axisymétrique est fondamentale pour la détermination de la masse d'une galaxie. Si la vitesse observée n'est pas seulement la vitesse circulaire mais la vitesse circulaire avec une perturbation, il convient alors de la comprendre, de la modéliser et de l'extraire des données. Or, les écarts aux mouvements circulaires dans les spirales sont principalement causés par des structures ellipsoïdales triaxiales, dites barres d'étoiles, qui induisent un potentiel non axisymétrique. Le comportement du gaz est alors modifié et les champs de vitesses observés ne tracent plus la vitesse circulaire. Les barres constituent une structure fondamentale dans une galaxie puisque plus des deux tiers des galaxies spirales à haute brillance de surface sont barrées (Knapen et al., 2000b). Les barres sont des moteurs actifs de l'évolution des galaxies. Elles peuvent être à l'origine des structures spirales (Toomre, 1969) et créer des anneaux par phénomènes de résonances (Buta, 1986). Les barres stellaires peuvent fournir un moyen de transporter de la matière (gaz) vers le centre des galaxies, et ainsi alimenter les noyaux actifs de galaxies (Kormendy, 1982), tout en transférant une partie du moment cinétique vers l'extérieur des galaxies (Block et al., 2002).

La connaissance approfondie de la rotation de la barre, donc de sa dynamique, est fondamentale pour l'étude de la non-axisymétricité des champs de vitesses, dans le but de corriger ou de modifier les courbes de rotation pour contraindre de façon plus efficace les modèles de masse des galaxies spirales. Un échantillon de galaxies spirales barrées, judicieusement choisi, constitue une base de travail solide dans cette recherche des mouvements non circulaires.

Cette thèse

Cette thèse a pour but de décoder les mouvements non circulaires dans les galaxies, en étudiant les spirales barrées. Cela passe par plusieurs étapes qui constituent le corps de ce travail. Le premier chapitre de ce document a pour but de poser les différentes bases à la compréhension des chapitres, présentés sous forme d'articles, qui le suivent.

Dans un premier temps, il est nécessaire de mettre en place des outils performants pour la détection, l'analyse et la modélisation des données. C'est donc par la conception et l'utilisation d'une caméra à comptage de photons, la plus sensible au monde, couplée à un interferomètre de Fabry-Perot, qui constituent l'intrument FANTOMM, que les efforts se sont concentrés. Le chapitre 2, met en valeur les performances technologiques de la caméra (l'instrument au complet étant décrit dans l'annexe C).

Le troisième chapitre, met l'accent sur la sélection d'un échantillon de galaxies - *BHαBAR* - la réduction des données et l'analyse rigoureuse des champs non axisymétriques. Cet échantillon constitue le seul échantillon de galaxies spirales barrées homogène pour une étude à grande échelle.

Le quatrième chapitre aborde, ensuite, la dynamique d'une galaxie de l'échantillon - M100 - en essayant de comprendre, grâce à des modèles numériques, quelles sont les limites d'une méthode - la méthode de Tremaine & Weinberg - qui permet de déduire des observations du gaz ionisé, la fréquence de rotation des barres et des autres ondes stationnaires présentes dans une galaxie.

Le cinquième chapitre, enfin, propose l'application de la méthode précédente sur tout l'échantillon *BHαBAR* et propose de faire le lien entre l'étude des dispersions des vitesses et la position des résonances des orbites des étoiles.

Suivent, pour achever ce travail, la conclusion et les annexes qui présentent le reste du travail accompli, au cours de ces trois dernières années, grâce aux données obtenues par FANTOMM.

Chapitre 1

Du photon à la corotation

1.1 Instrumentation

L'astronomie est la seule science dont la plupart des sujets d'études ne peuvent être analysés qu'à distance, grâce à des télescopes. La lumière (ou onde électromagnétique) est le support de toute l'information nécessaire à l'astronome pour la compréhension de ces phénomènes physiques lointains. Il est donc important de récupérer le maximum de lumière et de s'assurer de la qualité des données pour en soustraire toute l'information pertinente. Les télescopes se chargent de récupérer le plus de lumière possible, corrigeant au besoin les variations de l'atmosphère. Suivent, attachés aux télescopes, divers instruments dont la fonction est de disséquer la lumière et de la projeter sur un détecteur pour pouvoir l'étudier sous toutes ses formes. Les détecteurs, quant à eux, la transforment pour la rendre accessible aux astronomes. À chacune de ces trois étapes de l'observation astronomique, une partie de cette lumière se détériore et se perd. Ce sont les qualités combinées des télescopes, des instruments et des détecteurs qui font la qualité des données recueillies et analysées. La section 1.1, sur l'instrumentation, présente d'abord l'utilité des caméras à comptage de photons, l'interférométrie de type Fabry-Perot et enfin l'instrument FANTOMM.

1.1.1 Beaucoup de bruit pour rien

Ces dernières années, l'acquisition de l'image d'un objet du ciel (étoile, nébuleuse, galaxie,...) a bien évolué. De la simple plaque photographique, l'astronomie s'est dirigée vers des détecteurs beaucoup plus sophistiqués.

Les CCDs

Dans le domaine de l'optique visible, c'est à dire pour des longueurs d'onde variant de 350 nm à 750 nm, les détecteurs CCD (pour "Charge Coupling Devices" ou en français "dispositifs à transferts de charge") font maintenant l'unanimité pour ce qui est de la recherche utilisant l'imagerie, la spectroscopie, l'interférométrie... Ces détecteurs sont composés de pixels. Chaque pixel qui reçoit un photon le convertit en électron qui est transféré dans un registre et est ensuite lu par un système électronique. Leur efficacité quantique, c'est à dire la capacité à transformer un photon de l'objet observé en électron, approche maintenant les 90% pour les CCDs dits "minces" et 40% pour les CCDs dits "épais". L'inconvénient principal de ces dispositifs est leur bruit de lecture quand s'effectue le transfert de la charge.

Dans le cas de flux élevés, le bruit de lecture est très faible comparé au signal et le CCD devient le meilleur compromis pour l'observation. Le rapport signal sur bruit (en anglais **S**ignal-to-**N**oise-**R**atio), est alors élevé ($SNR \geq 10$). Par contre, dans le cas de flux faibles, il devient très difficile de différencier si le signal reçu sur le détecteur est le bruit ou le signal lui-même. Le rapport SNR est alors bas ($SNR \leq 10$). Une discussion plus précise sur le rapport SNR est proposée dans le chapitre 2 de ce travail.

Les caméras à comptage de photons

Dans le cas de très faibles flux, il est donc nécessaire de faire appel à un dispositif dont le bruit de lecture est nul. Les détecteurs à comptage de photons fonctionnent de façon différente des CCDs. Ils sont composés à la fois d'un détecteur CCD à lecture rapide (entre 20 et 40 images par seconde) et d'un tube intensificateur d'image. Ce dernier, placé devant le CCD, a pour fonction d'amplifier le signal reçu (typiquement d'un facteur 10^7) afin de l'amener très largement au dessus du niveau du bruit de lecture du CCD utilisé. L'amplification se fait par effet photoélectrique. Une photocathode - de type AsGa (Arsenure de Gallium) dans le cas de FANTOMM - reçoit le photon, puis le transforme en électron avec une efficacité quantique de 30%. Une comparaison des efficacités quantiques entre les CCDs et les photocathodes des tubes intensificateurs d'images est donnée par la figure 16 du chapitre 2. Grâce à deux plaques de microcanaux (MCP) positionnées en chevron, l'électron généré est alors multiplié par application d'une haute tension entre la photocathode et l'écran de phosphore sur lequel les électrons amplifiés sont projetés. Le chevronnage favorise le comptage des photo-électrons dont l'angle d'incidence dans le canal est très faible, et permet d'obtenir une distribution de l'énergie des photo-électrons plus "pointue" donc mieux discriminable. Les nouveaux photons ainsi créés par l'écran de phosphore et sont aussitôt imagés sur le CCD. La figure 1 (Hernandez et al., 2003) résume le principe de l'amplification.

Le CCD est alors lu très rapidement afin de détecter les événements supérieurs à un minimum fixé, ainsi que pour éviter les phénomènes de non-linéarité (lorsque plus de deux photons tombent successivement sur le même pixel). Cependant, la vitesse de lecture ne doit pas être trop élevée pour éviter le problème de la rémanence des photons sur l'écran de phosphore (il y a rémanence lorsqu'un pixel a été saturé et qu'il reste du flux après la lecture d'une image, flux qui pourrait être alors de nouveau comptabilisé dans l'image suivante). Le signal reçu sur chaque image est alors clairement identifié comme un photon. Contrairement

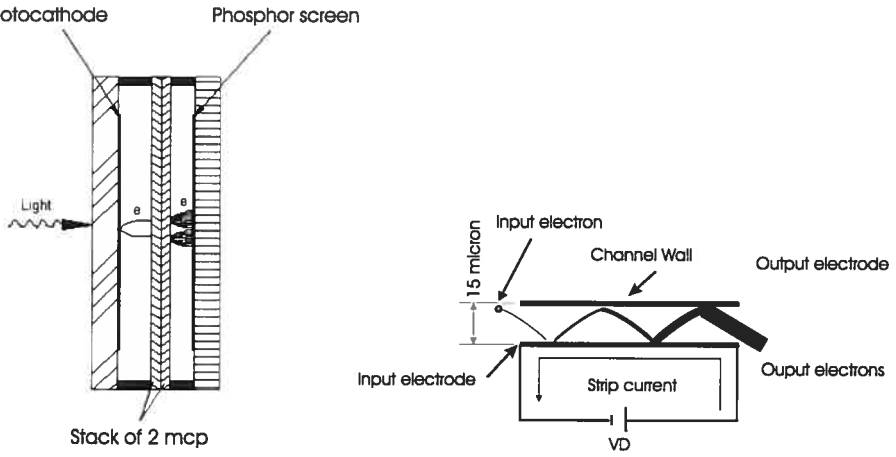

Fig. 1: **Gauche** : Principes d'amplification d'un intensificateur d'image avec l'utilisation de plaque de micro-canaux (MCP). **Droite :** Détail de l'amplification par haut voltage.

aux CCDs décrits auparavant, l'efficacité des systèmes à comptage de photons ne dépasse pas ici les 30%. Cependant, leur capacité à travailler pour de très faibles flux (ou des rapports SNR très petits) en font les meilleurs détecteurs pour les objets très peu lumineux.

Un autre avantage des caméras à comptage de photons est leur fonctionnement en mode **multiplex** d'observation. Dans le cas de l'interférométrie Fabry-Perot, afin de reproduire un spectre, il est nécessaire d'effectuer un balayage en longueur d'onde, c'est à dire d'obtenir plusieurs plans images (voir la section 1.1.2 pour les détails relatifs à la technique de l'interférométrie de type Fabry-Perot). Avec un CCD, chaque plan doit être exposé suffisamment longtemps pour que le rapport SNR soit suffisamment élevé. Ce temps est approximativement de 4 à 5 minutes par plan. Or, pour reconstituer le spectre total, c'est à dire imager la totalité des plans ou canaux, qui est typiquement de l'ordre de 40 canaux, le temps total d'observation requis sera donc de 2h30 à 3h00. Une telle durée pose, cependant, un problème pour les CCDs, car les conditions photométriques d'observation du ciel peuvent changer rapidement.

La masse d'air. L'objet observé change de position dans le ciel à cause de la rotation de la Terre pendant la durée de l'observation. La masse d'air, épaisseur d'atmosphère générant des perturbations de l'image, varie selon que l'objet est plus au moins proche du zénith. Plus l'objet est bas sur l'horizon, plus les couches d'atmosphère traversées par un photon provenant de l'objet sont épaisses et donc, plus la lumière se trouve déformée et subie des aberrations. Plus l'objet est proche du zénith, plus l'épaisseur de l'atmosphère sera petite

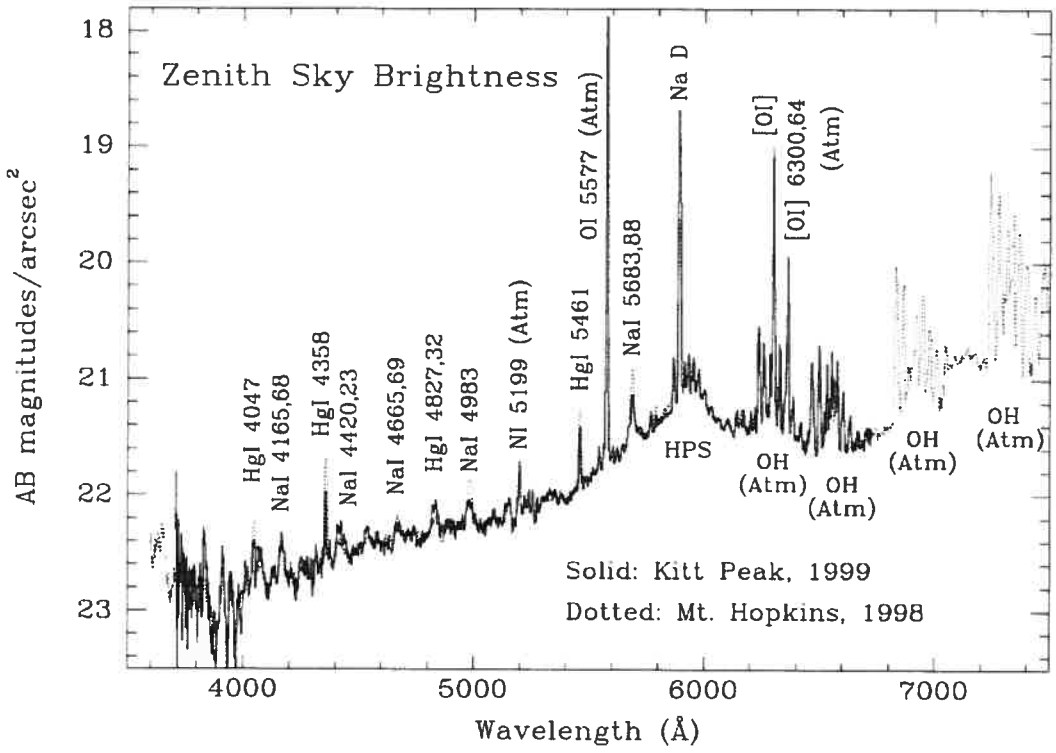

Fig. 2: Spectre du ciel nocturne, Massey & Foltz (2000)

et moins les rayons lumineux seront sensibles à cet effet. Les premiers canaux ne seront donc pas dans les mêmes conditions que les canaux finaux. L'information aura donc été déformée d'un canal à l'autre.

La variation du ciel nocturne. Les niveaux rotationels des radicaux OH qui peuplent la haute atmosphère du ciel (85 km d'altitude) causent une faible émission polychromatique qui pollue le signal étudié. Ces raies d'émission dont le spectre peut être vu sur la figure 2 varient en forme et en intensité sur un temps caractéristique d'une quinzaine de minutes. Dans le cas de l'utilisation de l'interférométrie Fabry-Perot, ce sont les variations d'intensité pixel à pixel qui sont mesurées physiquement et non pas la position d'une raie d'émission. À ce titre, un système tel que FANTOMM (décrit ci-après) est en fait un photomètre. Une normalisation photométrique de tous les canaux est donc nécessaire.

A ces deux effets, il faut aussi rajouter, les **variations de la transparence** du ciel et les **variations du continuum** (ex : lever de la Lune ou lever du jour).

Analyser des champs de vitesses obtenus avec un CCD requiert donc une maîtrise

totale de l'évolution photométrique et des raies du ciel au cours de l'observation. Ce n'est pas le cas avec le comptage de photons. Le temps de pose par canal est réduit à un temps élémentaire de 15 secondes (au lieu de 5 minutes en CCD) et le spectre total est rapidement constitué en quelques minutes. L'opération est répétée un certain nombre de cycles pour obtenir le bon rapport SNR désiré. Les variations photométriques et les raies sont donc facilement moyennées et normalisées naturellement, ce qui facilite leur suppression pour obtenir des champs de vitesses d'une qualité exceptionnelle.

1.1.2 L'interféromètre Fabry-Perot et le comptage de photons

La description de l'interférométrie de Fabry-Perot (FP) a déjà été faite maintes fois (Hernandez, 1986 (!) ; Amram, 1991 ; Vaughan, 1989 ; Plana, 1996 ; Blais-Ouellette, 1999 et Chemin, 2003) et le lecteur averti s'y réfèrera pour de plus amples informations. Mais dans un souci de clarté pour la compréhension globale de ce travail, un solide résumé est cependant présenté. Si on se limite à l'interférométrie FP à balayage piezo-électrique (les techniques de balayage par variation d'inclinaison ou de pression existaient depuis les années 1950), la route a été longue et la première publication remonte à Bates et al. (1966), suivie de plusieurs autres jusqu'à la principale Kicks et al. (1975).

L'interféromètre de FP, ou encore le FP, est un étalon constitué de deux lames à faces parallèles semi-réfléchissantes dont les faces intérieures sont recouvertes d'un dépôt de multicouches à très fort pouvoir de réflexion. L'espace entre les deux lames est généralement constitué d'air ou d'azote sec dont l'indice optique est voisin de l'unité.

Afin d'utiliser le FP dans les meilleures conditions, c'est à dire pour obtenir une résolution spectrale uniforme, celui-ci doit être placé dans un faisceau parallèle. Cette configuration permet l'obtention d'anneaux d'interférences à l'infini. Le réducteur de focale est optimal dans le cas de l'astronomie pour utiliser le FP dans ce mode de fonctionnement. Le FP, placé dans la pupille conjuguée de la pupille du télescope (voir figure 6), entre le collimateur (voir figure 3 L1) et l'objectif (voir figure 3 L2), est alors imagé sur le plan focal du réducteur de focale. Les interférogrammes sont ensuite recueillis par la caméra à comptage de photons.

La lumière pénétrant entre les lames du FP est réfléchie une infinité de fois. Chaque réflexion laisse passer une partie de la lumière avec un déphasage Φ. Des interférences à ondes multiples ont lieu à l'infini.

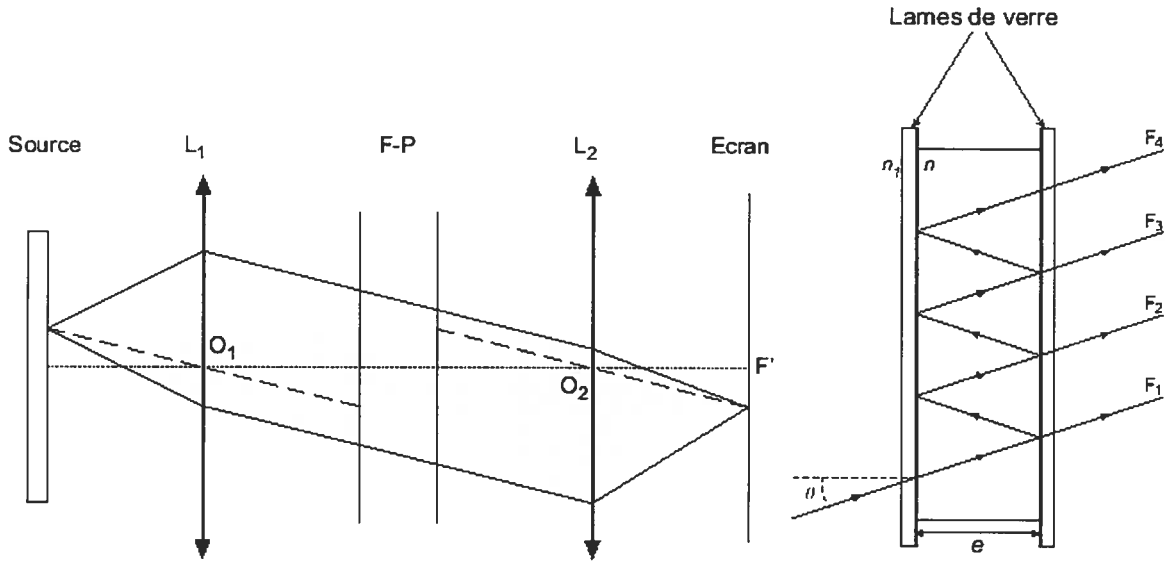

Fig. 3: **Gauche :** Anneaux interférométriques produit par un système imageur fonctionnant avec un interféromètre de Fabry-Perot. **Droite :** réflexions multiples entre les deux lames à faces parallèles.

L'intensité globale transmise obtenue à la sortie du FP s'exprime sous la forme :

$$I = \left(\frac{\tau}{1-\rho}\right)^2 \frac{1}{1+\frac{4F_\rho^2}{\pi^2}\sin^2\Phi/2}, \tag{1.1}$$

où τ est le coefficient de transmission, ρ le coefficient de réflexion, $\Phi = 2\pi \times \frac{2ne\cos\theta}{\lambda}$ la phase et $\mathrm{F}_\rho = \frac{\pi\sqrt{\rho}}{1-\rho}$ la finesse spatiale de l'interféromètre.

L'intensité I est maximale pour des interférences constructives, c'est à dire, quand Φ est un multiple de π, où encore lorsque : $p\lambda = 2ne\cos\theta$, avec n l'indice de réfraction optique du mileu considéré entre les deux lames (air ou azote sec), e l'espacement entre les deux lames, λ la longueur d'onde du faisceau de lumière, θ l'angle d'incidence des rayons sur le FP. Ce dernier représente l'angle sous lequel l'objet étudié est vu. p est appelé ordre d'interférence à la longueur d'onde λ.

La fonction $\frac{1}{1+\frac{4F_\rho^2}{\pi^2}\sin^2\Phi/2}$ est la fonction d'Airy qui caractérise les interférences liées au FP. Elle est représentée sur la figure 4 pour différentes valeurs de ρ (de haut en bas : ρ=0.2, 0.4, 0.6 et 0.9).

L'intervalle entre deux pics successifs s'apelle l'intervalle spectral libre (ISL) ou interfrange. Pour un angle fixe θ, en faisant varier l'épaisseur e entre les deux lames, il est

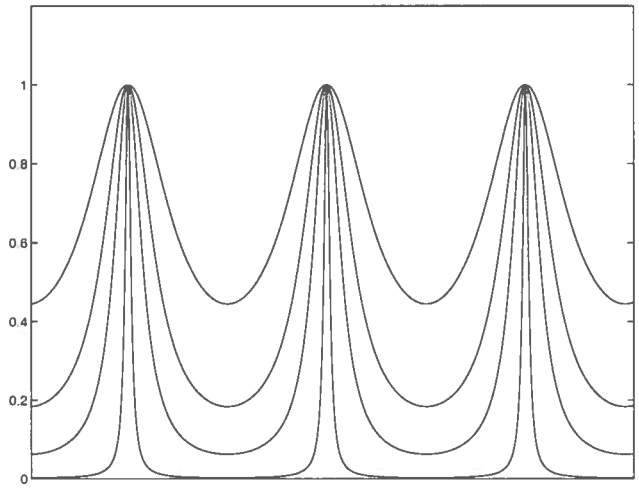

Fig. 4: La fonction de Airy en fonction de la longueur d'onde, présentée pour trois ordres successifs. Les différentes courbes correspondent à différentes valeurs de la Finesse.

possible de balayer l'intervalle spectral libre. Ainsi, pour échantillonner un spectre de l'ISL, il suffit de balayer par pas de e/n, n plans successifs - interférogrammes - appelés canaux.

Afin de contrecarrer les problèmes liés à la périodicité de la fonction d'Airy, des filtres interférentiels de bande passante très étroite, sont placés dans le plan focal du télescope pour ne sélectionner qu'un seul ISL et, ainsi, lever la dégénérescence sur la valeur de p. Ces filtres sont choisis de façon à ce qu'ils correspondent à la longueur d'onde de la galaxie observée. Il est donc utile, soit de constituer une banque de filtres interférentiels - tel que l'ont fait l'Observatoire du mont Mégantic et l'Observatoire de Marseille, soit de faire appel à un filtre ajustable (FP dont on peut faire varier l'épaisseur e dans de plus grandes proportions).

La position des anneaux dans le plan focal ne dépendra donc, pour une épaisseur e donnée, que de la longueur d'onde observée et de l'angle θ, angle d'incidence des rayons parallèles sur la face d'entrée du FP. Sur chaque pixel, en balayant successivement les canaux, l'intensité de la lumière reçue varie et il est ainsi possible de reconstruire le spectre lumineux du point considéré. Une condition toutefois, est de lever la dégénérescence entre le couple (θ, λ) (source étendue, non monochromatique telle que les galaxies observées), en prenant soin de faire des calibrations à une longueur d'onde connue et de comprendre ainsi les interférogrammes pour des variations de θ uniquement. La figure 5 schématise la reconstuction du spectre en chaque pixel du détecteur.

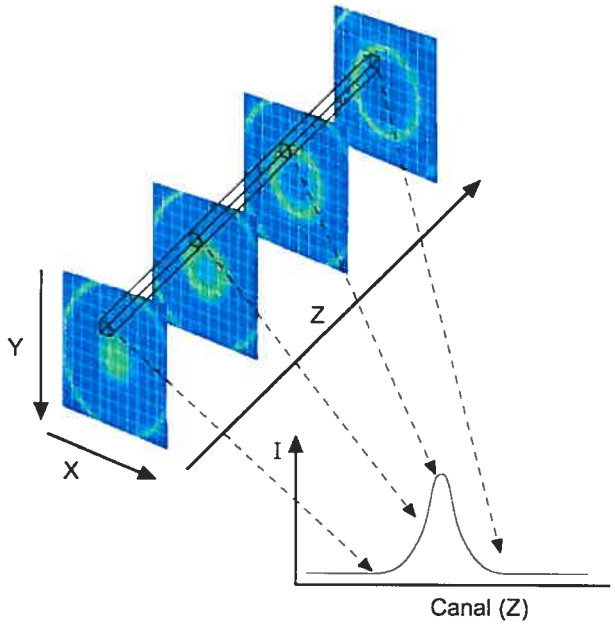

Fig. 5: Reconstruction d'un profil par balayage successif des canaux. x et y représentent le plan du détecteur, l'axe z perpendiculaire à ce plan est l'axe des longueurs d'onde ou des vitesses.

1.1.3 FaNTOmM

Le projet FaNTOmM, pour **Fa**bry-Perot de **N**ouvelle **T**echnologie pour l'**O**bservatoire du **m**ont **M**égantic, `www.astro.umontreal.ca/fantomm`, est donc la symbiose de quatre composantes, une **caméra à comptage de photons** ultraperformante, de bruit de lecture nul et pouvant fonctionner en mode multiplex très rapide, **un réducteur de focale** accueillant **l'étalon Fabry-Perot** et une banque de **filtres** interférentiels. FaNTOmM est une collaboration entre le Laboratoire d'Astrophysique Expérimentale (LAE) de Montréal et le Laboratoire d'Astrophysique de Marseille (LAM). Le design opto-mécanique et le système de refroidissement révolutionnaire utilisant un tube de Ranque-Hilsh (voir le chapitre 2) ont été développés au LAE par Olivier Hernandez. Les parties électronique et logicielle (ADHOCw, Boulesteix (2004)) ont été développées au LAM respectivement par Jean-Luc Gach et Jacques Boulesteix.

FaNTOmM a été construit sous un contrat d'ingénieur d'une durée d'un an qui m'a été attribué avant de commencer cette thèse. Plus de la moitié de cette thèse, a été consacrée à finir le développement de cette caméra, proposer un mode d'emploi pour la rendre utilisable

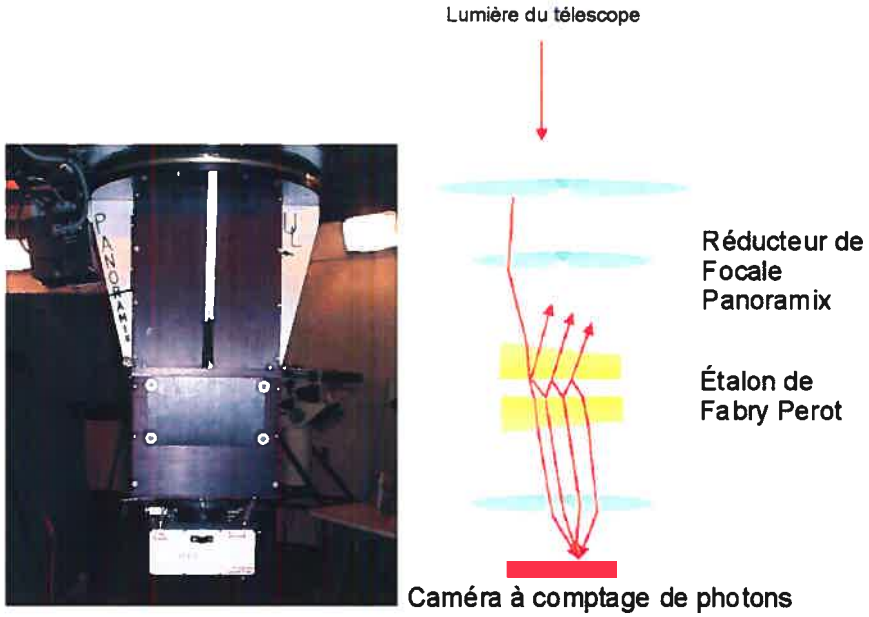

Fig. 6: FANTOMM à l'observatoire du mont Mégantic.

par tous et enfin l'adapter sur plusieurs autres télescopes. Cette thèse se veut un ensemble complet depuis la conception de l'instrument jusqu'à la compréhension physique des rotations des barres dans les spirales, en passant par la prise de données, son analyse et sa modélisation.

Il faudrait plus qu'une thèse pour décrire toutes les avancées techniques qui ont été accomplies au cours des quatre dernières années. Mais pour conclure cette partie instrumentale, le plan suivant résume les étapes importantes franchies au cours de ce doctorat au niveau instrumental.

- Mise en place du site Web
- Première lumière de FANTOMM sur le 3.6 m de l'ESO
- Conception et design d'un adaptateur optique pour le CFHT. Voir Annexe D
- Première lumière de FANTOMM sur le 3.6 m du CFHT. Total de 2 missions d'observations.
- Achat d'une banque de filtres interférentiels pour l'utilisation de FANTOMM
- Achat et installation d'un spectrophotomètre pour l'étude du vieillissement des couches minces des filtres interférentiels et des Fabry-Perot.
- Développement d'un laboratoire muni d'une table optique pour le test, la calibra-

tion et le développement d'un contrôleur de Fabry-Perot pour FaNTOmM et les projets connexes pour les grands télescopes.

1.2 Champs de vitesses et modèles de masse

1.2.1 Composantes d'une galaxie

Les galaxies sont classées suivant trois grandes classes ; les galaxies elliptiques, les galaxies spirales et les galaxies irrégulières. Les galaxies spirales sont l'objet de la présente étude. Les quatre structures principales qui composent une galaxie spirale sont décrites dans ce paragraphe, les barres sont étudiées plus en profondeur dans la section 1.3.

Le bulbe Fait d'étoiles vieilles de population II. Il est présent généralement sous forme de structure sphérique dans la plupart des spirales. Sa taille évolue en fonction du type morphologique et disparaît pour des galaxies dont le type est dit tardif, voir figure 9. L'étude des galaxies vues par la tranche montre de nos jours que le bulbe peut être sous forme de boîte cacahouète (García-Burillo et al., 1999). Il serait probablement le nid d'un barre (Bureau & Freeman, 1999).

Le disque Composé d'étoiles, de poussières et de gaz. On y retrouve des étoiles jeunes de population I. Il est le siège d'ondes quasi-stationnaires générant la structure spirale (cf. ci après). Le disque de gaz est généralement plan mais peut être gauchi à de grands rayons. La formation d'étoiles y est plus ou moins active, dépendant du type morphologique de la galaxie.

Le halo stellaire Halo d'étoiles vieilles de population II semblables à celles du bulbe. Sa forme est plus ou moins sphérique et des amas globulaires y sont présents en grands nombres.

Le halo de matière non lumineuse La matière non lumineuse, plus souvent appelée matière sombre ou masse manquante, est présente dans toute la galaxie. Il est encore de nos jours bien compliqué de donner une forme à cette composante de matière non lumineuse. Plusieurs hypothèses sur sa nature sont toujours à valider : (1) nature baryonique "ordinaire", sous forme d'objets compacts et sombres (naines blanches et brunes, gaz froid, mini-trous

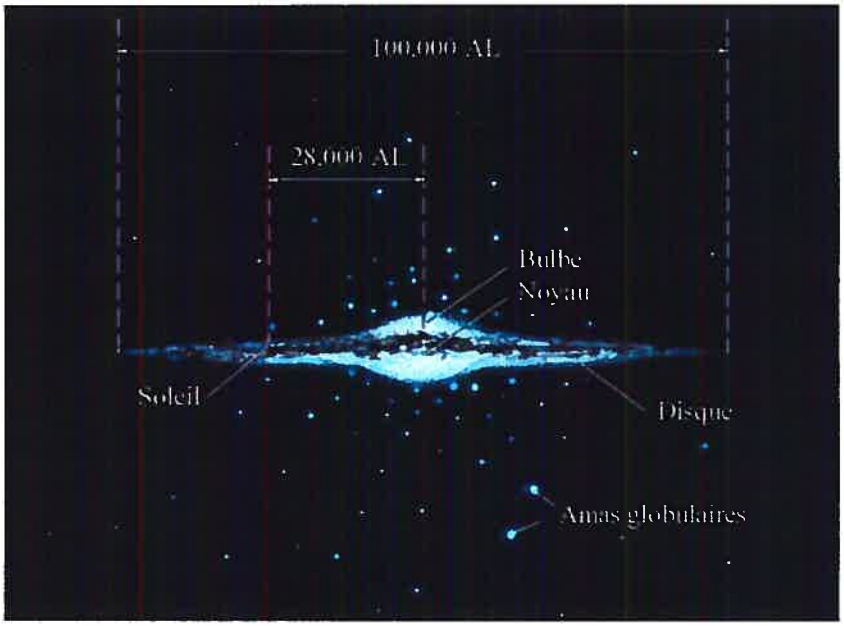

Fig. 7: La Voie Lactée, structure et composantes (Carignan et al., 2003).

noirs, etc...), (2) les lois de la gravité de Newton ne s'appliquent pas aux grandes échelles des galaxies, c'est la théorie de MOND - **Mo**dified **N**ewtonian **D**ynamics (Milgrom, 1983) et (3) la matière sombre est composée de matière exotique dont l'existence n'est encore qu'hypothétique, ce sont les WIMPs - **W**eakly **I**nteractive **M**assive **P**articules.

La figure 7 donne un aperçu de la forme de notre Galaxie, la Voie Lactée.

1.2.2 Les différentes formes de l'hydrogène

Bien que la masse totale du gaz ne représente qu'une très petite partie de la masse totale d'une galaxie, c'est pourtant un élément très important. C'est, en effet, un traceur des effets gravitationnels sous toutes ses formes : neutre, moléculaire ou ionisé. Depuis des années, les études de l'effet Doppler-Fizeau des lignes d'émission du HI, CO (traceur de l'hydrogène moléculaire H_2) et Hα, ont permis d'améliorer la connaissance de la cinématique et de la distribution de masse dans les galaxies spirales.

L'hydrogène neutre HI L'émission à la longueur d'onde 21 cm, dans le domaine radio du spectre électromagnétique, de la transition entre les deux niveaux de la structure hyperfine de l'hydrogène $J = 1 \longrightarrow J = 0$ rend possible la détection de l'hydrogène

neutre. Les radiotélescopes permettent de constater que le gaz HI est présent dans les disques de galaxies, notamment dans les bras spiraux, mais peut être absent au centre des galaxies. Le gaz HI s'étend de l'ordre de un à plusieurs fois le rayon optique du disque, dépendant du type morphologique de la galaxie. Cependant, la faible résolution des radiotélescopes amène souvent à une sous-estimation des vitesses de rotation quand des gradients de vitesses sont présents. C'est, en général, le cas des parties centrales des galaxies. La composante ionisée de l'hydrogène est alors utilisée.

L'hydrogène moléculaire H_2 Le gaz H_2 - deux atomes d'hydrogène s'associent pour former une molécule de di-hydrogène H_2 - n'est pas directement observé (sauf dans le domaine de l'ultra-violet). Présent dans les régions denses ($\propto 10^3$ particules/cm^3) de la galaxie, à une température de 10 K, c'est par l'intermédiaire du gaz CO que sa détection est possible grâce aux raies de transitions rotationnelles CO(2-1) à 1.3 mm et CO(1-0) à 2.6 mm. Le CO est observé en forte concentration dans le centre des galaxies, les bras spiraux, les anneaux et les barres.

L'hydrogène ionisé Formé dans les régions où sont présentes des étoiles chaudes, jeunes et massives de type spectraux O et B, plusieurs de ses raies sont observables. Pour les galaxies les plus proches, deux sont généralement étudiées : la transition Hα (λ = 6563 Å) et la transition $H\beta$ (λ = 4863 Å) de la série de Balmer. Ces régions sont appelées les régions HII et possèdent une température de l'orde de 10^4 K et sont le signe de formation d'étoiles. L'émission Hα se retrouve principalement dans les bras spiraux et là où on retrouve des zones de choc comme les anneaux autour du bulbe. Sous une forme ionisée diffuse, le Hα se retrouve principalement dans les régions inter bras des galaxies ou dans des filaments de galaxies dans des environnements non isolés. Grâce aux techniques de spectroscopie à haute résolution spatiale et spectrale, telle que FANTOMM, il est possible de mieux comprendre les gradients de vitesses et les centres galactiques contrairement au HI.

1.2.3 Les champs de vitesses

La forme ionisée Hα (par abus de language, le Hα) est utilisée comme traceur de la cinématique de la galaxie. Un instrument comme FANTOMM utilise cette longueur d'onde afin de produire des interférrogrammes. C'est grâce à un double effet Doppler-Fizeau que des cartes de vitesses d'une galaxie peuvent être produites. D'où provient ce double effet ? Il y a

tout d'abord un premier décalage de la raie Hα ($\lambda = 6562.8$ Å au repos) vers les longueurs d'onde rouges dû à l'éloignement global de la galaxie à une certaine vitesse d'échappement (ou rapprochement) - dite vitesse systémique - par rapport au Soleil. Le deuxième décalage provient de la rotation de la galaxie sur elle-même. Le côté qui s'éloigne de l'observateur sera donc plus décalé vers le rouge que celui qui s'approche de lui. La figure 8 illustre le système de coordonnées utilisé et la notion d'éloignement et de rapprochement.

Le décalage spectral, déduit des interférogrammes observés, est transformé en décalage en longueur d'onde selon la relation suivante :

$$\frac{\lambda_{\rm obs} - \lambda_{\rm repos}}{\lambda_{\rm repos}} = \frac{V_{\rm obs}}{c},$$

où c est la vitesse de la lumière dans le vide, le tout en tenant compte des calibrations faites pour replacer correctement l'origine des longueurs d'ondes. Dans ces conditions, la vitesse observée $V_{\rm obs}(x, y)$, le long de la ligne de visée, dans le plan du ciel s'écrit :

$$V_{\rm obs}(x, y) = V_{\rm sys} + V_{\rm rot}(R)\cos\theta\sin i + V_{\rm exp}(R)\sin\theta\sin i + V_{\rm z}\cos i, \qquad (1.2)$$

avec (x, y) les coordonnées cartésiennes dans le plan du ciel, (R, θ) les coordonnées polaires dans le plan de galaxie, $V_{\rm sys}$ la vitesse systémique de la galaxie, $V_{\rm rot}(R)$ la vitesse de rotation dans le plan de galaxie, $V_{\rm exp}(R)$ la vitesse d'expansion dans le plan de galaxie et $V_{\rm z}$ la vitesse perpendiculaire au plan galactique. En première approximation, $V_{\rm exp}(R)$ et $V_{\rm z}$ sont considérées comme étant nulles ou négligeables par rapport à $V_{\rm rot}(R)$.

L'étude de $V_{\rm obs}(x, y)$ conduit donc directement à la vitesse $V_{\rm rot}(R)$ qui est fondamentale dans la compréhension de la dynamique de la galaxie étudiée. Il convient alors de déterminer précisément le centre cinématique, l'angle d'inclinaison de la galaxie, l'angle de position sur le ciel (voir figure 8) et la vitesse systémique de la galaxie pour trouver de manière très rigoureuse $V_{\rm rot}(R)$. Toutes ces étapes sont réalisées grâce au logiciel GIPSY (Begeman, 1987) et ses routines ROTCUR et VELFI, telles que décrites dans le chapitre 3 et dans l'annexe A.

1.2.4 Problématique des champs non axisymétriques

De la vitesse de rotation circulaire d'une galaxie, il est possible de déduire le potentiel et donc de remonter à la masse totale de la galaxie, sachant que :

$$V_{\rm circ}^2(r) = r\frac{\partial\Phi}{\partial r}, \qquad (1.3)$$

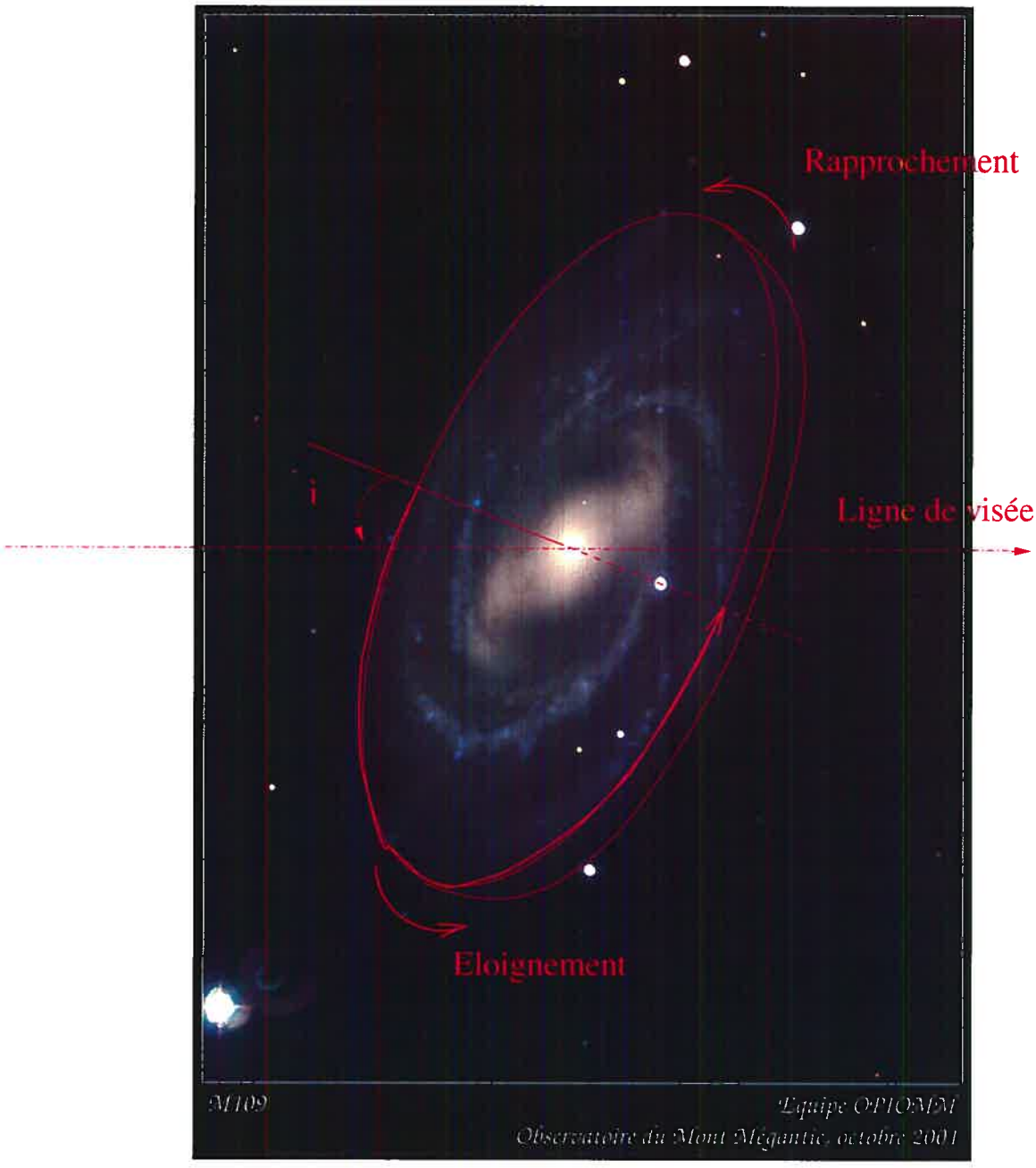

Fig. 8: Disque galactique en rotation. i représente l'inclinaison de la galaxie par rapport à la ligne de visée. Le plan de la galaxie est représenté par l'ellipse rouge dont l'épaisseur a été matérialisée par un effet de perspective.

avec, par exemple, $\Phi = \Phi_{\text{halo}} + \Phi_{\text{disque}}$ = le potentiel total de la galaxie, simplifié ici à la somme des potentiels d'un disque et d'un halo de matière non lumineuse, r étant le rayon galactocentrique. Dans le cas d'un champ purement axisymmétrique $V_{\text{rot}}(R) = V_{\text{circ}}(r)$, c'est à dire que la vitesse observée est directememnt reliée à la vitesse circulaire. La masse de la galaxie peut donc être déduite sans trop de difficultés. C'est d'ailleurs sous cette hypothèse d'axisymmétrie que les allures des courbes de rotation ont démontré l'existence d'un potentiel d'un halo de matière non lumineuse dans les galaxies. La partie plate à grands rayons galactocentriques des courbes de rotation ne pouvant s'expliquer par une décroissance quasi-képlérienne classique (comme dans notre système solaire) des disques exponentiels, la nécessité d'une matière dite "sombre" - que l'on qualifiera de non-lumineuse, c'est à dire n'émettant pas de lumière mais dont l'existence est prouvée par ses effets gravitationnels - s'imposa d'elle même.

Mais qu'arrive-t-il lorsque $V_{\text{rot}}(R)$ ne représente pas uniquement les mouvements circulaires dans une galaxie ? Il est alors très difficile d'affirmer que la relation est toujours vérifiée sans y ajouter un terme correctif. Certes au premier ordre, elle reste vraie et suffisante, mais les récents travaux montrent que des erreurs sur la masse de la galaxie et de chacune de ses composantes peuvent être très grandes. D'ailleurs, les modèles de masse issus des courbes de rotation sont extrêmement sensibles non pas à la partie plate de la courbe à de grands rayons, mais plutôt aux parties internes, à petits rayons. Ces parties internes des courbes de rotation sont généralement des courbes croissantes et sont les zones clés pour la contrainte des paramètres libres des modèles de masse Blais-Ouellette et al. (1999b, 2001, 2004). L'effet d'une barre peut modifier cette partie croissante et il convient de bien comprendre la cinématique de la barre, donc des mouvements non circulaires, pour corriger les courbes de rotation et obtenir la vitesse circulaire de laquelle sera déduite la masse exacte de la galaxie.

Enfin, les barres si elles transfèrent énergie et moment angulaire à d'autres structures de la galaxie (voir ci-après), ont elles une influence sur la quantité de matière non lumineuse dans les galaxies spirales ?

1.3 Les galaxies spirales barrées

Il existe deux types de galaxies spirales, les spirales normales (SA) et les spirales barrées (SX ou SB) dans la classification de de Vaucouleurs. Parmi les barrées, on en distingue deux types. De façon historique, cela provient du fait qu'il était plus évident de bien voir certaines barres par rapport à d'autres, avec les moyens technologiques disponibles. C'est l'avènement des détecteurs infrarouges qui a permis de mieux percevoir les barres. Les deux types sont les suivants :

- Type SB de SB0 à SB9 dit type barré, la barre est évidente.
- Type SAB ou SX de 0 à 9 dit type intermédiaire, la barre est moins évidente (parfois dû à l'inclinaison de la galaxie dans le plan du ciel) et nécessite des observations plus fines.

De Vaucouleurs et al. (1991) ont classé les galaxies, voir figure 9, selon différents critères morphologiques. Les galaxies elliptiques y sont représentées à gauche et les spirales à droite. Les galaxies irrégulières sont présentes à l'extrême droite de cette figure. Le long de cette séquence (Sa $\longrightarrow$ Sb $\longrightarrow$ Sc) le rapport bulbe sur disque décroît des types précoces (Sa) aux types tardifs (Sc et plus).

Les barres sont des structures multi-axiales (2 ou 3 axes) que l'on peut considérer comme des ellipsoïdes. Dans le plan du disque de la galaxie, le rapport des axes est très grand (de 2 à 5). Les barres seraient même visibles dans des galaxies vues par la tranche. Un bulbe ayant une forme de cacahouète ("peanut-bulge") ou de boîte ("boxy-bulge"), serait en fait une barre vue par sa tranche (Bureau & Freeman, 1999).

La présence d'une barre dans une galaxie spirale semble être une structure habituelle puisque près de 30% des galaxies spirales sont barrées (De Vaucouleurs et al., 1991) et un autre 25% sont faiblement barrées. Hackwell & Schweizer (1983) remarquèrent que les barres sont plus fréquentes dans le domaine de l'infra-rouge que dans celui de l'optique. Ceci est dû au fait que les observations dans le visible sont plus sensibles à l'extinction par la poussière interstellaire que dans l'infra-rouge (IR). Plus récemment, des études dans le proche IR ont démontré que 75% des galaxies à forte brillance de surface possédaient une barre plus ou moins prononcée (Knapen et al., 2000b ; Eskridge et al., 2000).

La création de couples de forces gravitationnelles générés par le potentiel d'une barre, dans une galaxie, peut orchestrer l'évolution des galaxies. Il y a alors transfert de moment cinétique de l'extérieur vers l'intérieur de la galaxie permettant à la galaxie de se

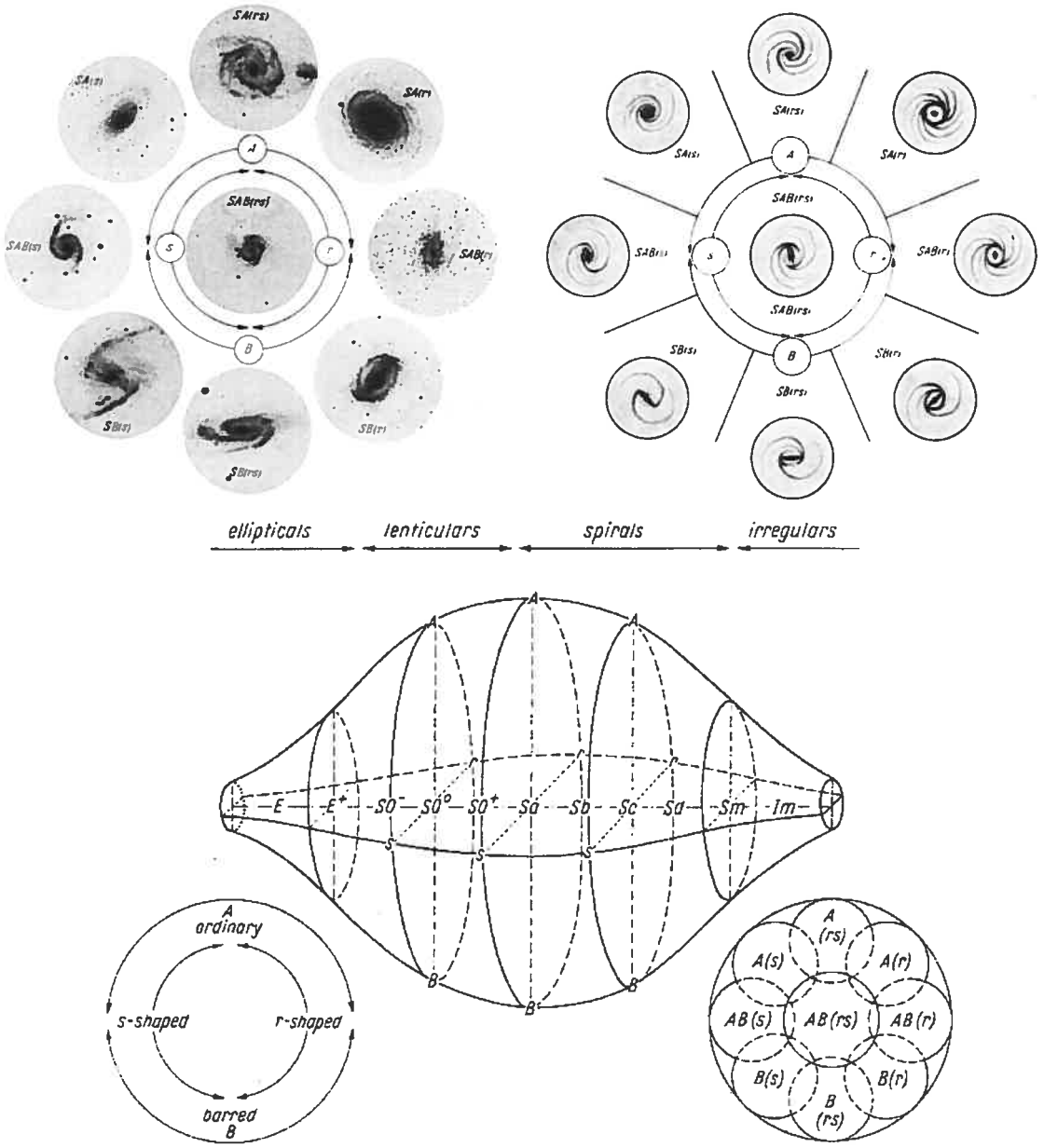

Fig. 9: La classification de de Vaucouleurs (De Vaucouleurs et al., 1991).

construire grâce à ces mouvements radiaux de matière (Buta & Combes, 1996).

Stabilité d'un disque

Les disques des galaxies sont des objets très "fragiles" et très sensibles à leur environement. Généralement, les disques qui possèdent de grandes dispersions de vitesses sont très affectés par les perturbations externes. Toomre (1964) a proposé un critère Q pour quantifier la stabilité d'un disque en un point r, impliquant la densité de surface $\Sigma(r)$, la dispersion moyenne des vitesses radiales $\sigma(r)$ et la fréquence épicyclique κ. La relation est la suivante :

$$Q \equiv \frac{\sigma(r)}{3.4\frac{G\Sigma(r)}{\kappa}} > 1. \tag{1.4}$$

Lorsque $Q < 1$, le disque devient instable et il y a automatiquement formation de barre. C'est un des mécanismes clés dans la formation des barres stellaires. Dans le voisinage du système solaire, pour $\sigma(r) \simeq 40\,\mathrm{km\,s^{-1}}$, $\kappa \simeq 35\,\mathrm{km\,s^{-1}\,kpc}$ et $\Sigma(R_\odot) \simeq 80 \pm 10 M_\odot/\mathrm{pc}^2$, $Q_\odot \simeq 1.2$ implique que le disque galactique peut être considéré comme marginalement stable.

Théorie des ondes de densité et de la structure spirale

Certaines constatations s'imposent d'elles mêmes en étudiant la structure spirale des galaxies. Les bras spiraux sont composés d'étoiles différentes à différents moments. La structure spirale est donc un phénomène d'ondes stationnaires ou quasi-stationnaires décrit par la théorie de Lindblad (1963) et Lin & Shu (1964).

Deux types d'ondes peuvent se propager dans beaucoup de représentations physiques de phénomènes, les ondes progressives et les ondes stationnaires. Les ondes progressives avancent dans l'espace, les ondes stationnaires, au contraire, oscillent sans se déplacer. À un temps t fixé, une onde stationnaire ressemble à une onde progressive. En revanche, son évolution temporelle est totalement différente. Une onde stationnaire possède des minimas (nœuds) et des maximas (ventres) d'amplitude fixes dans l'espace. Ainsi, en se plaçant aux nœuds de cette onde, l'amplitude est nulle quelque soit le temps. Avec une onde progressive, au même endroit, l'amplitude évolue de façon sinusoïdale avec le temps dans le cas d'une onde harmonique. Une façon simple de construire une onde stationnaire est de superposer deux ondes progressives se propageant en sens inverse. C'est d'ailleurs ce qui se passe lorsque une onde se réfléchit sur un miroir parfait. Les ondes stationnaires sont des objets physiques

très courants et se rencontrent notamment dans les cavités laser ou les lignes hyperfréquences et dans les galaxies.

De cette théorie, il découle que les barres peuvent favoriser la formation des bras spiraux (lorsqu'une barre est présente, les bras spiraux partent souvent du bout de la barre). Les ondes de densité peuvent générer barres et structures spirales et peuvent avoir des fréquences de rotation différentes (Grosbøl et al., 2004). Ces phénomènes peuvent s'amplifier et s'autogénérer et/ou se détruire, par résonances et couplage entre les ondes de densité (Tagger et al.,1987 ; Sygnet et al., 1988).

L'évolution séculaire des galaxies est donc fondamentale. Si les études de la formation d'une galaxie et de son évolution se sont toujours penchées soit sur un événement initial, soit sur une évolution subséquente des fusions ("mergers") entre galaxies ou interactions, un autre phénomène peut faire évoluer les galaxies. L'évolution séculaire est le résultat de l'interaction des différentes composantes même d'une galaxie. Par exemple, une barre dont la vitesse angulaire de rotation est différente du reste de la galaxie, peut redistribuer son énergie et son moment angulaire et forcer la galaxie à évoluer (Kormendy, 1993).

De plus, les simulations N-corps prenant en compte gaz et étoiles (Shaw et al., 1993) et les simulations SPH (Heller et al., 2001) ont révélé l'importance des mouvements radiaux de matière et la présence d'ondes imbriquées et de systèmes nucléaires découplés (barres et spirales nucléaires). L'hypothèse, selon laquelle les barres nucléaires seraient les moteurs d'accrétion de gaz alimentant un éventuel trou noir central, est fondamental et permettrait de mieux comprendre les noyaux actifs de galaxies.

Enfin, les interactions entre galaxies peuvent déclencher et amplifier les phénomènes ondulatoires et conduire à des spirales très bien définies (M51 et M81).

1.3.1 Approximation des épicycles

Cette section a pour objet de poser les bases théoriques à la compréhension de la dynamique des spirales barrées. Pour bien cerner la thématique des barres dans les spirales, il est nécessaire de comprendre les principales caractéristiques des orbites stellaires dans un potentiel ϕ de galaxie. Pour cela, ϕ est décomposé en deux termes. L'un, φ_0 correspondant à la partie axisymétrique de la galaxie et l'autre, ψ correspondant à la perturbation introduite par la barre : $\phi(r,\theta,z) = \varphi_0(r,z) + \psi(r,\theta,z)$, dans un système de coordonnées cylindriques pour simplifier l'écriture (Binney & Tremaine, 1987).

Cas d'un potentiel axisymétrique ($\psi = 0$)

L'équation du mouvement pour une particule (une étoile), dans une représentation N-corps de la galaxie, s'écrit :

$$\frac{d^2\vec{r}}{dt^2} = \ddot{\vec{r}} = \vec{\nabla}\varphi_0(r,z), \tag{1.5}$$

avec $\vec{r} = r\vec{e_r} + z\vec{e_z}$ dans le repère de coordonnées cylindriques de la galaxie.

$$\ddot{r} - r\dot{\theta}^2 = -\frac{\partial\varphi_0}{\partial r}, \qquad \ddot{z} = -\frac{\partial\varphi_0}{\partial z}, \tag{1.6}$$

$$\frac{dL_z}{dt} = \frac{d(r^2\dot{\theta})}{dt} = 0, \tag{1.7}$$

où L_z est le moment cinétique ("angular momentum" en anglais). Cette dernière relation exprime la conservation, sur l'axe z, du moment cinétique.

L'introduction de ϕ_{eff}, potentiel effectif, $\phi_{\text{eff}} = \varphi_0 + \frac{L_z^2}{2r^2}$, permet d'écrire :

$$\ddot{r} = -\frac{\partial\phi_{\text{eff}}}{\partial r}, \tag{1.8}$$

$$\ddot{z} = -\frac{\partial\phi_{\text{eff}}}{\partial z}. \tag{1.9}$$

$\Omega(R)$ représente la vitesse (ou fréquence angulaire) de l'orbite circulaire au rayon galactocentrique R, ainsi :

$$\Omega(R)^2 = \frac{1}{R}\left(\frac{\partial\varphi_0}{\partial r}\right)_{(R,z=0)} = \frac{L_z^2}{R^4}. \tag{1.10}$$

L'orbite d'une étoile quasi circulaire peut donc être considérée, au premier ordre d'un développement en série de Taylor du potentiel effectif, comme une oscillation épicyclique de fréquence horizontale κ :

$$\kappa^2 = \left(\frac{\partial^2\varphi_0}{\partial r^2}\right)_{(R,z=0)} + \frac{3L_z^2}{R^4} = \left(r\frac{d\Omega^2}{dr} + 4\Omega^2\right)_{(R,z=0)} \tag{1.11}$$

et de fréquence verticale ν :

$$\nu^2 = \left(\frac{\partial^2\phi_{\text{eff}}}{\partial z^2}\right). \tag{1.12}$$

Dans cette approximation de l'épicycle, l'orbite d'une étoile, dans le plan galactique, est donc la composition d'un mouvement circulaire prograde de rayon R, autour du centre O, de vitesse angulaire Ω et d'une oscillation dite "épicyclique" rétrograde de fréquence angulaire κ autour du centre C de l'ellipse tel qu'illustré sur la figure 10.

Les limites des valeurs de κ sont définies par les valeurs extrêmes que cette valeur peut prendre. Ainsi, trois cas de figures sont à noter :

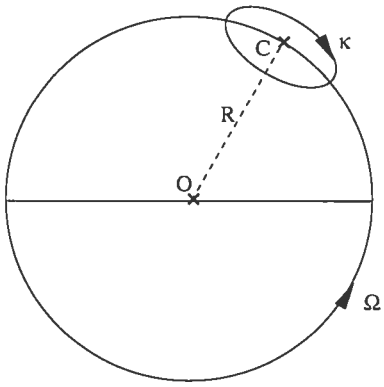

Fig. 10: Schématisation des épicycles dans une galaxie.

Rotation d'un corps solide $\Omega(R)$ = Constante. C'est le cas, en général, des parties centrales d'une galaxie. Alors, $\kappa = 2\Omega$.

Vitesse de rotation constante $\Omega(R) \propto R^{-1}$, dans ce cas $\kappa = \sqrt{2}\ \Omega$.

Vitesse de rotation képlérienne $\Omega(R) \propto R^{-3/2}$, qui est la décroissance la plus rapide pour une courbe de rotation, dans ce cas-ci, $\kappa = \Omega$.

Donc, κ varie dans un intervalle allant de Ω à 2Ω.

Cela veut dire que les étoiles oscillent tout doucement autour de leurs orbites circulaires et, qu'en général, elles ne sont pas fermées. L'action d'une perturbation avec une fréquence de rotation Ω_p^B - fréquence de rotation de la barre en $\mathrm{km\,s^{-1}\,kpc^{-1}}$ - (généralement de l'ordre de 10% en masse ou en terme de potentiel), va favoriser la fermeture des épicycles, ce sont les résonances.

Cas d'un potentiel non-axisymétrique ($\psi \neq 0$)

La barre d'étoiles, qui tourne dans la galaxie à la vitesse angulaire Ω_p^B, crée un potentiel bisymétrique (sa décomposition en série de Fourier comporte le terme prépondérant m=2, voir ci-après), telle que $\psi \neq 0$. Dans le référentiel tournant de la barre, le potentiel est indépendant du temps et, toujours en coordonnées cylindriques, il est alors égal à :

$$\phi_{\text{eff}} = \phi(r, \theta, z) - \frac{1}{2}(\Omega_p^B)^2 r^2. \tag{1.13}$$

L'équation du mouvement devient :

$$\ddot{\vec{r}} = -\vec{\nabla}\phi_{\text{eff}} - 2\left(\vec{\Omega}_p^B \wedge \dot{\vec{r}}\right). \tag{1.14}$$

L'énergie d'une particule dans ce référentiel est :

$$E_j = \frac{1}{2}v^2 + \phi - \frac{1}{2}(\Omega_p^B)^2 r^2. \tag{1.15}$$

E_j est une intégrale de mouvement appelé *Jacobien* ou *intégrale de Jacobi.*

Dans ce repère tournant, les points pour lesquels les épicycliques se referment en effectuant m lobes satisfont la relation suivante :

$$\frac{n}{m} = \frac{\kappa}{\Omega - \Omega_p^B}, \tag{1.16}$$

où n désigne le nombre d'oscillations radiales, m le nombre d'oscillations azimuthales, Ω la fréquence de rotation de l'étoile, Ω_p^B la fréquence de rotation de la barre et κ la fréquence épicyclique.

Ces points remarquables, pour lesquels l'équation 1.16 est vérifiée, sont appelés les **résonances.**

L'allure du potentiel ϕ_{eff} est donné par la figure 11, où les courbes des isopotentiels sont tracées dans les directions X et Y cartésiennes. Les points L_i sont des points stationnaires appelés points de Lagrange. L_3 est un minimum central, L_4 et L_5 des maxima et L_1 et L_2 des maxima dans la direction du grand axe de la barre (points de selle). En tous les points de Lagrange, une étoile se trouve en équilibre entre la force centrifuge et la force gravitationnelle et peut y rester immobile (correspondant à une trajectoire circulaire à la vitesse angulaire Ω_p^B dans le référentiel fixe). Le cercle (ou plus généralement l'ellipse) passant par les quatre points de Lagrange est le cercle de corotation. Seuls les points L_4 et L_5 sont stables, l'étoile peut osciller autour de ces points à la fréquence κ. Le nombre de résonances de type 2/1, couramment appelées **Résonance Interne de Lindblad**, notées *RIL* (ou *IRL*, en anglais) joue un rôle très important dans la morphologie des spirales barrées via la structure des orbitales des barres. Une autre résonance obtenue pour $\Omega = \Omega_p^B$ s'appelle la **corotation**, ou encore rayon de corotation *RC* (ou *CR*, en anglais). Enfin, notons aussi la présence de la **Résonance Externe de Lindblad** ou *REL* (ou encore *ELR*) (valeur de $\frac{n}{m} = -2/1$) qui n'intervient que dans l'étude de la structure spirale et des anneaux externes. Le tableau I, associé à la figure 12, met l'accent sur les indicateurs optiques de la présence de ces résonances dans des galaxies spirales. La Figure 13 montre les positions des résonances.

Il est à noter, que cette théorie peut s'appliquer pour chaque structure dans une galaxie. Ainsi, selon Tagger et al. (1987) et Sygnet et al. (1988), plusieurs "patterns" peuvent

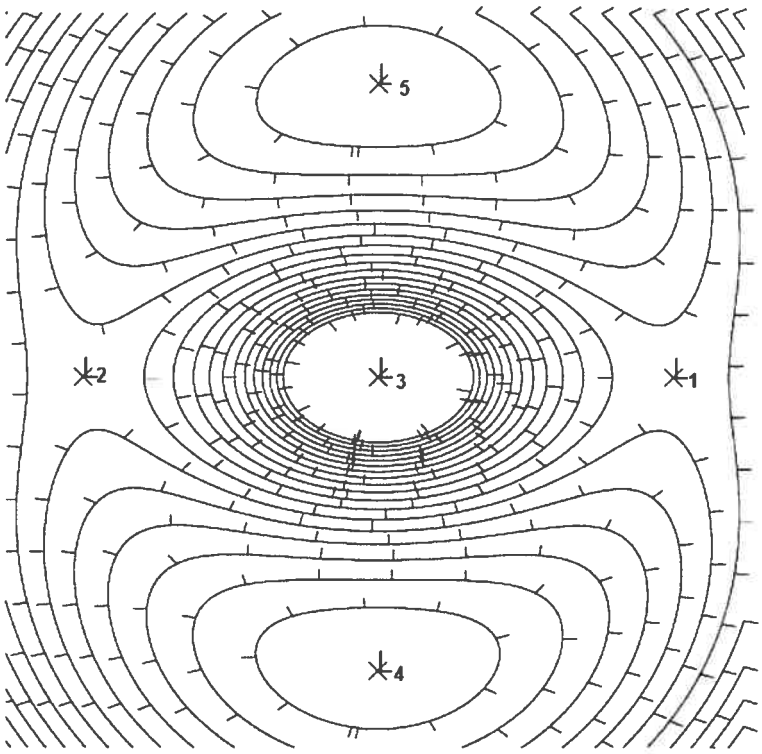

Fig. 11: Courbes de niveau du potentiel. La barre est parallèle à l'axe L_1-L_2.

"Pattern" optique	Résonances	Exemple de galaxie
Deux bras très lumineux	OLR	M81
Arrête intérieure de formation d'étoiles	Corotation	NGC5248
Lignes de poussières passant du côté concave au côté convexe du bras	Corotation	NGC1300
Anneau nucléaire	ILR	NGC 3351
Anneau interne	'−4 : 1'	NGC 1433
Structure spirale à 3 bras	'+3 : 1'	M101

Table I: Indicateurs optiques des résonances (Elmegreen, 1998), c.f. figure 12.

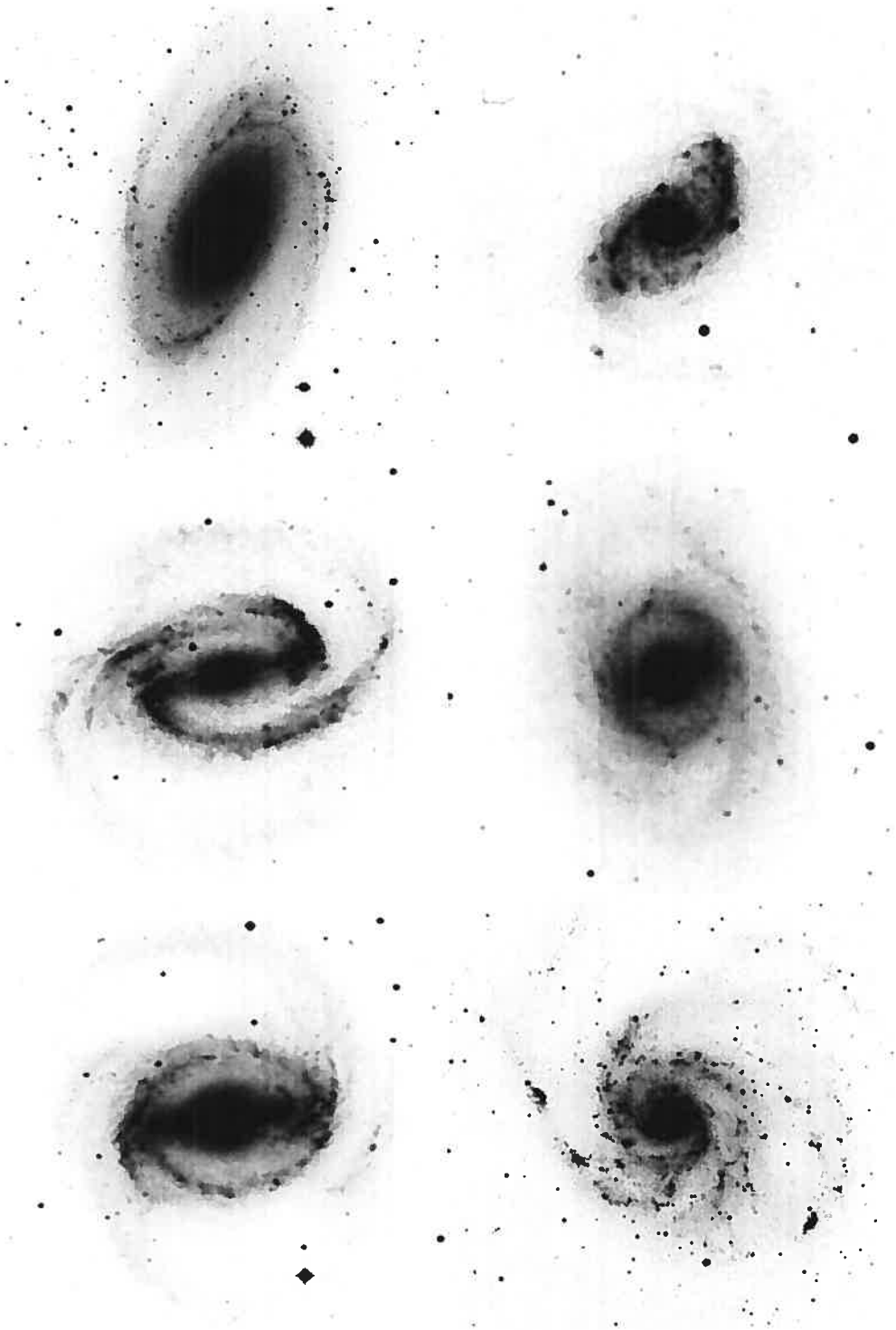

Fig. 12: De haut en bas et de gauche à droite : M81, NGC5248, NGC1300, NGC3351, NGC1433 et M101. Images du XDSS en bande B.

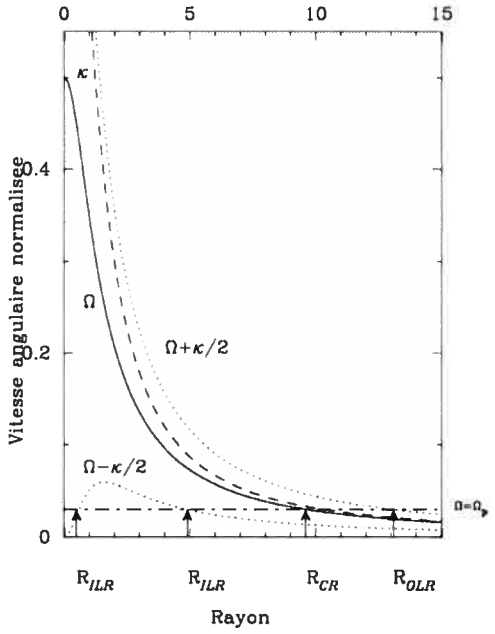

Fig. 13: Positions des résonances RIL, RC et REL pour un Ω_p donné pour une barre (Wozniak, 1991).

être présents dans une galaxie. Les résonances sont propres à chaque "pattern", et il ne faut pas oublier de préciser à quelle structure se rapporte une corotation ou une ILR.

Les orbites périodiques représentent les orbites les plus intéressantes (voir figure 14) car elles constituent le squelette des structures présentes dans une galaxie, comme la barre, l'anneau interne, externe... On en dénombre plusieurs de grand intérêt (Contopoulos & Papayannopoulos, 1980) :

(i) les familles "x_1", orbites elliptiques allongées suivant la barre, elles ne dépassent pas la corotation.

(ii) les familles "x_2", présentes entre les deux RILs, perpendiculaires à la barre. Même sens de rotation que la barre (comme pour les familles "x_1"). Dans le cas d'une barre très forte cette famille va disparaître, à moins que Ω_p augmente pour compenser l'effet de la force de la barre. Mais Ω_p ne peut pas augmenter indéfiniment, sinon les RILs disparaissent.

(iii) les familles "x_3" instables, ressemblent aux familles "x_2"

(iv) les familles "x_4", identiques aux familles "x_1" mais de sens rétrograde.

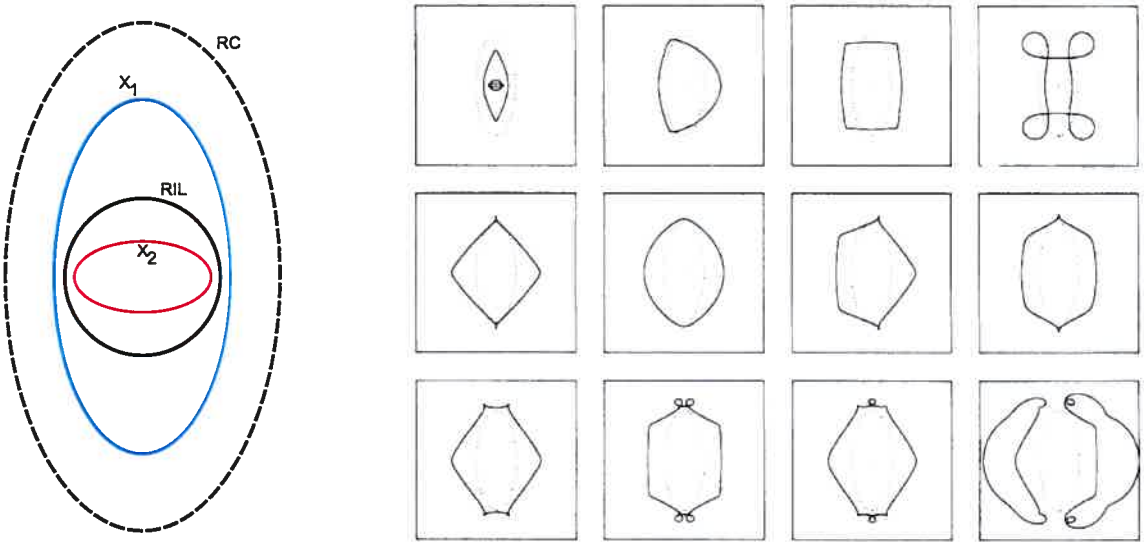

Fig. 14: Diversité des orbites dans la barre. **Gauche :** le modèle standard grossier, en pointillés la barre, en bleu une orbite x_1, en rouge une orbite x_2, le cercle noir représente la RIL. **Droite :** un modèle plus fin Athanassoula (1992a) où les orbites x_1 sont représentées sous diverses formes possibles.

Remarque : la décomposition en série de Fourier du potentiel est donnée par $\phi(r,\theta,t) = \phi_o(r) + \Sigma_m \phi_m(r) \cos\{m[\theta - \Omega_{p,m}.t - \varphi(r)]\}$ où $\phi_o(r)$ est un potentiel axisymétrique et la somme $\Sigma_m \ldots$ représente la somme des harmoniques m. C'est un outil puissant pour l'analyse du potentiel non-axisymétrique dans les galaxies spirales (Schoenmakers et al., 1997). Les termes d'ordre supérieur ou égal à m=2 sont analysés par transformée de Fourier et permettent une compréhension plus profonde des champs de vitesses et des écarts à la rotation circulaire (typiquement entre 0 et 5 km.s^{-1}). En principe, il ne reste plus qu'à faire le tri dans les harmoniques obtenues mais c'est là que tout se complique.

1.3.2 La méthode de Tremaine-Weinberg

Les modèles numériques de simulations d'évolution des galaxies - qu'ils soient de types N-corps, hydrodynamiques (SPH) ou bien les deux (c.f. section 1.4) comportent de nombreux paramètres libres. La masse de chacune des composantes de la galaxie simulée (disque d'étoiles, disque de gaz, halo stellaire, halo de matière sombre, barre, etc...), la forme, les dimensions sont autant de paramètres à déterminer. Pour une galaxie donnée, la connaissance par les observations du plus grand nombre de ces paramètres est un atout vers

la compréhension de l'évolution de la galaxie. La fréquence de rotation Ω_p^B de la barre est un paramètre précieux car il permet de mieux établir la dynamique de la galaxie.

Il est fondamental de connaître la fréquence de rotation de la barre, d'abord, pour tester les théories, ensuite, pour déduire l'étape d'évolution de la galaxie et enfin positionner le lieux des résonances, qui vont contrôler les zones de formation d'étoiles.

Cette quantité est difficilement quantifiable par l'observation et plusieurs méthodes sont mises à l'épreuve pour tenter d'extraire cette valeur.

- Le test de Canzian qui tient compte de l'inversion de signe des champs résiduels (champ de vitesses observé moins le champ de vitesses modélisé) près de la co-rotation (Canzian, 1993).
- La localisation de la résonance '+4 :1', ou résonance Ultra Harmonique, UHR, permet de déduire Ω_p^B par lecture inverse de la courbe $\Omega(R)$ (Elmegreen et al., 1992).
- Définition de la position de la corotation dans un intervalle de 1.0 à 1.4 fois la longueur de la barre (Athanassoula, 1992b).
- Modélisations N-corps et/ou SPH avec comparaison et ajustement de modèles (Sempere et al., 1995b).

Dans tous les cas, les méthodes sont indirectes et dépendantes des modèles. Tremaine & Weinberg (1984) proposent une méthode cinématique pour mesurer les fréquences de rotation des barres des galaxies barrées. Cette méthode ne fait référence à aucun modèle dynamique. Elle s'appuie sur les hypothèses suivantes :

Le disque de la galaxie est plat. Pour simplifier, le disque est considéré comme ayant une épaisseur nulle. $\{x, y\}$ sont les coordonnées cartésiennes dans le plan du disque et $\{X, Y\}$ dans le plan du ciel. Le centre de ce système d'axes est le centre de la galaxie et l'axe des abscisses est orienté selon la ligne des noeuds. Dans ce système, $(X, Y) = (x, y \cos i)$ où i est l'inclinaison de la galaxie ($i = 90°$ pour une galaxie vue par la tranche).

Le disque a une fréquence de rotation Ω_p^B bien définie. Si $\Sigma(x, y, t)$ représente la brillance de surface du traceur considéré, i.e. les étoiles ou le gaz, à chaque instant t, dans un système de coordonnées polaires (r, ϕ), où $x = r \cos \phi$ et $y = r \sin \phi$, elle est considérée comme étant constante dans le repère en rotation à la vitesse angulaire Ω_p^B . Ainsi,

$$\Sigma(x, y, t) = \tilde{\Sigma}(r, \phi - \Omega_p^B t). \tag{1.17}$$

La brillance de surface du traceur suit la loi de l'équation de continuité. Ceci est une excellente approximation pour les galaxies de type SB0, où peu de gaz est présent. Par contre, l'hypothèse est plus ou moins vérifiée pour le gaz neutre HI et le gaz ionisé Hα pour lesquels il y a conversion du gaz vers de l'hydrogène moléculaire ou formation stellaire. Néanmoins, cette hypothèse sera abordée dans le chapitre 4 de cette thèse. L'équation de continuité s'écrit de la façon suivante :

$$\frac{\partial \rho}{\partial t} + \mathrm{div}\,(\rho \vec{v}) = 0.$$

Sous les hypothèses précédentes, la brillance de surface du traceur considéré répond à l'équation de continuité. Ainsi,

$$\frac{\partial \Sigma(x,y,t)}{\partial t} + \frac{\partial}{\partial x}\left[\Sigma(x,y,t) v_x(x,y,t)\right] + \frac{\partial}{\partial y}\left[\Sigma(x,y,t) v_y(x,y,t)\right] = 0, \tag{1.18}$$

combinée à 1.17, devient

$$\frac{\partial \Sigma(x,y,t)}{\partial t} = -\Omega_p^B \frac{\partial \tilde{\Sigma}(r,\phi-\Omega_p^B t)}{\partial \phi} = \Omega_p^B \left(y \frac{\partial \Sigma(x,y,t)}{\partial x} - x \frac{\partial \Sigma(x,y,t)}{\partial y} \right). \tag{1.19}$$

En remplaçant ce résultat dans l'équation 1.18 et en intégrant le long de l'axe des abscisses, l'équation précédente devient :

$$\Omega_p^B y \int_{-\infty}^{\infty} \frac{\partial \Sigma}{\partial x} dx - \Omega_p^B \int_{-\infty}^{\infty} x \frac{\partial \Sigma}{\partial y} dx + \int_{-\infty}^{\infty} \frac{\partial \Sigma v_x}{\partial x} dx + \int_{-\infty}^{\infty} \frac{\partial \Sigma v_y}{\partial y} dx = 0. \tag{1.20}$$

Le premier et le troisième termes tendent vers 0 car $\Sigma(x,y,t)$ tend vers 0 quand $|x|$ tend vers $+\infty$. En intégrant par rapport à y, la simplification conduit à :

$$\Omega_p^B \int_{-\infty}^{\infty} \Sigma(x,y,t) x dx = \int_{-\infty}^{\infty} \Sigma(x,y,t) v_y(x,y,t) dx, \tag{1.21}$$

où la constante d'intégration reste égale à zéro puisque la brillance de surface Σ tend vers 0 quand $|y|$ tend vers $+\infty$. En passant dans le système de coordonnées dans le plan du ciel, en supprimant la dépendance de Σ et de la vitesse v sur le temps, en se rappelant que la vitesse radiale le long de la ligne de visée $< V_{LOS,Y} >= v_y \sin i$, on obtient :

$$\Omega_p \sin i = \frac{\int_{-\infty}^{\infty} \Sigma(x,y,t) V_y(x,y,t)\, dx}{\int_{-\infty}^{\infty} \Sigma(x,y,t) x(y,t)\, dx} = \frac{< V_{LOS,Y} >}{< X_Y >}, \tag{1.22}$$

où $< X_Y >$ représente la position moyenne pondérée par la luminosité le long d'une fente parallèle à l'axe x à une ordonnée Y.

La méthode de Tremaine-Weinberg est donc un outil puissant pour la détermination des fréquences de rotation des ondes dans les galaxies spirales. Le chapitre 4 montre comment cette théorie est exploitée dans le cas du gaz Hα même si celui-ci ne respecte pas toutes les hypothèses mentionnées ci-dessus.

1.4 Dynamique numérique des galaxies

1.4.1 Problèmes à N-corps

Lorsqu'on veut connaître l'évolution d'un ensemble de N particules de masse m_i, il est nécessaire de calculer chaque force $\overrightarrow{f_j}$ qui s'exerce sur une particule j par une particule i appartenant à cet ensemble de N particules (Wozniak, 2001).

$$\overrightarrow{f_i} = -G \sum_{i=1;i\neq j}^{N} \frac{m_i.m_j(\overrightarrow{r_j} - \overrightarrow{r_i})}{\mid \overrightarrow{r_j} - \overrightarrow{r_i} \mid^3}. \tag{1.23}$$

Cette sommation est à répéter sur les N particules, donc pour un grand nombre de particules cela équivaut à N^2 opérations, ce qui n'est pas très efficace comme algorithme. De plus, si deux particules s'approchent trop près l'une de l'autre $\overrightarrow{f_j}$ diverge. En pratique, il faut donc introduire un paramètre de lissage ε pour éviter les problèmes numériques. Le potentiel "adouci" obtenu, Φ_j pour la particule j, permet donc de simuler un système sans collision qui respectera l'équation de Boltzmann,

$$\Phi_j = -G \sum_{i=1,i\neq j}^{N} \frac{m_j}{\sqrt{\mid \overrightarrow{r_j} - \overrightarrow{r_i} \mid^2 + \varepsilon^2}}. \tag{1.24}$$

L'idéal serait que les résultats de simulation soient indépendants de la forme de ε, mais ce n'est malheureusement pas le cas. Mais selon le nombre de particules et la résolution de la grille, il peut y avoir des changements. Athanassoula et al. (2000) proposent le meilleur compromis pour les valeurs de ε dans le cas de simulation N-corps.

Intégration des équations du mouvement

Pour déterminer l'évolution d'un système dynamique dans le temps, il est nécessaire de connaître les équations du mouvement. Pour cela, le système est discrétisé par intervalles de temps Δt. Les forces sont calculées pour chaque pas de temps. Cet intégrateur porte le

nom de saute-mouton ("leap-frog"). Un seul calcul par pas de temps est nécessaire. Si n est l'indice du pas de temps, $\vec{v}_i^{(n)}$ la vitesse d'une particule i soumise à la force $\overrightarrow{f_i}^{(n)}$ alors :

$$\begin{cases} \vec{v}_i^{(n)} = \vec{v}_i^{(n)} + \Delta t \overrightarrow{f_i}^{(n-1)} \\ \vec{r}_i^{(n+1/2)} = \vec{r}_i^{(n-1/2)} + \Delta t \overrightarrow{n_i}^{(n)}. \end{cases} \tag{1.25}$$

Les modifications des positions et des vitesses ne se font pas en même temps d'où le nom de "saute-mouton". C'est l'intégrateur le plus fréquent qui est aussi utilisé dans le code GADGET décrit ci-après.

Intégration directe ou code PP

Le code à intégration directe **PP** (particule-particule) utilise la méthode directe de sommation. Ce code est utile dans le cas d'un faible nombre de particules (10^5 particules au maximum) pour rester dans des temps de calcul raisonnables, puisqu'il effectue tous les calculs des forces pour chaque particule. Cette méthode convient bien aux amas globulaires où le nombre de particules est relativement restreint. Des ordinateurs sont dédiés à ces genres de calcul, comme l'ordinateur GRAPE de l'Observatoire de Marseille.

Code "particule-grille" (PM)

Si l'on veut franchir la limite des 10^5 particules en conservant des temps de calcul raisonnables, les forces et le potentiel doivent être calculés par d'autres méthodes. Une de celles-ci est la méthode PM, une grille cartésienne est utilisée sur laquelle, en chaque point, une masse $M(i,j,k)$ est placée en chaque position étudiée $\overrightarrow{r(i,j,k)}$. Le potentiel s'écrit alors comme étant le produit de convolution de la masse M par la fonction de Green $\mathcal{G}_{green}(r)$:

$$\phi(r) = \mathcal{G}_{green}(r - r') * M(r') \tag{1.26}$$

et

$$\mathcal{G}_{green}(r - r') = -G \frac{1}{\sqrt{|\overrightarrow{r_j} - \overrightarrow{r_i}|^2 + \epsilon^2}}, \tag{1.27}$$

où ϵ est un paramètre de lissage pour éviter la divergence. On utilise alors une transformée de Fourier rapide (FFT) pour calculer le produit de convolution. Les forces sont alors obtenues par simple différenciation au premier ordre du potentiel obtenu. L'utilisation de la FFT permet de gagner énormément de temps.

Par contre, tout comme pour le code PP, les résultats ne sont pas indépendants du paramètre de lissage, ce qui est un problème.

Méthodes hybrides

Les méthodes précédentes et suivantes sont utilisées dans la plupart des codes numériques modélisant les écoulements de gaz dans des potentiels. Ainsi, pour vaincre le problème des codes **PM** aux courtes distances, les codes **P3M**, corrigent la force créée par les particules distantes de moins d'un pas (Δr) donné. Cette correction consiste en la sommation directe de type PP d'où le nom PP + PM =PPPM=P3M ! Il existe une autre classe de code très utile, le N corps hiérarchique, basé sur la même idée précédente des codes P3M de séparer les contributions des régions lointaines et proches à la force totale agissant sur une particule donnée. La contribution des plus proches voisins est obtenue par sommation directe PP. La contribution des masses lointaines est calculée en utilisant un regroupement des masses les plus éloignées et en ne tenant compte que de leur barycentre. Ce type de code est appelé **TREECODE** (code en arbre, Barnes & Hut (1986)).

Au départ de ce code, une cellule contient toutes les particules. Cette cellule est ensuite divisée par 2 sur chacun de ses cotés, puis encore par deux afin de n'obtenir plus qu'une seule particule par cellule. La cellule principale est appelée **racine de l'arbre** et chaque sous-cellule est appelée **feuille de l'arbre**. La figure 15 illustre la décomposition en cellulle en deux dimensions (dite décomposition en domaine) d'une racine. Une fois la décomposition faite, la force agissant sur la particule i est calculée de la façon suivante, pour chaque cellule j visitée :

1. Si j est une particule, la contribution de la particule j est directement sommée à la force agissant sur i (méthode PP)
2. Si j est une cellule, deux cas sont possibles :

   (a) Si j est suffisamment loin de i, la contribution de l'ensemble de la masse est située au barycentre de la cellule j et est sommée à la force sur i

   (b) Si j est trop proche de i, l'hypothèse que toute masse est concentrée au barycentre ne peut être satisfaite. L'exploration de l'arbre pour la recherche des plus proches voisins doit se poursuivre au niveau inférieur.

   La précision de l'algorithme réside dans la définition du "loin" et du "proche". Une

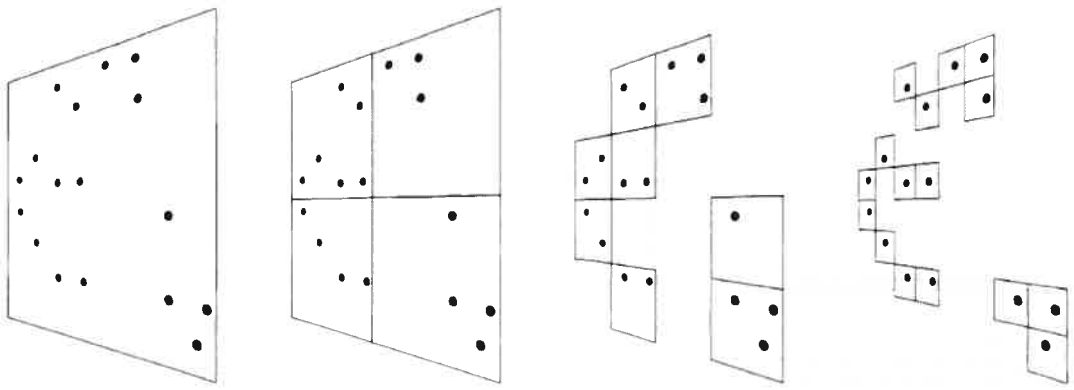

Fig. 15: Principe de décomposition de l'arbre pour la version série Gadget (Springel et al., 2001)

cellule est remplacée par sa masse totale placée au barycentre lorsque la condition suivante est respectée :

$$\frac{l_j}{\theta} + \delta_i < \mid \Delta\vec{r} \mid, \tag{1.28}$$

où l_j est la dimension de la cellule j, $\Delta\vec{r}$ la différence de position entre la particule i et le barycentre de la cellule j, et θ, un paramètre libre qui permet de contrôler la précision. Ce critère de précision est appelé critère d'ouverture.

Pour un nombre N de particules, le temps de CPU associé à un code en arbre est de l'ordre de $N \log N$.

1.4.2 Code hydrodynamique - SPH

Le seul code Lagrangien en trois dimensions, utilisé en dynamique galactique, est le code SPH (Lucy, 1977) pour Smooth Particule Hydrodynamics. Les principes sont les suivants. Chaque particule de masse m_j est lissée spatialement suivant une fonction $\mathcal{W}$ (dépendant de sa position et d'un paramètre h appelé adoucissement) appelée noyau, qui peut être vu comme la fonction de densité spatiale de la particule. Les éléments du fluide sont alors échantillonnés, par l'intermédiaire de la fonction $\mathcal{W}$ et représentés par des particules. Les équations dynamiques sont déduites des formes Lagrangiennes des lois de conservation. Il n'y a pas de grille ou de résolution spatiale, ce qui est bien différent des codes N-corps et qui fait que son utilisation va souvent de paire avec les codes en arbre. Le problème est

que l'équation d'Euler ne possède pas de terme de viscosité et par conséquent n'est pas adaptée pour décrire les phénomènes de dissipation et de chocs. Un fluide peut toujours transformer une partie de son énergie cinétique en chaleur grâce à l'établissement des chocs. Dans la plupart des fluides, en astrophysique, la viscosité de ces derniers est d'ailleurs très mal connue. Dans le code SPH, on introduit une viscosité artificielle formée par le couple (α, β) qui donnent lieu à deux pressions visqueuses :

$$\begin{cases} P^b = -\alpha \rho l s \vec{\nabla}.\vec{v} & \text{Pression de "bulk",} \\ P^{nr} = -\beta \rho l^2 \left(\vec{\nabla}.\vec{v}\right)^2 & \text{Pression de von Neumann-Richtmyer.} \end{cases} \tag{1.29}$$

Le couple (α, β) est libre, l est la longueur typique de la zone où le choc a eu lieu et s la vitesse du son dans le gaz dont l'influence est cruciale. Les simulations Patsis & Athanassoula (2000) ont montré que les valeurs (1,2) pour (α, β) sont idéales pour décrire l'écoulement du gaz. Une vitesse du son faible (10 km.s^{-1}) aura tendance à créer un anneau et des lignes de fortes densités semblables à celles décrites par d'autres modèles. Une vitesse du son plus forte (20 km.s^{-1}) aura tendance à faire "couler" le gaz plus au centre de la galaxie et créer des surdensités en forme de "T" au bout de la barre visible dans les galaxies réelles (voir NGC 1530). Si une viscosité artificielle n'était pas introduite, le gaz aurait tendance à tomber rapidement vers le centre de la galaxie et il pourrait disparaître en totalité en quelques millions d'années, temps très court pour la simulation.

1.4.3 Codes couplés étoiles-gaz

Les galaxies sont formées d'étoiles, de gaz, de poussières et même d'un halo de matière non lumineuse qui coexistent et interagissent. Il est évident que d'utiliser un code N-corps pour suivre l'évolution des étoiles ou bien un code SPH pour modéliser l'écoulement du gaz, revient à négliger l'existence des autres composantes et des autres interactions. L'introduction de codes couplés étoiles-gaz est donc fondamentale et est un processus qui en est à ses débuts. Trois types de codes existent. D'adord, le code **TREESPH** Hernquist & Katz (1989), qui fait la synthèse SPH pour le gaz et utilise un code en arbre pour les étoiles. Ensuite, le code **PMSPH** Friedli & Benz (1995), a confirmé l'accrétion de gaz vers le noyau des galaxies. Enfin, le code Gadget, Springel et al. (2001), faisant le couplage SPH et N-corps, reste à développer pour son utilisation avec une galaxie spirale barrée.

1.4.4 GADGET

Le code GADGET développé par Springel et al. (2001) est un code couplé étoiles-gaz idéal pour la simulation cosmologique et les interactions entre galaxies. GADGET pour **GA**laxies with **D**ark matter and **G**as int**E**rac**T**, est un code d'évolution pour des fluides sans collision autogravitants avec une approche N-corps et pour des fluides avec collision avec une approche SPH. Deux versions du code existent, une version série, à utiliser plutôt comme test, et une version parallèle qui peut être utilisée sur des super-ordinateurs multiprocesseurs. GADGET détient toujours le record du nombre de particules dans une simulation (7.5×10^7). Dans les trois paragraphes suivants, de brèves descriptions du code, de son adaptation au problème d'une galaxie sont données.

Algorithmique du code parallèle

Le code est utilisé dans sa version parallèle. GADGET est utilisé à la fois dans son mode SPH et à la fois comme entité complète (N-corps et SPH utilisés conjointement). Le code est donc un code couplé N-corps et SPH. Sa structure est en arbre. Un arbre est construit pour chaque type de particules. Il y a six types de particules possibles. Cinq des six types sont relatifs à un traitement par les équations de Boltzman sans collision et concernent donc :

- particules numérotées 2 : halo de matière non lumineuse
- particules numérotées 3 : disque
- particules numérotées 4 : bulbe
- particules numérotées 5 : étoiles
- particules numérotées 6 : laissé au libre choix. Peut servir à la formation d'étoiles.

Le traitement SPH s'effectue uniquement sur le gaz, "particules" numérotées 1 dans le code. À chaque type de particules peuvent être associées une longueur de lissage et une masse totale. Tous ces paramètres sont à définir dans des fichiers d'entrées disponibles dans l'annexe B. Après l'initialisation du code qui permet la lecture des Conditions Initiales, la lecture des fichiers des paramètres de la simulation en cours, la lecture des forces générées par la barre (c.f. ci-après), la séquence du code sera donc la suivante pendant le déroulement d'un pas de temps Δt.

1. Recherche du prochain pas de temps selon le critère sélectionné[a].
2. Ecritures des différents "snapshots" et des fichiers log.
3. Parcours des arbres et prédiction du prochain pas de temps.
4. Calcul des accélérations + ajouts des forces dues à la barre.
5. Intégration des équations du mouvement. Avancement de toutes particules actives. Rotation du référentiel à la fréquence Ω_p^B .
6. Recherche du nouveau pas de temps.
7. Test pour refaire une décomposition du domaine et/ou reconstruction des arbres.
8. En option - ajout de formation stellaire.

Recherche du potentiel

Le potentiel gravitationnel de la barre est directement déduit des images infrarouges en bande K issues de 2Mass ou du télescope Spitzer à 3.6 μm (pour éviter la présence de poussière). Chaque image est d'abord nettoyée. Les étoiles y sont soustraites. L'image est ensuite déprojetée et dilatée en trois dimensions selon une loi de *sech* avec une échelle de hauteur standardisée à 250 pc. L'annexe B présente les différentes routines utilisées. Le potentiel trouvé est alors décomposé en 4 de ses composantes de Fourier. La partie axisymétrique (m=0) est utilisée dès le début des simulations. Tandis que les 3 autres composantes (m=2, 4, 6) sont introduites après une rotation de barre suivant une loi linéaire pour éviter tout problème numérique.

Cette technique est directement inspirée des techniques déjà appliquées avec succès dans le cas de plusieurs galaxies, comme Messier 51, NGC 4321 ou NGC 7479 (Garcia-Burillo et al. 1993, 1995, Sempere et al. 1995).

1.4.5 La science en mouvement

Ce projet de thèse laisse encore beaucoup de travail à accomplir, notamment dans la partie numérique des simulations. Chaque sous routine ajoutée dans GADGET doit être encore validée avant d'entreprendre des simulations numériques de qualité visant à reproduire les observations. Cependant, grâce à la méthode de Tremaine-Weinberg développée dans le cadre

[a] À cet effet le critère de pas de temps est dans notre cas la condition de courant qui met à la fois l'accent sur l'effet de viscosité, précédemment défini et sur la dispersion des vitesses.

de ce travail pour le Hα, il sera possible de réduire maintenant le nombre de paramètres libres associés aux simulations et donc de mieux contraindre les modèles de rotation des galaxies. Une fois les simulations capables de reproduire les champs de vitesses, grâce à l'échantillon homogène *BHαBAR*, une meilleure compréhension des courbes de rotation sera alors permise. Les pentes des courbes $V(R)$, qui contraignent fortement les modèles de masse aux faibles rayons, pourront donc être corrigées des mouvements non circulaires et la masse déduite n'en sera que plus réaliste.

Contribution aux différents articles

– Article I, Chapitre 2, 30% de la conception globale de l'instrument, 100% de la conception optomécanique, 90% de la conception du système de refroidissement, 30% de la rédaction de l'article.

– Article II, Chapitre 3, 90% de la rédaction de l'article et 100 % de l'analyse des données.

– Article III, Chapitre 4, 50% de la rédaction de l'article et 90 % de l'analyse des données.

– Article IV, Chapitre 5, 90% de la rédaction de l'article, 100 % de l'analyse des données.

– Article V, Annexe C, 100% de la rédaction de l'article, mise en place de la documentation et du site web de l'instrument.

– Article VI, Annexe E, 20 % de la rédaction de l'article et 30% de l'analyse des données.

– Article VII, Annexe F, 5 % de la rédaction de l'article. 10 % de l'analyse des données.

Chapitre 2

FaNTOmM : Le Fabry-Perot au sommet de son art

Fabry Perot Observations Using a New GaAs Photon Counting System

JEAN-LUC GACH

Observatoire de Marseille, 2 Place Le Verrier, F–13248 Marseille Cedex 04, France

OLIVIER HERNANDEZ

Département de physique and Observatoire du mont Mégantic, Université de Montréal, C.P. 6128, Succ. centre ville, Montréal, Québec, Canada. H3C 3J7 and

Observatoire de Marseille, 2 Place Le Verrier, F–13248 Marseille Cedex 04, France

JACQUES BOULESTEIX

Observatoire de Marseille, 2 Place Le Verrier, F–13248 Marseille Cedex 04, France

CLAUDE CARIGNAN

Département de physique and Observatoire du mont Mégantic, Université de Montréal, C.P. 6128, Succ. centre ville, Montréal, Québec, Canada. H3C 3J7

PHILIPPE AMRAM

Observatoire Astronomique de Marseille Provence, LAM, 2 place Le Verrier, F-13248 Marseille Cedex 04, France

OLIVIER BOISSIN

Observatoire Astronomique de Marseille Provence, LAM, 2 place Le Verrier, F-13248 Marseille Cedex 04, France

OLIVIA GARRIDO

Observatoire Astronomique de Marseille Provence, LAM, 2 place Le Verrier, F-13248 Marseille Cedex 04, France

MICHEL MARCELIN

Observatoire Astronomique de Marseille Provence, LAM, 2 place Le Verrier, F-13248 Marseille Cedex 04, France

HENRY PLANA

Observatorio Nacional MCT, 20912-400 Rio de Janeiro RJ, Brazil

ROBERTO RAMPAZZO

Osservatorio Astronomico di Brera, Via Brera 28, I-20121 Milano, Italy.

Published in The Publications of the Astronomical Society of the Pacific, 2002, Volume 114, Issue 799, pp. 1043-1050.

Abstract

A third generation Image Photon Counting System (IPCS) camera is presented, based on a GaAs photocathode that can achieve a quantum efficiency of up to 23%, which is comparable to a thick CCD, but without readout noise. This system is 10 times more sensitive at Hα than previous photon-counting cameras. In terms of S/N ratio, the system outperforms CCDs for extremely faint fluxes - for the same exposure time -, including AR-coated, low-noise, thin CCDs. This system, with up to 1K×1K pixels, is one of the largest monolithic IPCS. An unique cooling system, based on a Ranque-Hilsh vortex tube, is used for this camera. Real-time centering is done by a scalable Digital Signal Processor (DSP) board. Astrophysical projects and preliminary results obtained with this new camera coupled with a scanning Fabry-Perot at the Cassegrain focus of the 3.6m ESO telescope, the 1.93m Observatoire de Haute Provence (OHP) telescope, and the 1.6m Observatoire du mont Mégantic (OMM) telescope, are presented.

Keywords : instrumentation : detectors — instrumentation : spectrographs — galaxies : kinematics and dynamics

2.1 Introduction

In the last two decades, several multiplex scanning instruments, e.g. Fourier Transform Spectrographs (FTS) (Maillard et al., 1992), scanning Fabry-Perot integral-field spectrometers such as TAURUS (Atherton et al., 1982), CIGALE (Boulesteix et al., 1984), HIFI (Bland et al., 1989), and PYTHEAS (Le Coarer et al., 1995), have been developed and tested at the foci of 2-6 m class telescopes. Starting with the first successful photon counting system built (Boksenberg, 1977 ; Blazit et al., 1977), IPCSs continued to be developed for space astronomical applications mainly because of their sensitivity in the far UV. Since the last development achieved in the 80's for ground applications (see e.g. Boulesteix, 1980 ; Blazit, 1985 ; Foy, 1988), it is only recently that IPCSs open new perspectives to the full exploitation of multiplex scanning instruments. Indeed, a new generation of GaAs and GaAsP

photocathodes appeared, with high quantum efficiency (QE), and proximity-focused image-intensifiers, without image distortion, associated with fast frame read-out rate and large format CCDs that can be used as detectors behind the image intensifier, leading to a large format IPCS.

This paper presents the study and the application of a third generation of IPCSs based on a GaAs photocatode that can achieve a quantum efficiency of up to 23%, comparable to a thick CCD (see Fig. 16), but without read-out noise. The paper is organized as follows. Section 2 develops basic considerations about the advantage of using IPCSs in multiplex scanning instruments. Section 3 presents an overview of the GaAs system and discusses the system performances. In Section 4, astrophysical fields to which the system has been applied are introduced, along with a discussion of preliminary results obtained at different observatories during recent observing runs. Finally, future applications are sketched in section 5.

2.2 Basic considerations about the use of IPCSs with multiplex instruments

2.2.1 Photon counting systems vs CCDs : the readout noise problem

The problem of read-out noise affects CCDs at low light levels. Despite the remarkably high quantum efficiency achievable, up to 95%, and the very low read-out noise, down to 2-3 electrons, the maximal signal-to-noise ratio (SNR) per pixel achievable by an "ideal" CCD is described by :

$$SNR = \frac{N}{\sqrt{N + \sigma^2 + T}}, \tag{2.1}$$

where N is the number of photons collected per pixel during the exposure time, σ is the readout noise of the CCD in electrons and T the thermal noise in electrons/pixel. Although the T term is close to zero in more recent CCD or IPCS devices and can be neglected, additional limitations constrain the usage of CCDs. In particular, long exposures are severely polluted by cosmic rays. Observations need to be split into several short exposures, which are not equivalent in terms of SNR to a long, single one. In this case, the above formula should be re-written as :

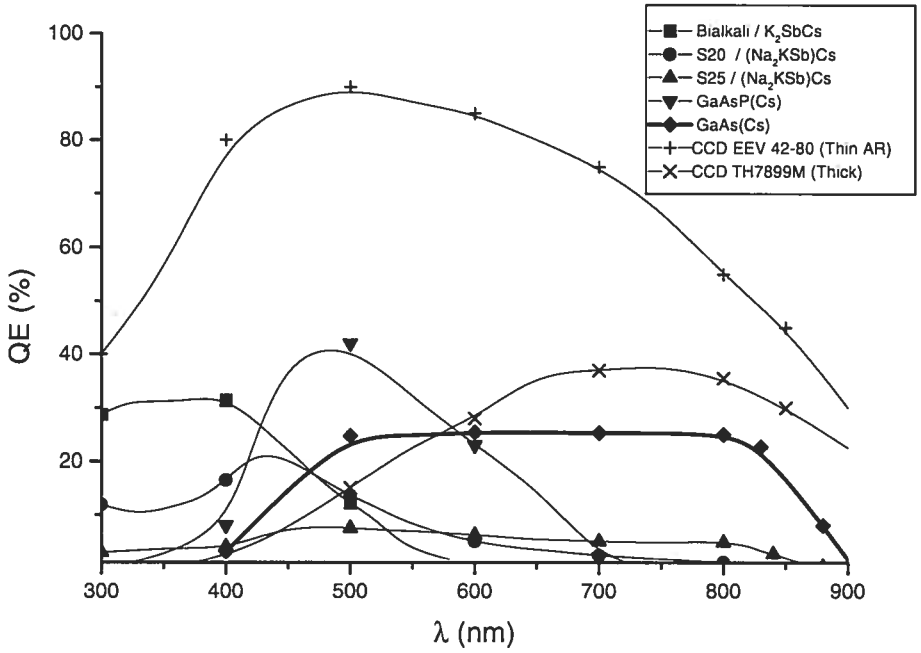

Fig. 16: Quantum efficiency of different types of photocathodes compared to CCDs.

$$SNR = \frac{N}{\sqrt{N + n\sigma^2 + T}}, \tag{2.2}$$

where n is the number of exposures. The SNR decreases dramatically when N is small and n is large. This is the case in multiplex instruments (scanning instruments). For an IPCS, the S/N is expressed by the formula :

$$SNR = \frac{N}{\sqrt{N + T}} \approx \sqrt{N}. \tag{2.3}$$

These kind of detectors, in fact, do not have readout noise and are less affected by cosmic rays since one event is seen as one photon only, a decisive advantage with respect to CCDs, when long exposures are required as in the case of faint objects. Although first generation IPCSs offer a poorer quantum efficiency with respect to CCDs and are affected by image distortion, they are still competitive in multiplex instruments or in speckle interferometry.

In Figure 17 are given the expected SNR of CCDs and GaAs IPCS systems achieved with an 8m telescope in 1 hour exposure (a 0.25x0.25 arcsec^2 pixel and a total efficiency - allowing for atmosphere, telescope, instrument and filter- of 20% is assumed) and 1nm bandwidth for narrow band imaging.

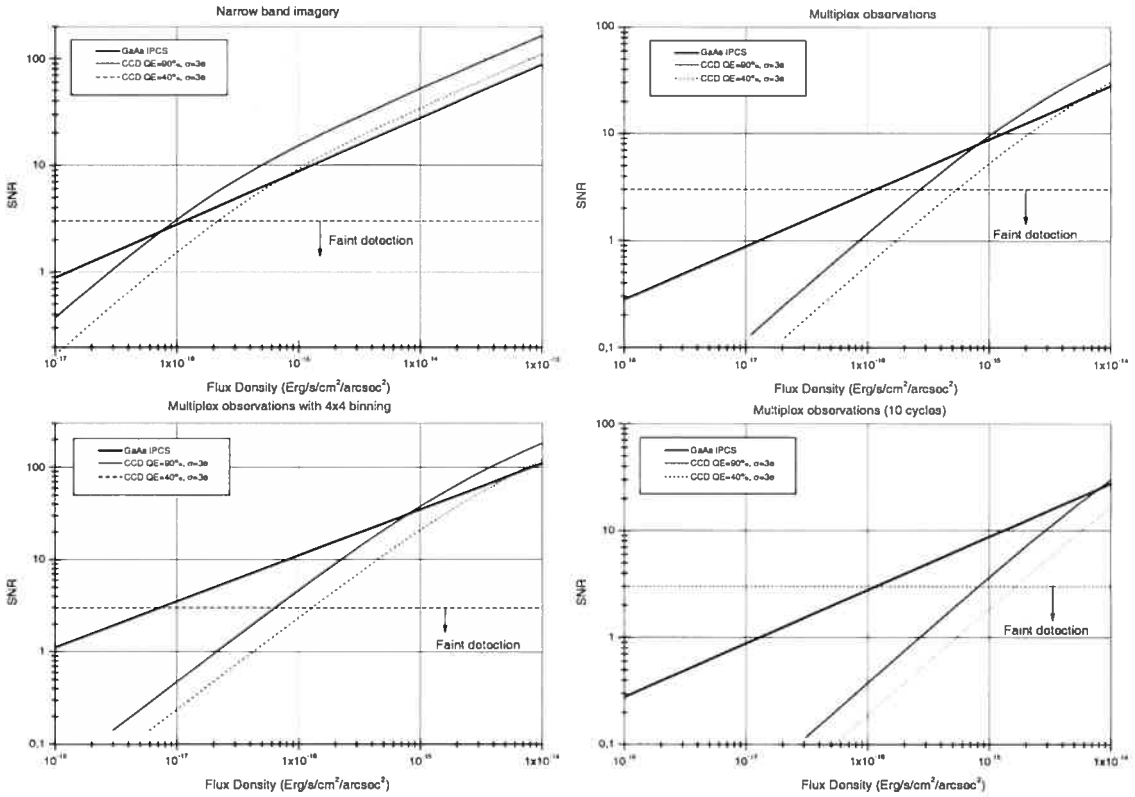

Fig. 17: SNR obtained by different detectors in narrow band imagery at an 8m telescope with 1 hour exposure. Top left : assuming narrow band imagery conditions (1 nm badwidth around Hα). Top right : using a scanning Fabry Perot with a 48-channel observation (R=20000, around Hα). Bottom left : Same scanning Fabry Perot observation, doing an a-posteriori binning of pixels to increase SNR. Bottom right : using a scanning Fabry Perot with a 48-channel observation and 10 cycles to average night sky variations

2.2.2 Using CCDs and IPCS with multiplex instruments : the real-time advantage

Multiplex instruments collect a large number of images. For example, *CIGALE* (CInematique des GALaxiEs), a scanning Fabry–Perot, uses up to 96 channels to reconstruct the interferometric map of an object emission line, in order to determine its velocity field (see Boulesteix et al., 1984). We define the global SNR of a multiplex observation (SNR_m) as the quadratic sum of the SNRs of each channel, since there is no noise correlation between channels. For an observation, this is given by (neglecting thermal noise) :

$$SNR_m = \sqrt{n\left(\frac{\frac{N}{n}}{\sqrt{\frac{N}{n}+\sigma^2}}\right)^2} = \frac{N}{\sqrt{N+n\sigma^2}}, \tag{2.4}$$

where N is the number of photons expected during the whole exposure, n is the number of channels and σ is the readout noise of the CCD.

With multiplex instruments, the emission usually appears only in a few channels, which could be different for each pixel according to the Doppler shift. The experience with *CIGALE* showed that, emission lines appears most of the time in only 25% of the channels. This lowers the above "ideal" SNR_m. The "worst" case is when the line is detected only in 2 channels. This does not affect the comparison between CCD and IPCS usage, but gives a more precise idea of the kind of objects that could be observed with such instruments. In this "worst" case the SNR_m is given by (and taken as a base to compute the expected SNR in figure 17) :

$$SNR_m = \sqrt{2\left(\frac{\frac{N}{n}}{\sqrt{\frac{N}{n}+\sigma^2}}\right)^2} = \frac{\frac{2N}{n}}{\sqrt{\frac{2N}{n}+2\sigma^2}}. \tag{2.5}$$

This equation reflects the outside-the- atmosphere detectivity since the first and the last images may not be comparable in terms of seeing and transparency when observing with a ground based telescope. Because of the very small readout time (25 ms for our camera) in the case of an IPCS, it is possible to observe each channel several times during the observation, then averaging all these variations. Typically, each channel is observed 5 to 10 seconds, and when the last channel has been integrated, the first is observed again. Each set of n channels is called a cycle, the duration of which is typically 3 to 10 minutes (depending

on the exposure time per channel and the number of channels). The total observation consists of several cycles. Technically, it is possible to make one whole cycle within a few seconds, taking only one 25ms exposure per channel, but we found that unnecessary and preferred instrument stability instead. Since there is no readout noise, it is then possible to sum up each i^{th} channel of all the cycles without losing any SNR. Obviously, adapting this observing technique to CCDs would degrade considerably the SNR, due to the large number of images produced. We can evaluate this nevertheless, by the following equation, taking equation 2.5 as a base :

$$SNR_m = \frac{\frac{2N}{n}}{\sqrt{\frac{2N}{n} + 2m\sigma^2}}, \tag{2.6}$$

where N is the number of photons expected during the whole exposure, n the number of channels, m the number of cycles and σ the readout noise of the CCD.

Meanwhile, the IPCS SNR_mobtained is independent of the number of cycles and the atmosphere-free SNR is :

$$SNR_m = \sqrt{\frac{2N}{n}}. \tag{2.7}$$

Figure 17 shows the SNR obtained with an 8m telescope in a 1-hour observation using a multiplex observation of 10 cycles of 48 channels with 0.25x0.25 arcsec^2 pixels.

2.3 GaAs system overview

2.3.1 Camera head

The camera head is composed of a GaAs proximity-focused 2-stage Micro Channel Plate (MCP) image-intensifier tube, fiber-coupled to a 1K×1K 40-frame per second (fps) CCD. The cathode is cooled down to -25 ^{o}C with a cold air flow in the cold finger. Vacuum is maintained between the cathode and the input window, which is isolated with a thermally non-conductive ceramic to avoid thermal losses or condensation and ice on the window. The CCD can work in 1K×1K mode (12 μm pixels) at 40 fps or in hard-binned mode 512×512 pixel at 80 fps (24 μm pixels). Each photon interacting with the photocathode is amplified up to 10^6 to 10^7 times by the image intensifier, producing a signal much larger than the

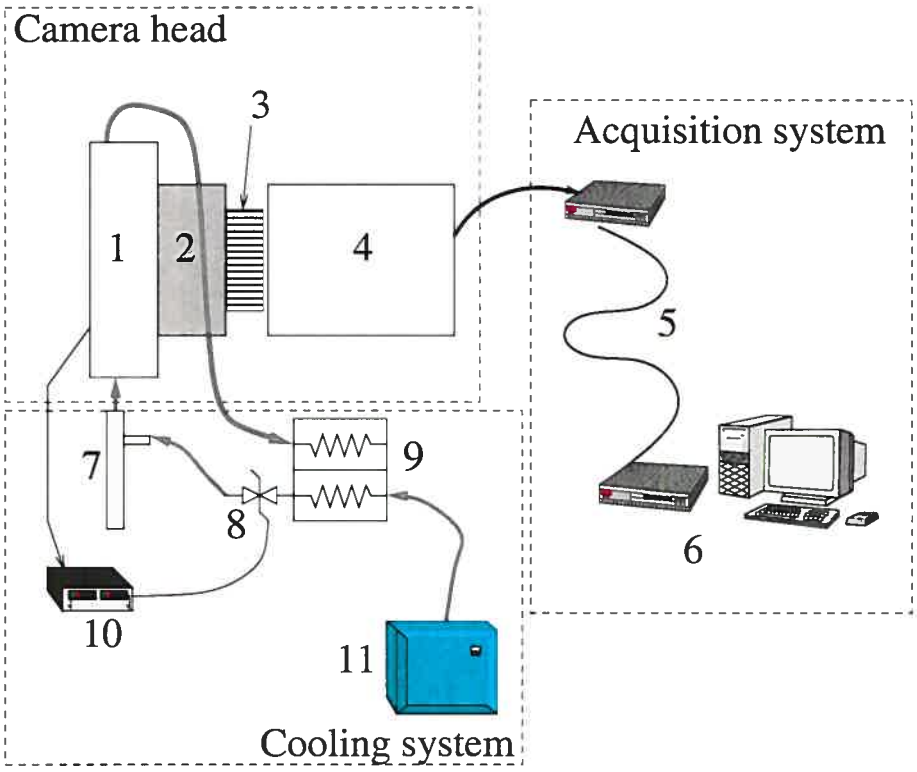

Fig. 18: Synoptic of the system : 1- Cold finger. 2-GaAs tube. 3- Fiber coupling. 4- 1k×1k CCD camera. 5- 1250 Mbits/s fiber link. 6- Host centering computer. 7- Vortex tube. 8- Proportioning valve. 9- Heat exchanger. 10- Temperature controller. 11- Air compressor and air dryer.

internal noise of the CCD. Figure 18 shows a schematic diagram of the system.

2.3.2 Acquisition

The acquisition system is completely different from those used in classical CCD systems. The philosophy is not to accumulate flux on pixels but to detect events that correspond to the arrival of each photon. Each event is then accumulated in the computer memory, forming the final image. The main difference between this new IPCS camera and older ones is the centering system. In previous IPCSs, the centering of the spot produced by amplified photons was done by a hard-wired system. Here, the camera is connected to a scalable DSP board based on the TMS 320C80 Multimedia Video Processor (MVP) chip consisting of 4 DSP cores working in Multiple-Instruction Multiple-Data scheme (MIMD). This board acquires data from the camera, puts them into a buffer, and then centers each

spot. This allows more versatility and even would permit one to center events at a better resolution than the physical pixel of the readout CCD, by fitting a gaussian to the event spot. The centering work is done in real time at the frame readout rate. The computing power is of prime importance here since the ability to acquire all frames is directly connected to it. With one TMS 320C80 chip, the system is limited to 1.6×10^4 photons/s. If the number of photons is greater, some frames would be lost since the DSP is still computing the centering of events in the previous frame when the new frame arrives. This is equivalent to a QE loss directly proportional to the number of frames missed. The solution is to use a parallelized DSP system (up to 14 DSP in our case). Parallelization of tasks is very easy : the idea is to allocate one incoming frame to one DSP processor core, up to the maximal number of cores present in the system. In our case, the gain adding processors is fully linear, leading to a maximal flux of 2.24×10^5 photons/s when the 56 cores (14 DSP) are present.

2.3.3 Cooling

A new cooling system has been developed based on a Ranque-Hilsh vortex tube. A vortex tube uses compressed air as a power source and produces hot air from one end and cold air from the other, with no moving parts. Differential temperatures close to -70^oC are possible between compressed air and cold air. Hence, the flow of cold air passes through the cryostat chamber, in front of the GaAs proximity-focused image-intensifier tube. The calories not used are directed towards a heat exchanger to cool down compressed air before it goes through the vortex tube (figure 18).

The flow of cold air is regulated with an electronically-controlled proportioning valve and a temperature process meter. Temperature is set to -25^oC in order to obtained a thermal noise close to 5 events per frame, to assure good quantum efficiency and to protect the GaAs tube from thermal shocks. This system is very stable and does not need any maintenance.

2.3.4 Performances

The measured QE of the whole system (including MCP losses) was measured to be 23% at Hα. The mean thermal noise of the cathode is 5 events/frame at -10^oC, which is equivalent to 0.7 photon/hour/pixel and drops to 3 events/frame at -25^oC. This dark current should drop to 0.5 events/frame if it was due only to the thermal emissivity of the

photocathode. This background noise, which shows no dependence on temperature, could be explained by K^{40} beta disintegration, which is present in the MCP glass (Siegmund et al., 1988). The typical event spot intensity profile half-width is 20μm despite the two stage MCP. This good performance is mainly due to the fact that these two MCPs are stacked. The expected MCP lifetime is 10 000 hours despite the high gain. Up to now the system has not been used sufficiently to confirm or reject this, but after 500 hours, it did not show any gain decay. Afterglow of the P-43 phosphor screen at the output of the tube was not detectable at 80 frames/s. This is not surprising since this phosphor has a decay time of 5 ms to reach 0.1 % of the initial intensity. The more classical P-20 phosphor widely used in image intensifiers is still emitting 20% of the initial intensity after 5 ms.

Whereas the system is limited by the acquisition computing power, it is also limited by the process itself. When two events occur within the same frame (25 ms) at the same location, only one event is counted instead of two. The mean number M of missed photons can be evaluated assuming a Poissonian process for the photon emission by the following equation :

$$M = 1 - \frac{1 - e^{-\lambda}}{\lambda}, \tag{2.8}$$

where λ is the mean number of photons expected during the resolved period of the detector.

Figure 19 shows the linearity response of an IPCS detector at different possible frame rates. This shows that the system loses its linearity when the flux increases. Therefore this detector is used exclusively for faint fluxes. Figure 19 shows also that this effect is less important for higher frame rates.

2.4 Observations

The new IPCS camera has been tested, coupled with the scanning Fabry-Perot interferometer *CIGALE* at the Cassegrain foci of the 3.6m ESO telescope (La Silla : September 2000, April 2002), and the 1.93m OHP telescope (October 2000, May 2001, November 2001, March 2002, June 2002), and with the scanning Fabry-Perot interferometer *PANORAMIX* at the 1.6m OMM telescope (March 2001, October 2001, March 2002). The observations are part of different scientific studies ranging from gas-rich, late–type galaxies (GHASP project : Garrido et al., 2002) to gas-poor ($\approx 10^6$ $M_\odot$), early–type systems (Rampazzo et al., 2002).

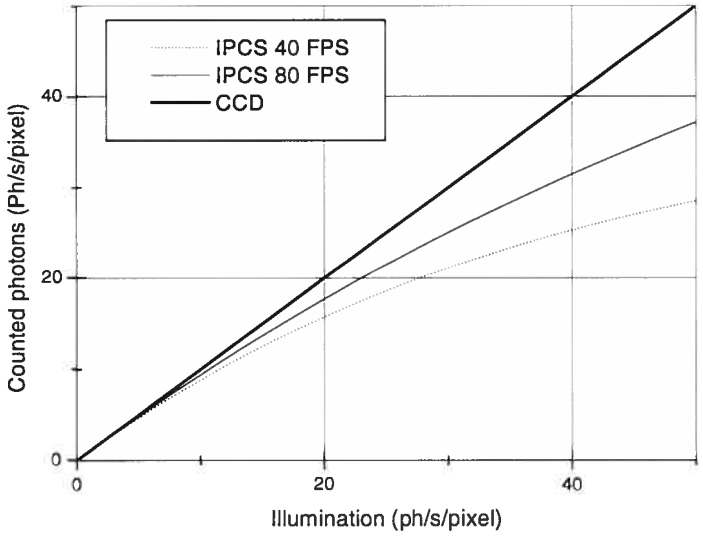

Fig. 19: Computed linearity of an IPCS detector at different frame rates.

2.4.1 Star formation triggering in blue compact galaxies

In August 1995, six luminous blue compact galaxies (LBCGs) and two companions were observed in the Hα emission-line with the CIGALE scanning Fabry-Perot interferometer attached to the ESO 3.6m telescope. The observations were obtained with the 20-year old Thomson IPCS with a S20ER photocatode. Still, these observations provide unique kinematical data, revealing large-scale perturbations and in many cases secondary dynamical components (Östlin et al., 1999 & 2001 ; Amram & Östlin, 2001). The results indicate that these LBCGs are caused by dwarf galaxy mergers.

However, this conclusion was based on a small biased sample, and in Septemer 2000, the same instrument equipped with the new GaAs tube was used to observe a new extended sample. Using the new detector, already after a few minutes it was possible to compute a velocity field in real time. Figure 20 shows the resulting Hα map and velocity field for ESO 249-31 based on a 40-minute exposure (15s per cycle, 32 channels, 5 cycles).

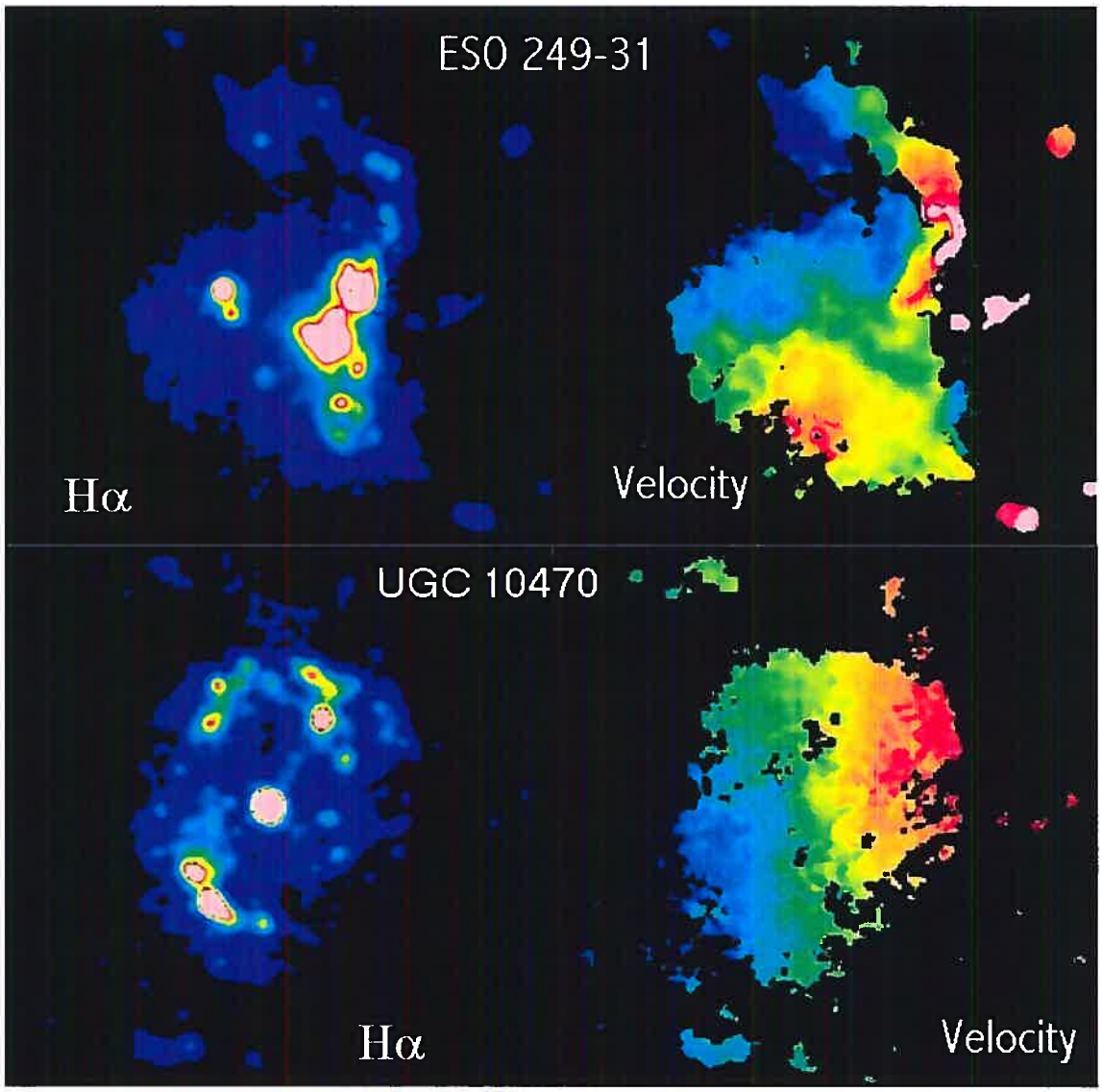

Fig. 20: **(Top) :** Hα emission-line map (left) and radial velocity field (right) of the galaxy ESO 249-31. The field of view of each image is 104" square. The pixel size is ~0.4 arcsec. The velocities range from 760 km/s (violet) to 960 km/s (white). The velocity field of this star forming galaxy is strongly perturbed. **(Bottom) :** Hα emission-line map (left) and radial velocity field (right) of UGC 10470, a galaxy observed for the *GHASP* project. The field of view of each image is 5.8′ square. The pixel size is ~0.7 arcsec. The velocities range from 1230 km/s to 1420 km/s. The signature of the bar is clearly seen in the velocity field (where the central isovelocity lines are inclined towards the major axis instead of being perpendicular to it). North is up, East is left.

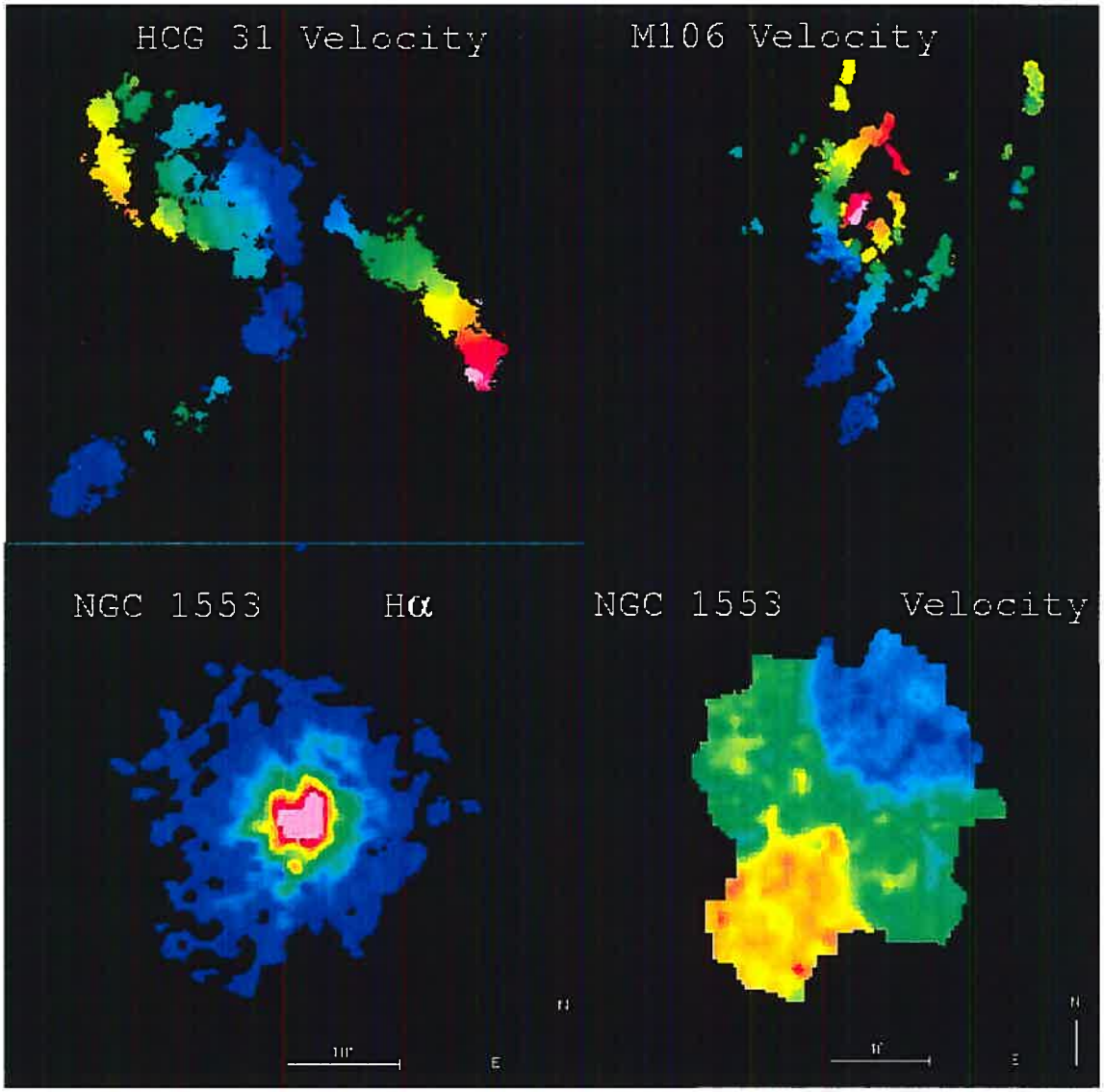

Fig. 21: **(Top–left)** : Radial velocity field of the compact group of galaxies HCG 31. The field of view of the image is 104" square. The pixel size is ~0.4 arcsec. The velocities range from 3840 km/s to 4160 km/s. This group contains 3 galaxies overlapping in projection in the velocity field, which looks strongly perturbed. **(Top–right)** : Hα emission-line map of NGC 4258 (M 106). The field of view is 12.5′ square. The pixel size is ~1.5 arcsec. The velocities range from 260 km/s to 755 km/s. The optical jet has been highlighted. **(Bottom–left)** : Hα emission-line map of NGC 1553. The clumpy structure of the emission, probably due to dust, is evident. **(Bottom–right)** : The velocity field of NGC1553 appears distorted. This is interpreted as due to the accretion event suffered by the galaxy. The velocities range from 1100 km/s (blue) to 1340 km/s (red).

2.4.2 The GHASP project

GHASP (Gassendi Hα survey of SPirals) is a survey of Hα in spiral galaxies. Its aim is to provide a homogeneous 2D kinematical sample of the ionized gas (HII regions and diffuse emission) of about 200 nearby spiral and irregular galaxies. The observations of the GHASP survey began in 1998, and up to now $\approx$ 100 galaxies have been observed and reduced (Garrido et al., 2002).

The GHASP instrument is attached to the Cassegrain focus of the OHP 1.93m telescope. This instrument is basically the same as the CIGALE instrument at ESO or the PANORAMIX instrument at Mont Megantic. The original f/15 aperture ratio of the OHP 1.93m telescope is brought to f/3.9 through the focal reducer. Since 2000, the detector is the new GaAs IPCS, offering a field of view of about 5.8 arcmin x 5.8 arcmin and pixels of $\sim$0.7 arcsec. Scanning the interferometer through 24 channels, the sampling step is about 15 km/s and the resolution reached is 3-5 km/s when the S/N is high. Figure 20 shows some results for UGC 10470, a GHASP target. More details and illustrations can be found on the Web sites http ://www-obs.cnrs-mrs.fr/interferometrie/ghasp/ghasp.html and http ://www.astro.umontreal.ca/fantomm

2.4.3 Velocity fields of galaxies in compact groups

The goal of this project is threefold : (1) determine the Tully-Fisher (TF) relation for a sample of compact-group (CG) galaxies and compare it with that for galaxies in different environments ; (2) obtain velocity fields and rotation curves for candidate tidal dwarf galaxies identified on R images (Plana et al. 1999 ; Mendes de Oliveira et al., 2001) ; (3) compare the properties of groups at different evolutionary stages : from a) false group, (HCG 18, Plana et al., 2000) ; b) kinematically undisturbed group (H88) ; c) mildly interacting group (HCG 89) ; d) strongly interacting group (HCG 16, Mendes de Oliveira et al., 1998) and forming dwarf galaxies (Stephan's Quintet - HCG 90, Plana et al., 1998 ; Mendes de Oliveira et al., 2001), up to e) merging group (HCG 31) or encounters (the Cartwheel CG, Amram et al. 1998). Using GIGALE attached to the ESO 3.6m, we observed a set of CGs in August 1995, but this sample was biased towards mild to strong emission-line objects. Using the same instrument, but upgraded with the new GaAs detector, we observed velocity fields in September 2000 for a new set of CGs dominated by faint emission-line galaxies (see fig 21).

2.4.4 Early-type galaxies

We also observed nearby early-type galaxies with shells (Malin & Carter, 1983). A major merging or the acquisition of a small system by a pristine elliptical galaxy (see e.g. Quinn, 1984 ; Dupraz & Combes, 1986) is the more reliable hypothesis for the origin of such stellar features although a weak interaction between galaxies (Thomson & Wright, 1990 ; Thomson, 1991) may also account for the development of shells. Recent observations revealed molecular gas interleaved with stellar shells in Cen A (Charmandaris et al., 2000) and in addition, in NGC 2865, Shiminovic et al. (1995) found that cold gas and stars have almost identical kinematics. This challenges merging models, which predict a rapid segregation of the gas toward the center, where it could ignite a star formation episode (see e.g. Weil & Hernquist, 1993). CIGALE coupled with the GaAs tube permits mapping of the warm gas distribution and of the velocity field. The latter proves to be an invaluable indicator of the mechanism leading to shell formation, once compared to the stellar velocity field.

2.4.5 Active galaxies

The SABbc galaxy NGC 4258 (M 106) is a LINER/Seyfert galaxy (Cecil et al., 2000) which shows a well-known low-energy jet which was discovered optically by Courtès and Cruvellier (1961) on Hα images and initially described as *anomalous arms*. It is a typical active galactic nucleus (AGN) system with an estimated central black hole mass of 3.6×10^7 $M_\odot$ (Chary & Becklin, 1997). It is a rare case of a nearby galaxy (5.5 Mpc) with a radio jet for which we can study, with sufficient resolution, the optical counterpart from ground-based telescopes. Most other similar systems are at much higher redshifts.

These observations will allow one to study in detail the kinematics of the ionized gas. This can be done in a ~2.5 hour observation obtained on the OMM 1.6m telescope. Despite the poor observing conditions (high clouds), the improved sensitivity of the camera allowed us to obtain usable data as shown in Figure 21. The optical jet coming from the center can clearly be seen as well as the arm pointing toward the companion. More details and illustrations can be found on the Web site http ://www.astro.umontreal.ca/fantomm.

2.5 Future developments and other applications

Current developments on GaAs tubes should make available up to 40% QE tubes with flat response in the 500-800 nm domain in the very near future, reducing the difference with backside AR coated CCDs and making them even more competitive when used in scanning instruments. Another interesting path to explore, which will be done in the near future, consists in centering the events at a better resolution than the readout CCD resolution as described above, increasing then the virtual size of the array and keeping a reasonable size for the detector itself. Finally this kind of system could find interesting applications in bioluminescence and all other fields where time resolution and high sensitivity are needed at the same time.

Acknowledgements

We would like to thank the ESO (La Silla), OHP, and OMM staff for their assistance during the commissioning of the new camera, and Mathieu Ouellet for the mechanical design. Many thanks to Tony Moffat for reviewing the English of the paper. Many thanks also to our collaborators Chantal Balkowski, Nils Bergvall, Sébastien Blais–Ouellette, Isabel Marquez, Josefa Masegosa, Claudia Mendes de Oliveira.

Chapitre 3

BHαBAR : un échantillon de galaxies spirales barrées

BHαBAR : Big H-Alpha kinematic sample of BARred spiral galaxies - I. Fabry-Perot observations of 21 galaxies

OLIVIER HERNANDEZ[a]

Département de physique and Observatoire du mont Mégantic, Université de Montréal, C.P. 6128, Succ. centre ville, Montréal, Québec, Canada. H3C 3J7 and

Observatoire de Marseille, 2 Place Le Verrier, F–13248 Marseille Cedex 04, France

CLAUDE CARIGNAN[a]

Département de physique and Observatoire du mont Mégantic, Université de Montréal, C.P. 6128, Succ. centre ville, Montréal, Québec, Canada. H3C 3J7

PHILIPPE AMRAM[a]

Observatoire Astronomique de Marseille Provence, LAM, 2 place Le Verrier, F-13248 Marseille Cedex 04, France

LAURENT CHEMIN

Département de physique and Observatoire du mont Mégantic, Université de Montréal, C.P. 6128, Succ. centre ville, Montréal, Québec, Canada. H3C 3J7 and

OLIVIER DAIGLE[a]

Département de physique and Observatoire du mont Mégantic, Université de Montréal, C.P. 6128, Succ. centre ville, Montréal, Québec, Canada. H3C 3J7

Submitted to the Monthly Notices of the Royal Astronomy Society

Abstract

The Hα gas kinematics of twenty-one representative barred spiral galaxies belonging to the *BHαBAR* sample is presented. The galaxies were observed with FaNTOmM, an integral-field spectrometer, on three different telescopes. The 3D data cubes were processed through a robust pipeline with the aim of providing the most homogeneous and accurate dataset possible useful for further analysis. The data cubes were spatially binned to a constant signal-to-noise ratio, typically around 7. Maps of the monochromatic Hα emission line and of the velocity

[a]Visiting Astronomer, Canada–France–Hawaii Telescope, operated by the National Research Council of Canada, the Centre National de la Recherche Scientifique de France, and the University of Hawaii.

field were generated and the kinematical parameters were derived for the whole sample using tilted-ring models. The photometric and kinematical parameters (position angle of the major axis, inclination, systemic velocity and kinematical center) are in relative good agreement, except maybe for the later-type spirals. Nevertheless, the determination of the kinematical parameters is more accurate than the photometric parameters. A preliminary analysis of the velocity fields suggests that the dark halo component is rather faint in the inner optical region of the galaxies.

Keywords : galaxies : barred - galaxies : spiral - galaxies : kinematics and dynamics.
Methods : observational. Techniques : radial velocities.

3.1 Introduction

The presence of a bar in disk galaxies seems to be a common feature. Bars have been recognized in galaxies since the time of Curtis (1918) and Hubble (1926). In the optical, roughly 30% of spiral galaxies are strongly barred (de Vaucouleurs, 1963) while another 25% are weakly barred. Evidence that bars in spirals are more obvious in the near-infrared (NIR) than in the visible goes back to Hackwell & Schweizer (1983). Recent surveys in the NIR wavelength band have shown that up to 75% of high surface brightness galaxies may have a more or less strong bar (e.g. Knapen, Shlosman & Peletier, 2000 ; Eskridge et al., 2000).

When present, such bars will introduce non-circular motions that should be seen in the radial velocity fields. Since the kinematics of barred spirals is different from that of more or less axisymmetric disks, it is important to model them properly if one wants to derive, as accurately as possible, the overall mass distribution. This distribution is directly derived from the knowledge of the circular velocities. Since the gas in axisymmetric galaxies is nearly on circular orbits, and its random motions are small compared with the rotation, its kinematics can be used to derive rotation curves (RC).

However, when a galaxy is barred, the gas response to the non-axisymmetric part of the potential cannot be neglected. Thus, a rotation curve derived without correcting for those non-circular motions cannot be said to represent the circular motions and be used to derive the mass distribution. The presence of a bar is expected to leave signatures mainly in the central regions of the RCs (Schoenmakers et al., 1997), which is the region where the free parameters of the mass models are really constrained (Blais-Ouellette et al., 1999, 2004 ;

Blais-Ouellette, Amram & Carignan, 2001). Indeed, the parameters of mass models are not constrained by the flat part but by the rising part of RCs.

This study is dedicated to the kinematics and the dynamics of barred galaxies. The aim will be to derive the most accurate velocity fields possible for a representative sample of barred galaxies in order to analyze their kinematics. The *BHαBAR* sample should provide the most homogeneous dataset on barred spiral galaxies to date. Once this database will be available, the following goal will be to model those galaxies, extract the non-circular component of the velocities and thus recover the circular motions and derive proper RCs. Only then will it be possible to model accurately their mass distributions.

This homogeneous study of the kinematics of twenty-one nearby barred spiral galaxies, based on the two-dimensional (2D) kinematics of the Hα gas, is presented in this paper. Section 2 gives an overview of the observational campaign and presents the global properties of the *BHαBAR* sample while Section 3 discusses the data reduction and especially the adaptive binning that was performed. In Section 4, the kinematical parameters are derived and the FP maps are presented in Section 5. The conclusions can be found in Section 6 and an appendix presents a short observational description of the galaxies of the *BHαBAR* sample.

3.2 The *BHαBAR* sample : Observations

3.2.1 The sample

The twenty-one galaxies of the *BHαBAR* sample (pronounced "Babar") were selected according to the following criteria :

- northern nearby barred galaxies selected in de Vaucouleurs et al., 1991 (hereafter the RC3) catalog e.g. $\delta_{J2000} \geq +5.0$.
- galaxies not in obvious interaction ;
- inclination $< 75°$;
- systemic velocity $\leq 3000\,\mathrm{km\,s^{-1}}$;
- $D_{25} \geq 3.5\,'$, for the OmM field of view (FOV) ;
- $2.0\,' \leq D_{25} \leq 4.3\,'$ for the CFHT FOV ;
- $2.0\,' \leq D_{25} \leq 6.0\,'$ for the OHP FOV ;
- well distributed in Hubble types, from SBb (or SABb) to SBdm (or SABdm), see

Fig. 22 ;

- if possible, no nuclear activity (two exceptions : Seyferts) ;
- HI data available, to constrain the mass models ;
- J,H,K_s band high resolution images (2MASS), or Sptizer 3.6 μm images, if available, to reconstruct the potential of the bar in future N-body models ;
- surface photometry available to constrain the mass models ;
- $M_B \leq$ -17 ;

The twenty-one velocity fields of the galaxies are mapped in Fig. 23 and the basic information on the objects can be found in Table II. The global distribution versus morphological type and blue absolute Magnitude (M_B) is mapped in Fig. 22. Galaxy types are taken from the RC3. The photometric inclinations i were calculated using $q = b/a$, the ratio of the minor to the major axis, extracted from the value of R_{25} given in the RC3 and applying the following formula :

$$\cos^2 i = \frac{q^2 - q_0^2}{1 - q_0^2}$$

where q_0 is the intrinsic axial ratio of the disk (for an edge-on system). q_o was not considered as a function of morphological type since the variation from its nominal value of $q_0 = 0.2$ is only significant for late type galaxies (types $\geq$ Sd) which represent only 3 of the 21 galaxies in the sample. Since the inclinations of the galaxies in the *BHαBAR* sample were chosen with i $\leq 75°$, the problem of extinction along the line of sight (as in the case of a nearly edge-on galaxy) and the associated uncertainty on the observed velocities are greatly reduced.

The criteria of the field of view (FOV) was an important one in order to have a correct physical sampling on the detector and an appropriate scale on the sky. According to this, the more extended galaxies on the sky (see $D_{25}^{b,i}$ - diameter computed at the 25th magnitude/arcsecond^2 in blue light adjusted for the effects of projection and obscuration from Tully 88 -, Table II, column 6) were observed at the OmM which has a large field of view (FOV$\simeq 20'$). Table IV summarizes the optical characteristics of FANTOMM on the three telescopes.

The idea was to try to get a complete and homogeneous coverage of the Hubble sequence. However, due to their poor gas content, only one early type galaxy (SBb) was observed. At the other end of the sequence, only one Sdm was observed. Figure 22 gives a histogram of the sample. Another criteria was to avoid galaxies with nuclear activity in order to have galaxies with only non-axisymmetric motions due to the bar itself. Nevertheless, two

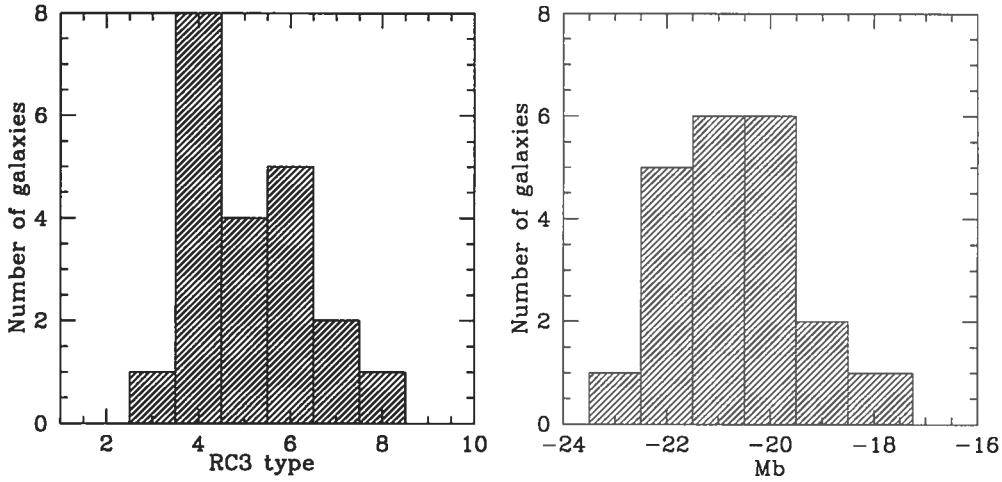

Fig. 22: Histogram of the sample morphological types and M_B. **Left :** The type goes from SBb (type 3) to SBdm (type 8). **Right :** M_B varies from -17 to -23.

galaxies of the sample turned out to have Seyfert type nuclear activity : NGC 6217 and NGC 7479. This confirmation of nuclear activity was not clear at the moment of the selection of the *BHαBAR* sample, so it was decided to keep them in the sample. This will be taken into account when, in further work, N-body simulations coupled to SPH will be done (forthcoming papers).

3.2.2 Observing runs

The observations were obtained using FANTOMM[a], a wide integral-field spectrometer. This instrument is a permanent instrument on the OmM telescope, and a visitor instrument on various telescopes. FANTOMM is basically a focal reducer containing an interference filter wheel, a Fabry-Perot (hereafter FP) interferometer and an image photon counting system (IPCS). The IPCS used is a third generation photocathode with high quantum efficiency over a large wavelengths range (Hernandez et al., 2003 and Gach et al., 2002). This camera is very efficient to reach a good Signal-to-Noise ratio (S/N) for objects with very faint fluxes since, compared with CCDs, it has no read-out noise. Its multiplex mode also allows a rapid and

[a]FANTOMM means **F**abry-Perot of **N**ew **T**echonolgy for the **O**bservatoire du **m**ont **M**égantic (http ://www.astro.umontreal.ca/fantomm).

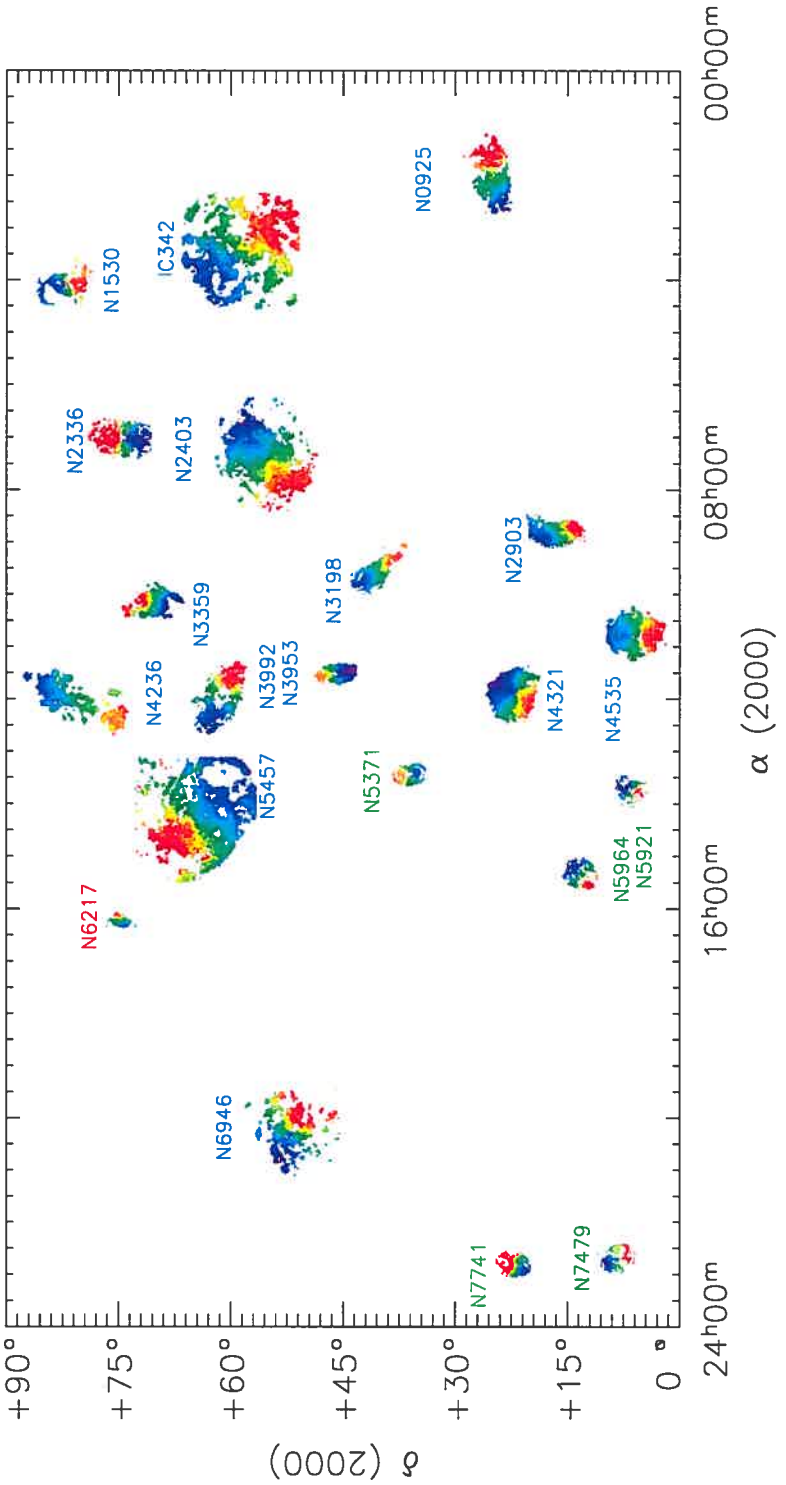

Fig. 23: The *BHαBAR* sample sky coverage. The names in blue correspond to the observations done at the OmM, in green at the CFHT and in red at the OHP. .

Table II: Observational data for the *BHαBAR* sample.

Galaxy Name	α(J2000) hh mm ss	δ(J2000) ° ′ ″	Type RC3	D Mpc	$D_{25}^{b,i}$ ′	$M_B^{b,i}$	$B_T^{b,i}$	$L_b^{b,i}$ ″	PA_b °	V_{sys}
NGC 0925	02 27 16.8	+33 34 41	SAB(s)d	9.3[a]	11.2	-20.0	10.6	56.5	112	554
IC 0342	03 46 49.7	+68 05 45	SAB(rs)cd	3.9[1]	27.9	-21.6	6.4	n/a[2]	32	32
NGC 1530	04 23 28.5	+75 17 50	SB(rs)b	36.6[1]	4.8	-21.3	11.5	137.0[2]	116	2460
NGC 2336	07 27 04.5	+80 10 41	SAB(r)bc	22.9[1]	5.2	-22.1	11.1	72.8	5	2196
NGC 2403	07 36 54.5	+65 35 58	SAB(s)cd	4.2[a]	21.4	-19.7	8.5	n/a[2]	n/a	132
NCG 2903	09 32 09.7	+21 30 02	SB(s)bc	6.3[1]	10.0	-19.8	9.13	143.4	26	554
NGC 3198	10 19 54.9	+45 33 09	SB(rs)c	14.5[a]	7.8	-20.2	11.1	81.8	12	660
NCG 3359	10 46 37.7	+63 13 22	SB(rs)c	19.2[1]	7.2	-20.4	10.8	87.0	15	1013
NGC 3953	11 53 49.5	+52 19 39	SB(r)bc	17.0[1]	5.2	-20.6	10.5	70.6	55	1054
NGC 3992	11 57 36.0	+53 22 28	SB(rs)bc	17.0[1]	6.6	-20.7	10.4	136.5	37	1051
NGC 4236	12 16 42.1	+69 27 45	SB(s)dm	2.2[1]	16.4	-17.3	9.5	170.7	143	2
NGC 4321	12 22 55.2	+15 49 23	SAB(s)bc	16.1[a]	7.4	-22.1	10.0	53.4	107	1590
NGC 4535	12 34 20.3	+08 11 53	SAB(s)c	16.0[a]	6.9	-22.0	10.6	70.0[2]	45	1966
NGC 5371	13 55 40.6	+40 27 44	SAB(rs)bc	37.8[1]	4.0	-21.6	11.3	47.2	97	2558
NGC 5457	14 03 12.5	+54 20 55	SAB(rs)cd	7.4[a]	30.2	-22.7	8.3	86.5	84	231
NGC 5921	15 21 56.4	+05 04 11	SB(r)bc	25.2[1]	4.9	-20.7	11.3	73.5	21	1480
NGC 5964	15 37 36.3	+05 58 28	SB(rs)d	24.7[1]	4.0	-19.5	12.5	56.0[2]	150	1447
NGC 6217	16 32 39.2	+78 11 53	(R)SB(rs)bc*	23.9[1]	3.6	-20.2	11.7	68.8	153	1359
NGC 6946	20 34 52.0	+60 09 15	SAB(rs)cd	5.5[1]	14.9	-20.8	7.92	34.5	166	46
NGC 7479	23 04 57.1	+12 19 18	SB(s)c*	32.4[1]	3.8	-21.1	11.4	114.7	2	2382
NGC 7741	23 43 54.0	+26 04 32	SB(s)cd	12.3[1]	3.8	-18.8	11.7	89.0	103	750

PA_b refers to the PA of the bar. V_{sys} is the systemic velocity in $\mathrm{km\,s^{-1}}$. References for the distances : [1] - Distances are based on velocities, an assumed value of the Hubble Constant of $75\,\mathrm{km\,s^{-1}}\,Mpc^{-1}$, and the model that describes the velocity perturbations in the vicinity of the Virgo Cluster, c.f. Tully (1988). [a] - distances calculated from Cepheids (NGC 0925 - Silbermann et al. (1994), NGC 2403 - Freedman & Madore (1988), NGC 3198 - Kelson et al. (1999), NGC 4321 - Ferrarese et al. (1996), NGC 4535 - Macri et al. (1999), NGC 5457 - Kelson et al. (1996). $D_{25}^{b,i}$, optical diameter at the 25 magnitude/arcsecond^2 in the blue light, $M_B^{b,i}$ absolute magnitude in the blue band, $B_T^{b,i}$ apparent magnitude in the blue band and $L_b^{b,i}$ bar lengths from Martin 1995, all adjusted for the effects of projection and obscuration. [2] - values not available in Martin (1995) are calculated from isophote fitting (except for NGC 1530 where the data are from Zurita et al,. 2004). V_{sys} represents the systemic velocities provided by Tully (1988). The symbol * refers to nuclear activity.

Table III: Journal of the Fabry Perot Observations.

Galaxy	Date	Filter			Exposure		Fabry-Perot				Sampling	
Name		$\lambda_c^{(4)}$	L[5]	T[6]	$t_{tot}^{(7)}$	$t_{ch}^{(8)}$	p[9]	FSR[10]	F[11]	R[12]	nch[13]	stp[14]
NCG 0925[1]	02/11/02	6584	15	75	132	2.75	765	391.77	16	12240	48	0.18
IC 0342[1]	02/11/03	6578	15	60	144	3	765	391.77	16	12240	48	0.18
NGC 1530[1]	03/01/30	6622	15	70	240	5	899	333.36	20	17980	48	0.15
NGC 2336[1]	02/11/10	6617	15	69	240	5	765	391.77	16	12240	48	0.18
NGC 2403[1]	02/11/17	6569	10	50	120	3	765	391.77	14	10670	40	0.21
NCG 2903[1]	03/02/08	6599	15	74	180	3.75	899	333.36	20	17980	48	0.15
NGC 3198[1]	03/03/06	6584	15	75	260	5	899	333.36	23	20976	52	0.14
NCG 3359[1]	01/11/17	6569	10	50	130	3.25	765	391.77	14	10670	40	0.21
NGC 3953[1]	03/02/26	6599	15	74	273	5.25	899	333.36	23	20976	52	0.14
NGC 3992[1]	03/02/27	6599	15	74	260	5	899	333.36	23	20976	52	0.14
NGC 4236[1]	04/02/27	6578	15	60	182	3.5	899	333.36	23	20976	52	0.14
NGC 4321[1]	03/02/25	6605	15	75	260	5	899	333.36	23	20976	52	0.14
NGC 4535[1]	03/03/06	6617	15	69	156	3	899	333.36	23	20976	52	0.14
NGC 5371[2]	03/04/04	6622	15	70	88	1.83	899	333.36	16	17980	48	0.15
NGC 5457[1]	03/02/28	6578	15	60	260	3.5	899	333.36	23	20976	52	0.14
NGC 5921[2]	03/04/09	6599	15	74	120	2.5	899	333.36	16	17980	48	0.15
NGC 5964[2]	03/04/08	6599	15	74	120	2.5	899	333.36	16	17980	48	0.15
NGC 6217[3]	01/10/17	6595	10	60	72	3	793	377.94	11	8722	24	0.34
NGC 6946[1]	02/11/19	6569	10	50	120	2	765	391.77	14	10670	40	0.21
NGC 7479[2]	02/10/04	6617	15	69	60	6	1162	257.92	11	12782	24	0.23
NGC 7741[2]	02/10/06	6584	15	75	60	6	1162	257.92	11	12782	24	0.23

[1] OmM : Observatoire du mont Mégantic, Québec, Canada. 1.6m telescope.

[2] CFHT : Canada-France-Hawaii Telescope, Hawaii, USA. 3.6m telescope.

[3] OHP : Observatoire de Haute-Provence, France. 1.93m telescope.

[4] λ_c : Filter central wavelength in Å

[5] L = FWHM = Filter Full Width at Half Maximum in Å

[6] T : Filter maximum transmission at λ_c

[7] Total exposure time in minutes

[8] Exposure time per channel in minutes

[9] Fabry-Perot interference order at Hα

[10] Fabry-Perot Free Spectral Range (FSR) at Hα in $\mathrm{km\,s^{-1}}$

[11] Mean *Finesse* through the field of view

[12] For a signal to noise ratio of 5 at the sample step

[13] nch : number of channels done by cycle in multiplex observations

[14] Wavelength step in Å

Table IV: FANTOMM characteristics on various telescopes.

Telescope Name	F/D	pixel size (")	FOV (′)	FOV (vign.) (′)
OmM	2.3	1.61	19.4	19.4
OHP	3.92	0.68	8.2	5.5
CFHT	2.96	0.48	5.8	3.9

F/D represents the ratio focal length over telescope diameter. The pixel size after binning is 2 × 2, the original GaAs system providing 1024×1024 px^2. FOV is the diagonal Field Of View of the detector. FOV (vign.) represents the effective unvignetted FOV (without the vignetting due to the filter used).

efficient suppression of the OH sky lines since their variations can be averaged out. FANTOMM was used in its low spatial resolution mode of 512 × 512 pixels^2 (instead of 1024 pixels^2).

The observations of the sample were spread over nine different observing runs over a three year period. Six runs were at the 1.6m of the Observatoire du mont Mégantic (OmM), one at the 1.93m of the Observatoire de Haute-Provence (OHP) and two at the the 3.6m of the Canada-France-Hawaii Telescope (CFHT). FANTOMM was attached at the Cassegrain focus of the three telescopes ; the different FOVs on various telescopes are given in Table IV. Various FP interferometers were used in order to fit the adequate spectral resolution. The interference orders vary from p=765 to p=1162, calculated for λ_0=6562.78Å (see Table III).

All the calibrations were done using the same neon lamp (see below for more details on the data reduction). With the rapid analogic detector mode, calibrations were done in less than a minute. This allowed us to perform as many calibrations as needed during the runs with very little overhead. A new bank of interference filters was also used covering a velocity range from 0 to 10,000 km s^{-1} (from 6562Å to 6785Å).

3.3 Data reduction

The reduction of the data cubes was performed using the package ADHOCw (Boulesteix, 2004 and Amram et al., 1992) rewritten with large improvements under the IDL package. The major improvements are the following :

- the elementary interferograms (elementary images obtained with an exposure time ranging between 10 and 15 seconds, depending on the sky transparency

conditions and on the number of scanning steps) were corrected for sky fluctuations before summation;
- adaptive Hanning smoothing was performed in order to increase the S/N over the field;
- WCS astrometry on the images was performed;
- a robust procedure to remove OH night sky lines was used;
- full automated and reproduceable reduction and data analysis were performed.

3.3.1 Phase Calibration

Raw interferograms must be corrected to obtain data cubes sorted in wavelength. This operation is called the "phase calibration" or wavelength calibration. These calibrations are obtained by scanning the narrow Ne 6599 Å line under the same conditions as the observations. Two phase calibrations were done, one before the exposure and the other after. Using the mean of the calibrations, a "phase map" is computed, indicating the scanning step at which the maximum of the interference pattern inside a given pixel is observed. The FP formula below, giving the shape of the interference pattern on the detector as a function of the observed wavelength, helps us to find the observed Doppler-shifted wavelength λ at each point by comparison with

$$p\lambda = 2n\cos\theta,$$

where p is the interference order at λ_0 (here 6562.78Å), n the refractive index of the medium and θ the incidence angle on the FP (angular distance on the sky). An uncertainty remains since the velocity is only known modulo the Free Spectral Range (column 10 in Table III, note 11). This ambiguity is easily solved by using comparisons with long-slit spectroscopy or 21 cm HI line data to provide the zero point of the velocity scale. However, this means that when the redshift emission line of the galaxy is far from the calibration line, absolute values of the systemic velocity could be wrong (which is not a problem since we are mainly interested in relative velocities for our kinematical studies). In such cases, two solutions are beeing developed : a correction using the dispersion in the multi-layer, semi reflective high Finesse coating, which is hard to model for high multilayer coatings, or/and an absolute calibration done at the scanning wavelength. Nevertheless, the *relative* velocities with respect to the systemic velocity are very accurate, with an error of a fraction of a channel width ($< 3\,\mathrm{kms}^{-1}$) over the whole field. In this study, systemic velocities of the sample, presented

in Table II, were taken directly from Tully 88.

The signal measured along the scanning sequence was separated in two parts : (1) an almost constant level produced by the continuum light in a narrow passband around Hα and (2) a varying part produced by the Hα line (referred hereafter as the monochromatic map). After this calibration step, an adaptive binning was performed.

3.3.2 Adaptive binning and maps

Hanning smoothing was performed on all the data cubes along the spectral axis. The Hanning smoothing can suppress the problems connected with the frequency response (artifacts in the spectra caused by the sampling and the Fourier transform) of the spectra as a real function of finite length. The strong OH night sky lines passing through the filter were reconstructed into a cube and subtracted from the galaxy's spectrum (Daigle, Carignan & Hernandez, 2005).

In order to increase the signal-to-noise ratio (S/N), an adaptive spatial smoothing, based on the 2D-Voronoi tessellations method (Cappellari & Copin, 2002) was also applied to the 3D data cubes (Daigle, Carignan & Hernandez, 2005) before producing the monochromatic images and velocity fields. Each pixel was binned to reach a S/N of typically 5 to 10, depending on the observation conditions and the morphological type of the galaxy. This clever smoothing is effective not only in high S/N regions but also in regions of low S/N. First, in high S/N regions (S/N value superior to a fixed limit of 5, 7 or 10), the smoothing will not act and a bin is only one pixel. This will ensure to have the best spatial resolution possible in high S/N regions. This differs from classical gaussian smoothing (Garrido et al., 2003 ; Zurita et al., 2004) where the kernel used will do a mix between a pixel and its adjacent ones, and will cause a cross-pollution between the two regions. Second, for low S/N regions, pixels are binned until the S/N required is reached or the size of the resultant bin is reached (typically $30px^2$). This is very useful in interarm regions where the signal is dominated by the diffuse Hα and not by HII regions. Thus, velocity maps have the best possible coverage without losing any spatial resolution in the high S/N regions.

Finally, the intensity-weighted mean (barycentre) of the Hα emission line profile was converted into wavelength and then into heliocentric radial velocity. Monochromatic images were obtained by integrating the Hα profiles.

3.3.3 WCS astrometry

SAOIMAGE DS9 developed by the Smithsonian Astrophysical Observatory (Joye & Mandel, 1999) has been used to find the correct astrometry of the monochromatic and Hα images. KARMA (Gooch, 1996) and its routine KPVSLICE have been used to apply a co-ordinate system header to all images and data cubes. Systematic comparison between K-band and XDSS Blue band images and the field stars in rough continuum images (with no adaptive binning) were made in order to find the correct World Coordinate System for each images. For the 21 galaxies of the *BHαBAR* sample, stars were easily found in rough continuum images.

3.4 Kinematics

3.4.1 Analysis of the data

For each galaxy in the sample, Figures 26 to 46 provide : the XDSS blue image, the K-Band image or the SPITZER 3.6μm image (if available), the monochromatic image, the velocity field and the Position-Velocity (PV) plot.

Once the astrometry was done on all the images and data cubes, the kinematical parameters were derived using GIPSY and KARMA.

The ROTCUR routine in the GIPSY package was used to find the kinematical parameters of the galaxies studied. ROTCUR (Begeman, 1987) derives the kinematical parameters from the observed velocity field by fitting tilted-ring models. The observed velocities given in the velocity maps, $V_{\rm obs}$, are obtained by solving the following equation

$$V_{\rm obs} = V_{\rm sys} + V_{\rm rot}(R)\cos\theta\sin i + V_{\rm exp}(R)\sin\theta\sin i,$$

where $V_{\rm rot}$ is the rotation velocity, $V_{\rm exp}$ the expansion velocity, R and θ the polar coordinates in the plane of the galaxy and i the inclination. The same procedure was used for all the galaxies in the sample. The physical width of the rings is always the same : $4.83''$ for the OmM, $2.04''$ for the OHP and $1.44''$ for the CFHT data, in order to have a good sampling of the signal.

For each galaxy in the sample, a fit is first done simultaneously for the kinematical center (x_{pos}, y_{pos}) and the systemic velocity V_{sys}, fixing the position angle $P.A.$ and the

inclination i. Since all the galaxies in the *BHαBAR* sample are barred, it was decided to derive the kinematical parameters only in the axisymmetric part of the disk of the galaxy. This means that the central regions of the galaxy were systematically masked to avoid contamination from non circular motions due to the presence of the bar. In order to determine the range of galactic radii to apply ROTCUR, the values of the deprojected bar lengths given by Martin (1995, and reported in Table II, column 9) were used. For five galaxies not belonging to the "Martin" sample (IC 0342, NGC 1530, NGC 2403, NGC 4535 and NGC 5964), an ellipse fitting was done to determine an approximate bar length. Second, the V_{sys} and the kinematical center found were kept fixed and both $P.A.$ and i were allowed to vary over the same radius range and their mean values derived. It was decided to use mean values of $P.A.$ and i because disks are rarely warped inside the optical disks. Warps are mainly seen in disks for R > R_{opt}. The $V_{\rm rot}$ are then derived keeping the 4 derived parameters, (x_{pos}, y_{pos}), V_{sys}, $P.A.$ and i fixed over the whole radius range. In all the fits, $V_{\rm exp}$ was not considered and fixed to zero. Finally, a 2D kinematical model for each galaxy of the *BHαBAR* sample was constructed using the VELFI routine of GIPSY and subtracted from the data to get a residual velocity field. This whole process was repeated until the residuals were found to be minimal and with a distribution as homogeneous as possible over the whole FOV. For all the galaxies, this is indeed the case, except in the central regions were non-circular motions due to the bar are found.

Once the most suitable 2D kinematical model was found, the KPVSLICE routine of KARMA was used to derive a Position-Velocity (PV) diagram. This PV plot is useful to check if the rotation curve derived from the whole 2-D velocity field is a good representation of the kinematics on the major axis. When the range of velocities in a galaxy was superior to the Free Spectral Range of the etalon used, the overall velocity range was distributed over two or three orders. In this case, data cubes have been replicated in the spectral dimension (twice or three times) to construct the PV plots. This is the case for NGC 7479, NGC 5371, NGC 4535, NGC 3992, NGC 3953, NGC 2903, NGC 2336 and NGC 1530.

Table V gives the results for the kinematical parameter fitting, compared with the photometric data of RC3 and indicates the shift between the photometric and kinematical centers. Since in the ROTCUR task the kinematical value of $P.A.$ is defined as the angle measured counterclockwise from the North to the receding side of the velocity field, it may thus differ from the RC3 value by 180°. A photometrical $P.A.$ is indeed often given without taking into account which side of a galaxy is receding or approaching.

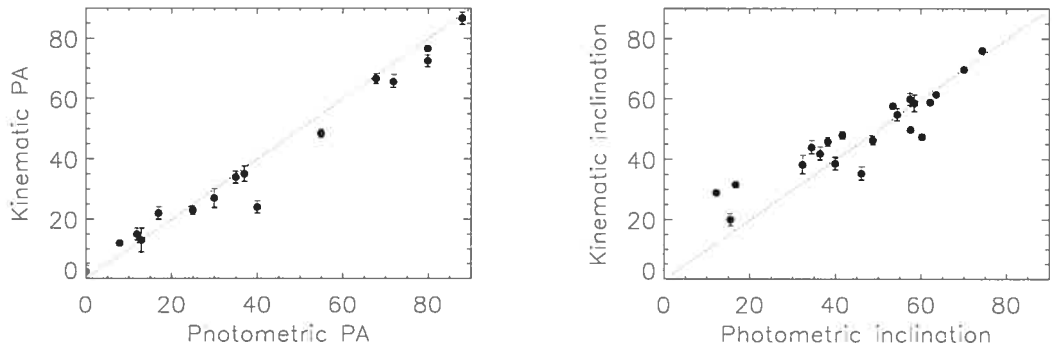

Fig. 24: Comparison between the kinematic and photometric position angles and inclinations. Position angles are given modulo 90°. The dashed line represents the y=x equation.

The agreement is good between the photometric and the kinematical position angle, even for low inclination galaxies for which the photometric position angle is difficult to determinate accurately. The agreement is still acceptable but the dispersion higher for the determination of the inclinations by both methods. Noticeable discrepancies can nevertheless be seen for two galaxies having a round shape (IC 0342 and NGC 4321) and a low morphological inclination (<20°). The morphological method used to determine the inclination, in fitting ellipses along the external levels of constant surface brightness (or simply from the axis ratios), minimizes the inclination, while the kinematic method is much less sensitive to this "face-on" effect. The shift between the position of the center of the galaxy determined from the photometry and the kinematics is clearly a function of the morphological type of the galaxy (see Fig. 25). The strongest discrepancies occur for later type spirals for which the morphological center is not always easy to identify. The large value of the offset when plotted in units of *arcsec* on Fig. 25 (left panel) shows that, for a large majority of galaxies, this difference may not be explained by seeing or spatial resolution effects. On the other hand, this offset is not statistically significant : NGC 2403, IC 0342, NGC 0925, and NGC 5457 have an offset of 1.17, 0.89, 0.67 and 0.30 kpc, respectively, while the bulk of the 19 galaxies has an offset lower or equal to 0.1 kpc (the determination of the photometric center for NGC 4236 and NGC 5964 remain highly uncertain).

Future N-body models coupled to a SPH code will help understand the gas behavior in a non axysimmetrical potential and provide an explanation for such differences.

Table V: Kinematic and photometric position angles, inclinations and offsets between centers.

Galaxy	Photometric		Kinematics		Offset from photometric center	
name	*P.A.* (°)	Incl.(°)	*P.A.* (°)	Incl.(°)	(arcsec)	(kpc)
NGC 0925	102	57.6	105.0±1.0*	50.0±1.5	26.0	0.670
IC 0342	n/a	12.0	42.0±2.0	29.0±0.4	16.2	0.830
NGC 1530	n/a	60.3	5.0±1.0*	47.6±0.6	2.9	0.020
NGC 2336	178	58.5	177.0±1.3†	58.7±2.7	4.1	0.002
NGC 2403	127	57.5	125.0±1.0	60.0±2.0	25.4	1.167
NGC 2903	17	63.6	22.0±1.0*	61.5±0.5	2.4	0.083
NGC 3198	35	70.1	33.9±0.3*	69.8±0.8	8.4	0.105
NGC 3359	170	54.5	167.0±2.0*	55.0±2.0	6.1	0.015
NGC 3953	13	62.2	13.0±0.8	59.0±0.4	6.5	0.086
NGC 3992	68	53.5	67.0±1.0*	57.8±0.8	2.9	0.015
NGC 4236	162	74.4	156.1±1.6	76.1±0.7	55.5	0.498
NGC 4321	30	16.5	27.0±1.0†	31.7±0.7	8.7	0.101
NGC 4535	0	46.1	2.3±0.4*	35.0±2.0	3.6	0.057
NGC 5371	8	38.3	12.0±1.0	46.0±1.5	2.0	0.011
NGC 5457	n/a	15.3	53.0±1.0	20.0±2.0	17.7	0.297
NGC 5921	130	36.5	114.0±0.7	42.0±2.0	4.5	0.045
NGC 5964	145	40.0	138.7±0.7	38.8±2.1	15.0	1.130
NGC 6217	n/a	34.5	250.0±1.0	44.1±2.1	3.34	0.014
NGC 6946	n/a	32.4	239.0±1.0	38.4±3.0	8.2	0.163
NGC 7479	25	41.7	23.0±1.0*	48.2±1.3	7.2	0.060
NGC 7741	170	48.8	162.9±0.5*	46.5±1.5	3.9	0.023

P.A. = Position Angle of the major axis of the galaxy.

† indicates that *P.A.* = 180°- kinematical *P.A.*

∗ indicates that *P.A.*=180 + *P.A.*

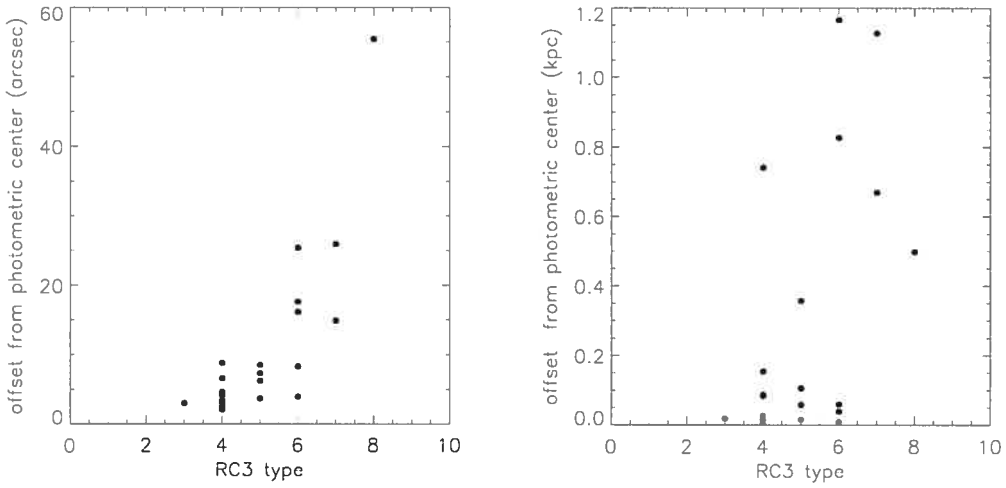

Fig. 25: Left : Distance (in arcsec) between the photometrical and kinematical centers as a function of the morphological type. The offsets are computed in the plane of the sky (not corrected for inclination). **Right** : Deprojected distance (in kpc) between the photometrical and kinematical centers as a function of the morphological type. The offsets have been computed in the plane of the galaxy, using the position angles and the inclinations given in Table V.

3.4.2 Signatures of the Bar in the Velocity Fields.

Bars in galaxies have very different masses, lengths, axial ratios, colour distributions, gas content, pattern speeds, shapes and kinematics. The determination of the fundamental bar parameters is a delicate task. Even if the observational constraints are numerous, their determinations are rarely unambiguous. Difficulties come from the fact that

- the various galactic components (bar, disk, spiral arms, bulge, rings) are closely intertwined in disk galaxies : observations as well as models integrate the various components and one cannot observe them separately ;
- 3D shapes in galaxies are observed projected on the plane of the sky and their deprojection is not unambiguous, particularly for barred galaxies ;
- the parameters of bars depend on the luminous to dark matter ratio distribution, e.g. galaxies having initially the same disk and the same halo-to-disk mass ratio but different central halo concentrations have very different properties (Athanassoula & Misiriotis, 2002).

Bars observed from 2D radial velocity fields contain a fraction of hidden information in tracing the total mass distribution (luminous & dark) and they may be directly compared to N-body + SPH simulations. Moreover, the signature of the bar can appear more significantly through the 2D gaseous velocity field (non symmetrical features due to gas shocks, SF regions of high density, i.e. related to the dissipative nature of the gas) than through the stellar velocity field. So, 2D gaseous velocity fields give valuable additional observational information that will help to disentangle the parameters of the bar.

For instance, the existence of a velocity gradient along the minor axis, in both stellar and gaseous 2D velocity field, is not a very good criterion to pick out bars, while the angle between the kinematical major and minor axes and the twists of the isovelocity contours, are better criteria (Bosma, 1981b).

Theoretical predictions from N-body simulations (e.g. Kormendy, 1983 ; Lütticke et al., 2000 ; Athanassoula & Misiriotis, 2002) may be summarized as follow.

When the position angle of the bar is :

- roughly parallel to the major axis, the isovelocities show a characteristic concentration towards the central region due to the fact that particle orbits are elongated along the bar and the velocity along an orbit is larger at pericentre than at apocentre ;
- intermediate between the major and the minor axis position angles, the velocity field shows the "Z" structure characteristic of barred galaxy velocity fields (see e.g. Peterson et al., 1978, for NGC 5383) ;
- roughly parallel to the minor axis, the velocity field shows a sizeable area of solid body rotation in the inner parts.

In the case of a dark halo more concentrated in the central regions of the galaxy, several of these features remain but some notable differences appear (Athanassoula & Misiriotis, 2002).

When the position angle of the bar is :

- roughly parallel to the major axis, the isovelocities show a strong pinching in the innermost region, on or near the bar minor axis ;
- intermediate between the major and the minor axis positions angles, the "Z" shape velocity field is much more pronounced ;
- roughly parallel to the minor axis, the innermost solid-body rotation part does

not show strong differences but as we move away from the kinematical minor axis the isovelocities show a clearly wavy pattern, indicating that the mean velocity is lower at the ends of the bar than right above or right below it.

If one follows the N-body simulations, a quick analysis of the 21 barred velocity fields presented in this paper, with the previous criteria (e.g. based on the angle of the velocity gradient, the twist of isovelocity contours and the kinematical major and minor axes. A much more detailed analysis will be given in a forthcoming paper using coupled N-Body/SPH model and the *BHαBAR* sample) illustrates a trend : in all the cases, the dark halo is often more weakly concentrated than highly concentrated. Another result is that the shape of the velocity field is not always that expected from the position of the bar with respect to the position angle of the major/minor axes of the galaxies. Finally, N-body simulations always show symmetric structures, while the real velocity fields do not.

A strong limitation on the interpretation between N-body and observational velocity fields comes from the fact that N-body simulations produce stellar components which should be compared to stellar observational velocity fields rather than to gaseous velocity fields. Gaseous Hα velocity fields must be compared to hydrodynamical or to hybrid N-body + hydrodynamical simulations. Nevertheless, encouraging results on the relevance of the Tremaine-Weinberg method (Tremaine & Weinberg 1984) applied to Hα velocity fields to determine the pattern speeds of M100 (Hernandez et al., 2005a) and of the galaxies in the present sample (Hernandez et al., 2005b) are very promising.

3.5 Concluding remarks and further work.

The 3D data presented in this paper are the results of a survey of the Hα kinematics of nearby barred galaxies with the FP integral-field spectrometer FANTOMM. This study provides a homogenous sample of barred galaxies. The 3D data were processed through a robust reduction pipeline. An adaptive binning method has been used to achieve optimal spatial coverage and resolution at a given signal-to-noise ratio, typically around 7. High spatial and spectral resolution Hα monochromatic maps and velocity fields are presented. Bar signatures in velocity fields and position-velocity plots, reveal strong non circular motions and thus provide observational constrains to extract the parameters of the bar and of the disk. Fine tuning of position angles and inclinations have been done. The kinematical parameters have been determined using a tilted-ring model, by taking into account only the axisymme-

tric part of the disk to avoid any kind of contamination due to non-circular motions from the bar (in the inner parts of the disk) or to a possible warp (in the outer parts).

The analysis of the sample shows that the photometric and kinematics parameters (position angle of the major axis, inclination and center) are in relatively good agreement, except maybe for the later-type spirals. Nevertheless, the determination of the kinematical parameters is more accurate than the photometric parameters. On the other hand, a preliminary analysis of the velocity fields shows that the dark halo component is rather a minor component in the inner optical region of the galaxies.

The main purpose of the paper is to provide and present a homogenous 3D data sample of nearby barred galaxies useful for further analysis. Velocity patterns of the bar(s) and of the spiral will be accurately determined using the Tremaine-Weinberg method on the Hα velocity fields in two forthcoming papers. In Paper II the Tremaine-Weinberg method applied to the gaseous component will be discussed using numerical simulations and illustrated on the galaxy M100. In Paper III, the rest of the sample will be analyzed using this Tremaine-Weinberg method. In paper IV, the rotation curves will be derived, properly corrected for non-circular motions in order to retrieve the actual mass distributions. This will be achieved with N-body coupled with SPH simulations for each velocity field of the *BHαBAR* sample. This kind of approach has been used by Pérez et al. (2004). However, our study will differ in two major aspects. First, their comparison is relative to a small sample, whereas *BHαBAR* is homogeneous and well distributed over the Hubble sequence. Second, they only used long-slit data, whereas Hα velocity fields and Hα monochromatic images will be used to provide more accurate results avoiding, for example, the uncertainties on $P.A.$ and i present in 1D data. This will be the first step toward the determination of accurate mass models for barred spiral galaxies, until the time when full 2D mass models using the whole velocity fields will become available.

Acknowledgments

We thank Chantal Balkowski for her help and support at the different stages of this work. We also thank Olivia Garrido, Jacques Boulesteix, Jean-Luc Gach, Philippe Balard and Olivier Boissin for their support. It is a pleasure to thank the OmM staff, in particular Bernard Malenfant and Ghyslain Turcotte for their enthusiastic and competent support. Let

us, also, acknowledge Pierre Martin and the CFHT team for their support at the top of Mauna Kea. The FANTOMM project has been carried out by the Laboratoire d'Astrophysique Expérimentale (LAE) of the Université de Montréal using a grant from the Canadian Foundation for Innovation and the Ministère de l'Education du Québec. This project made use of the LEDA database : http ://leda.univ-lyon1.fr/. The Digitized Sky Surveys were produced at the Space Telescope Science Institute under U.S. Government grant NAG W-2166. The images of these surveys are based on photographic data obtained using the Oschin Schmidt Telescope on Palomar Mountain and the UK Schmidt Telescope.

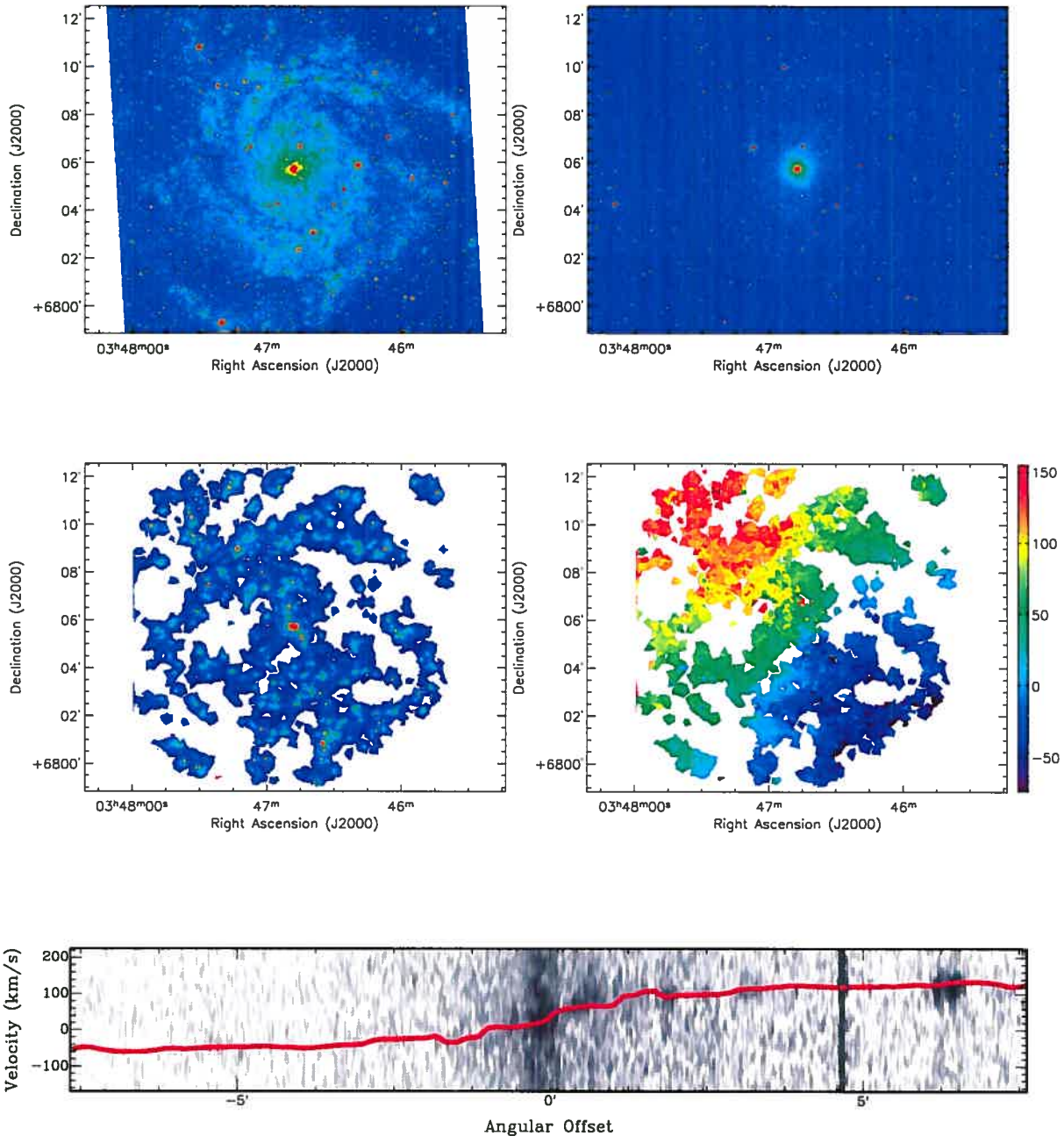

Fig. 26: IC 0342. **Top left** : XDSS Blue Band image. **Top right** : 2Mass K-band image. **Middle left** : Hα monochromatic image. **Middle right** : Hα velocity field. **Bottom** : PV diagram. The red line is the PV diagram obtained while integrating over a slit of 3 pixels wide using the velocities of the model extracted from GIPSY and the data cube from the observations. The Hα velocity field and Hα monochromatic image were spatially binned using an adaptive binning. The scale of the color used to represent the velocity is located to the right of the Hα map.

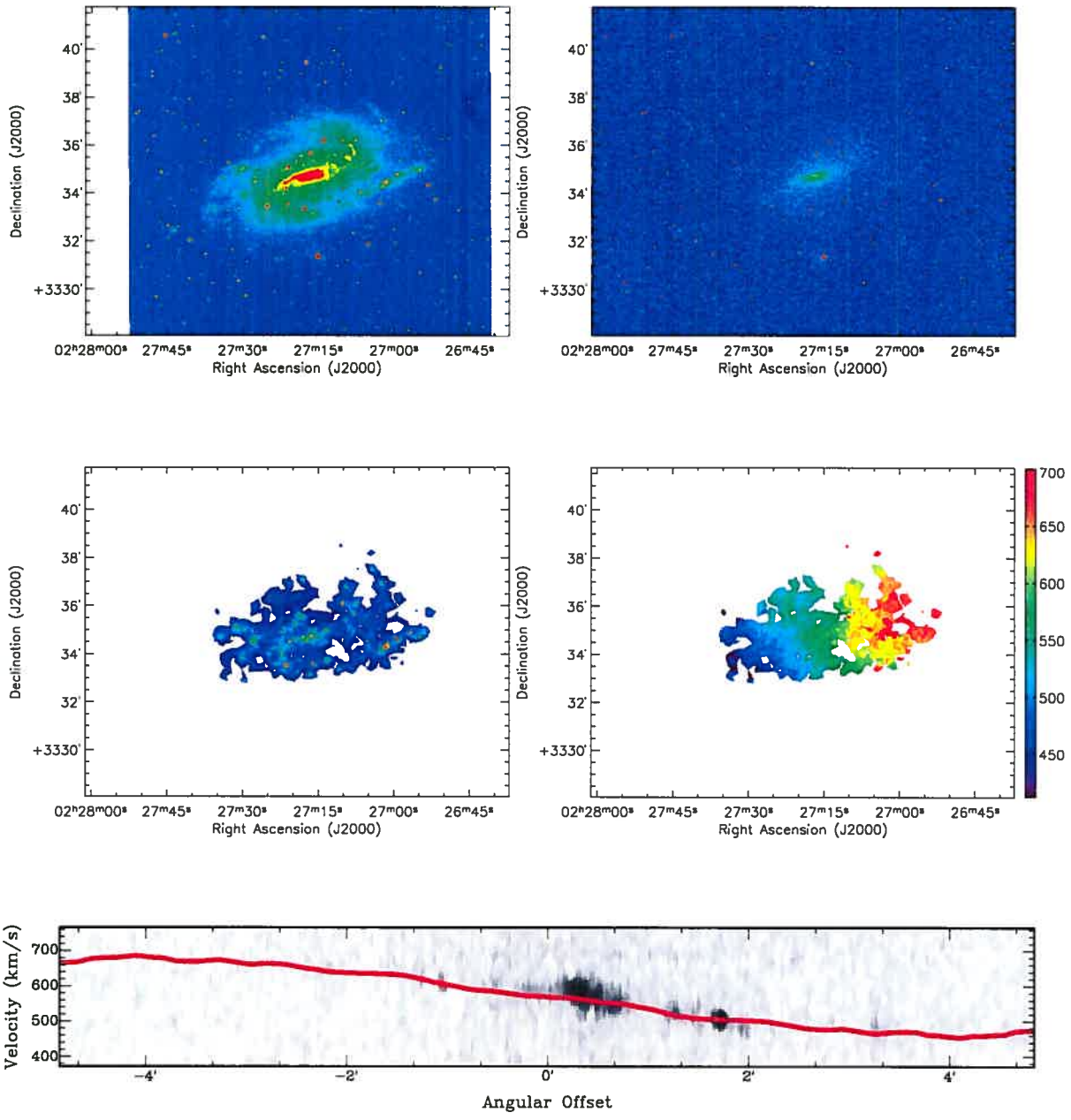

Fig. 27: NGC 0925. **Top left** : XDSS Blue Band image. **Top right** : 2Mass K-band image. **Middle left** : Hα monochromatic image. **Middle right** : Hα velocity field. **Bottom** : PV diagram.

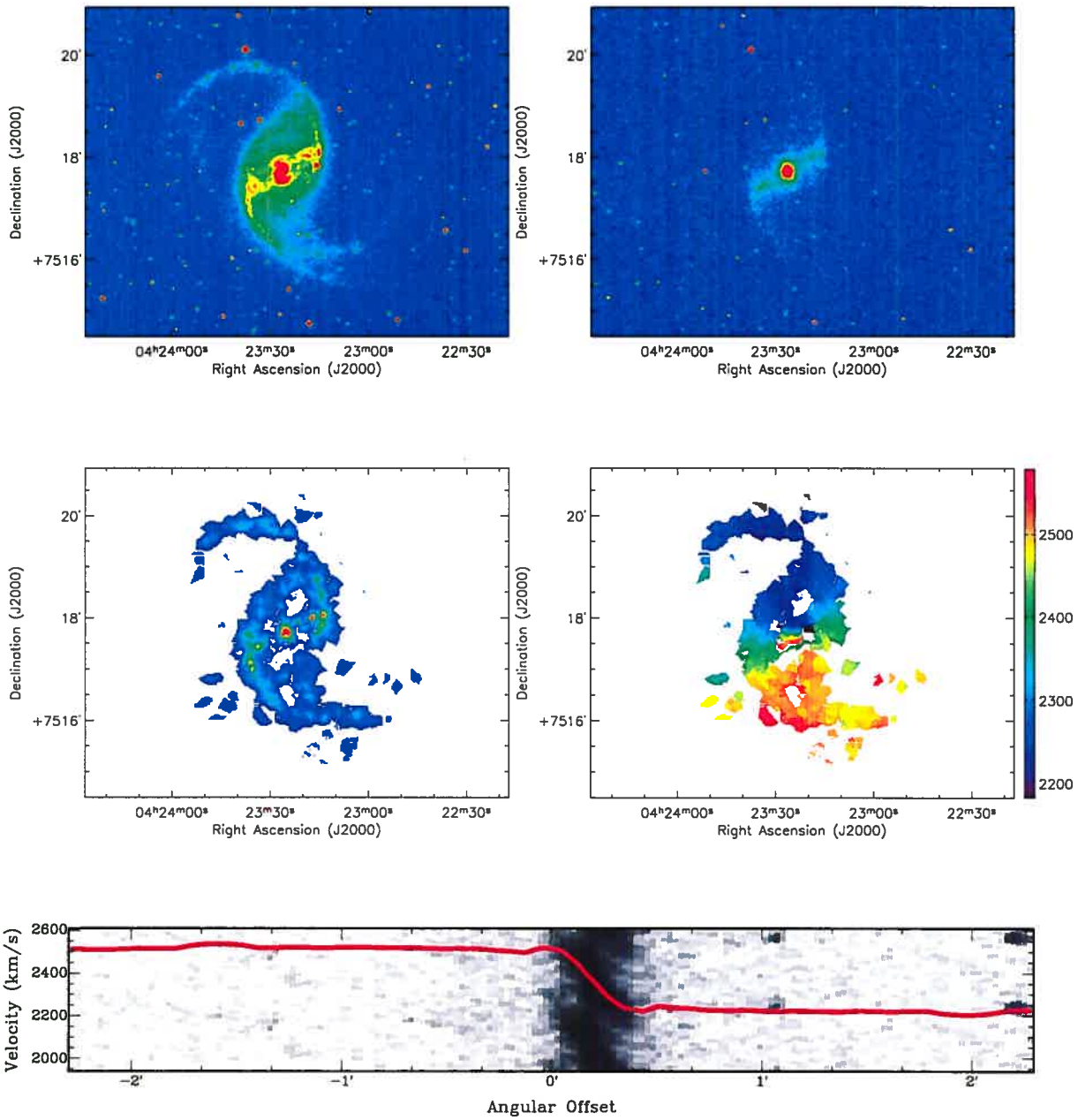

Fig. 28: NGC 1530. **Top left** : XDSS Blue Band image. **Top right** : 2Mass K-band image. **Middle left** : Hα monochromatic image. **Middle right** : Hα velocity field. **Bottom** : PV diagram.

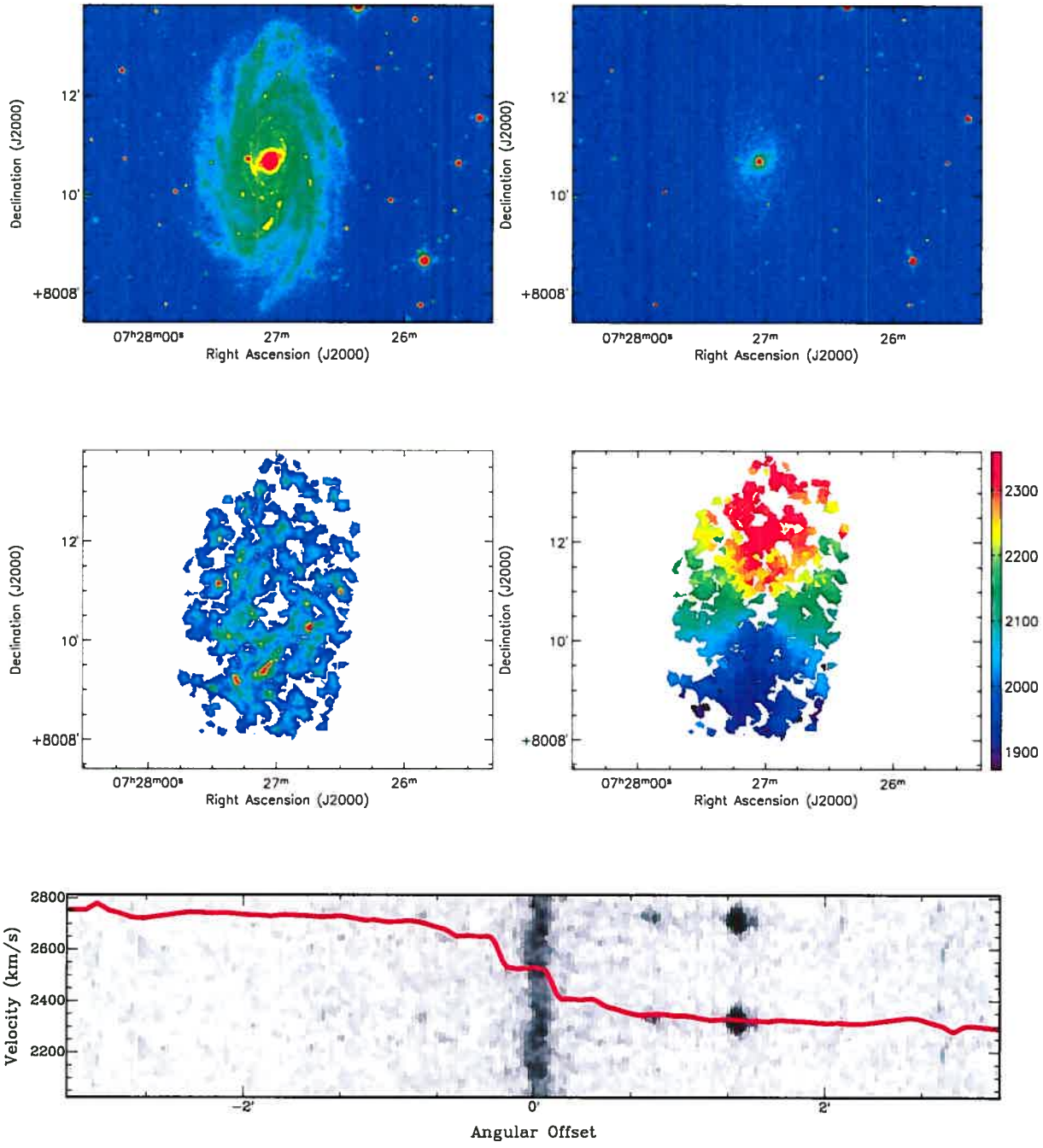

Fig. 29: NGC 2336. **Top left** : XDSS Blue Band image. **Top right** : 2Mass K-band image. **Middle left** : Hα monochromatic image. **Middle right** : Hα velocity field. **Bottom** : PV diagram.

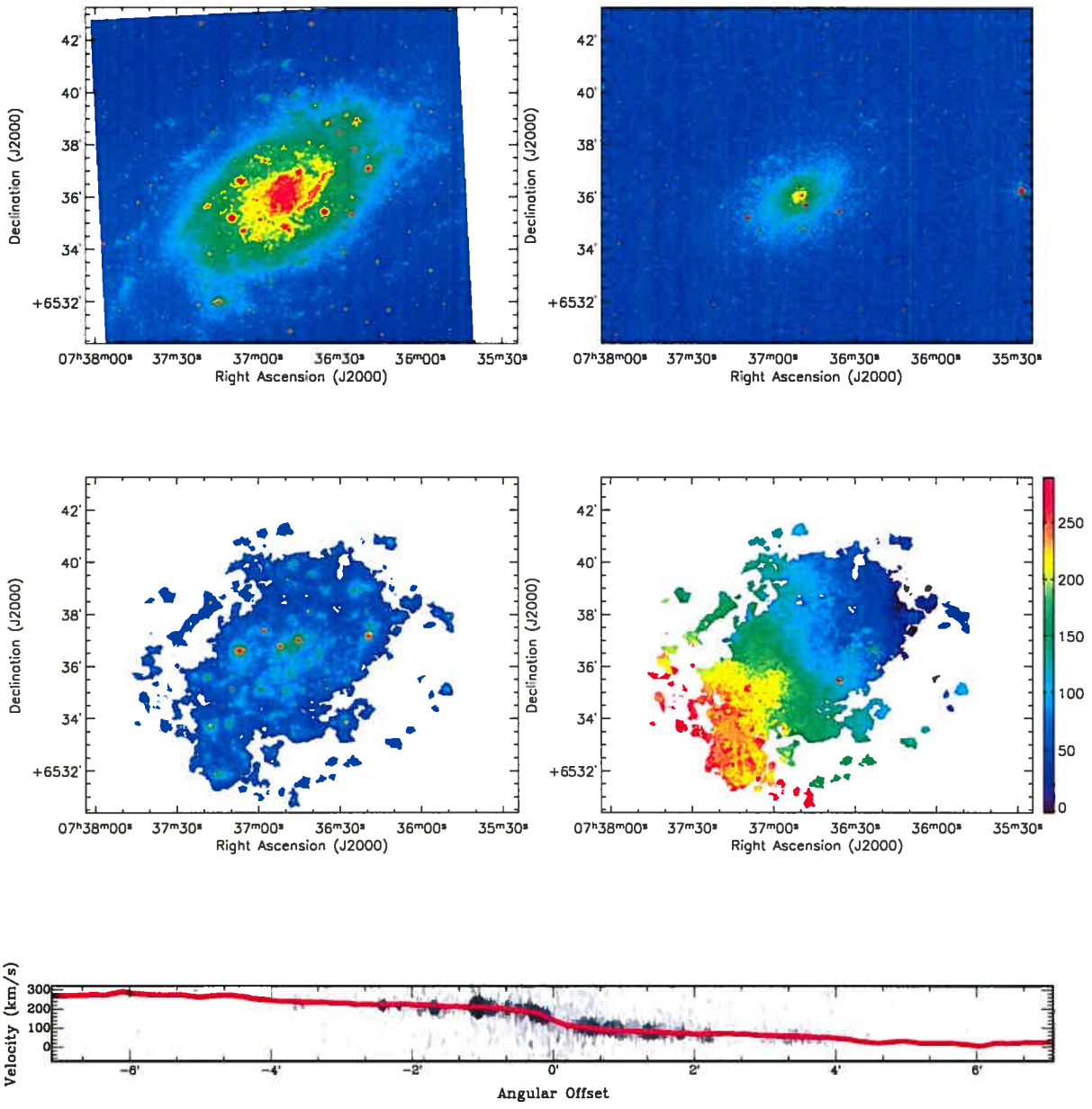

Fig. 30: NGC 2403. **Top left** : XDSS Blue Band image. **Top right** : 2Mass K-band image. **Middle left** : Hα monochromatic image. **Middle right** : Hα velocity field. **Bottom** : PV diagram.

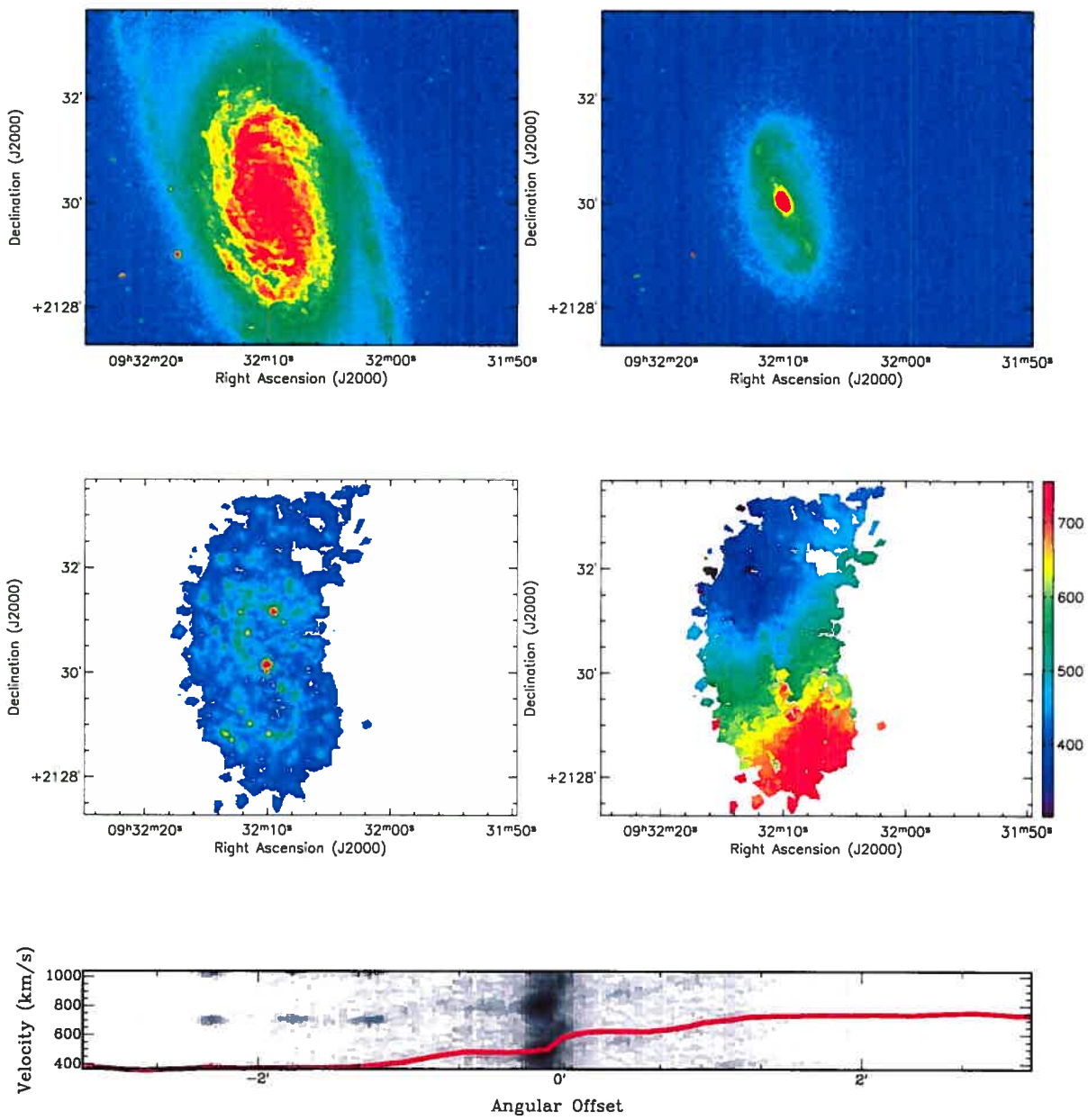

Fig. 31: NGC 2903. **Top left** : XDSS Blue Band image. **Top right** : 2Mass K-band image. **Middle left** : Hα monochromatic image. **Middle right** : Hα velocity field. **Bottom** : PV diagram.

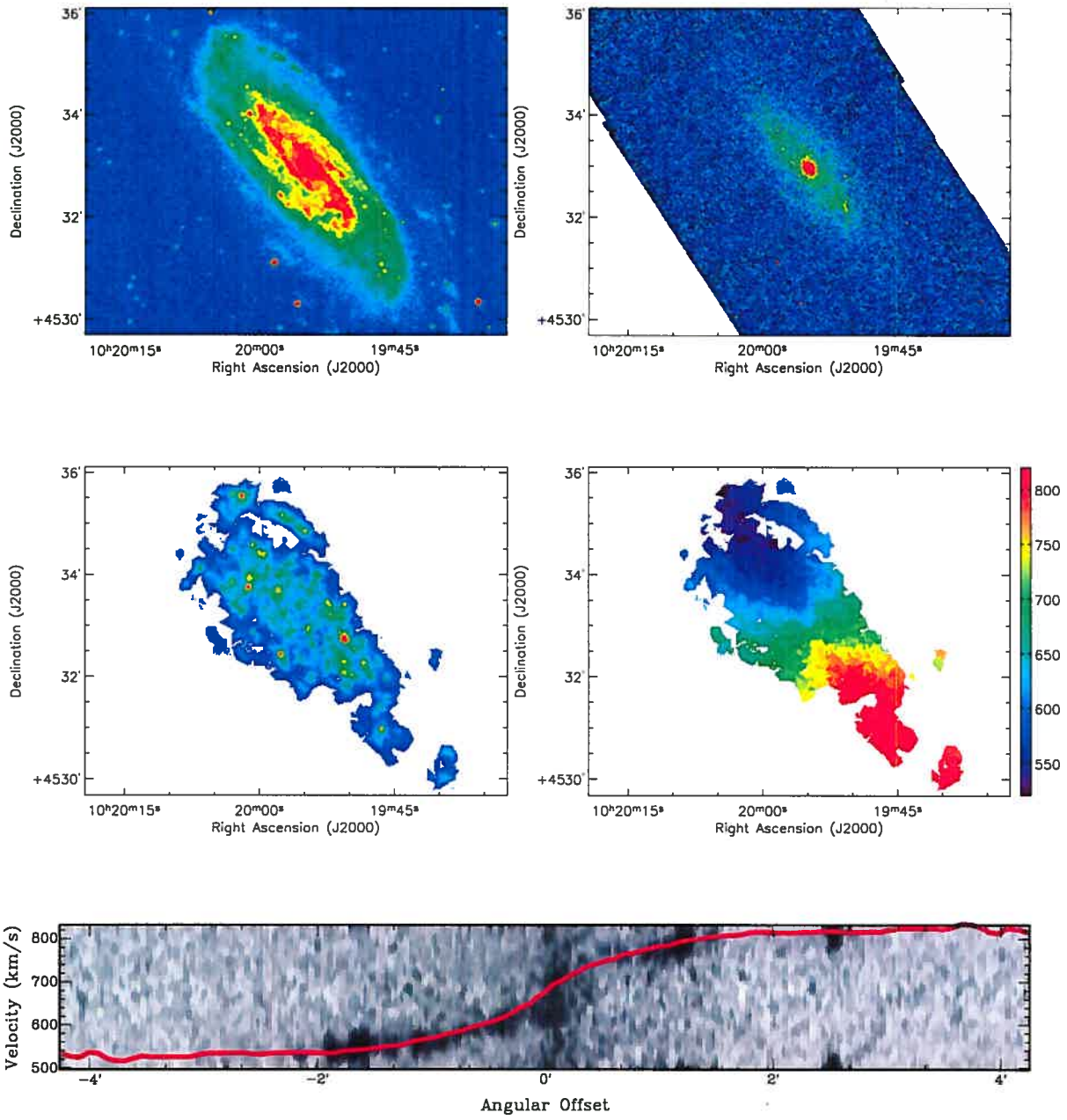

Fig. 32: NGC 3198. **Top left** : XDSS Blue Band image. **Top right** : SIRTIF image. **Middle left** : Hα monochromatic image. **Middle right** : Hα velocity field. **Bottom** : PV diagram.

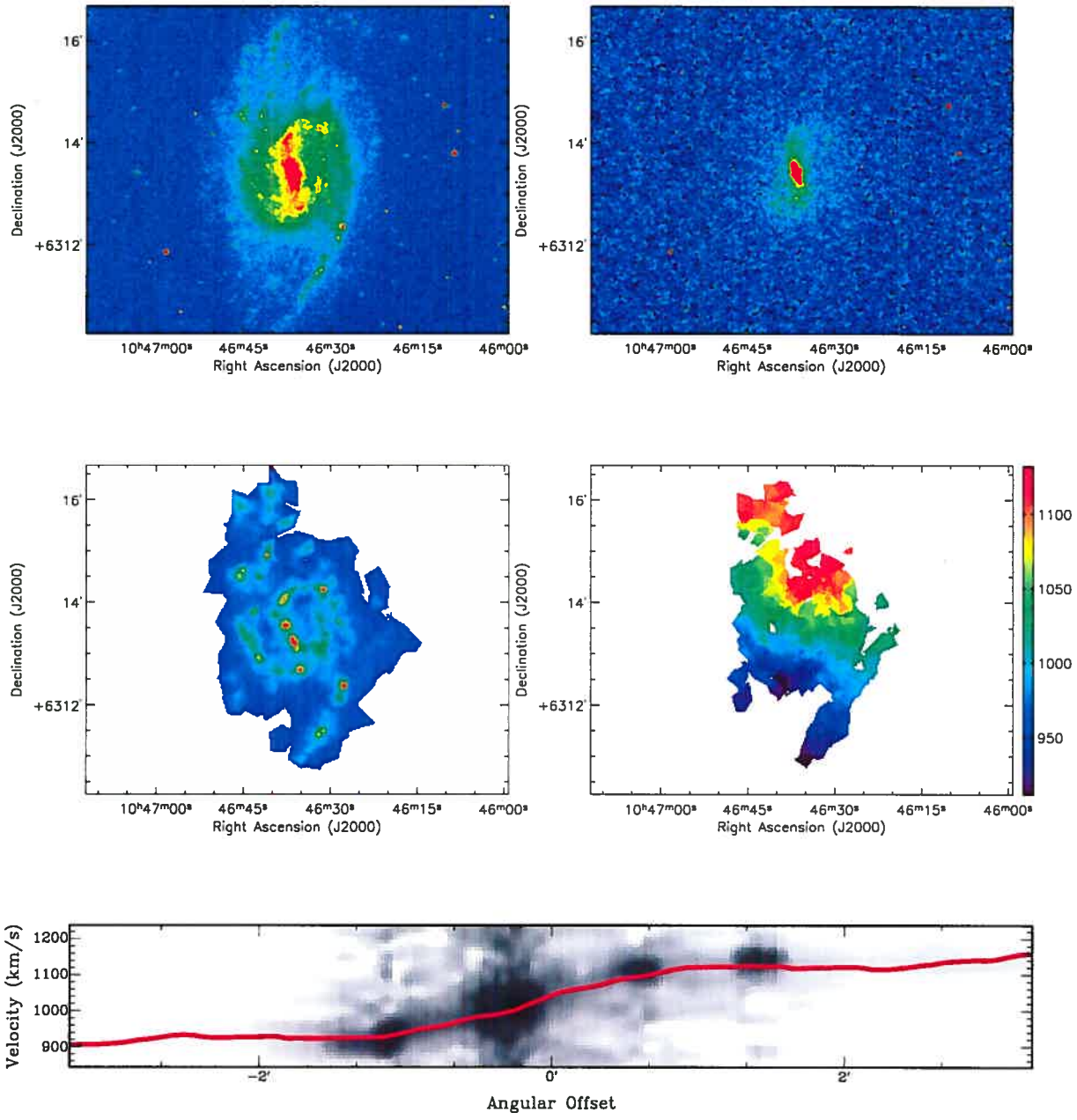

Fig. 33: NGC 3359. **Top left** : XDSS Blue Band image. **Top right** : 2Mass K-band image. **Middle left** : Hα monochromatic image. **Middle right** : Hα velocity field. **Bottom** : PV diagram.

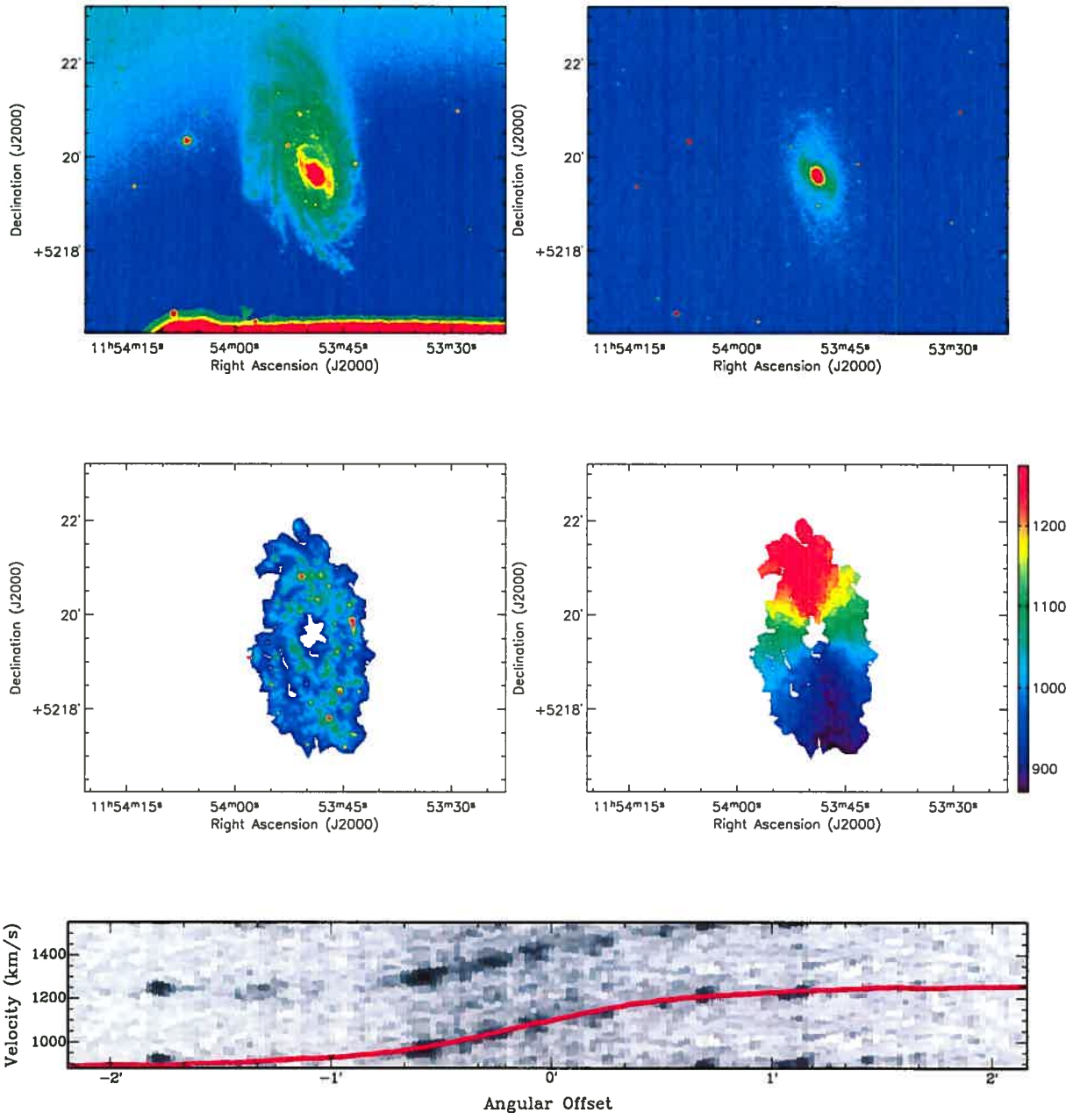

Fig. 34: NGC 3953. **Top left** : XDSS Blue Band image. **Top right** : 2Mass K-band image. **Middle left** : Hα monochromatic image. **Middle right** : Hα velocity field. **Bottom** : PV diagram.

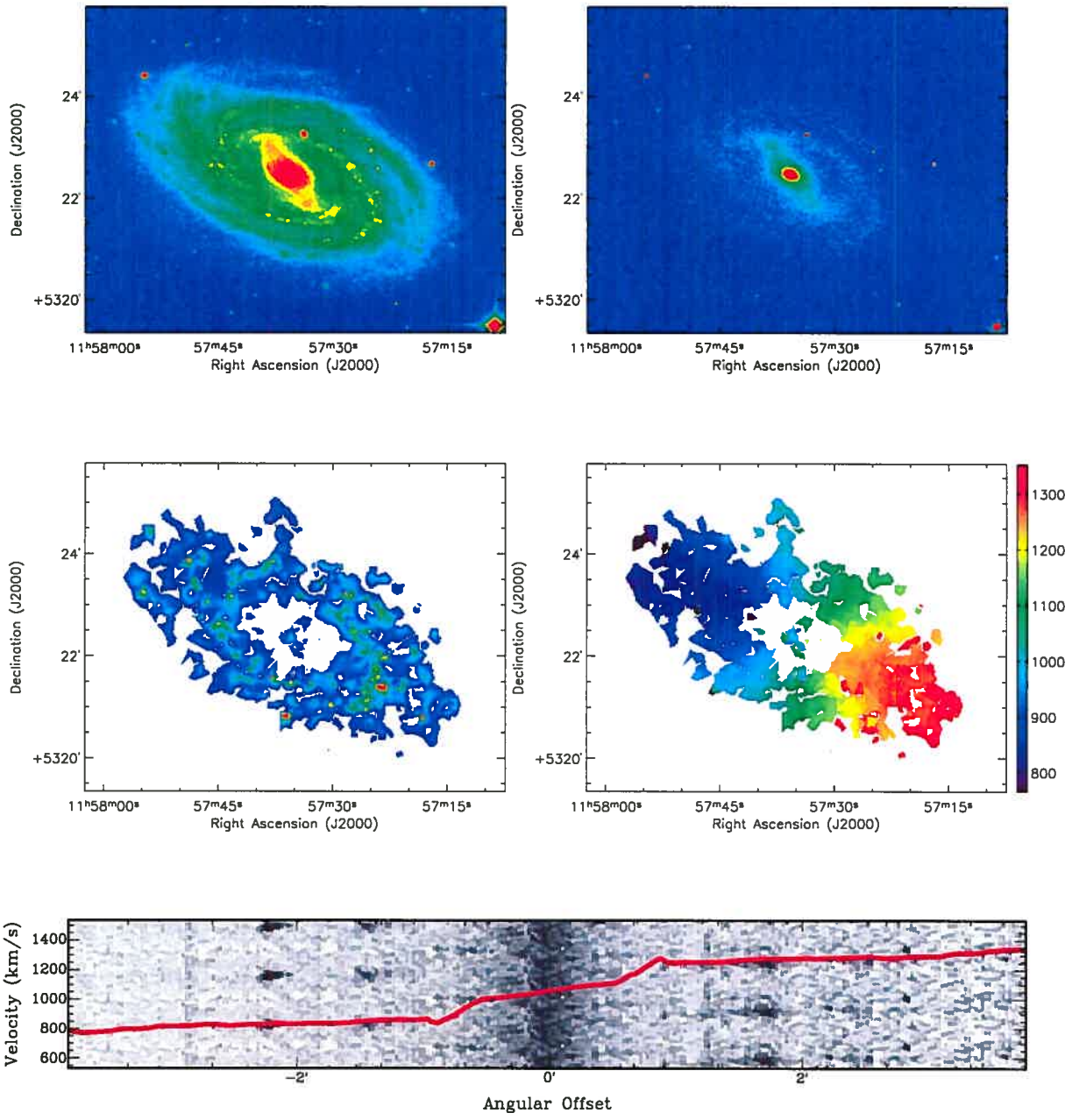

Fig. 35: NGC 3992. **Top left** : XDSS Blue Band image. **Top right** : 2Mass K-band image. **Middle left** : Hα monochromatic image. **Middle right** : Hα velocity field. **Bottom** : PV diagram.

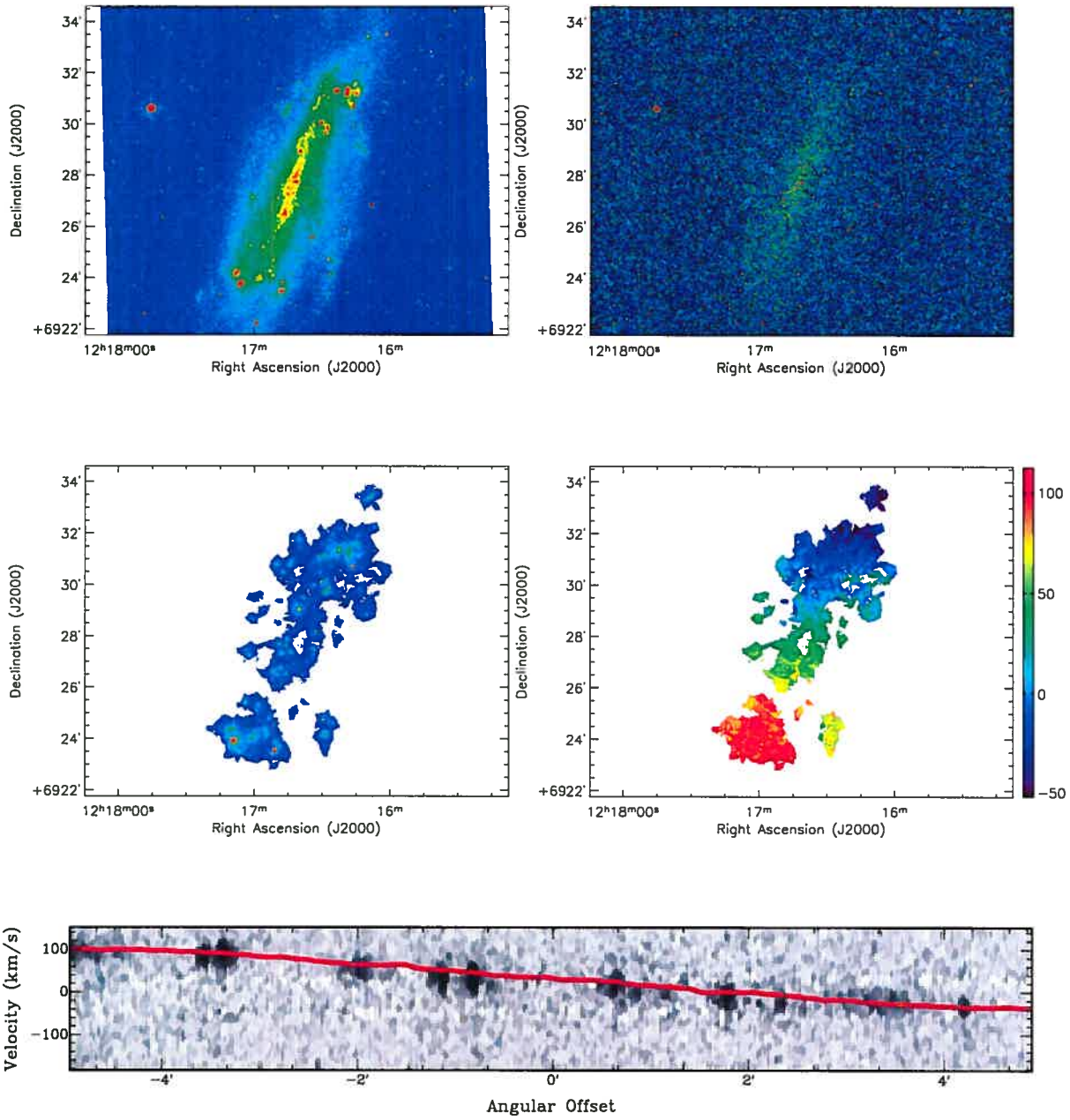

Fig. 36: NGC 4236. **Top left** : XDSS Blue Band image. **Top right** : 2Mass K-band image. **Middle left** : Hα monochromatic image. **Middle right** : Hα velocity field. **Bottom** : PV diagram.

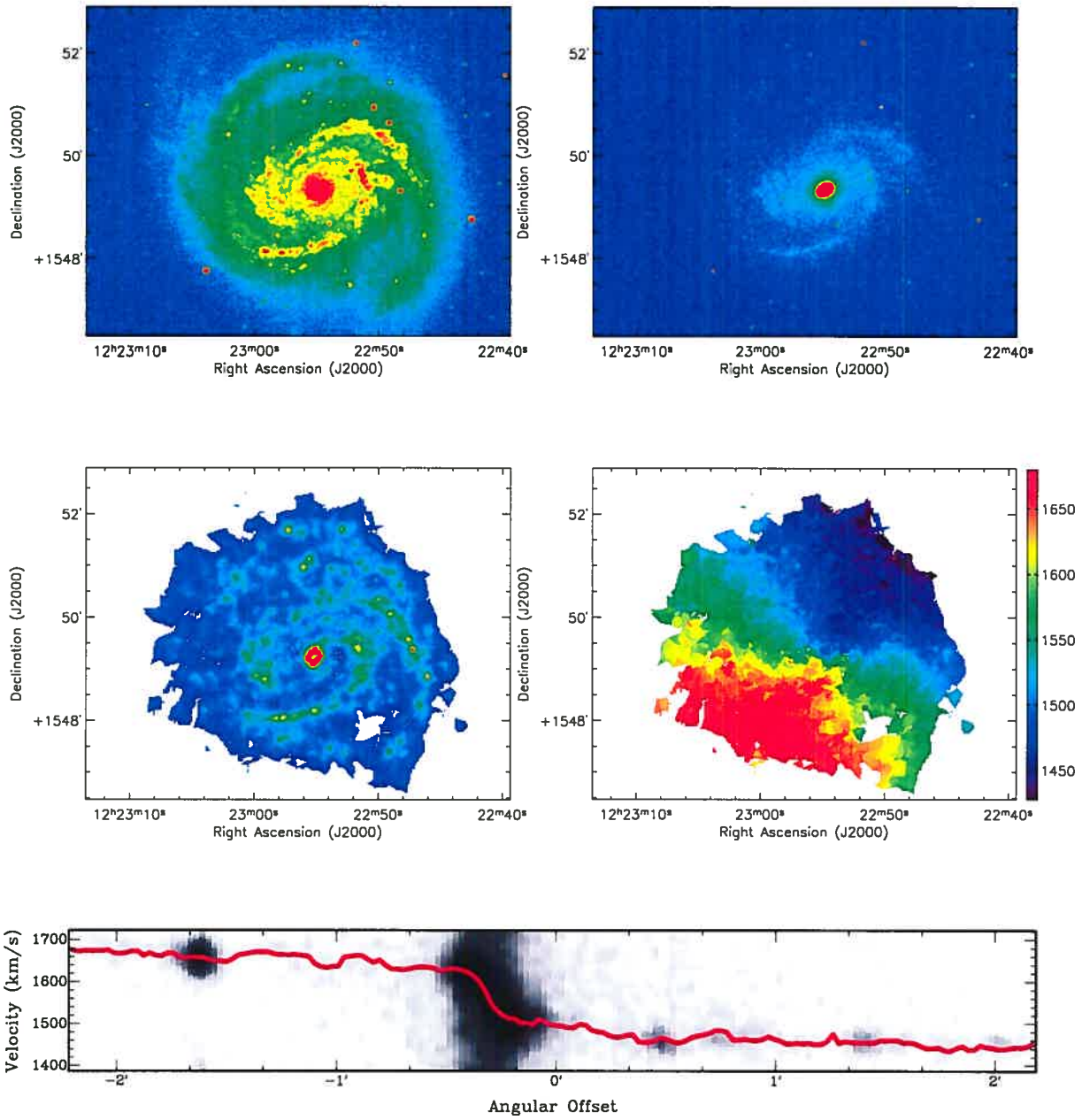

Fig. 37: NGC 4321. **Top left** : XDSS Blue Band image. **Top right** : 2Mass K-band image. **Middle left** : Hα monochromatic image. **Middle right** : Hα velocity field. **Bottom** : PV diagram.

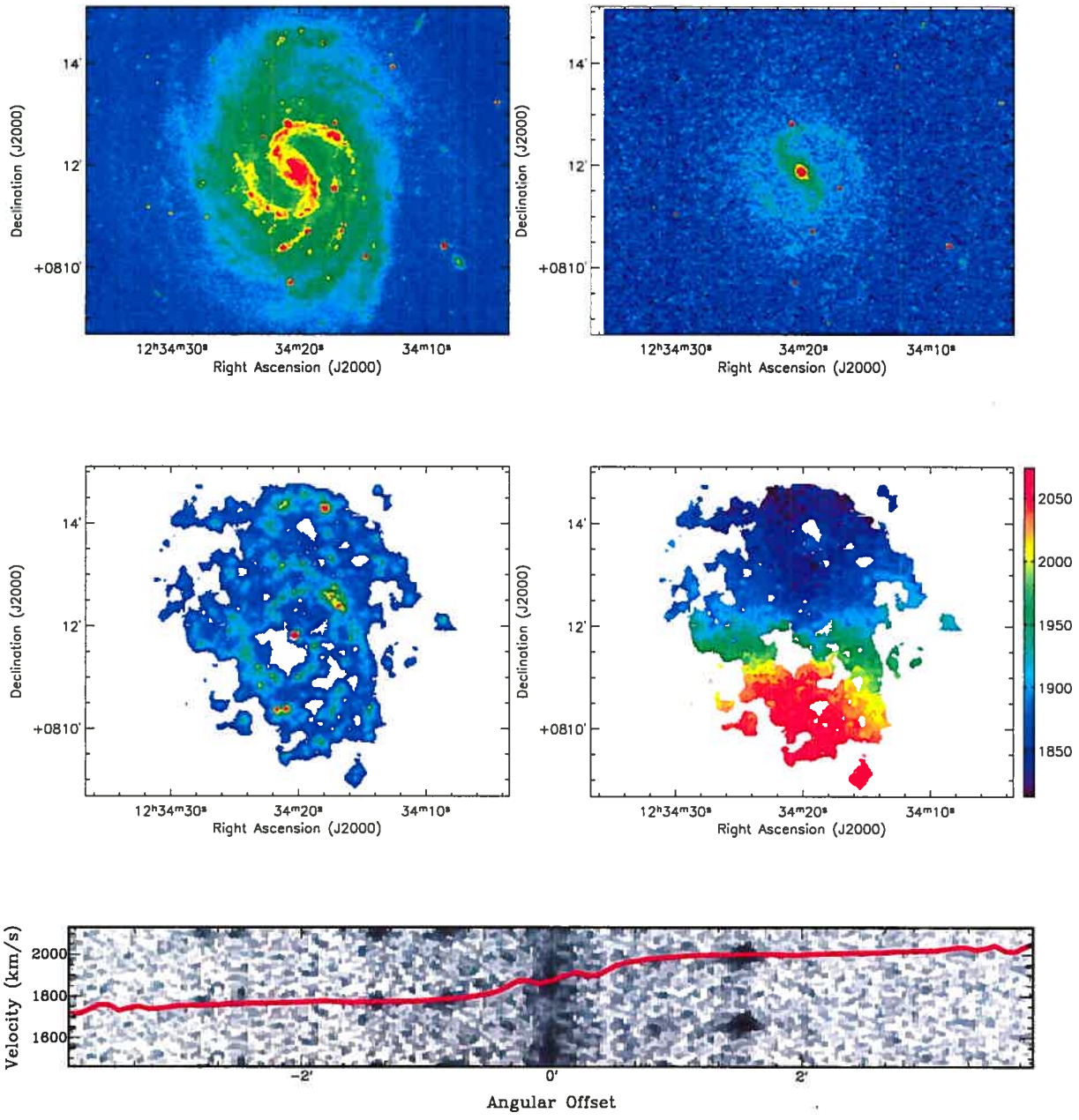

Fig. 38: NGC 4535. **Top left** : XDSS Blue Band image. **Top right** : 2Mass K-band image. **Middle left** : Hα monochromatic image. **Middle right** : Hα velocity field. **Bottom** : PV diagram.

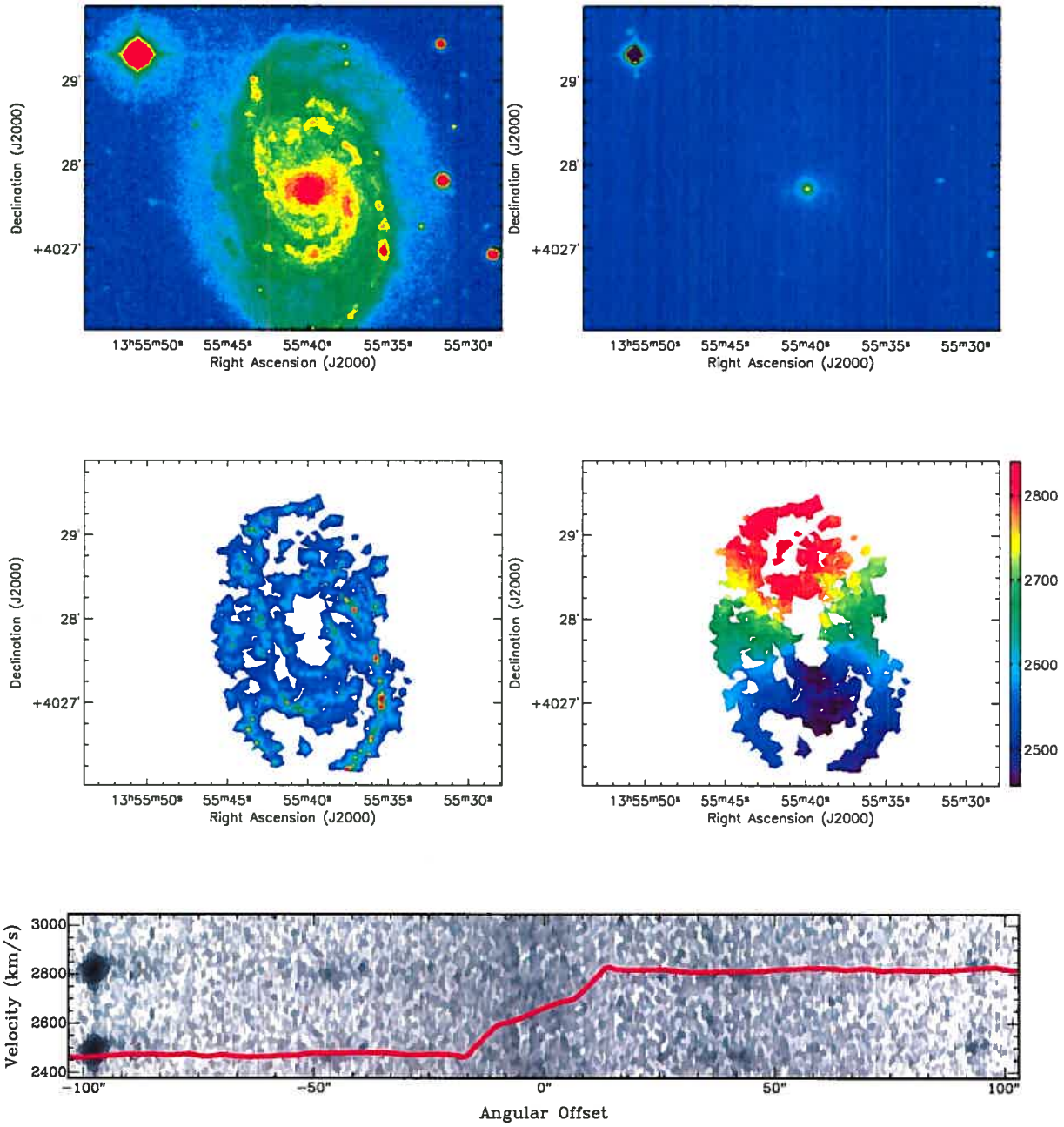

Fig. 39: NGC 5371. **Top left** : XDSS Blue Band image. **Top right** : 2Mass K-band image. **Middle left** : Hα monochromatic image. **Middle right** : Hα velocity field. **Bottom** : PV diagram.

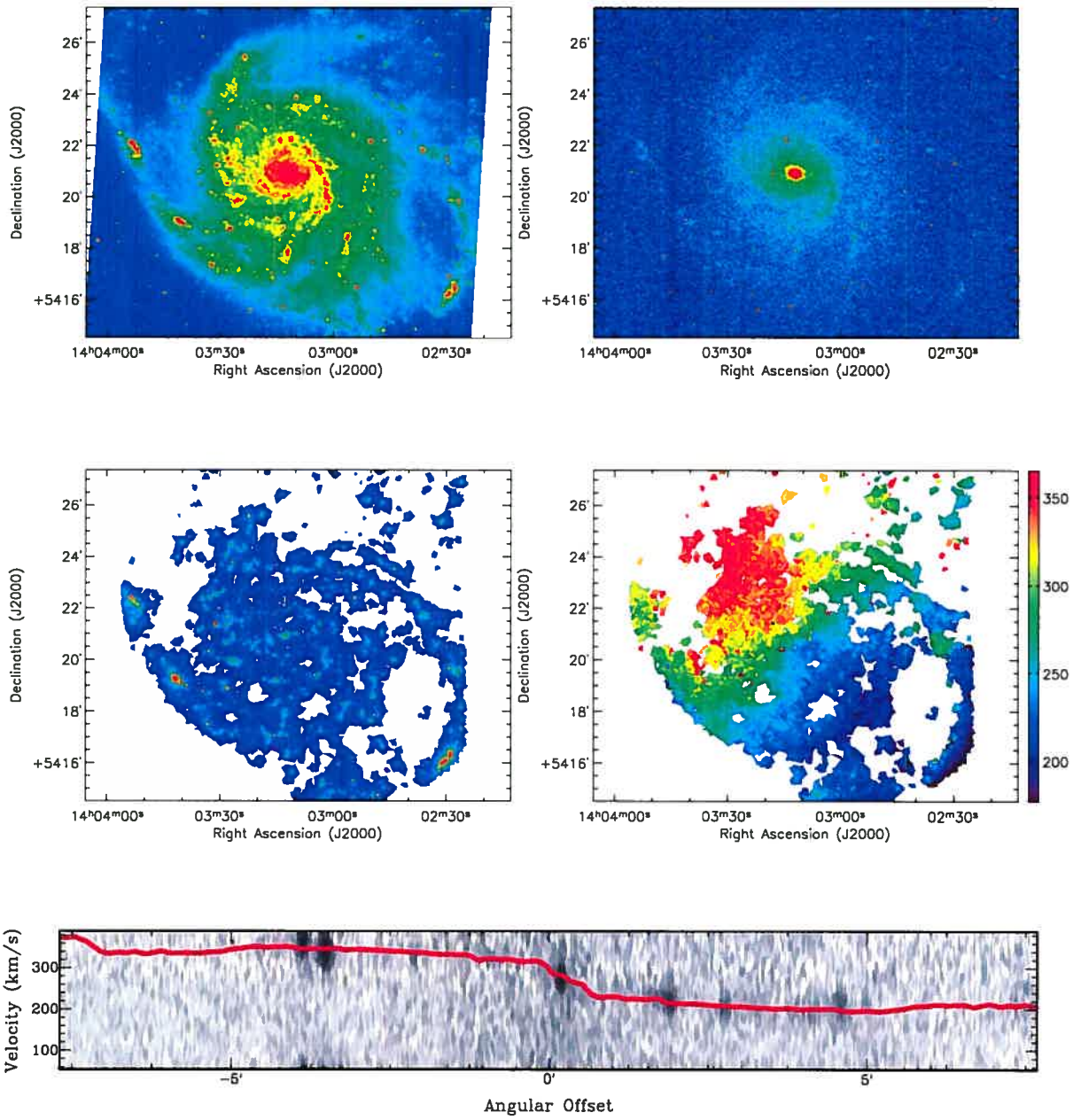

Fig. 40: NGC 5457. **Top left** : XDSS Blue Band image. **Top right** : 2Mass K-band image. **Middle left** : Hα monochromatic image. **Middle right** : Hα velocity field. **Bottom** : PV diagram.

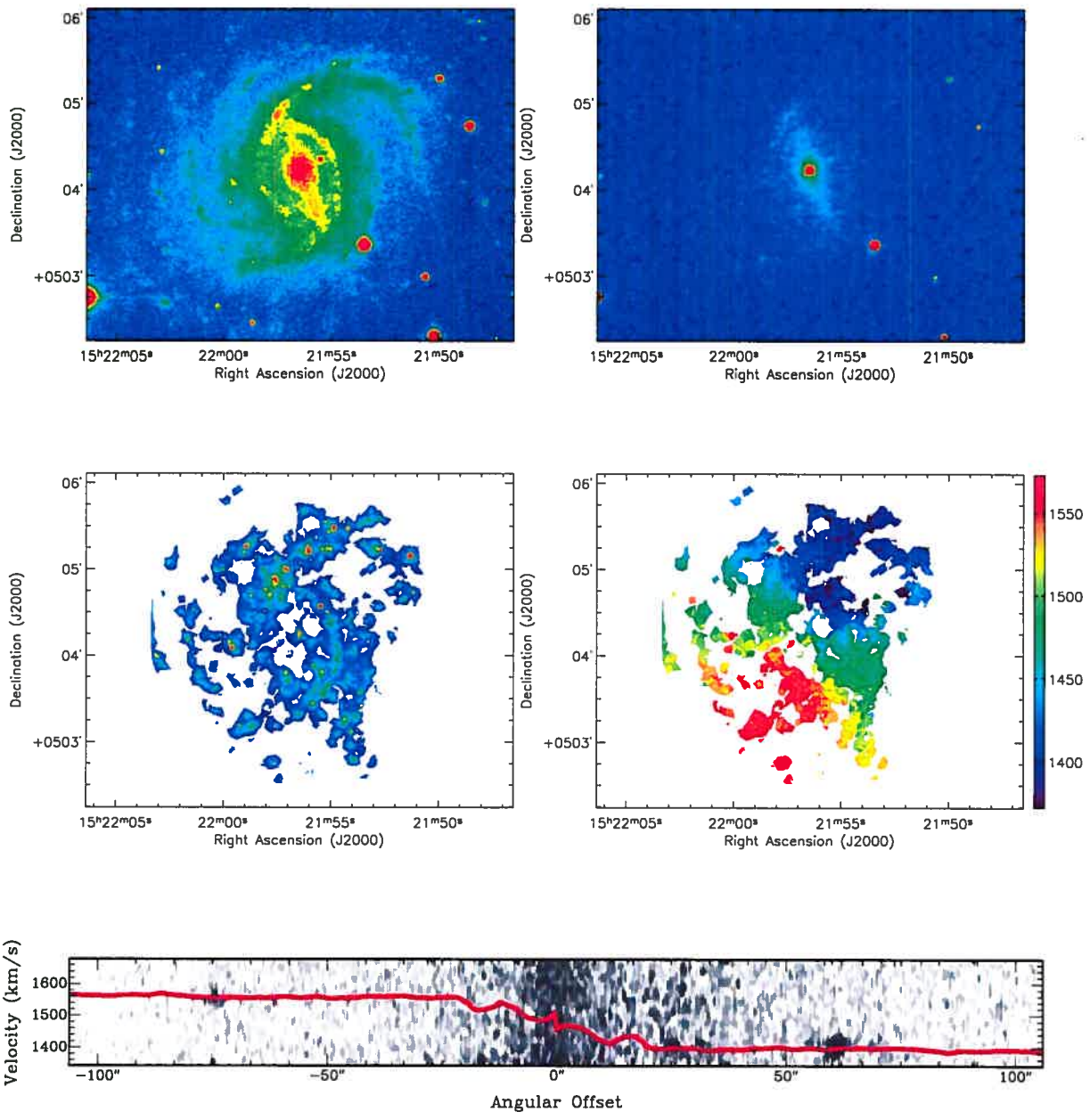

Fig. 41: NGC 5921. **Top left** : XDSS Blue Band image. **Top right** : 2Mass K-band image. **Middle left** : Hα monochromatic image. **Middle right** : Hα velocity field. **Bottom** : PV diagram.

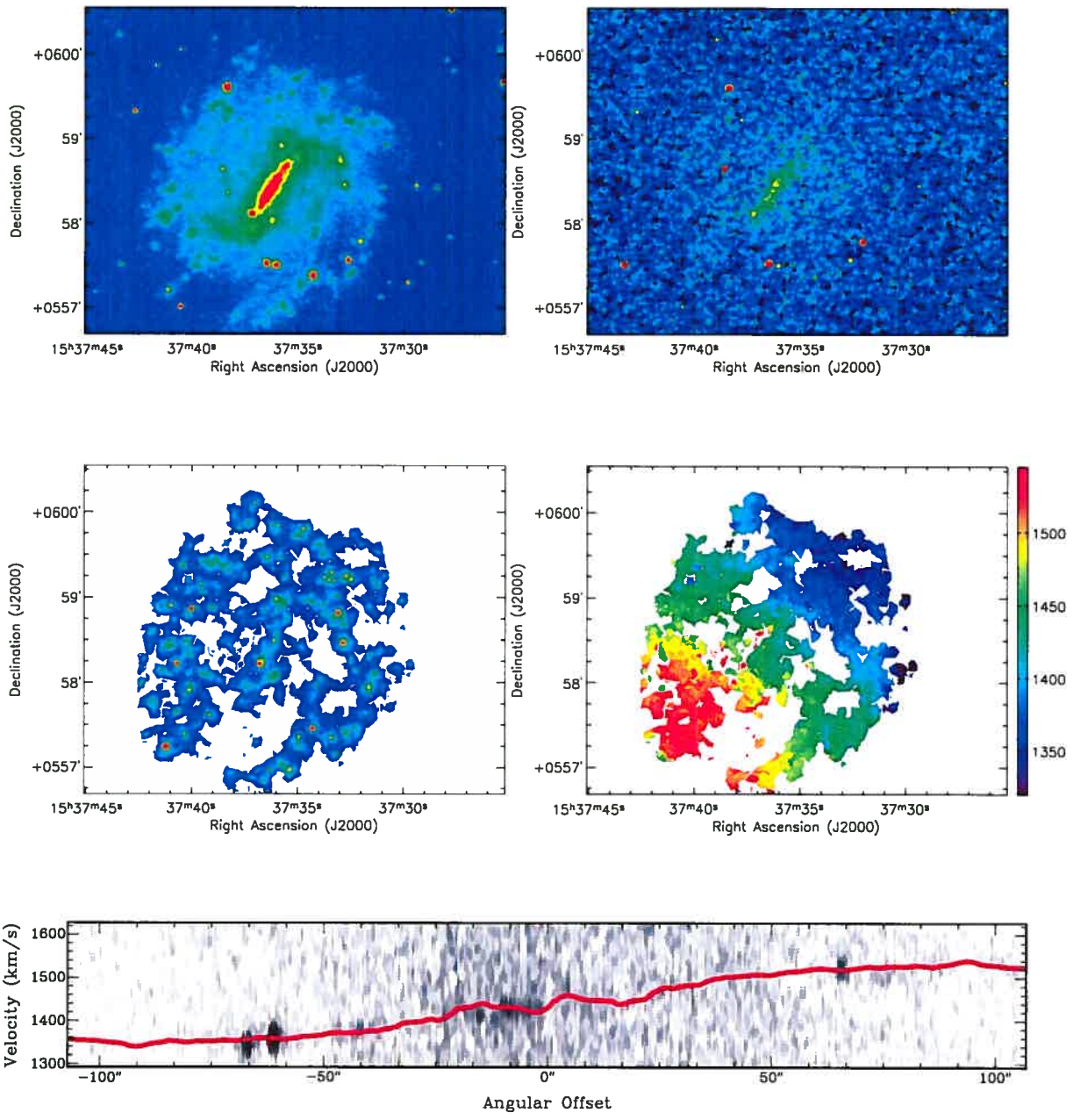

Fig. 42: NGC 5964. **Top left** : XDSS Blue Band image. **Top right** : 2Mass K-band image. **Middle left** : Hα monochromatic image. **Middle right** : Hα velocity field. **Bottom** : PV diagram.

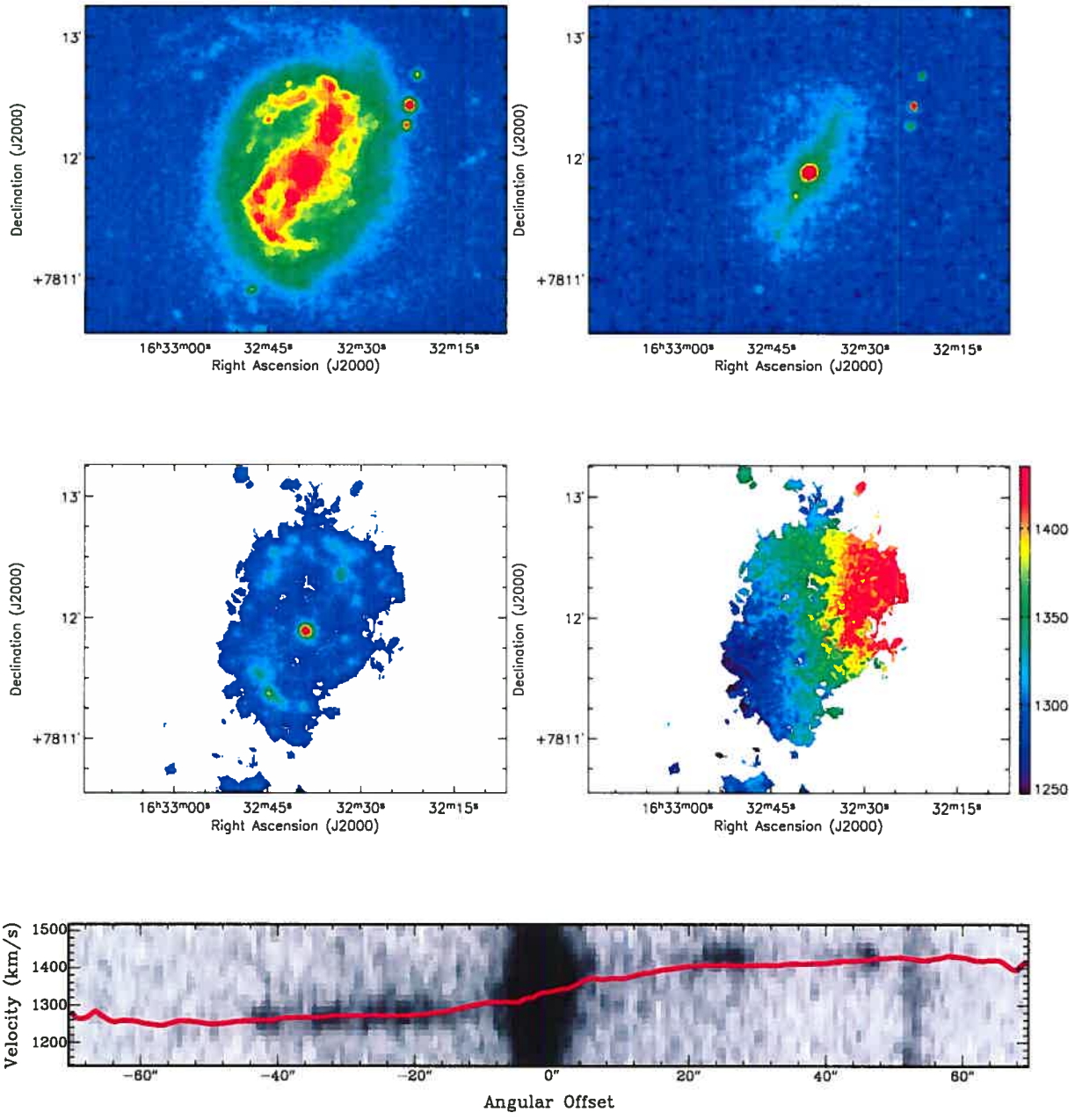

Fig. 43: NGC 6217. **Top left** : XDSS Blue Band image. **Top right** : 2Mass K-band image. **Middle left** : Hα monochromatic image. **Middle right** : Hα velocity field. **Bottom** : PV diagram.

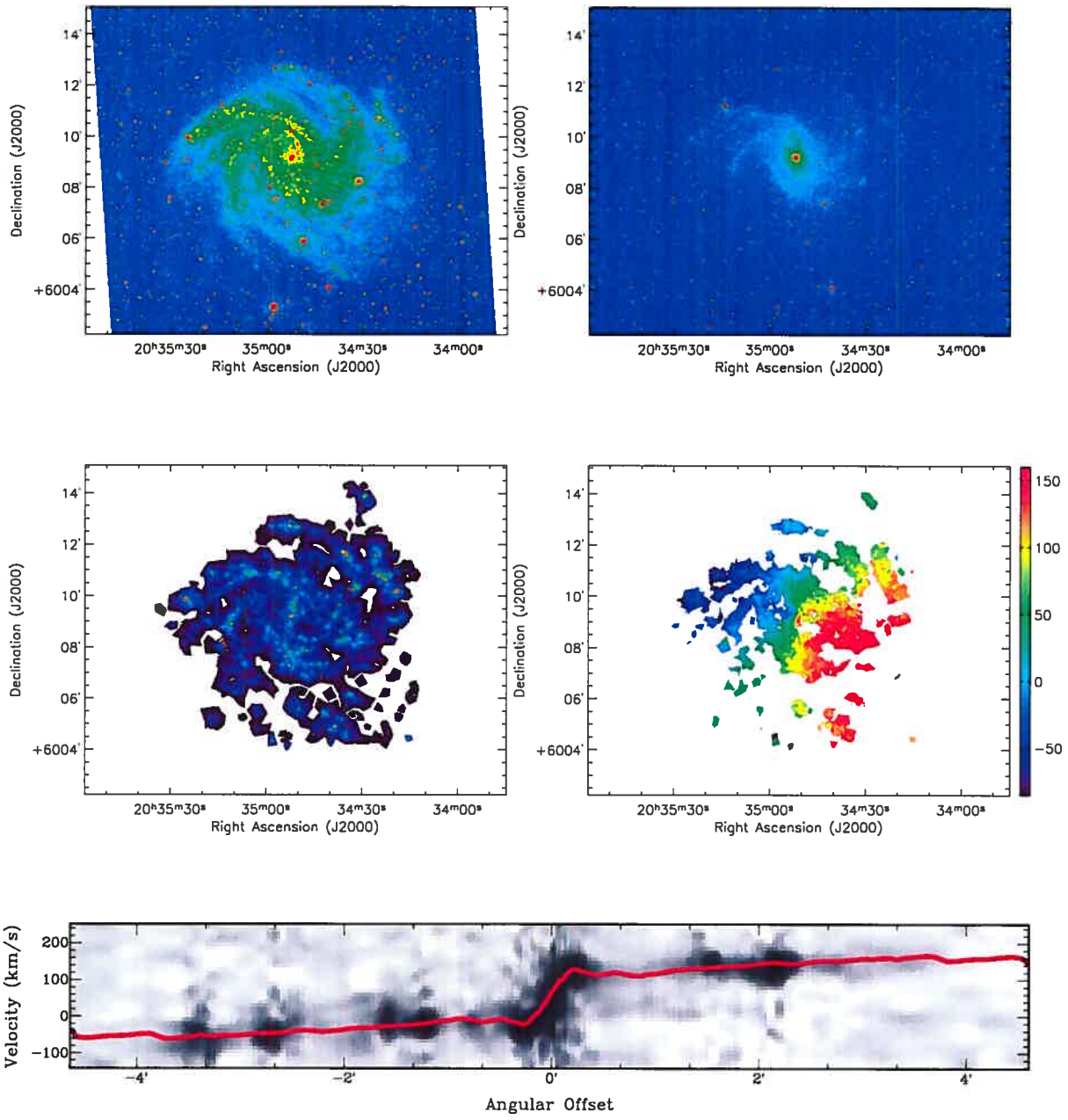

Fig. 44: NGC 6946. **Top left** : XDSS Blue Band image. **Top right** : 2Mass K-band image. **Middle left** : Hα monochromatic image. **Middle right** : Hα velocity field. **Bottom** : PV diagram.

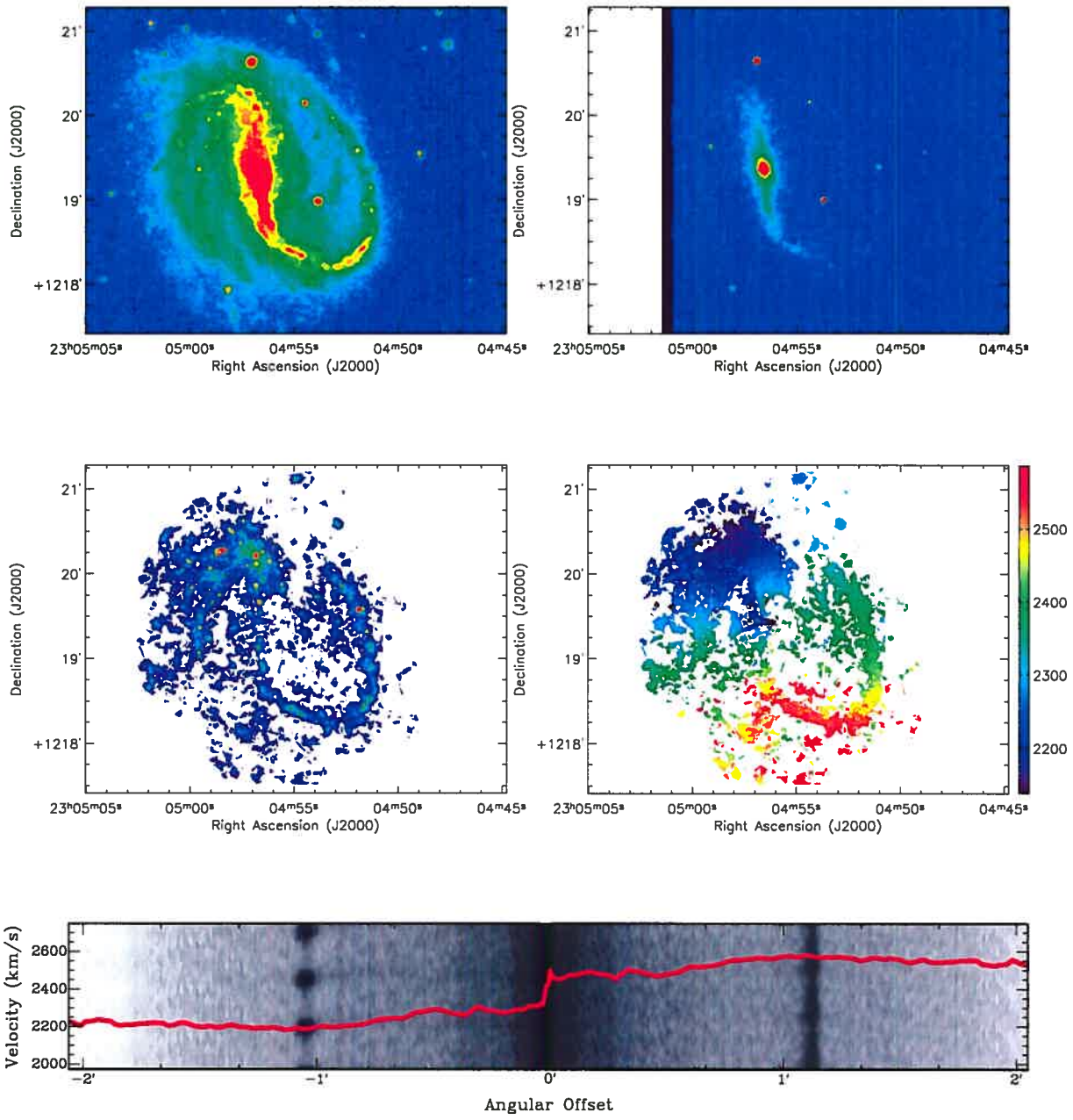

Fig. 45: NGC 7479. **Top left** : XDSS Blue Band image. **Top right** : 2Mass K-band image. **Middle left** : Hα monochromatic image. **Middle right** : Hα velocity field. **Bottom** : PV diagram.

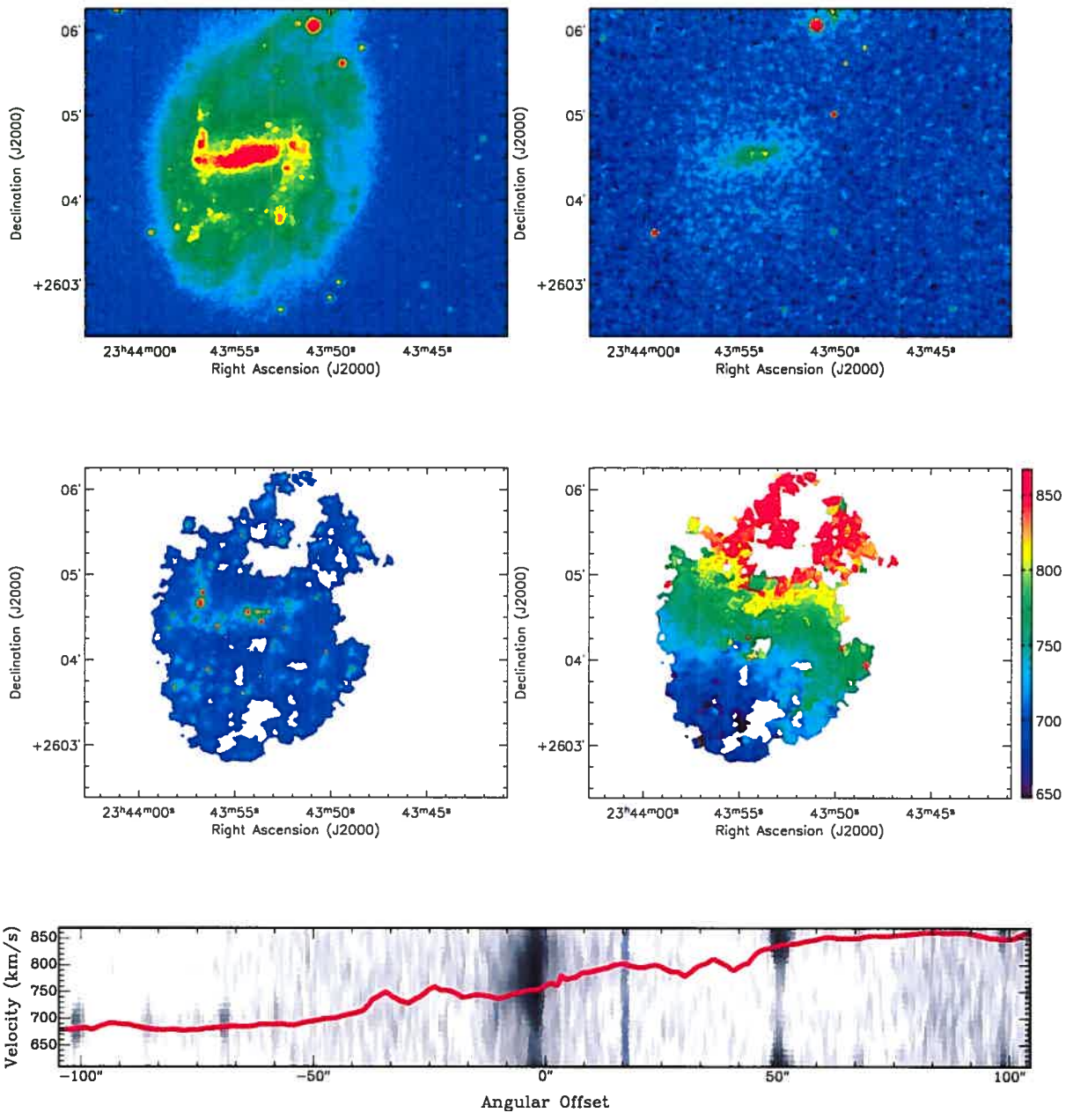

Fig. 46: NGC 7741. **Top left** : XDSS Blue Band image. **Top right** : 2Mass K-band image. **Middle left** : Hα monochromatic image. **Middle right** : Hα velocity field. **Bottom** : PV diagram.

Description for individual galaxies

A brief description of the structures observed in the Hα velocity fields and monochromatic images of the *BHαBAR* sample is given in this section.

IC 0342 : This large SAB(rs)cd nearby galaxy is nearly face-on so its photometrical position angle (*P.A.*) is uncertain. A strong difference between its kinematical and photometrical inclination is noted. Observations in CO and HI (Crosthwaite et al., 2000) suggest that its kinematical *P.A.* is 37°. The kinematical data from CO, HI and Hα are comparable. An Hα spiral structure near the center can be seen.

NGC 0925 : This late type SBcd galaxy has a bright optical and Hα bar and two bright patchy spiral arms beginning at the ends of the bar. Many HII regions lie along the bar. Photometrical and kinematical data agree. The PV diagram shows non axisymmetric motions near the center. NGC 0925 is well studied in HI (Elmegreen et al., 1998; Pisano et al., 1998), in CO (Helfer et al., 2003) and in Hα (Marcelin et al., 1982) showing strong streaming motions.

NGC 1530 : This strongly barred spiral galaxy has been extensively studied by Zurita et al. (2004). Here the FaNTOmM observation provides many more details of the kinematics along the major axis due to its large FOV and high sensivity. A nuclear spiral and a large velocity gradient are observed. In the V-band images, a nuclear bar (Buta & Crocker, 1993) with hot spots (Sérsic, 1973) can be seen.

NGC 2336 : NGC 2336 is an intermediate-type ringed barred spiral galaxy with a prominent bar. This galaxy shows a very regular morphological structure with no major asymmetries, except for the central regions where HI maps show a lack of gas in the center (van Moorsel, 1983). The Hα monochromatic image suggests the same lack. The NW part of the disk has been cut off by the wings of the interference filter. Although NGC 2336 belongs to an apparent pair of galaxies (together with IC 467) with a projected linear distance of 135 kpc, its undisturbed disk does not exhibit any distinct sign of recent interactions (Wilke et al., 1999).

NGC 2403 : This SABc galaxy shows amorphous spiral features. The Hα velocity maps and the PV diagram show an almost rigid structure near the center of the galaxy. Bright HII regions can be seen in the Hα monochromatic image. It is not clear whether this

galaxy is barred or not. According to Schoenmakers et al. (1997), their Fourier harmonic analysis of the HI velocity field shows that non-circular motions are not important in this galaxy. Moreover, Schaap et al. (2000) stress that the thin hydrogen disk of NGC 2403 is surrounded by a vertically extended layer of HI that rotates more slowly than the disk. A complete modeling of the galaxy will provide more details on its structures. Fraternali et al. (2001) suggest that this anomalous HI component may be similar to a class of high velocity clouds observed in the Milky Way. In CO data, no molecular gas is detected (Helfer et al., 2003).

NGC 2903 : This starburst galaxy shows several peaks of star formation in the circumnuclear region. These peculiar "hotspots" have been identified and described in different ways by various authors in Hα (Marcelin et al., 1983), in radio and in the infrared by Wynn-Williams & Becklin (1985). A strong velocity gradient can be seen along the bar in the velocity map. The PV diagram shows a clear step in the RC. This step-like structure could be related to its strong bar. The molecular gas, visible in CO observations (Helfer et al., 2003), follows the bar.

NGC 3198 : This SB(rs)c galaxy has been extensively studied in HI (Bosma, 1981a; Begeman, 1989a), FP Hα (Corradi et al., 1991; Blais-Ouellette et al., 1999) and Hα and [[NII]] long-slit spectroscopy (Sofue et al., 1998; Vogt et al., 2004). According to the PV diagram, non circular motions near the centre can be seen. A strong velocity gradient is also seen perpendicular to the bar major axis.

NGC 3359 : NGC 3359 is a strongly barred galaxy. Its HII regions have been studied (Martin & Roy, 1995) and cataloged (Rozas et al., 2000a). The structure and kinematics of the HI were analyzed in detail by Gottesman (1982) and Ball (1986) showing a clumpy distribution and a low surface density within the annular zone of strong star formation, which can be explained as due to the effect of the bar sweeping up gas as it rotates. Analysis of the Hα velocity map shows a disk with an axisymmetric rotation and also evidence of strong non circular motions as confirmed by Rozas et al. (2000b). Analysis of the Hα residual velocity map (not shown here) shows strong streaming motions in the spiral arms and a strong gradient of gas in the bar.

NGC 3953 : As one of the most massive spirals of the M81 group, NGC 3953 has been studied in HI by Verheijen & Sancisi (2001). It is rather poor in HI and the surface density drops near D_{25}. Moreover, in CO, the gas seems to be located in a ring at the near

end of the bar. In Hα , the same lack of gas in the center can be seen, whereas the arms are well developed.

NGC 3992 : This galaxy is the most massive spiral of the M81 group. Its HI distribution is regular. It has a prominent bar and very well defined spiral arms. It has a faint radial HI extension outside its stellar disc. There is a pronounced central HI hole in the gas distribution at exactly the radial extent of the bar (Bottema & Verheijen, 2002), also visible in the Hα emission line. Some Hα can be seen toward the center of the galaxy. It is not clear whether this feature could exist in HI because of the poor spatial resolution of the HI data measurements. Observations in CO (Helfer et al., 2003) stress the lack of molecular gas in the galaxy.

NGC 4236 : This late type SBdm galaxy is seen nearly edge-on. Its kinematical inclination is 76°. The Hα image shows that the HII regions are distributed along the bar, with two bright regions near the end of the bar. These features are also seen in HI (Shostak, 1973). An extensive region of solid-body rotation coincides with the bar.

NGC 4321 : This grand-design spiral galaxy has been frequently mapped in the *H*α emission line using high-resolution FP interferometry (Arsenault et al., 1990; Cepa & Beckman, 1990; Canzian & Allen, 1997; Knapen et al., 2000a), in CO (Canzian, 1990; Sakamoto et al., 1995; Rand, 1995; Garcia-Burillo et al., 1998; Helfer et al., 2003) and in HI (Cayatte et al., 1990; Knapen et al., 1993). The HI disk is almost totally confined within the optical disk but with a slight lopsidedness towards the SW (Knapen et al., 1993). The HI, CO and Hα velocity fields show kinematical disturbances such as streaming motions along the spiral arms and a central S-shape distortion of the iso-velocity contours along the bar axis. The circum-nuclear region (CNR) and the presence shows the presence of an enhanced star formation region as a four-armed Hα ring-like structure and a CO & Hα spiral-like structure. Many more details can be found in Hernandez et al. (2005a).

NGC 4535 : With NGC 4321, this is another Virgo cluster galaxy with a known Cepheid distance. It is not located in the main sub-structure of the cluster close to the core elliptical galaxy M87 but it lies in the southern extension related to M49. Although the Hα morphology appears perturbed, with an obvious indication of multiple spiral arms (these features are even present in the NIR Ks image), its velocity field is regular. No HI was found in the central parts (Cayatte et al., 1990).

NGC 5371 : In this galaxy, there is no evidence of Hα emission in the center.

NGC 5457 : M101 is a large nearby galaxy. Observations in CO (Helfer et al., 2003) show that the molecular gas is only distributed along the bar. In the Hα image the gas is distributed over the whole field. Two large arms can be seen.

NGC 5921 : This galaxy shows a ring like structure in both the Hα and the XDSS blue images. The bar is not clearly seen in Hα but many HII regions lie at the end of the bar. The center of the galaxy is the host of a strong velocity gradient well defined in the Hα velocity map. Nevertheless, no Hα gas is present between the ring like structure and the center.

NGC 5964 : This galaxy shows strong HII regions distributed along its bar. Nevertheless, no strong velocity gradient can be seen in this direction.

NGC 6217 : This galaxy presents a prominent bar, with a prominent region of stellar formation on it located at 10" in the southeastern direction from the galactic center (Artamonov et al., 1999). The galactic center reveals the presence of a different structural component, a ring. The diameter of the ring in Hα observations is approximately 43", which agrees with previous work in HI on this galaxy (van Driel & Buta, 1991). The inner ring structure in the center of the galaxy can be easily seen in the Hα monochromatic image.

NGC 6946 : According to Carignan et al. (1990), the HI distribution is not symmetric but is more extended to the NE side. This feature is also seen in the Hα emission map. The overall Hα velocity map is regular but shows some non-circular motions near the center, confirmed by the PV diagram. It has been recently observed in FP by Blais-Ouellette et al. (2004) leading to the same conclusions. Once again the wide field of FANTOMM and its high sensitivity is clearly an advantage to obtain better Hα velocity fields.

NGC 7479 : This SB(s)c galaxy has been studied in HI by Laine & Gottesman (1998). The HI distribution shows considerable asymmetries and distortions in the outer disk. The HI and Hα kinematics suggest that, while the global velocity field is fairly regular, a severe perturbation is present in the western spiral arm. There is also a strong velocity gradient along the bar confirmed in the PV diagram. The Hα monochromatic image shows strong HII regions at one end of the bar.

NGC 7741 : This galaxy shows a strong bar in the Hα, blue and K-band images. Many HII regions are located along the bar. The velocity map clearly shows non-circular motions, whereas the velocity gradient is not too strong (compared with NGC 2903 for example).

Chapitre 4

Analyse bidimentionelle des champs de vitesses : La méthode de Tremaine-Weinberg

BHαBAR : The *BHαBAR* sample - II. On the relevance of the Tremaine-Weinberg method applied to Hα velocity fields. Multiple pattern speed determination in M100.

OLIVIER HERNANDEZ

Département de physique and Observatoire du mont Mégantic, Université de Montréal, C.P. 6128, Succ. centre ville, Montréal, Québec, Canada. H3C 3J7 and

Observatoire de Marseille, 2 Place Le Verrier, F–13248 Marseille Cedex 04, France

HERVÉ WOZNIAK

Centre de Recherche Astronomique de Lyon, 9 avenue Charles André, F-69561 Lyon, France

CLAUDE CARIGNAN

Département de physique and Observatoire du mont Mégantic, Université de Montréal, C.P. 6128, Succ. centre ville, Montréal, Québec, Canada. H3C 3J7

PHILIPPE AMRAM

Observatoire Astronomique de Marseille Provence, LAM, 2 place Le Verrier, F-13248 Marseille Cedex 04, France

LAURENT CHEMIN

Département de physique and Observatoire du mont Mégantic, Université de Montréal, C.P. 6128, Succ. centre ville, Montréal, Québec, Canada. H3C 3J7 and

OLIVIER DAIGLE

Département de physique and Observatoire du mont Mégantic, Université de Montréal, C.P. 6128, Succ. centre ville, Montréal, Québec, Canada. H3C 3J7

Submitted to the Astrophysical Journal

Abstract

The relevance of the Tremaine-Weinberg (TW) method is tested to measure the bar, spiral and inner structure pattern speeds using a gaseous velocity field. The TW method is applied to various simulated barred galaxies in order to demonstrate its validity in seven different configurations, including star formation or/and dark matter halo. The reliability of the different physical processes involved and of the various observational parameters are also tested.

The simulations show that the TW method could be applied to the gaseous velocity fields to get a good estimate of the bar pattern speed, under the condition that regions of shocks are avoided and measurements are confined to regions where the gaseous bar is well formed. We successfully apply the TW method to the Hα velocity field of the Virgo Cluster Galaxy M100 (NGC 4321) and derive pattern speeds of 55 ± 5 km s^{-1} for the nuclear structure, 30 ± 2 km s^{-1} for the bar and 20 ± 1 km s^{-1} for the spiral pattern, in full agreement with published determinations using the same method or alternative ones.

Keywords : galaxies : individual (M100 = NGC 4321) — galaxies : kinematics and dynamics — galaxies : bar and spiral — methods : numerical — galaxies : fundamental parameters (masses) — techniques : interferometric

4.1 Introduction

The presence of a barred structure appears to be a common attribute of disk galaxies. Roughly 30% of spiral galaxies are strongly barred in the optical (de Vaucouleurs, 1963) while another 25% are weakly barred. Evidence that bars in spirals are more obvious in the near-infrared (NIR) than in the visible goes back to Hackwell & Schweizer (1983). More recent surveys in the NIR have shown that up to 75% of high surface brightness galaxies may have a more or less strong bar (e.g. Knapen, Shlosman & Peletier, 2000 ; Eskridge et al., 2000). Strong bars are nearly twice as prevalent in the NIR than in the optical. The high frequency of occurence of bars means that they are long-lived attributes of disk systems. While bars should be destroyed rapidly, it is thought that continuous accretion produces multi-phase bars (Bournaud & Combes, 2002).

The fact that bars may contain a large mass fraction of the disk suggests that they are a fundamental component of the mass distribution in spiral galaxies. Since their kinematics is different from that of the more or less axisymmetric disk, it is important to model them properly to derive, as accurately as possible, the overall mass distribution. This is especially important since bars are in the inner parts of disk systems where the free parameters of the mass models are best constrained (Blais-Ouellette et al., 1999, 2004 ; Blais-Ouellette, Amram & Carignan, 2001). The parameters of mass models are not constrained by the flat part but by the rising part of rotation curves (RC).

The determination of the bar pattern speed (Ω_p) in spiral galaxies is one of the

most important kinematical parameters since it drives a large part of their evolution (e.g. Block et al., 2004). It is essential for understanding the so-called dark matter problem and, more generally, the structure of spiral galaxy halos.

A determination of the bar pattern speed and other non-axisymmetric and asymmetric structures is important for a number of reasons :

- Orbital calculations show that a bar can only be built self-consistently if it lies entirely within its corotation radius, the point at which the bar pattern rotates at the same speed as a star on a circular orbit at that radius (Contopoulos, 1980). Further studies using hydrodynamical simulations have shown that the corotation radius has to lie in the interval of 1.2 ± 0.2 times the length of the semi-major bar axis (Athanassoula, 1992a).
- Bars may initiate spiral density waves (e.g. Toomre, 1969) and stellar rings (e.g. Buta, 1986). A clear determination of the corotation may give insight on the nature of density waves and on the energy and angular momentum exchanges between the bar and the disk (Sellwood, 1985 ; Masset & Tagger, 1997).
- Stellar bars may provide a means to transport gas towards the nuclear regions of galaxies by inducing gravitational torques (Block et al., 2002) and fuel nuclear starbursts or active galactic nuclei (e.g. Kormendy, 1982). The transfer of material (inflow or outflow) may be linked to the pattern speed (Athanassoula, 1992b).
- Bars may drive the secular evolution of bulges, by triggering nuclear starbursts and by kinematic heating of the inner disk (e.g. Combes et al., 1990). The bar pattern speed depends critically on the relative bulge mass and the disk scale-length (e.g. Combes & Elmegreen, 1993).
- Bars' pattern speeds may help to discriminate (Noguchi, 2004) between spontaneous bars (large Ω_p) and tidal bars (small Ω_p).
- Bars may introduce errors in determining the mass distribution of spiral galaxies from their rotation curves. Indeed, non-circular motions are usually azimuthally averaged and may have for consequence to flatten the shape of the inner regions of the RCs (e.g. Swaters et al., 2003). These non-circular motions must be modeled properly and removed from the observed kinematics in order to retrieve the true circular kinematics which trace the mass distribution.
- Strongly barred galaxies may have maximal (or nearly maximal) disks. The absence of slow bars may require maximum disks, which transfer very little angular

momentum to the low density halos (Debattista & Sellwood, 1998). Alternatively, the strongest bars and higher pattern speeds may be found in sub-maximum disks where the amount of angular momentum exchanged by resonant particles between the disk and the halo is the largest (Athanassoula, 2003). Bars are often associated with rings (e.g., Buta, 1995) and may require a maximal disk for stability (e.g. Quillen & Frogel, 1997).

The TW method is described in Sect. 2, tests on numerical simulations are presented in Sect. 3, the case of M100 is examined in Sect. 4 and the discussion and conclusions are given in Sect. 5 and 6.

4.2 Description of the Method

Bar pattern speeds of spirals are determined by identifying theoretically predicted resonances (Lindblad resonances, corotation) with periodic motions of the stars and gas (extracted from the RC). The determination of bar pattern speeds relies on observational methods or, alternatively, on matching numerical models (N-body + SPH codes, see next section) to the observed velocity fields. A number of reviews describing these methods in detail can be found (e.g. Teuben, 2002).

Two methods, somewhat indirect, are based on the identification of morphological features associated with resonance radii (measuring the inner resonance 4 :1, Elmegreen, Elmegreen & Montenegro, 1992; or alternatively, measuring the sign inversion of the radial streaming motions across corotation; Canzian, 1993). Theoretical evidence argues that the corotation radius lies just beyond the end of the bar (e.g. pioneer work of Contopoulos, 1980). Based on this result, many bar pattern speeds have been estimated (see a compilation in Elmegreen et al., 1996).

A more direct model independent method, not relying on any particular theory of density waves, is due to Tremaine & Weinberg (1984, hereafter TW). The pattern speed is determined from two observationally accessible quantities : the luminosity-weighted mean velocities and the luminosity-weighted mean densities throughout the disk of the galaxy. In the plane of the sky, X is the coordinate along the major axis of the galaxy, Y along the minor axis and V_{LOS}(X,Y) the line of sight velocity. $< X_Y >$ is the luminosity-weighted mean X-position integrated along a strip parallel to the X-axis at Y coordinate, $< V_{LOS,Y} >$

is the luminosity-weighted mean velocity along the X-axis at Y coordinate. Thus,

$$\Omega_p \sin i = \frac{\int_{-\infty}^{\infty} \Sigma(x,y,t) V_y(x,y,t)\, dx}{\int_{-\infty}^{\infty} \Sigma(x,y,t) x(y,t)\, dx} = \frac{< V_{LOS,Y} >}{< X_Y >},$$

where Ω_p is the pattern speed and Σ is the surface density of the component.

The underlying assumption is therefore that the density is proportional to intensity. Therefore, a corollary statement is that disks must be close to maximum in the inner parts for the method to work. The TW method also requires a tracer population that satisfies the continuity equation (no significant creation or destruction of matter over an orbit). It may be the case for the stellar population, even if, in reality, the continuity equation is never strictly satisfied because of continuous star formation. Nevertheless, old stars may survive many passages through the pattern. As long as the star formation efficiency is low, conversion of gas into stars (and vice versa through winds and supernovae) can be ignored

For these reasons, the TW method has preferentially been applied to early-type bars using starlight and absorption-line kinematics from long-slit spectra : NGC936 (Kent, 1987 ; Kent & Glaudell, 1989 ; Merrifield & Kuijken, 1995) ; NGC4596 (Gerssen, Kuijken & Merrifield, 1999) ; NGC1023 (Debattista, Corsini & Aguerri, 2002) ; NGC7079 (Debattista & Williams, 2001) ; ESO 139-G009, IC874, NGC1308, NGC1440 and NGC3412 (Aguerri, Debattista & Corsini, 2003) ; NGC271, NGC1358, ESO 281-31, NGC3992 (Gerssen, Kuiken & Merrifield, 2003).

Application of the TW method to gaseous phases is complicated especially since the method assumes that the disk component obeys the continuity equation and that the relation between the emission and its surface density is linear (or can be modeled). Atomic hydrogen and molecular gas will not obey the continuity equation, because of the conversion of gas between the three phases (molecular, atomic and ionized) and because the star formation timescales are shorter than the orbital timescales. However, Zimmer, Rand, & McGraw (2004) and Rand & Wallin (2004) have argued that, in galaxies in which either the HI or H_2 everywhere dominates the large majority of the ISM, the conversion processes can be neglected and the TW method applied.

Pattern speeds using the TW method were recently derived using HI for M 81 by Westpfahl (1998) and for NGC 2915 by Bureau et al. (1999). Using CO observations, pattern speeds were also determined in galaxies with molecule-dominated ISMs for M51, M83, and N6946 by Zimmer, Rand, & McGraw (2004) and for NGC1068, NGC3627, NGC4321 (M100),

NGC4414, NGC4736 and NGC4826 (from the BIMA SONG survey) by Rand & Wallin (2004).

Gas in its ionized phase will never dominate the ISM ; the equation of continuity for the ionized gas will never be satisfied on an orbital period and the Hα luminosity is not supposed to trace the mass. HII regions are bright ionized regions surrounding massive and hot newborn O and B stars. The OB stars have main-sequence lifetime of only a few 10^6 years, HII regions are furthermore short-lived gas clouds (which only exist during the lifetime of their ionizing OB stars) embedded in a star-forming region in a molecular cloud. A given HII region, associated to its parent stars, cannot survive to a typical galactic rotation of 10^8 years. Nevertheless, HII regions and OB stars have not enough time to wander far from their parent molecular cloud and are, if we neglect the expansion processes, a tracer of the molecular gas density. Moreover, $< V_{LOS,Y} >$ determined from Hα, is as good a tracer as any of the galactic potential well (as it is the case when deriving a RC).

It is true to say that the application of the TW method to Hα may apparently violate several of the TW conditions. However, we suppose that, to first order, the continuity equation is satisfied, but only for very short times ($\ll$ orbital period), we neglect the internal kinematics of HII regions and we suppose that the luminosity-weighted mean X-position integrated along a strip parallel to the X-axis, $< X_Y >$, is a valuable indicator of the mean mass distribution.

Preliminary results on the determination of bar pattern speeds using HII regions were already presented for NGC2903, NGC3359, NGC4321 (M100), NGC5194 and NGC6946 (Hernandez et al., 2004).

4.3 Tests on Numerical Simulations

The TW method will be applied to simulated barred galaxies in order to demonstrate its validity and to understand its sensitivity to various observational parameters.

4.3.1 Description of the simulations

The codes

This section will describe the techniques used to perform self-consistent simulations including stars, gas and star formation. In order to check for model and/or code dependent results, two significantly different numerical schemes were applied for the computation of the forces.

A particle–mesh N-body code was used which includes stars, gas and recipes to simulate star formation (SF). The broad outlines of the code are the following : the gravitational forces are computed with a particle–mesh method using a 3D polar grid with $(N_R, N_\phi, N_Z) = (31, 32, 64)$ active cells, the hydrodynamical equations are solved using the SPH technique and the star formation process is based on Toomre's criterion for the radial instability of gaseous discs (see Michel-Dansac & Wozniak, 2004 for more details). When star formation is active, the radiative cooling of the gas has been computed assuming solar metallicity.

When an extended live dark matter component was added (halo potential non fixed), our computations were performed with `GADGET`, a tree-based N-body+SPH code developed by Springel et al. (2001). An adaptative time step was used, based on the dynamical time and limited by the Courant condition (Springel et al., 2001).

Initial conditions

For all the simulations, an initial stellar population is set up to reproduce a disc galaxy with an already formed bulge. These particles form the 'old population' as opposed to particles created during the evolution ('new population') for simulations with star formation switched on.

For all runs, the initial positions and velocities of the stellar particles are drawn from a superposition of two axisymmetric Miyamoto-Nagai discs (Miyamoto & Nagai, 1975) of mass respectively 10^{10} and $10^{11}\mathcal{M}_\odot$, of scale lengths respectively 1 and 3.5 kpc and common scale height of 0.5 kpc. Velocity dispersions are computed solving numerically the Jeans equations. Runs numbered "2" have 5 times more particles than those numbered "1" (cf. Table VI). For runs with a dissipative component (`SG1` `SF1`, `SF2`, `Ha` and `Hb`), the gas is represented by 50 000 particles for a total mass of $10^{10}\mathcal{M}_\odot$ distributed in a disc of scale length

Table VI: Run parameters. The mass unit is $10^{11}\mathcal{M}_{\odot}$. The number of particles is 10^5.

Model	S1	SG1	SF1	S2	SF2	Ha	Hb
M_{stars}	1.21	1.1	1.1	1.21	1.1	1.1	1.1
N_{stars}	5.5	5	5	25.5	25	11	11
M_{gas}		0.11	0.11		0.11	0.11	0.11
N_{gas}		0.5	0.5		0.5	0.5	0.5
M_{halo}						2.42	6.46
N_{halo}						22	22
M_{tot}	1.21	1.21	1.21	1.21	1.21	3.63	7.67
SF		off	on		on	off	off

3 kpc. For Run SG1 the gas is kept isothermal while, when the star formation is switched on, a cooling function is assumed for a solar metallicity and the energy conservation equation is solved at each step (Michel-Dansac & Wozniak, 2004).

For the sake of comparison, we have also computed pure N-body models (Run S1, S2), i.e. without gas and star formation. The total mass is the same mass as the total initial mass of the visible components of runs SF1, SF2, Ha and Hb. Of course, because of star formation, the stellar mass increases for runs SF1 and SF2 while it remains constant for all other runs. These runs tell us what should be the evolution of the stellar mass and kinematical properties in the absence of any dissipative component.

Apart from the number of stellar particles (1.1×10^6 particles), the setup of the stellar and gas distributions of runs Ha and Hb are similar to the other runs. Run Ha and Hb include an additional dark halo made of 2.2×10^6 live particles distributed in a Plummer sphere of scalelength 50 kpc and of mass respectively 2.42 and 6.46 $\times 10^{11}\mathcal{M}_{\odot}$. As our intention is to check the robustness of our results against the presence of the massive dark halo, a Plummer sphere is a simple but sufficient description of the halo. The setup of velocities and velocity dispersions is made consistent with the dark matter distribution.

Typical evolution of the models

For all runs without star formation, the initial disc quickly develops a typical strong bar and a spiral structure both in the stellar and the gaseous components. The gravity torques due to the bar and the spiral structure drive the gas inwards and the angular momentum outwards. The mass distribution is reorganized even for the old stellar population; this gas inflow occurs on a rather short timescale. The bar can be unambiguously determined (in size

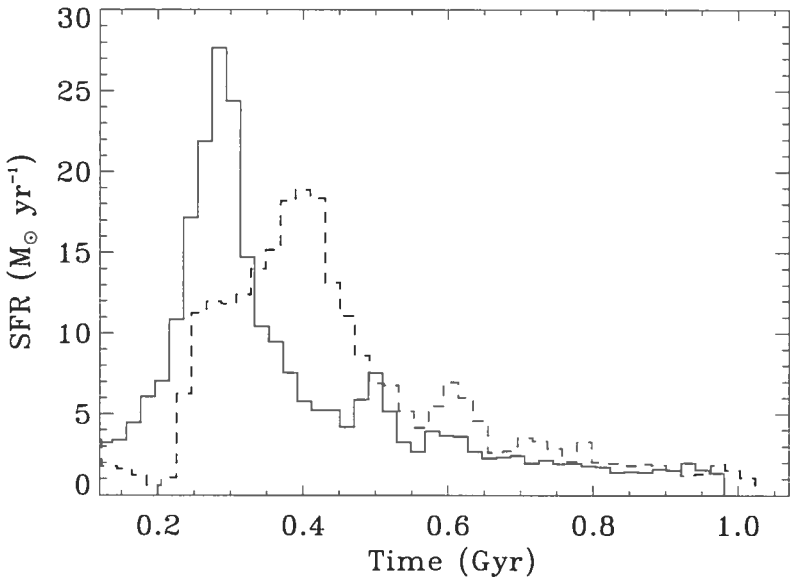

Fig. 47: Global star formation rate ($\mathcal{M}_\odot$ yr^{-1}) versus the elapsed time from the beginning of `Run SF1` (full line) and `SF2` (dotted line). Star formation is inhibited during the first 50 Myr for `Run SF1` and 100 Myr for `SF2`

and position-angle) after 300 Myr. For runs with star formation, the global Star Formation Rate (SFR) is displayed in Figure 47. For `Run SF1` three SFR maxima occur around 0.3, 0.5 and 0.6 Gyr. For `Run SF2`, star formation is inhibited during the first 0.1 Gyr in order to delay the SFR peak. Thus two main SFR peaks occur at $t \sim 0.4$ and ~ 0.6 Gyr. The SFR reaches 19–28 $\mathcal{M}_\odot$ yr^{-1}.

For $t \lesssim 300$ Myr, the bar and a bi-symmetric spiral structure spontaneously form as for the runs without star formation. The gravitational torques applied on the gas by the bar and the spiral arms create several regions of very high gas density in which star formation is ignited. As shown in previous works, during the first Myrs the SF is not homogeneously distributed over the whole disc but is mainly concentrated along the bar major axis and along the spiral arms. After ~ 1 Gyr a nuclear gas disk is formed from the accumulation of gas in the centre and new stars are actively formed only in this region. The secondary SFR peaks are the result of the gas inflow towards the central regions of the disc. Indeed, such inflow is not stationary, but rather proceeds by burst.

Runs `Ha` and `Hb` are stabilized by a live massive dark matter halo. The formation

of the bar is slightly delayed by 0.1 Gyr for `Run Ha` but after 1 Gyr this run looks like `Run SG1`. For `Run Hb` the bar appears after $\approx$ 1.5 Gyr. Both runs develop a bar and a spiral structure. `Run Hb` develops an additional inner ring inside the corotation, which is typical of the interaction of disc particles with halo particules (cf. Athanassoula & Misiriotis, 2002).

4.3.2 Application of the TW method

The TW method was applied in an automated way since we are dealing with numerical simulations. Particle positions and velocities have been projected to an inclination of 45 °. Particles have also been rotated so that the projected position-angle of the bar with respect to the line of nodes (PA_{bar}) lies between 30 and 50 °. These are optimal values for a best estimate of Ω_p (Merrifield & Kuijken, 1995). For each component (stellar or gas particles), two (X,Y) frames are computed, one for the mass integrated along the LOS, another for V_{LOS}. The field-of-view is limited to the projected bar length (between 2 and 5 kpc). The spatial resolution is 200 pc. The process is repeated for each available snapshot from $t = 0$ to $t = 1$ Gyr (2 Gyr in the case of `Run Hb`).

The mass-weighted line-of-sight velocity $< V_{LOS,Y} >$ and the mass-weighted position coordinate, $< X_Y >$ are computed for each value of Y. Each Y position thus acts as a long slit. A linear fit between $< V_{LOS,Y} >$ and $< X_Y >$ is made using a robust least square algorithm. Since we exactly know the line-of-nodes position-angle and the inclination angle, the slope determination of the $< V_{LOS,Y} >$ versus $< X_Y >$ relationship is the only source of errors on Ω_p. Finally we obtain two estimates of Ω_p, one using the stellar component Ω_p^s, another with the gas component Ω_p^g.

First, we have tested our method on the stellar velocity field of `Run SF1` (cf. Fig. 48). The values of Ω_p^s are very similar to those directly computed with the bar position-angles determined every Myr during the computation of the simulations. Thus, we confirm that the TW method is a very efficient tool to determine the bar pattern speed in numerical simulations. In the case of `Run S1`, a pure N-body simulation without gas and star formation but with the same *initial* mass as `Run SF1`, the bar rotates more slowly than for `Run SF1`. This effect is obviously due to a completely different evolution of mass transfers. Indeed, for `Run SF1`, the gas inflow towards the center is quick enough to sustain the bar pattern speed at a high value when the bar appears ($\sim$ 0.2 Gyr for `Run SF1`). The new stellar population created during the gas inflow remains inside the corotation, increasing the stellar mass. As

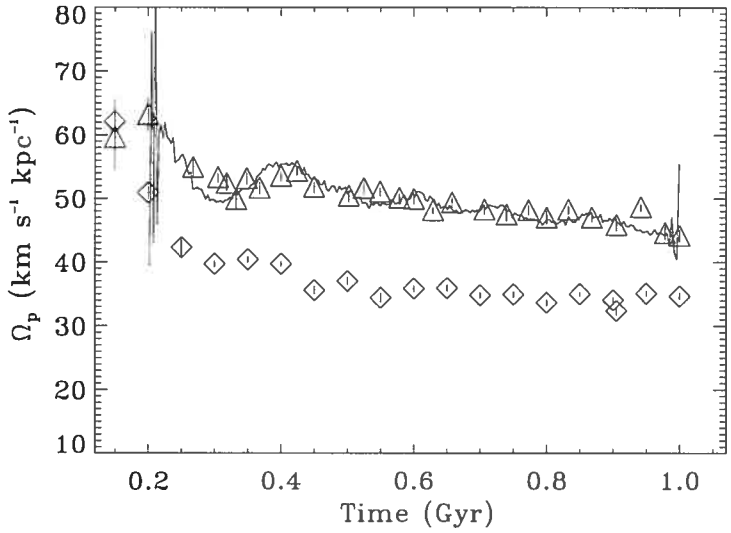

Fig. 48: Stellar pattern speeds Ω_p^s measured with the automated TW method using the stellar velocity field of `Run SF1` (open triangles) and `Run S1` (open diamonds). $1-\sigma$ errors are overplotted as vertical lines but are often smaller than the symbols. The pattern speed computed during the simulation is plotted as a continuous line.

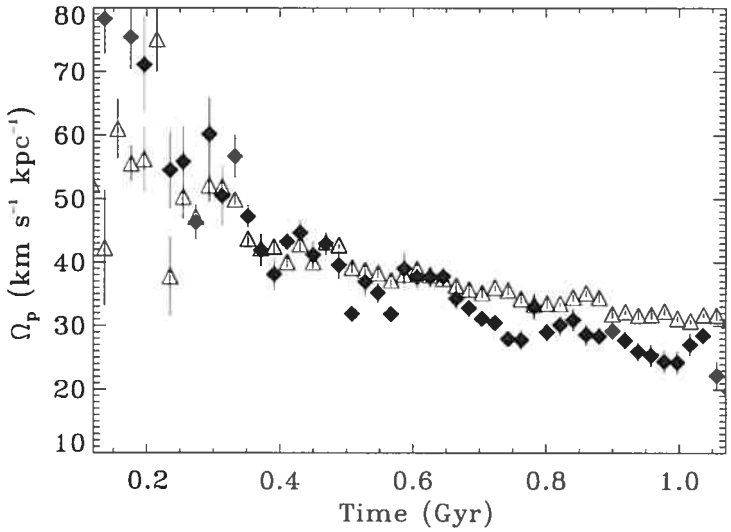

Fig. 49: Pattern speeds determined using the stellar velocity field (Ω_p^s open triangles) and the gas one (Ω_p^g full diamonds) for `Run SG1`. $1-\sigma$ errors are overplotted as vertical lines.

for the observations (cf. Sect. 4.4.3), the velocity field of the gaseous component was also used to compute $< V_{LOS,Y} >$. Fig. 49 shows the results obtained with `Run SG1` . For this run, star formation was switched off. Once the bar had settled in ($t \gtrsim 0.25$ Gyr), and strong shocks had faded away, Ω_p^s and Ω_p^g give similar estimations of the pattern speed. Indeed, in the absence of strong shocks, the gas velocity field is close to the stellar velocity field, at least in the central region of the bar. Thus, for real data, it is mandatory to avoid including any region of strong shocks in the computation of $< V_{LOS,Y} >$.

For $t \gtrsim 0.6$ Gyr, Ω_p^g gives lower values than Ω_p^s. This bias can be removed by a careful selection of the regions where the LOS velocities and mass densities are measured. Indeed, a careful inspection of the projected mass density and velocity fields shows that the gaseous bar could be sometimes significantly shorter than the stellar bar. Since the automated TW method inconveniently selects some regions outside the gaseous bar, this leads to an underestimation of the bar pattern speed. Thus, the application of the TW method to observational gas velocity fields needs a careful selection of the region included in the $< V_{LOS,Y} >$-$< X_Y >$ fit.

A living dark halo does not change significantly the results. As expected, the gravitational interaction made by a low mass dark halo (`Run Ha`) does not change much the bar pattern speed. In the case of `Run Hb` (Fig. 50), once the bar is formed, Ω_p^g can be a good estimator of Ω_p on condition that the gaseous inner ring is excluded from the measurements. Otherwise, Ω_p^g is biased towards lower values. When star formation is switched on, the TW method applied to the gaseous component is less accurate (Fig. 51). Indeed, Ω_p^g slightly overestimates the real bar pattern speed, especially when the SFR is high ($\gtrsim 5\ \mathcal{M}_\odot\,\mathrm{yr}^{-1}$). The reason for this behaviour is indirectly linked to the star formation process. Indeed, the main source of errors is the presence of strong and persistent gradients in the gaseous velocity fields. These regions of high density are obviously the privileged sites of stellar formation. Since the mass distribution is completely different from `Run SG1` because of the new stellar population, shocks regularly occur, especially in the inner region of the bar where the gas inflow is stopped. Finally, when most of the gas has been consumed by star formation (i.e. $t \gtrsim 0.9$ Gyr), its velocity field tends to be like the stellar velocity field, leading to better estimates of Ω.

However, the discrepancies between Ω_p^s and Ω_p^g remain within $\pm 10\ \mathrm{km\,s^{-1}\ kpc^{-1}}$. Thus the TW method could be applied to the gaseous velocity fields to get a rough estimate

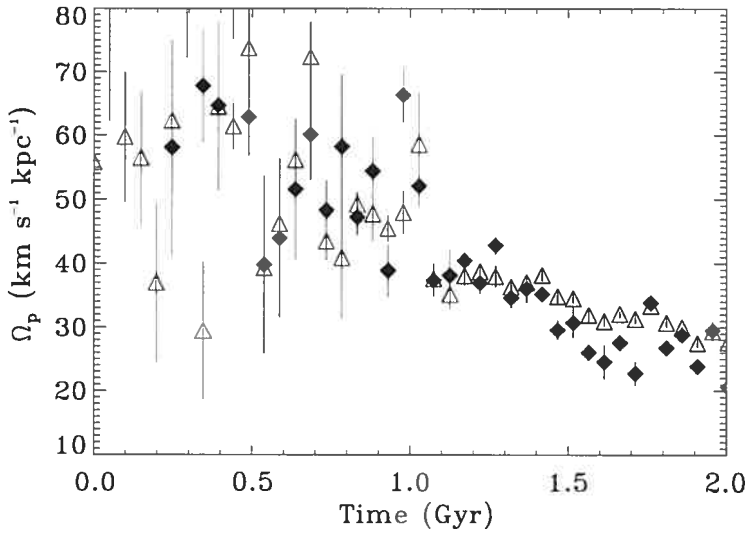

Fig. 50: As Fig. 49 for Run Hb. Star formation is inhibited.

of the bar pattern speed, under the condition that regions of shocks are avoided and measurements are confined to regions where the gaseous bar is well formed. All our results have been checked with Run S2, the same simulation as Run SF1 but with 5 times more particles. The SFR history is different (cf. Fig. 48) from Run SF1 but we reach the same conclusions. We have also applied the same method as the one used with real data (cf. Sect. 4.4.3). Such a method uses an adaptive spatial smoothing algorithm based on the Voronoi tesselation to produce maps of mass and velocity fields. We do not show the results here since they are very similar to the automated TW method.

4.4 The Case of M100 (NGC 4321)

4.4.1 General description of M100

M100 (NGC 4321, VCC 596) is one of the most studied objects among the nearby barred spirals. The main parameters of M100 can be found in Table VII and its Hα velocity field is shown in Figure 52, superimposed on the Hα monochromatic image. This grand-design SAB(s)bc galaxy lies in the Virgo galaxy cluster, projected at $\sim$ 1.1 Mpc from M87 in the cluster core and has two apparent dwarf companions, VCC 608 and VCC 634, which

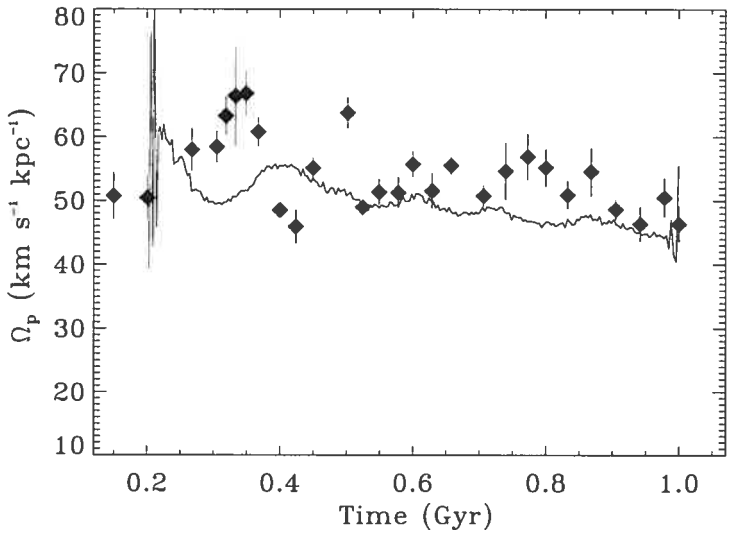

Fig. 51: As Fig. 49 using the velocity field and mass density of the gaseous component for Run SF1. Ω_p^s is not plotted again as it closely follows the pattern speed measured during the simulation.

are only at 24 and 28 kpc respectively (in projection) from its nucleus. M100 shows a small bulge, two prominent symmetric spiral arms lying within a more complex spiral structure and two diffuse stellar extensions to the North and South. The northern extension appears to end close to VCC 608. Classical dust lanes are observed throughout the whole disk along the spiral arms and the leading sides of the weak bar.

The galaxy has been frequently mapped in the Hα emission-line using high-resolution Fabry-Perot interferometry (Arsenault, Roy & Boulesteix, 1990; Cepa & Beckman, 1990; Knapen et al., 1995; Canzian & Allen, 1997; Knapen et al., 2000), in the molecular CO emission-line (Canzian, 1990; Sakamoto et al., 1995; Rand, 1995; Garcia-Burillo et al., 1998; Helfer et al., 2003) and in the 21-cm HI emission-line (Cayatte et al., 1990; Knapen et al., 1993). The HI disk is almost totally confined within the optical disk but with a slight lopsidedness towards the SW (Knapen et al., 1993). This asymmetry could be either due to ram pressure stripping by the Virgo intra-cluster medium or to a tidal perturbation from a companion. The HI , CO and Hα velocity fields show kinematic disturbances such as streaming motions along the spiral arms and a central S-shape distortion of the iso-velocity contours along the bar axis.

The circumnuclear region (CNR) of M100 has particularly received a great deal

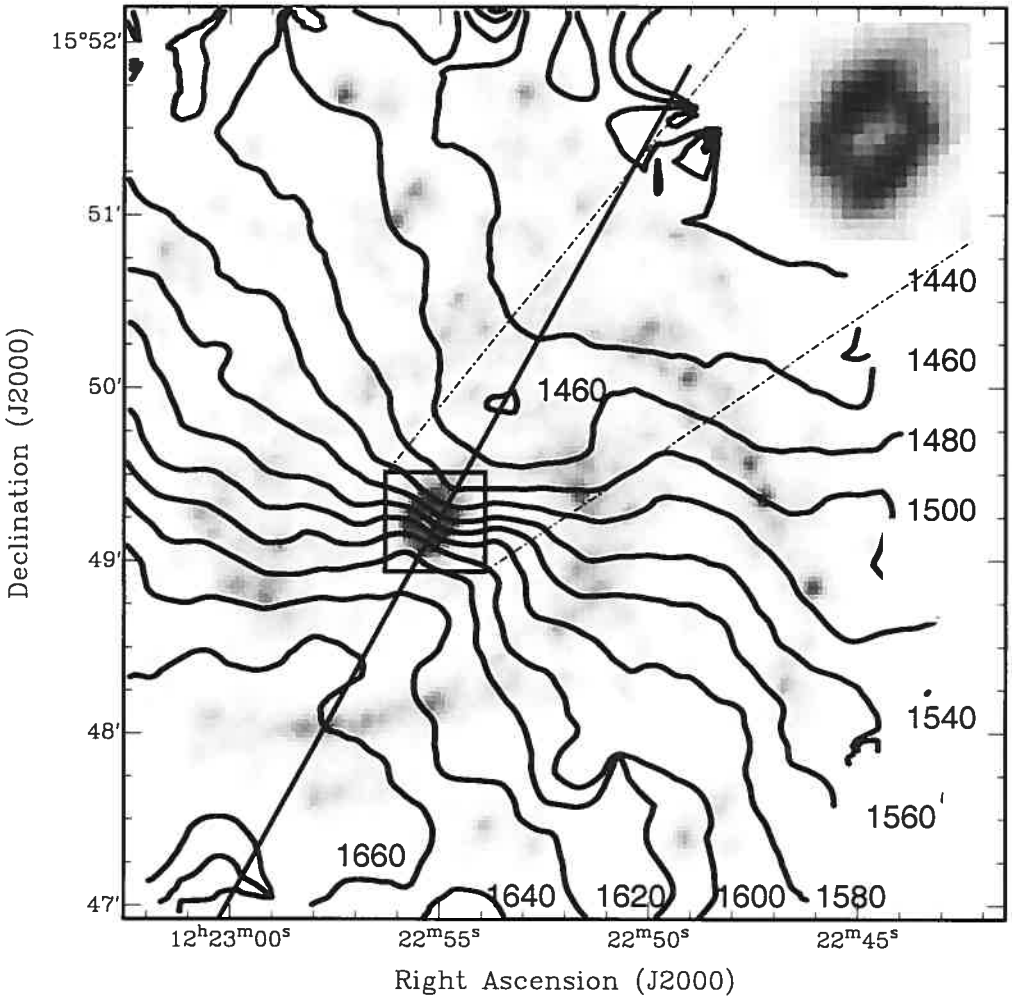

Fig. 52: M100 : Isovelocity contours superimposed on the Hα monochromatic image of the galaxy. The observations were obtained at the 1.6m of the Observatoire du mont Mégantic with FANTOMM. The labels of the isovelocities are given in $\mathrm{km\,s^{-1}}$. The major axis of the galaxy is indicated by a thick line. The top-right zoom is an enlargement of the central region of the galaxy.

Table VII: Main Parameters of M100 (NGC4321).

α (J2000)	$12^h\ 22^m\ 54.9^s$	
δ (J2000)	$+15°\ 49'\ 21''$	
Morphological type	SAB(s)bc	(1)
Heliocentric radial velocity	1586±3 $\mathrm{km\,s^{-1}}$	(1)
Adopted Distance	16.1 Mpc (78 pc/arcsec)	(2)
Isophotal major diameter, $D_{25}{}'$	7.4′±0.2′(34.6±0.9 kpc)	(1)
Exponential disk scale length (K band), α^{-1}	59.7″±2.2″(4.6±0.2 kpc)	(3)
Mean axis ratio	0.85±0.04	(1)
Inclination, i	31.7°±0.7°	(4)
Position angle, PA	27.0°±1.0°	(4)
Total apparent magnitude, $B_T(0)$	9.98	(1)
Absolute magnitude, M_B	-21.05	(2)

(1) RC3 data (de Vaucouleurs et al., 1991); (2) Cepheid-based distance from Ferrarese et al.(1996); (3) 2MASS K-band ellipse fitting; (4) Based on the velocity field of Fig 6, for more details see the *BHαBAR* sample kinematics form Hernandez et al. (2005a).

of attention in multi-wavelength observations because of the presence of an enhanced star formation region as a four-armed Hα ring-like structure and a CO spiral-like structure (e.g. Sakamoto et al., 1995 ; Knapen et al., 2000). Both the ionized and molecular gas components extend up to $R \sim 20''$ and show a central peak of emission centered on the galactic nucleus. However, the location of gas intensity maxima in the Hα ring and in the CO nuclear spiral arms do not coincide with the Hα peaks located more inward than those of the CO emission. A lower limit to the CNR total molecular mass is $\sim 2 \times 10^9\ \mathcal{M}_\odot$, as inferred from the CO integrated intensity (Sakamoto et al., 1995). The kinematics of the Hα nuclear ring shows non-circular motions and the Hα RC steeply rises in the innermost 2″ (160 pc), reaching a velocity of 150 $\mathrm{km\,s^{-1}}$ (Knapen et al,. 2000).

The origin of the CNR SF-region is supposed to be due to gas accumulation in the vicinity of the inner Lindblad resonances of the disk with density waves induced by the bar potential (Knapen et al., 1995 ; Sakamoto et al., 1995 ; Sempere et al., 1995). Hence, the determination of the pattern speed Ω_p of the large-scale bar of M100 (or reciprocally of the corotation radius) has become a crucial imperative in order to understand the role of resonances in the evolution of the galaxy. A value of Ω_p within the range $\sim$ 20-40 $\mathrm{km\,s^{-1}\,kpc^{-1}}$ has thus emerged from several observational methods and theoretical models (see Table X).

The presence or absence of a secondary bar in the nuclear region remains an open question. On one hand, some numerical simulations need two nested bars rotating at significantly different pattern-speeds to explain the CNR gaseous morphology (Garcia-Burillo et al., 1998). In this framework, the secondary nuclear bar rotates about seven times faster than the large-scale primary bar, having its corotation region near the inner Lindblad resonances of the primary bar. However, other simulations require a nuclear bar that would rotate only three times faster than the large scale bar (Wada, Sakamoto & Minezaki, 1998). On the other hand, Knapen et al. (2000) claimed that only a single $R \sim 60''$ large-scale bar is observed in M100 by means of numerical models and isophotal analysis of NIR images, which show an almost perfect alignment of the isophotes in the innermost and external parts of the bar. Their simulations predict that the nuclear structure, which was formed from a single-barred potential, corotates with the bar. Hence, the use of the TW method should in principle help to resolve this question.

4.4.2 New Fabry-Perot Observations.

New observations of M100 were obtained in February 2003 with the Fabry Perot instrument FaNTOmM[a] (Hernandez et al., 2003) on the mont Mégantic Observatory (OMM) 1.6m telescope in the frame of a new large observational program of barred galaxies (*BHαBAR* sample : Hernandez, et al., 2005a). FaNTOmM is composed of a focal reducer (bringing the original f/8 focal ratio of the Cassegrain focus to f/2), a scanning Fabry-Perot and an Image Photon Counting System (IPCS) based on a new technology GaAs amplifier tube which has a high quantum efficiency (Gach et al., 2002). The journal of the observations and the observational setup is given in Table VIII.

The reduction of the data cubes was performed using the package ADHOCw (Boulesteix, 2004) rewritten with large improvements under the IDL package. The signal measured along the scanning sequence was separated into two parts : (1) an almost constant level produced by the continuum light in a narrow passband around Hα (image not shown) and (2) a varying part produced by the Hα line (referred hereafter as the monochromatic map).

In order to increase the signal-to-noise ratio, an adaptive spatial smoothing based on the Voronoi tesselations method (Cappellari & Copin, 2002) and applied to the 3D data

[a] FaNTOmM (for **F**abry-Perot de **N**ouvelle **T**echnologie pour l'**O**bservatoire du **m**ont Mégantic) was developed by the Laboratoire d'Astrophysique Expérimentale (LAE, Montréal), `http ://www.astro.umontreal.ca/fantomm`

Table VIII: Journal of Fabry Perot observations.

Telescope	Observatoire du mont Mégantic	1.6 m
Equipment	FANTOMM@ Cassegrain	
Calibration	Neon Comparison light	λ 6598.95 Å
Interference filter	Central wavelength	λ 6605 Å
	FWHM	15 Å
	Transmission at maximum	0.75
	Temperature during the observations	-25^{o}C
Date		2003, February, 25
Exposure time	Total	260 minutes
	Elementary	15 secondes
	Per channel	5 minutes
Detector	IPCS	GaAs tube
Fabry–Perot	Interference Order	899 @ 6562.78 Å
	Free Spectral Range at Hα	333.36 km s^{-1}
	Finesse[(1)] at Hα	23
	Spectral resolution at Hα	20 677[(2)]
Sampling	Number of Scanning Steps	52
	Sampling Step	0.14 Å (16 km s^{-1})
	Total Field	824"×824" (512×512 px^2)[(3)]
	Pixel Size	1.61" (0.126 kpc)
	Seeing	~1.42"

(1) Mean *Finesse* through the field of view

(2) For a signal to noise ratio of 5 at the sample step

(3) After binning 2*2, the original GaAs system providing 1024×1024 px^2

cubes (Daigle et al., 2005) was used to produce the monochromatic images and the velocity fields. The strong OH night sky lines passing through the filter were reconstructed into a cube and subtracted from the galaxy's spectrum. The wavelength calibration was obtained by scanning the narrow Ne 6599 Å line under the same conditions as the observations. The velocities measured relative to the systemic velocity are very accurate, with an error of a fraction of a channel width (< 3 km s^{-1}) over the whole field. Details on the observations and on the data reduction will be given in forthcoming papers (Hernandez et al. 2005a; Daigle et al., 2005).

The position angle (PA), inclination, systemic velocity and rotation center (X_{cen}, Y_{cen}) have been calculated using ROTCUR provided by the GIPSY package and KARMA to construct the Position-Velocity plot (Hernandez et al., 2005). The fit was performed using a robust χ^2 model and the central regions of the velocity field were masked to avoid contamination due to the bar. Debattista (2003) has shown that the TW measurements of bar pattern speeds are sensitive to errors in the PA of the disc. 2D velocity fields of extended galaxies allow an accurate determination of the PA, reducing the errors when using the TW method.

4.4.3 Results.

In Figure 53 (top), the intensity-weighted line-of-sight velocity $< V_{LOS,Y} >$ is plotted versus the intensity-weighted position coordinate, $< X_Y >$. The Hα velocity field and the Hα monochromatic image have been used to measure $< V_{LOS,Y} >$ and $< X_Y >$. The degeneracy introduced during the calculation of $< X_Y >$ (integration along the X-axis) may be followed on Figure 53 (bottom) which gives the position of $< X_Y >$. For instance, the red dots in the center of the galaxy correspond to $< Y_X >$ located near the nuclear structure. The blue dots stress the bar region, and the green dots the disk structure.

Figure 53 shows that if more than one pattern is present for a given aperture (as in e.g., the bar-within-bar models of Friedli & Martinet, 1993), Ω_p will have contributions from the various patterns. The Hα image allows one to disentangle clearly the pattern speed of the inner ring from the pattern speeds of the bar and of the spiral. In the internal regions of the galaxy (between -10 and +10 arcsec from the center), the slight change in the slope of the ($< X_Y >$,$< Y_X >$) plot is more obvious in the ($< X_Y >$,$< V_X >$) plot. We performed a robust χ^2 linear fit on the three series of points (blue, green, red).

Ω_p of the bar is found to be 30.3±1.8 km s^{-1} kpc^{-1}. The distance has been chosen

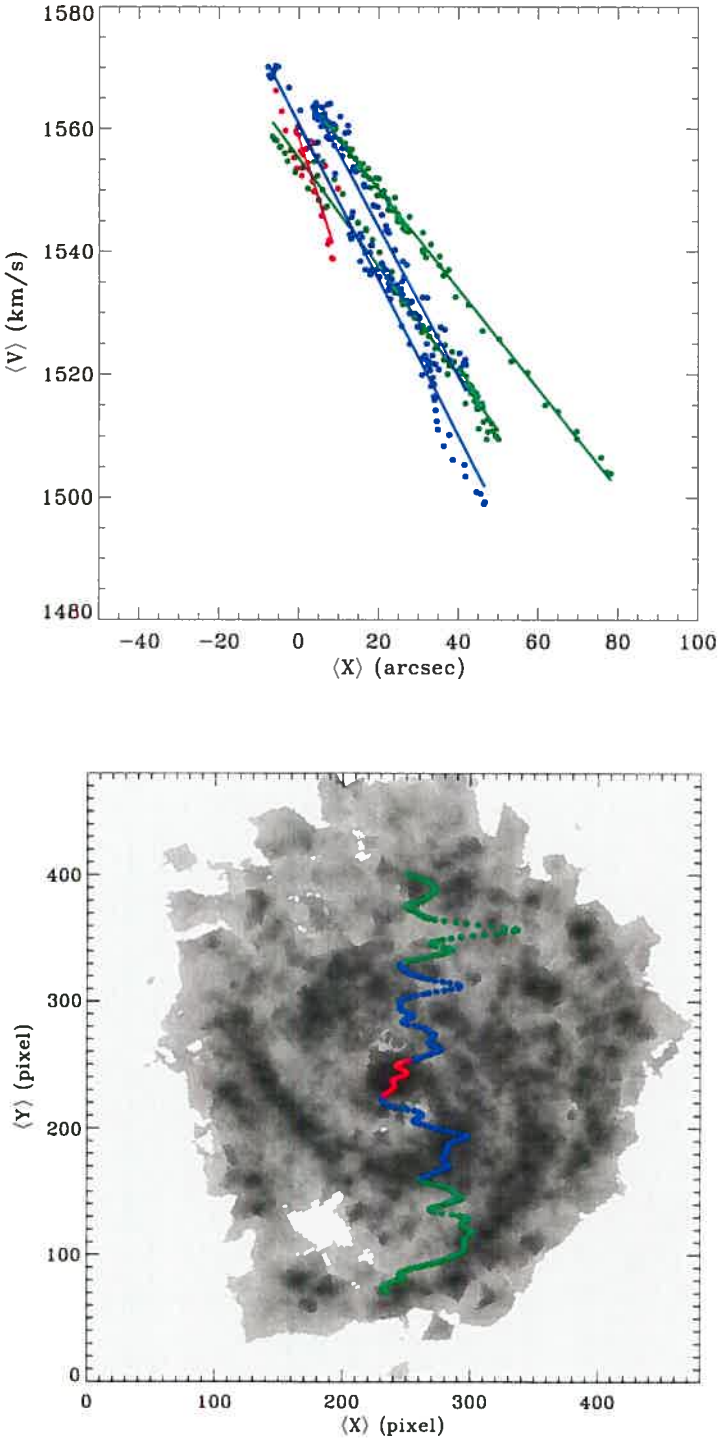

Fig. 53: (top) Mean line-of-sight velocity versus mean position for M100. Both quantities are averaged along the same strip parallel to the major axis. The degeneracy introduced during the integration along the X-axis may be followed with the colors using the right hand side plot. Straight lines represent the linear fits. (bottom) Mean Y-position versus mean X-position. Both quantities are averaged along the same strip parallel to the major axis. Red is for the nuclear structure, blue for the bar region and green for the disk spiral.

such that we can compare with Ω_p from other sources. The error calculation takes into account the error on the inclination, on the mean line of sight velocity, on the mean position along the line of node and on the PA. The errors are computed from the tilted ring models. Table X presents the results of the TW method applied to M100. All the pattern speeds are scaled to our inclination of 31.7° and distance of 16.1 Mpc.

4.5 Discussion.

4.5.1 Multiple Pattern Speeds.

The pattern speed of the spiral arms may differ from that of the bar (e.g. Sellwood & Sparke, 1988 ; Sellwood, 1993 ; Rautiainen & Salo, 1999). Different scenarii may explain the connection between bar and spiral arms : *(a)* corotating bar and spiral arms ; *(b)* independent bar and spiral arms possessing different pattern speeds connected by non-linear mode coupling.

(a) In some cases, the bar and the spiral structure are clearly corotating : *(i)* the spiral arms start from the ends of the bar (e.g. NGC 1365) ; *(ii)* the fraction of grand design spirals is higher in early type barred galaxies as compared to non-barred galaxies (this may be the case also for late type barred galaxies, e.g. NGC 157) ; *(iii)* the size of the two armed spiral in galaxies correlates with the size of the bar (e.g. Elmegreen & Elmegreen, 1989, 1995) ; *(iv)* the response to an analytic bar potential is a bar driven spiral (e.g. Sanders & Huntley, 1976) ; *(v)* the outer rings usually correspond to the outer Lindblad resonance in barred galaxies (e.g. Buta, 1995). Considering this scenario *(a)*, it is hard to explain *(i)* multi-armed barred galaxies (e.g. ESO 566-24) ; *(ii)* spiral arms which do not start from the ends of the bar ; *(iii)* flocculent barred galaxies (Buta, 1995) ; *(iv)* the absence of rings in many barred galaxies (Sellwood & Wilkinson, 1993). These observations may be explained if bars and spiral arms are either independent features or non-linearly coupled as it could be the case for instance in galaxies like NGC 1068, NGC 1398, NGC 1566, NGC 2273.

(b) Bars and spiral arms may be independent features and have different pattern speeds (e.g. simulations by Sellwood 1985 ; Sellwood & Sparke, 1988). Bars and spirals have different pattern speeds connected by a non-linear mode coupling (Tagger et al., 1987 ; Masset & Tagger, 1997 ; Rautiainen & Salo, 1999). In this scenario, the corotation of the bar and the inner Lindblad resonance of the spiral overlap in radius, which results in a transfer of energy

and angular momentum between the modes. Several simultaneous spiral modes can also coexist in the disk, even overlapping in radius. These galaxies have inner spiral (corotating with the bar) and outer spiral with a separate and lower pattern speed (Rautiainen & Salo, 1999). On the other hand, mode coupling may be stronger when the halo contribution to the rotation curve is large (e.g. Debattista & Sellwood, 1997; Rautiainen & Salo, 1999). Gnedin et al. (1995) have shown that a gravitational angular-momentum flux, or torque, can be measured directly from the mass distribution in spirals. These authors have carried out this measurement for M100 and concluded that the spiral structure seen in M100 may not be typical of its past or its future. These torques depend not on the pattern speed or permanence of the arms but only on the non-axisymmetric mass distribution.

In addition to the main bar component, many nuclear bars have been observed (e.g. Buta & Crocker, 1993; Wozniak et al., 1995; Friedli et al., 1996). At least some of these small scale bars have higher pattern speeds than the main bar (Friedli & Martinet, 1993) and inner bar formed before the main bar (Rautiainen & Salo, 1999). In the case of M100, the nuclear bar has a fast pattern (Ω_p =160 $\mathrm{km\,s^{-1}}$ kpc^{-1}; Garcia-Burillo et al., 1998) and is decoupled from the slow pattern of the outer bar+spiral (Ω_p=23 $\mathrm{km\,s^{-1}}$ kpc^{-1}; Garcia-Burillo et al., 1998). Solutions based on a single pattern hypothesis for the whole disk cannot fit the observed molecular gas response and fail to account for the relation between other stellar and gaseous tracers (Garcia-Burillo et al., 1998).

From deep surface photometry in the K band obtained for 54 normal spiral galaxies, Grosbøl et al. (2004) found in several cases that bars are significantly offset compared to the starting points of the main spiral pattern. This indicates that bars and spirals have different pattern speeds.

4.5.2 M100 : Comparison with other studies.

The number of barred galaxies that have been observed to date using the TW method, mainly SB0 galaxies, is too small to ascertain unequivocally whether centrally concentrated dark matter haloes are truly absent in barred galaxies.

- In stellar dynamical theory, the spiral arm amplitudes oscillate because of differential crowding near and between wave-orbit resonances. Three cycles of such oscillations have been found in B- and I-bands by Elmegreen et al. (1989). Using $R_{25} = D_{25}/2$ =3′.42 (de Vaucouleurs et al., 1976), these authors supposed that

the inner gap located at $0.35 \times R_{25}$ is the "+4 : 1" resonance. Thus, power law extrapolation of the RC of M100 (extracted from Rubin et al. (1980), where $V(R) = r^{\alpha}$ with $\alpha = 0.1$ for Rubin et al. instead of $\alpha = 0.35$ for this present study) locates the corotation at $0.6 \times R_{25}$, the OLR at $1.1 \times R_{25}$ and the ILR at $0.13 \times R_{25}$. With a corotation at $0.6 \times R_{25}$, the pattern speed is $21\,\mathrm{km\,s^{-1}}$ $\mathrm{kpc^{-1}}$ (scaled to the same distance of 16.1 Mpc).

- The corotation resonance has been found within the range 101-128 arcsec (see Table IX) from the Hα kinematics of the gas (Canzian et al. 1993).
- Garcia-Burillo et al. (1994) discussed two different methods to measure the pattern speeds. Firstly, using CO observations, they were seeking the detection of the change of sign of the radial streaming motions, as predicted by the theory, when going beyond the corotation. They found no change of sign in the radial streaming motions. Therefore, according to the observed kinematics, they inferred that the whole inner spiral structure is located inside corotation. Secondly, they made numerical simulations of the molecular cloud hydrodynamics and compared the gas response with the spiral structure seen in the optical and CO observations. Their best fit solution lead to $\Omega_p = 25\,\mathrm{km\,s^{-1}}$ $\mathrm{kpc^{-1}}$ (scaled to our distance and inclination), implying that corotation lies at a radius approximately equal to 110 arcsec. This value, based on a global fit of the spiral using numerical simulations, gives a much more trusty determination for the corotation but is in clear contradiction with the observational determination quoted above that places corotation in the outer disk.
- Two different methods to derive the pattern speed have also been used by Sempere et al. (1995). The first method, based on the change of sign of the radial streaming motions beyond the corotation (Canzian, 1993) lead to $\Omega_p = 25\,\mathrm{km\,s^{-1}}$ $\mathrm{kpc^{-1}}$, that locates corotation in the middle of the disc (8-11 kpc i.e. 82"-113"). The second method, involving hydrodynamic numerical simulations of the molecular cloud in a potential derived from an R-band image of the galaxy lead to $\Omega_p \simeq 25\,\mathrm{km\,s^{-1}}$ $\mathrm{kpc^{-1}}$. This validates the picture where the stellar bar ends within the corotation and the outer spiral lies outside the corotation.
- Rand (1995) estimates a value lower than $37\,\mathrm{km\,s^{-1}}$ $\mathrm{kpc^{-1}}$ by identifying the CR with the location where no tangential streaming is observed when the CO arm crosses the major axis.

- Wada et al. (1998) compared CO observations by Sakamoto et al. (1995) with a two-dimensional hydrodynamical and analytical bar model. Their best model agrees well with Knapen et al. (2000) about the double ILR, and with M100 having a single stellar bar with a pattern speed of $69\,\mathrm{km\,s^{-1}\ kpc^{-1}}$ (in excellent agreement with $70\,\mathrm{km\,s^{-1}\ kpc^{-1}}$ found in Knapen et al.).
- Garca-Burillo et al. (1998) claimed that two bars rotate at different angular speeds. The present study indicates clearly that the inner structure has a different pattern speed from the bar but it can not determine precisely the pattern speed of the secondary bar.
- Knapen et al. (2000) studied the circumnuclear starburst region of M100 and concluded that both morphology and kinematics require the presence of a double inner Lindblad resonance in order to explain the observed twisting of the near-infrared isophotes and the gas velocity field. The results of Knapen et al. (2000) are different from those of Garca-Burillo et al. (1998).
- Using this empirical relationship and deprojected bar, Sheth et al. (2002) measured a bar pattern speed of $35\,\mathrm{km\,s^{-1}\ kpc^{-1}}$ on the CO rotation curve of M100 by Das et al. (2001).
- Rand & Wallin (2004) applied the TW method of pattern speed determination to CO emission (Sempere & Garcia-Burillo, 1997). They assumed this galaxy is molecule-dominated and found that the method is insensitive to the bar pattern speed because the bar is nearly parallel to the major axis. They found a spiral pattern speed of $28\pm5\ \mathrm{km\,s^{-1}\ kpc^{-1}}$. Nevertheless, these authors found that the spiral pattern speed found agrees with previous estimates of the bar pattern speed, suggesting that these two structures are parts of a single pattern.
- Corsini et al. (2004) measured the bar pattern speed using the TW method. They compared the value with recent high-resolution N-body simulations of bars in cosmologically-motivated dark matter halos (Valenzuela & Klypin, 2003), and conclude that the bars are not located inside centrally concentrated halos and that N-body models produce slower bars than observed. We found the corotation of M100 at the radius R_{CR} (r=94") and the outer Lindblad resonance OLR (r=145"). If we conjecture that the end of the bar and the OLR match, thus M100 is in the forbidden area of their plot.

Table IX presents the location of resonances for all the previous resonances of the bar. The comparison with the present study is very consistent, especially for the bar corotation radius (CR).

Figure 54 presents the rotation curve of M100, $\Omega(R)$, where R is the galactic radius, with the position of the resonances using Hα data obtained with FaNTOmM and HI data extracted from Knapen et al. (1993). The other curves are respectively, from the top to the bottom, the $\Omega + \kappa/2$ (dash), $\Omega + \kappa/4$ (dash-dot), Ω (thick continuous), $\Omega - \kappa/4$ (dash-dot) and $\Omega - \kappa/2$ (dash) curves. The solid horizontal lines represent respectively, from the top to the bottom, Ω^{IS} from the nuclear structure, Ω_p^B from the bar and Ω^{Sp} from the spiral pattern derived from the TW method using Hα. $\sigma \pm 1$ errors, on the three Ω are drawn in the lower right hand side of the graph. For the bar, these errors are reported in terms of radii to determine the range of resonance radii.

Fig. 54 gives clear evidence that the '+4 :1' resonance of the bar, located in the middle of the disc, is very close to the corotation of the spiral. Beyond this radius ($\approx 11 - 12$ kpc) the spiral arms vanish. This is a rather unexpected result since, in the case of a single pattern speed, it has been shown that **1)** a massive self-gravitating spiral lies between the ILR and the UHR and **2)** in the presence of a bar which fixes the pattern speed, a perturbative (i.e. non self-gravitating) spiral structure lies between the corotation and the OLR. However, all these results have been obtained with the linear theory of density waves.

Since the original simulations of Sellwood (1985) and the theoretical explanations of Tagger et al. (1987) and Sygnet et al. (1988), the non-linear coupling of density waves has been recognized as an efficient coupling mechanism between large scale morphological features such as bars and spiral arms. In most cases of non-linear coupling reported so far, waves are coupled thanks to the coincidence of the bar corotation and the spiral ILR. The coupling of two $m = 2$ modes generates two beat waves of modes $m = 0$ and $m = 4$. It has been shown that such coincidence of resonances is the most efficient configuration for energy and momentum transfers because the beat waves also have a Lindblad resonance at the same radius. The coupling between a '+4 :1' resonance and corotation is not forbidden even if it seems to be a less favourable configuration. The theory of non-linear coupling allows however the existence of others kinds of coupling : Rautinainen & Salo (1999) reported a case of coupling between the bar corotation and the spiral ultra harmonic resonance (UHR or '-4 :1').

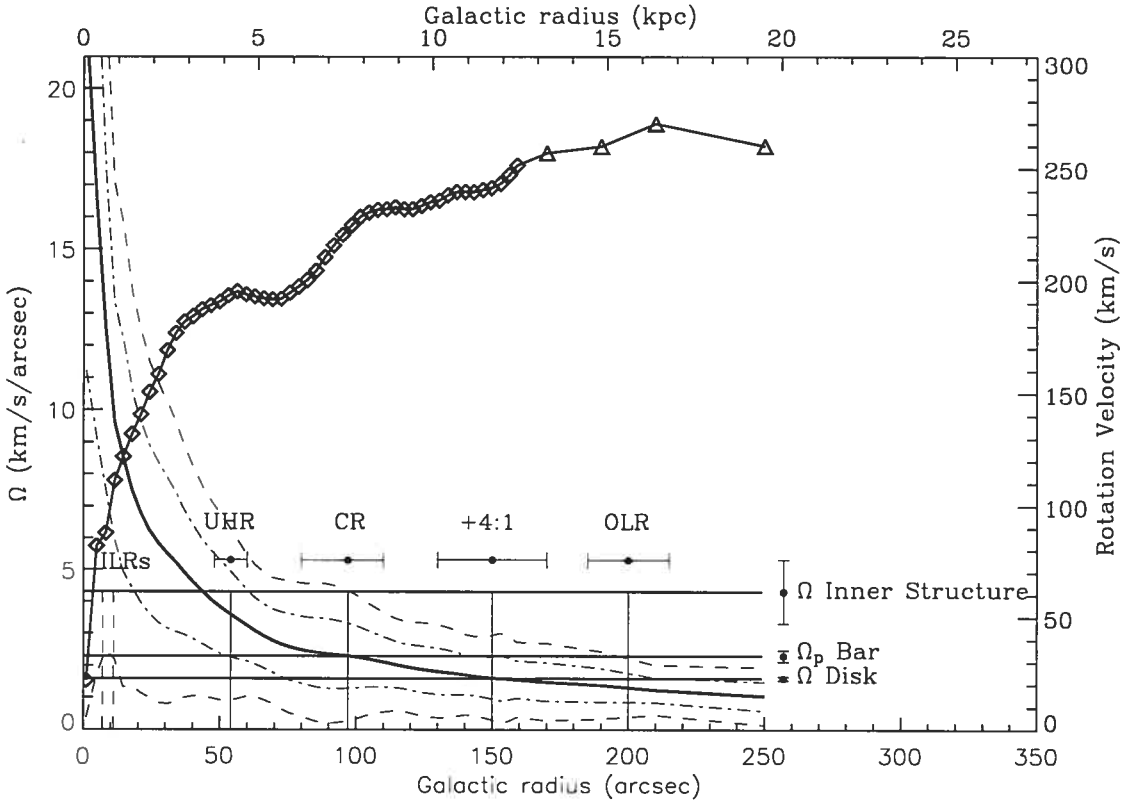

Fig. 54: M100. The rotation curve of the galaxy is drawn by the thin continuous line and the velocity scale is on the right of the plot. Hα data are represented by losanges and are used for galactic radii $\leq 159''$. HI data (Knapen et al. 1993) are represented by triangles and are only used for galactic radii $\geq 160''$, due to their poor spatial resolution ($\simeq$45"). The other curves are respectively, from the top upper to the bottom, the $\Omega + \kappa/2$ (dash), $\Omega + \kappa/4$ (dash-dot), Ω (thick continuous), $\Omega - \kappa/4$ (dash-dot) and $\Omega - \kappa/2$ (dash) curves. The expected positions of the bar resonances for Ω_P =2.3 km s^{-1} arcsec^{-1} are indicated by the vertical thin lines - surrounded by dark thick filled dots including error bars - respectively the two inner resonance ILR_1 (r= 0.9 kpc), ILR_2 (r=0.5 kpc) ; the UHR resonance (r=4.2 kpc) ; the corotation radius R_{CR} (r=7.4 kpc), the '+4 :1' resonance (r=11.3 kpc), and the OLR (r=15.22kpc). The values of Ωs for the 3 patterns are indicated on the right hand side of the figure, with the appropriate vertical error bars. See text for more details.

Table IX: Location of the resonance radii in *arcsec* for the bar. This study vs the literature scaled to our inclination and distance.

ref.	OLR	+4 : 1	**CR**	UHR	ILR1	ILR2
This study	200	150	97	54	11	7
[range in "]	[185 :205]	[130 :167]	[80 :110]	[48 :60]	n/a	n/a
Elmegreen et al. (1992)			118			
Elmegreen et al. (1989)	225	n/a	123	71	n/a	n/a
Canzian et al. (1993)			114-[101 :128]			
Canzian et al. (1997)			98-[88 :108]			
Sempere et al. (1995)			97-[82 :113]			
Garcia-Burillo et al. (1994)			110			

If we disregard the error on Ω^{IS} of the structure inside the circum-nuclear ring, we could be tempted to see another resonance overlap between the OLR of the nuclear structure and the bar corotation. This location is indeed associated with an abrupt change of the pitch angle of the spiral arms. However, the inaccurate location of the resonances due to the error on Ω^{IS} prevents us to draw any definite conclusion on a possible coupling.

Another noteworthy property must be emphasized : the three different pattern speeds could be related by $\Omega^{Sp} + \Omega_p^B \approx \Omega_p^{IS}$. The non-linear coupling of two density waves predict such a relationship between the two initial waves and the beat waves. But, in our case, the nuclear structure cannot be considered as a beat wave resulting from the interaction of the bar and the spiral structure since it has neither the right location nor the right azimuthal wave number m. Thus, a complete understanding of M100 certainly needs the development of a model based on the non-linear coupling of three density waves, which is outside the scope of this paper.

4.6 Conclusions.

High spectral and spatial resolution Hα monochromatic images and Hα velocity fields have been presented in order to study the multiple pattern speeds of M100 using the Tremaine-Weinberg method. At the same time, the TW method has been tested on various numerical simulations to test its relevance. The main conclusions are the following :

- The TW method can be applied to the gaseous velocity fields to get the bar pattern speed, under the condition that regions of shocks are avoided and mea-

Table X: M100 : Comparison of pattern speeds

Method	Spectral Range	Pattern Speed $\Omega_p^{(1)}$ ($km\,s^{-1}\ arcsec^{-1}$)	Pattern Speed $\Omega_p^{(2)}$ ($km\,s^{-1}\ kpc^{-1}$)	Ref.
TW[(a)] Nuclear Struct.	Hα	4.3±1.0	55±5	(b)
TW Bar	Hα	2.30±0.18	30.3±1.9	(b)
TW Spiral pattern	Hα	1.6±0.06	20.4±0.8	(b)
TW	CO	2.53	32.4	(c)
Canzian, 1993	Hα [(d)]	1.92	19.8	(d)
Resonance 4 :1	B&I-band	1.73	17.9	(e)
N-body[(f)]		1.92	19.8	(d)
SPH-Hydrodynamical		1.89	22.8	(g)
N-body simulation		3.36	40.5	(h)

(1) Scaled to our inclination of 31.7° ; (2) Scaled to our inclination of 31.7°**and** distance of 16.1 Mpc.

(a) Tremaine-Weinberg, 1984 ; (b) Present work ; (c) Rand and Wallin, 2004 ; (d) Sempere et al., 1995 ; (e) Elmegreen et al., 1989 ; (f) Combes & Gérin, 1985 ; (g) Wada et al., 1998 ; (h) Rand, 1995.

surements are confined to regions where the gaseous bar is well formed.

- The application of the TW method to gas velocity fields needs a careful selection of the region included in the $< V_{LOS,Y} >-< X_Y >$ fit.
- A living dark halo does not change significantly the results.
- When star formation is switched on, the TW method applied to the gaseous component is less accurate. The main source of error is the presence of strong and persistent gradients in the gaseous velocity fields.
- The TW method provides clear information about multiple pattern speeds.
- M100 has been analyzed using the TW method. Three pattern speeds are clearly seen and measured with a good precision compared to other studies. Errors on the PA and the inclination have been minimized due to the nature of the two dimensional velocity maps, improving the relevance of the results obtained for the three pattern speeds.
- Coupling between the '+4 :1' resonance of the bar and the corotation of the spiral is found and are in agreement with the theory of non linear coupling of spiral modes. The coupling is not forbidden even if it seems to be a less favourable

configuration. The theory of non-linear coupling allows however the existence of others kinds of coupling as reported by Rautinainen & Salo (1999).

- A restriction for a more accurate determination of the different radii and resonnaces comes from the intrinsic nature of M100. The central bar distorts the spiral arm structure and the corotation is not a narrow, but a relatively extended region.

Chapitre 5

Fréquences de rotation des barres des galaxies de *BHαBAR* en utilisant la méthode de Tremaine-Weinberg

The *BHαBAR* sample - III. Pattern speeds of barred spiral galaxies using the Tremaine-Weinberg method.

OLIVIER HERNANDEZ[a]

Département de physique and Observatoire du mont Mégantic, Université de Montréal, C.P. 6128, Succ. centre ville, Montréal, Québec, Canada. H3C 3J7 and

Observatoire de Marseille, 2 Place Le Verrier, F–13248 Marseille Cedex 04, France

CLAUDE CARIGNAN[a]

Département de physique and Observatoire du mont Mégantic, Université de Montréal, C.P. 6128, Succ. centre ville, Montréal, Québec, Canada. H3C 3J7

PHILIPPE AMRAM[a]

Observatoire Astronomique de Marseille Provence, Laboratoire d'Astrophysique de Marseille, 2 place Le Verrier, F-13248 Marseille Cedex 04, France

In preparation.

Abstract

The Tremaine-Weinberg (TW) method is applied to the 21 Hα velocity fields and monochromatic images of the *BHαBAR* sample in order to find the different pattern speeds of the galaxies studied. While the TW method is very robust when applied to the stellar component, it needs carefull attention with the selection of the "slits" used when applied to the gaseous component. Nevetheless, it has been successfully shown (Hernandez et al., 2005b) that this method could derive the correct pattern speeds of bar, disc and/or nuclear structure in a galaxy when using the Hα radial velocity map and its Hα monochromatic image. Thanks to the well distributed *BHαBAR* sample, a systematic study could be done. Including the data from other galaxies using the same method, an empirical relation is drawn between the bar pattern speed and the morphological type, stressing a clear decreasing trend of bar pattern speeds with increasing morphological type. Using the location of the resonance radii, another

[a]Visiting Astronomer, Canada–France–Hawaii Telescope, operated by the National Research Council of Canada, the Centre National de la Recherche Scientifique de France, and the University of Hawaii.

way to use the global information present in the three-dimensional data cubes provided by FANTOMM for the *BHαBAR* sample, is to derive, when possible, the velocity dispersion maps. A large study using our SPH/N-Body models must be done to understand all the features of the different curves obtained. However, resonances seem to be clearly identifiable on those '$\sigma(r)$ vs. r' curves.

Keywords : galaxies : individual — galaxies : kinematics and dynamics — galaxies : bar and spiral — methods : numerical — galaxies : fundamental parameters (masses) — galaxies : pattern speeds — galaxies : velocity dispersion— techniques : interferometric

5.1 Introduction

Since more than two thirds of the high surface brightness spiral galaxies are barred (e.g. Knapen, Shlosman & Peletier, 2000; Eskridge et al., 2000), the presence of this multiaxial structure must be analyzed to understand the secular evolution of galaxies. The fact that bars may contain a large mass fraction of the disk suggests that they are a fundamental component of the mass distribution in spiral galaxies. Since their kinematics is different from that of the more or less axisymmetric disk, it is important to model them properly to derive, as accurately as possible, the overall mass distribution. This is especially important, since bars are in the inner parts of disk systems, which is the region where the free parameters of the mass models are best constrained (Blais-Ouellette et al., 1999, 2004; Blais-Ouellette, Amram & Carignan, 2001). The parameters of mass models are not constrained by the flat part but by the rising part of rotation curves (RC).

The determination of the bar pattern speed (Ω_p^B) in spiral galaxies is one of the most important kinematical and dynamical parameters since it drives a large part of their evolution (e.g. Block et al., 2004). It is also essential for understanding the so-called dark matter problem and, more generally, the structure of spiral galaxy halos. Bar pattern speeds of spirals are determined by identifying theoretically predicted resonances (Lindblad resonances, corotation) with periodic motions of the stars and gas (extracted from the RC). The determination of bar pattern speeds relies on observational methods or, alternatively, in matching numerical models (N-body + SPH codes, see next section) to the observed velocity fields. A number of reviews describing these methods in detail can be found (e.g. Teuben, 2002).

Two methods, somewhat indirect, are based on the identification of morphological features associated with resonance radii (measuring the inner resonance '4:1', Elmegreen, Elmegreen & Montenegro, 1992 ; or alternatively, measuring the sign inversion of the radial streaming motions across corotation, Canzian, 1993). Theoretical evidence argues that the corotation radius lies just beyond the end of the bar (e.g. pioneer work of Contopoulos, 1980). Based on this result, many bar pattern speeds have been estimated (see a compilation in Elmegreen et al., 1996).

A more direct model independent method, not relying on any particular theory of density waves, is due to Tremaine & Weinberg (1984, hereafter TW). The pattern speed is determined from two observationally accessible quantities : the luminosity-weighted mean velocities and the luminosity-weighted mean densities throughout the disk of the galaxy. In the plane of the sky, X is the coordinate along the major axis of the galaxy, Y along the minor axis and V_{LOS}(X,Y) the line of sight velocity. $< X_Y >$ is the luminosity-weighted mean X-position integrated along a strip parallel to the X-axis at Y coordinate, $< V_{LOS,Y} >$ is the luminosity-weighted mean velocity along the X-axis at Y coordinate. Thus,

$$\Omega_p \sin i = \frac{\int_{-\infty}^{\infty} \Sigma(x,y,t) V_y(x,y,t)\, dx}{\int_{-\infty}^{\infty} \Sigma(x,y,t) x(y,t)\, dx} = \frac{< V_{LOS,Y} >}{< X_Y >}.$$

Many studies using the TW method have been done generally using long slit spectroscopy on the stellar component. The present study will focus only on the determination of the bar pattern speeds of spiral galaxies using 2D Fabry-Perot (FP) observations of the gaseous component.

Merrifield & Kuijken (1995) have applied, for the first time, the TW method to the SBO falaxy, NGC 936. Using stellar kinematics from long-slit spectra, they were able to determine the value of the pattern speed (Ω_p^B) of the bar for this galaxy. NGC 936 is at an ideal inclination of ~41°, and the bar lies at a position angle of ~45°. Five slits parallel to the major axis were used, providing five points for the $< V_{LOS,Y} >$-$< X_Y >$ fit. In order to minimize systematic errors due to uncertainties on the systemic velocity and kinematic center of the galaxy, their slits were chosen by pairs on both sides of the major axis. Gerssen et al. (1999) used the same technique on a second system, the SBa galaxy NGC 4596. They derived under the same hypothesis the pattern speed of the bar. The corotation, deduced from this method, just lies beyond the bar, indicating a fast bar. Using their data with high-resolution bar major-axis spectra from the Hubble Space Telescope, they were also able to detect evidence for a nuclear disc.

The bar pattern speed of the SBO galaxy NGC 1023 has been derived using the TW method (Debattista et al., 2002). This galaxy was chosen because it shows evidence of weak interaction in the past, without being, at present, significantly perturbed. The pattern speed found places the bar ends near the corotation radius. From those results, they argued that NGC 1023 is rapidly rotating and must have a maximum disc. They concluded that, if the disc had been stabilized by a massive dark matter halo and had formed the bar in the interaction, then the bar would have rotated slowly, which is not the case.

Corsini et al. (2003) pushed the analysis further with the direct determination of two patterns in the RSB0(r) galaxy NGC 2950. They proposed a modification of the TW formula decoupling the total surface brightness into two terms rotating with two different patterns. In these conditions, the $< V_{LOS,Y} >-< X_Y >$ fit is able to provide information of the two pattern speeds, one for the primary bar and the other for the nuclear bar. Since they suggested that the two bars cannot be in exact solid rotation, they concluded that the two bars of NGC 2950 must have different pattern speeds, with the secondary bar having a larger Ω_p^B .

More recently, large samples of early type barred galaxies were studied using the TW method applied to stellar (absorption line) kinematics and photometric observations. This is the case for five SBO type galaxies (ESO-139G009, IC 874, NGC 1308, NGC 1440 and NGC 3412, Aguerri et al. (2003)) and four other objects, with Hubble types ranging from SB0 to SBbc (Gerssen et al., 2003) (NGC 271, NGC 1358, ESO 281-31 and NGC 3992). In this study, the lack of slow bars is consistent and suggests that bars do not have centrally concentrated dark matter halos. This contradicts simulations of cosmological structure formation, which suggest *cuspy* central dark matter density profiles.

Fabry-Perot absorption-line spectroscopy of NGC 7079 (Debattista & Williams, 2004) provided the two-dimensional stellar kinematics. This was the first time 2D data were used with the TW method. This provided much more accuracy as the TW method is very dependent on the Position Angle (PA) of the disc (Debattista, 2003). They found a bar pattern speed with very small errors; this is the best constrained pattern speed ever measured for a bar using the TW method. Many more data points are also used to perform the $< V_{LOS,Y} >-< X_Y >$ fit in comparison to the traditional long slit spectrograms used before. Since the Fabry-Perot samples a large area on the sky, the determination and the subtraction of the background night sky spectrum can be performed with much better accuracy. However, the

use of a CCD camera is still a problem because of the difficulty to get constant photometric conditions over a long enough period. Exposure times need to be long enough with CCDs to beat down the read-out noise. The result is that the first and last channels are obtained in different sky conditions. Photon counting cameras such as FANTOMM which has no read-out noise, avoid this problem since they can scan through the channels very rapidly.

The power of the two dimensional velocity fields is also used with other tracers but special care must be taken with the fundamental hypothesis of the TW method : the tracer must satisfy the continuity equation. This is the case, for example, with CO observations where a total of nine galaxies were studied (Zimmer et al., 2004 and Rand & Wallin, 2004). Application of the method to the gaseous phase remains complicated especially because the tracer does not stricly obey the continuity equation. Nevertheless, Nbody + SPH simulations (Hernandez et al., 2005b and Rand & Wallin, 2004) show that the gas component can be used, under certain conditions, in order to apply the TW method.

Finally, Bureau et al. (1999) studied NGC 2915, a blue compact dwarf galaxy. Using the HI component, they derived a very low value for the pattern speed. However, it is not clear whether this pattern speed relates to the spiral pattern or to the bar. Table XI summarizes the **bar** pattern speeds derived for 19 galaxies using the TW method. Special attention is given to the bar pattern speeds in the present study, even if the spiral pattern could also be derived.

Section 2 will present the results obtained when applying to the TW method to the *BHαBAR* sample, giving also the locations of the resonances for 20 of the galaxies. Section 3 will compare the features of the velocity dispersion profiles to the locations of the resonances for 6 galaxies. Finally, section 4 will discuss those results and the conclusions will be given in section 5.

5.2 The TW method applied to the *BHαBAR* sample

The TW method has been applied to the gaseous component of simulated barred galaxies in order to demonstrate its validity and to understand its sensitivity to various observational parameters (Hernandez et al., 2005b). It has been successfully tested on M100 (NGC 4321) deriving its multiple pattern speeds.

Table XI: Published bar pattern speeds, in $\mathrm{km\,s^{-1}\,arcsec^{-1}}$.

Galaxy Name	Ω_p^B	Morphological type	Tracer used	Ref.
NGC 936	4.71±1.10	SB0	a	1
NGC 4596	3.89±0.97	SBa	a	2
NGC 1023	5.00±1.80	SB0	a	3
NGC 7079	8.40±0.20	SB0	b	4
ESO 139-G009	21.40±5.80	SB0	a	5
IC874	7.00 ± 2.40	SB0	a	5
NGC 1308	39.70±13.90	SB0	a	5
NGC 1440	7.40±1.70	SB0	a	5
NGC 3412	4.4±1.12	SB0	a	5
NGC 271	7.80±4.50	SBab	a	6
NGC 1358	9.33±4.50	SB0a	a	6
ESO 281-31	10.52±4.10	SB0	a	6
NGC 3992	5.72±0.35	SBbc	a	6
M83	1.09±0.19	SBc	c	7
NGC 6946	1.04±0.19	SAB(rs)cd	c	7
NGC 1068	5.23±0.35	SBb	c	8
NGC 3627	2.69±0.10	SBb	c	8
NGC 4826	7.11±2.20	SBab	c	8
NGC 2950	11.20±2.40	RSB0(r)	a	9

Tracer : a - Stellar absorption line kinematics from long-slit spectra, b - Stellar absorption line kinematics from Fabry-Perot, c - CO observations

References : 1 - Merrifield & Kuijken (1995), 2 - Gerssen et al. (1999), 3 - Debattista et al. (2002), 4 - Debattista & Williams (2004), 5 - Aguerri et al. (2003), 6 - Gerssen et al. (2003), 7 - Zimmer et al. (2004), 8 - Rand & Wallin (2004) and 9 - Corsini et al. (2003).

5.2.1 What about the gaseous component ?

The TW method was applied in an automated way with numerical simulations. Particle positions and velocities have been projected to an inclination of 45°. Particles have also been rotated so that the projected position-angle of the bar with respect to the line of nodes (PA_{bar}) lies between 30 and 50°. These are optimal values for a best estimate of Ω_p (Merrifield & Kuijken, 1995). For each component (stellar or gas particles), two (X,Y) frames were computed, one for the mass integrated along the LOS, another for V_{LOS}.

The mass-weighted line-of-sight velocity $< V_{LOS,Y} >$ and the mass-weighted position coordinate $< X_Y >$ are computed for each value of Y. Each Y position thus acts as a long slit. A linear fit between $< V_{LOS,Y} >$ and $< X_Y >$ is made using a robust least square algorithm. Since we exactly know the line-of-nodes position angle and the inclination angle, the slope determination of the $< V_{LOS,Y} >$ versus $< X_Y >$ relationship is the only source of error on Ω_p. Finally, two estimates of Ω_p were obtained, one for the stellar component Ω_p^s, the other for the gas component Ω_p^g.

First, the TW method has been tested on the stellar velocity field. Globally, the values of Ω_p^s were found to be very similar to those directly computed with the bar position-angle determined every Myr during the computation of the simulations. The TW is a very efficient tool to determine the bar pattern speed in numerical simulations.

The velocity field of the gaseous component was also used to compute Ω_p^s. Indeed, in the absence of strong shocks, the gas velocity field is close to the stellar velocity field, at least in the central region of the bar. Thus, on real data, it is mandatory to avoid including any region of strong shocks in the computation of $< V_{LOS,Y} >$. This bias can be removed by a careful selection of the regions where the LOS velocities and mass densities are measured. Indeed, a careful inspection of the projected mass density and velocity fields shows that the gaseous bar could be sometimes significantly shorter than the stellar bar. Since the automated TW method inconveniently selects some regions outside the gaseous bar, this leads to an underestimate of the bar pattern speed. Thus, the application of the TW method to observational gas velocity fields needs a careful selection of the region included in the $< V_{LOS,Y} >$-$< X_Y >$ fit.

The presence of a dark halo does not change significantly the results. As expected, the gravitational interaction made by a low mass dark halo does not change much the bar pattern speed. When star formation (SF) is switched on, the TW method applied to the

gaseous component is found to be less accurate. Indeed, Ω_p^g slightly overestimates the real bar pattern speed, especially when the star formation rate (SFR) is high. The reason for this behavior is indirectly linked to the SF process. Indeed, the main source of error is the presence of strong and persistent gradients in the gaseous velocity fields. These regions of high density are obviously the privileged sites of SF. Finally, when most of the gas has been consumed by SF, the gaseous velocity field tends to be like the stellar velocity field, leading to a better estimate of Ω.

The discrepancies between Ω_p^s and Ω_p^g remain within ± 10 $\mathrm{km\,s^{-1}\ kpc^{-1}}$. Thus the TW method can be applied to the gaseous velocity fields to get a good estimate of the bar pattern speed, under the condition that regions of shocks are avoided and measurements are confined to regions where the gaseous bar is well formed.

5.2.2 Sources of incertainty

The TW method is very sensitive to two sources of error : first, the regions of strong shocks must be avoided ; second, the Postion Angle of the disc (PA_{disc}) must be well determined.

Continuity equation

The TW method requires a tracer population that satisfies the continuity equation (no significant creation or destruction of matter over an orbit). It may be the case for the stellar population, even if, in reality, the continuity equation is never strictly satisfied because of the continuous SF. Nevertheless, old stars may survive many passages through the pattern. As long as the SF efficiency is low, conversion of gas into stars (and vice versa through winds and supernovae) can be ignored.

The equation of continuity for the ionized gas will never be satisfied on an orbital period and the Hα luminosity is not supposed to trace the mass. HII regions are bright ionized regions surrounding massive and hot newborn O and B stars. The OB stars have main-sequence lifetimes of only a few 10^6 years ; HII regions are furthermore short-lived gas clouds (which only exist during the lifetime of their ionizing OB stars) embedded in a star-forming region in a molecular cloud. A given HII region, associated to its parent stars, cannot survive to a typical galactic rotation of 10^8 years. However, HII regions and OB stars have

not enough time to wander far from their parent molecular cloud and are, if the expansion processes are neglected, a tracer of the molecular gas density.

Moreover, $< V_{LOS,Y} >$ determined from Hα, is as good a tracer as any of the galactic potential well (as is the case when deriving a RC). It is true to say that the application of the TW method to Hα may apparently violate several of the TW conditions. However, if one supposes that, to first order, the continuity equation is satisfied, but only for very short times ($\ll$ orbital period), neglecting the internal kinematics of HII regions and making the assumption that the luminosity-weighted mean X-position integrated along a strip parallel to the X-axis, $< X_Y >$ is a valuable indicator of the mean mass distribution.

Errors due to PA_{disc}

Debattista (2003) proposed a detailed study of the errors introduced in the TW method by uncertainties on PA_{disc}. If one considers a long-slit observation, the Y slit must be exactly parallel to the major axis (X axis). The results of the TW depend on the ability to find the correct orientation of the major axis and to place the slit parallel to it. For long slit spectra, careful surface photometry of target galaxies must be done to measure as accurately as possible PA_{disc}. Galaxies with inclinations in the range of $50 \leqslant i \leqslant 60$ are to be preferred since they are less sensitive to PA_{disc} errors. Furthermore, if the difference $PA_{disc}-PA_{bar}$ (PA of the bar) is $\sim 45°$, then the TW method will give optimal results.

Thus, according to Debattista (2003), galaxies with strong outer rings do not make good candidates for TW measurements because of the inherent uncertainty on PA_{disc} and should be avoided. In the case of two dimensional observations, especially with Hα observations made with FaNTOmM, where the spatial resolution is of the order of the seeing and where the spectral resolving power is typically around 50 000, the inherent uncertainty in PA_{disc} could be minimized. The robust analysis of the Hα velocity fields (Hernandez et al., 2005a) combined with an optimal adaptive binning (Daigle et al., 2005) provide the tools to extract the correct kinematical PA_{disc} using only the most axisymmetrical part of the velocity field.

5.2.3 Determination of multiple pattern speeds : bars and spiral

N-body studies have shown that pattern speeds of the bar and spiral arms can be different, the structures being either separate or in a non-linear mode coupling (Sellwood &

Sparke, 1988 ; Masset & Tagger, 1997 ; Rautiainen & Salo, 1999). The presence of two strong modes can induce cyclic evolution in the shape and orientation of the rings (Rautiainen & Salo, 2000 ; Rautiainen et al., 2002).

The TW method has been applied to the whole ***BHαBAR*** sample to derive as much information as possible from the $< V_{LOS,Y} >$-$< X_Y >$ fit. As for the case of M100 (Hernandez et al., 2005b), multiple pattern speeds are generally seen. Due to the nature of the Hα emission, it becomes difficult, for very early types, to have Hα within the center of the galaxy and the bar pattern speed determination becomes impossible. Also, when the $\mathrm{PA_{disc}}$ is nearly parallel or perpendicular to the PA of the bar, it is impossible to find Ω_p^B . In these two cases, strong incertainties remain either on $< V_{LOS,Y} >$ ($\mathrm{PA_{disc}}$ roughly parallel to $\mathrm{PA_{bar}}$) or on $< X_Y >$ ($\mathrm{PA_{disc}}$ roughly perpendicular to $\mathrm{PA_{bar}}$). This explains why only 12 Ω_p^B were derived for the whole ***BHαBAR*** sample. For the other galaxies Ω^{Sp} (spiral pattern speed) have been calculated. For six galaxies, both Ω^{Sp} and Ω_p^B were found. In two cases (NGC 4321 and NGC 2903), Ω^{IS} (pattern speed of the nuclear (or inner) structure) were also calculated. The values of the different pattern speeds are reported in Table XII.

5.2.4 Location of resonance radii

The location of the resonance radii were found using the approximation of the epicycles for the stars' orbits in a galaxy. $\Omega(r)$ is derived directly from the rotation curve :

$$\Omega(r) = V_{\mathrm{rot}}(r)/r \tag{5.1}$$

where r is the galactic radius. One must identify $V_{\mathrm{rot}}(r) \simeq V_{\mathrm{circ}}(r)$ to be able to derive the epicycle frequency κ given by the following formula :

$$\kappa^2(r) = \left[r\frac{d\Omega^2(r)}{dr} + 4\Omega^2(r) \right]_{(R,z=0)} \tag{5.2}$$

For the present study, only $\Omega - \kappa/2$, $\Omega + \kappa/2$ and Ω vs r were considered. In order to avoid rapid changes in the derivative of the $\Omega(r)$ function, gaussian smoothing was used for the data. The data points of the rotation curves near the galactic center were discarded since strong non-axisymmetric motions are often seen in this region.

The following figures (fig. 55 to 58) illustrate for 20[a] out of the 21 galaxies of the ***BHαBAR*** sample, the rotation curve (scale on the right hand side), the $\Omega(r)$ curve (scale on

[a]NGC 5964 was not studied using the TW because of the poor SNR and its $\mathrm{PA}_{bar} \perp \mathrm{PA}_{disc}$

Table XII: Bar pattern speeds (in $\mathrm{km\,s^{-1}\,arcsec^{-1}}$) of the *BHαBAR* sample from the TW method using Hα.

Galaxy Name	Type (RC3)	Ω_p^B	Ω^{Sp}	Ω^{IS}
NGC 0925	SAB(s)d	n/a	0.44±0.30	n/a
IC 342	SAB(rs)cd	n/a	0.54±0.02	n/a
NGC 1530	SB(rs)b	3.00±0.42	n/a	n/a
NGC 2336	SAB(r)bc	2.94±0.10	1.45±0.06	n/a
NGC 2403	SAB(s)cd	1.02±0.03	0.44±0.01	n/a
NGC 2903	SB(s)bc	1.72±0.20	n/a	3.91±0.4
NGC 3198	SB(rs)c	n/a	0.87±0.1	n/a
NGC 3359	SB(rs)c	1.8±0.08	n/a	n/a
NGC 3953	SB(r)bc	n/a	1.92±0.1	n/a
NGC 3992	SB(rs)bc	n/a	1.82±0.1	n/a
NGC 4236	SB(s)dm	0.21±0.01	n/a	n/a
NGC 4321	SAB(s)bc	2.3±0.18	1.6±0.06	4.3±1.0
NGC 4535	SAB(s)c	2.0±0.20	1.0±0.30	n/a
NGC 5371	SAB(rs)bc	n/a	2.67±0.10	n/a
NGC 5457	SAB(rs)cd	n/a	0.59±0.02	n/a
NGC 5921	SB(r)bc	n/a	1.87±0.10	n/a
NGC 6217	(R)SB(rs)bc	2.7±0.2	n/a	n/a
NGC 6946	SAB(rs)cd	1.23±0.03	0.54±0.04	n/a
NGC 7479	SB(s)c	1.61±0.10	n/a	n/a
NGC 7741	SB(s)cd	3.9±0.3	2.9±0.1	n/a

Table XIII: Inner structure, bar and/or spiral corotation radii in arcsec for the *BHαBAR* sample

Galaxy Name	CR_B (")	CR_{Sp} (")	CR_{IS} (")
NGC 0925	n/a	$289\pm^{21}_{19}$	n/a
IC 342	n/a	$350\pm^{40}_{60}$	n/a
NGC 1530	68±10	n/a	n/a
NGC 2336	78±6	$180\pm^{14}_{23}$	n/a
NGC 2403	74±6	345±45	n/a
NGC 2903	$122\pm^{18}_{13}$	n/a	23±4
NGC 3198	n/a	180±20	n/a
NGC 3359	$64\pm^{5}_{13}$	n/a	n/a
NGC 3953	n/a	$115\pm^{6}_{10}$	n/a
NGC 3992	n/a	152±15	n/a
NGC 4236	$330\pm^{10}_{20}$	n/a	n/a
NGC 4321	$97\pm^{8}_{17}$	150±20	42±20
NGC 4535	97±10	$250\pm^{??}_{60}$	n/a
NGC 5371	n/a	$90\pm^{6}_{10}$	n/a
NGC 5457	n/a	$330\pm^{20}_{30}$	n/a
NGC 5921	n/a	$64\pm^{6}_{10}$	n/a
NGC 6217	42±6	n/a	n/a
NGC 6946	112±6	$310\pm^{20}_{30}$	n/a
NGC 7479	63±6	82±5	n/a
NGC 7741	87±10	n/a	n/a

the left hand side), and the positions of the resonances. Lozenges indicate the high spatial and spectral resolution data points obtained with FANTOMM to determine the Hα rotation curve. In the case of five galaxies, the HI data were used to derive the curves at large radii. The upper dotted curve represents the $\Omega + \kappa/2$ and the lower curve represents $\Omega - \kappa/2$. The horizontal lines indicate the value of Ω_p^B and/or Ω^{Sp} and/or Ω^{IS} . The solid dots to the right show the exact value, surrounded by the vertical errors. Special radii (bar or spiral corotation radius) are indicated with solid dots surrounded by horizontal errors. Finally, the values of these resonances are reported in Table XIII.

5.3 Velocity dispersion maps

The second moment of the intensity-wavelength distribution was extracted from the data cube obtained with FANTOMM. More details on the complete data reduction can be

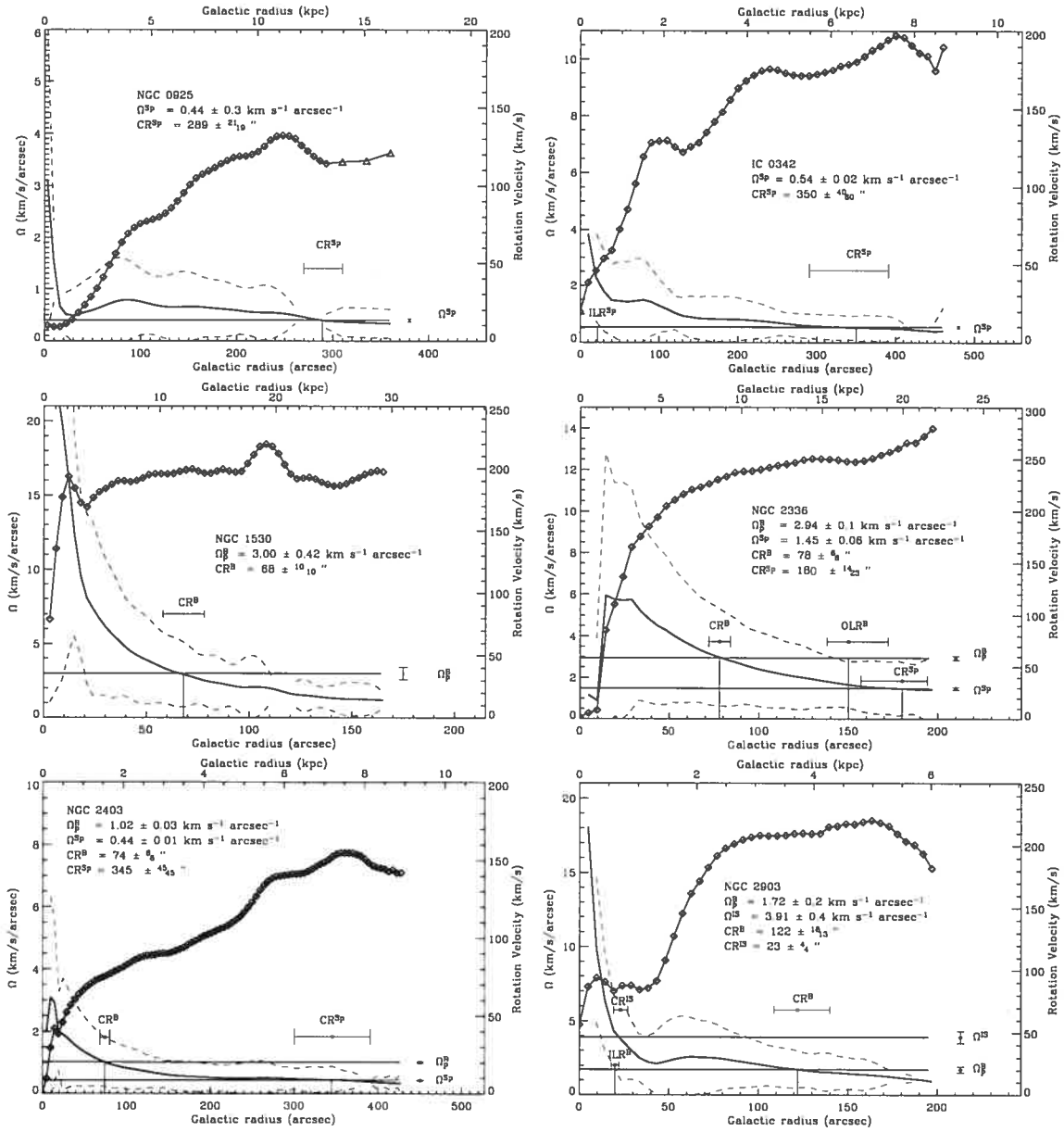

Fig. 55: Location of resonances for NGC 0925, IC 0342, NGC 1530, NGC 2336, NGC 2403 and NGC 2903. HI data for NGC 0925 from Elmegreen et al. (1998).

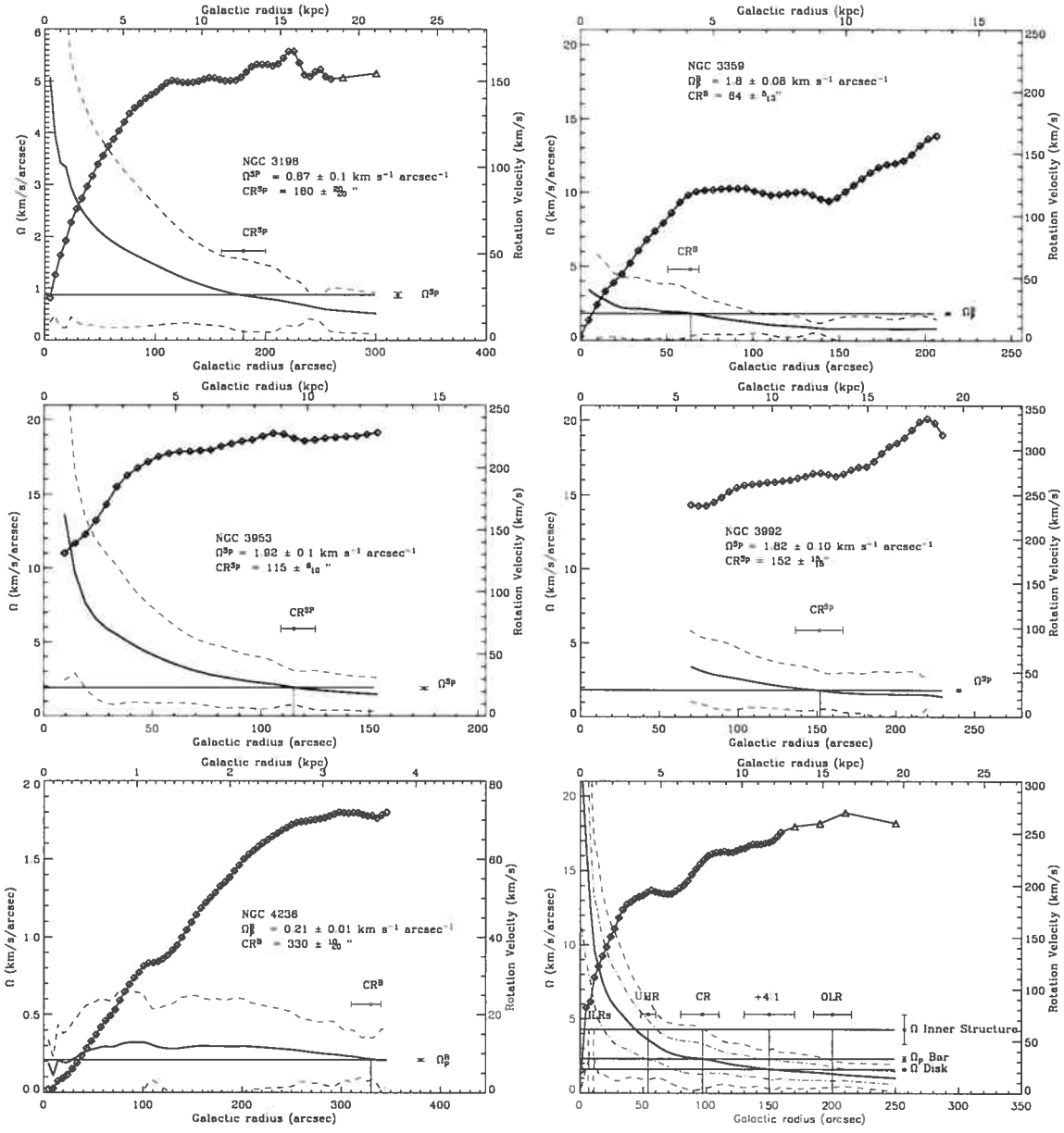

Fig. 56: Location of resonances for NGC 3198, NGC 3359, NGC 3953, NGC 3992, NGC 4236 and NGC 4321. HI data for NGC 3198 from Begeman (1989b) and for NGC 4321 from Knapen et al. (1993).

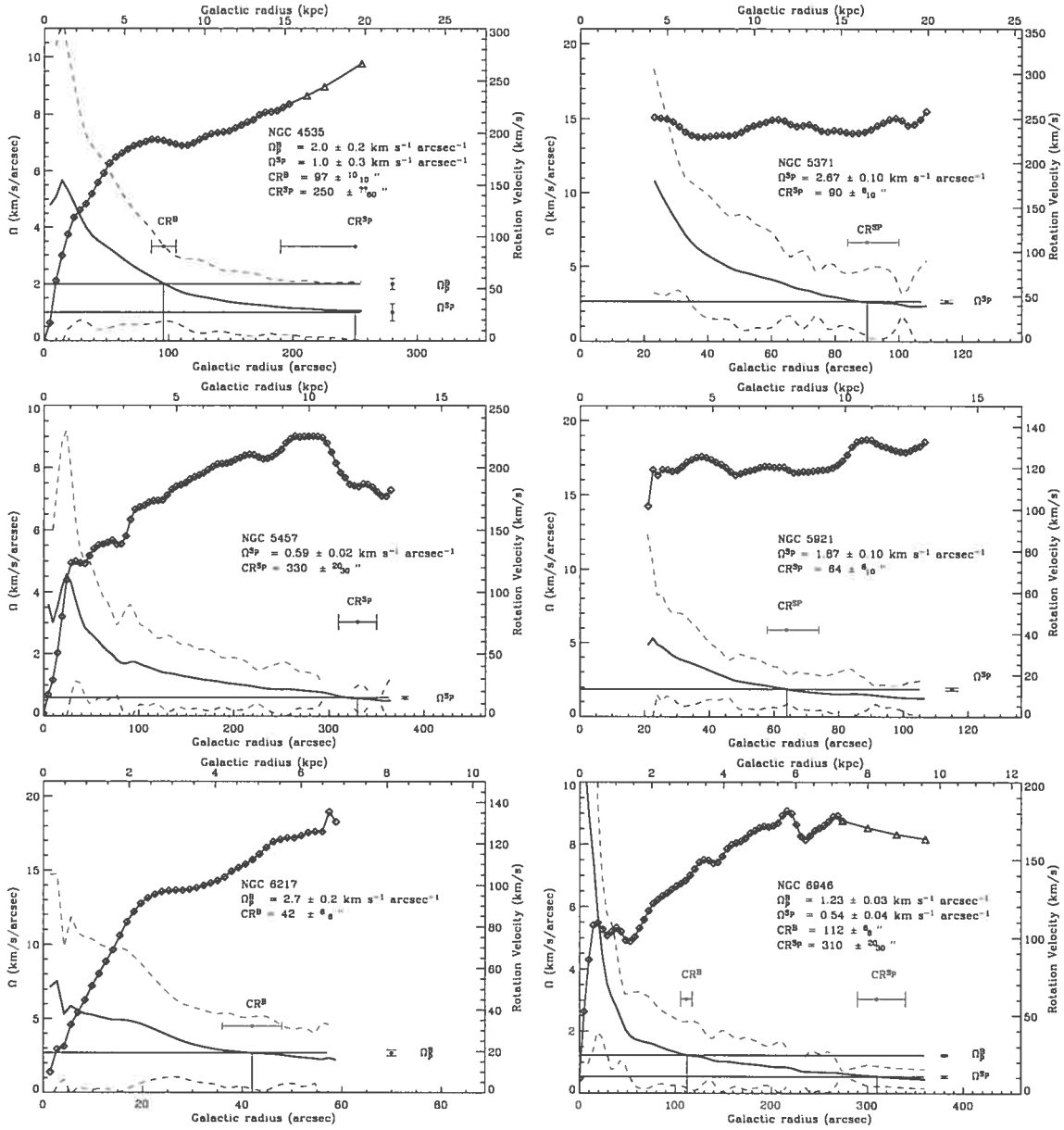

Fig. 57: Location of resonances for NGC 4535, NGC 5371, NGC 5457, NGC 5921, NGC 6217 and NGC 6946. HI data for NGC 4535 from Cayatte et al. (1990) and for NGC 6946 from Carignan et al. (1990).

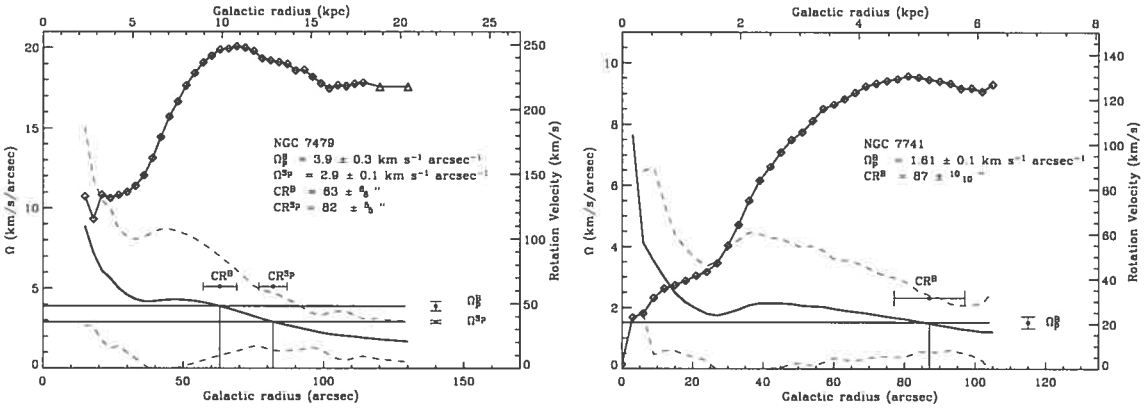

Fig. 58: Location of resonances for NGC 7479 and NGC 7741. HI data for NGC 7479 from Laine & Gottesman (1998).

found in Hernandez et al. (2005a). This second moment represents the velocity dispersion of the Hα emission line. Many effects must be taken into account to derive, from the second moment, the exact dispersion due to the turbulent (non-thermal) motions of the Hα gas.

Part of the dispersion is due to the internal motions within an HII region. It was thus necessary to correct the observed dispersion $\sigma_{\rm obs}(r)$ for the effects of natural line broadening, thermal broadening, and broadening due to the instrumental function, in order to obtain the kinematical, non-thermal broadening $\sigma_{\rm nt}(r)$. The expression used is :

$$\sigma_{\rm obs}(r)^2 = \sigma_N(r)^2 + \sigma_{\rm Ins}(r)^2 + \sigma_{\rm nt}(r)^2 + \sigma_t(r)^2,$$

where $\sigma_N(r)$ is the natural broadening, $\sigma_{\rm Ins}(r)$ the instrumental contribution, $\sigma_{\rm nt}(r)$ the non-thermal contribution and $\sigma_{\rm t}(r)$ the thermal contribution (Zurita et al., 2004).

The natural broadening is essentially a constant for hydrogen and takes the value 0.16Å, which corresponds to $3\,{\rm km\,s^{-1}}$ (O'Dell & Townsley, 1988). The instrumental width comes directly from the analysis of the calibration lines emitted by the Ne lamp at 6598Å, which was used to produce the data cube for the wavelength calibrations. The result of a careful analysis of the calibration cube showed that it contained no systematic structures due to calibration problems and that the instrumental dispersion map showed a constant value for a fixed etalon at a fixed Finesse (resolution). Depending on the FP etalon and the Finesse, the instrumental $\sigma_{\rm Ins}(r)$ varies from 12 to 23 $\rm km\,s^{-1}$. Computing a value for $\sigma_(r)$ is standard procedure, since this is just the Doppler broadening of the emission line from the ionized region. The Doppler broadening of HII regions at a temperature of 10 000 K, leads

to the corresponding value of $9.1\,\mathrm{km\,s^{-1}}$ (Osterbrock, 1989). For simplicity, a global value of $10\,\mathrm{km\,s^{-1}}$ was chosen for the six galaxies selected from the *BHαBAR* sample.

In order to analyse the velocity dispersion due to the gas flow along the bar, a mean was calculated in a sector, centered at the kinematical center with a free angle of 30°, and aligned with the Position Angle of the bar (see Hernandez et al. 2005a for more details on bar PAs). Figure 59 presents the results. The dots represent the mean at each point of the sector for each side (receding and approaching). The vertical continuous lines represent the location of the resonance of the bar pattern derived from the TW method. The green line is the corotation radius surrounded by two dotted lines representing the errors associated. The red line is the position of the outer Linblad resonance (OLR). The blue line is the deprojected bar lengths (Martin, 1995 and Hernandez et al., 2005a). For NGC 2903, the inner structure corotation has been indicated in orange.

First, strong asymmetries can be seen in the six diagrams. The most symmetrical $\sigma(r)$ curve is found for NGC 6946 apart from a bump at the radius r=−170" that is due to a large HII region in the disc. Globally the bar Outer Linblad Resonance (OLR) corresponds to a local maximum. This is the case for NGC 1530, the right side of NGC 2336, NGC 2903, NGC 3359. This feature is not obvious for NGC 4321 and NGC 6946. Second, the corotation radii are located within local maxima or minima, except for NGC 1530. The bar radii, also, correspond to an important feature in the $\sigma_(r)$ curve, but once again, NGC 1530 does not follow this trend. Finally the inner structure corotation radius of NGC 2903 corresponds to the maximum velocity dispersion.

Athanassoula (2003) showed that the bar pattern speed is difficult to be used as an argument for either high or low halo-to-disc mass ratios : when the halo or disc-velocity dispersion is increased, the bar slowdown rate also decreases. The relation between $\sigma(r)$ and the resonances could help to determine the halo-to-disc mass ratios. Trends can be seen on the several plots but N-Body coupled to SPH models may help us to understand these correlations.

5.4 Forthcoming Comparisons with Simulations.

The gas responds strongly to non-axisymmetries in a gravitational field. Thus, more than two decades ago, the gas was recognized as a sensitive tracer of galactic potentials. A

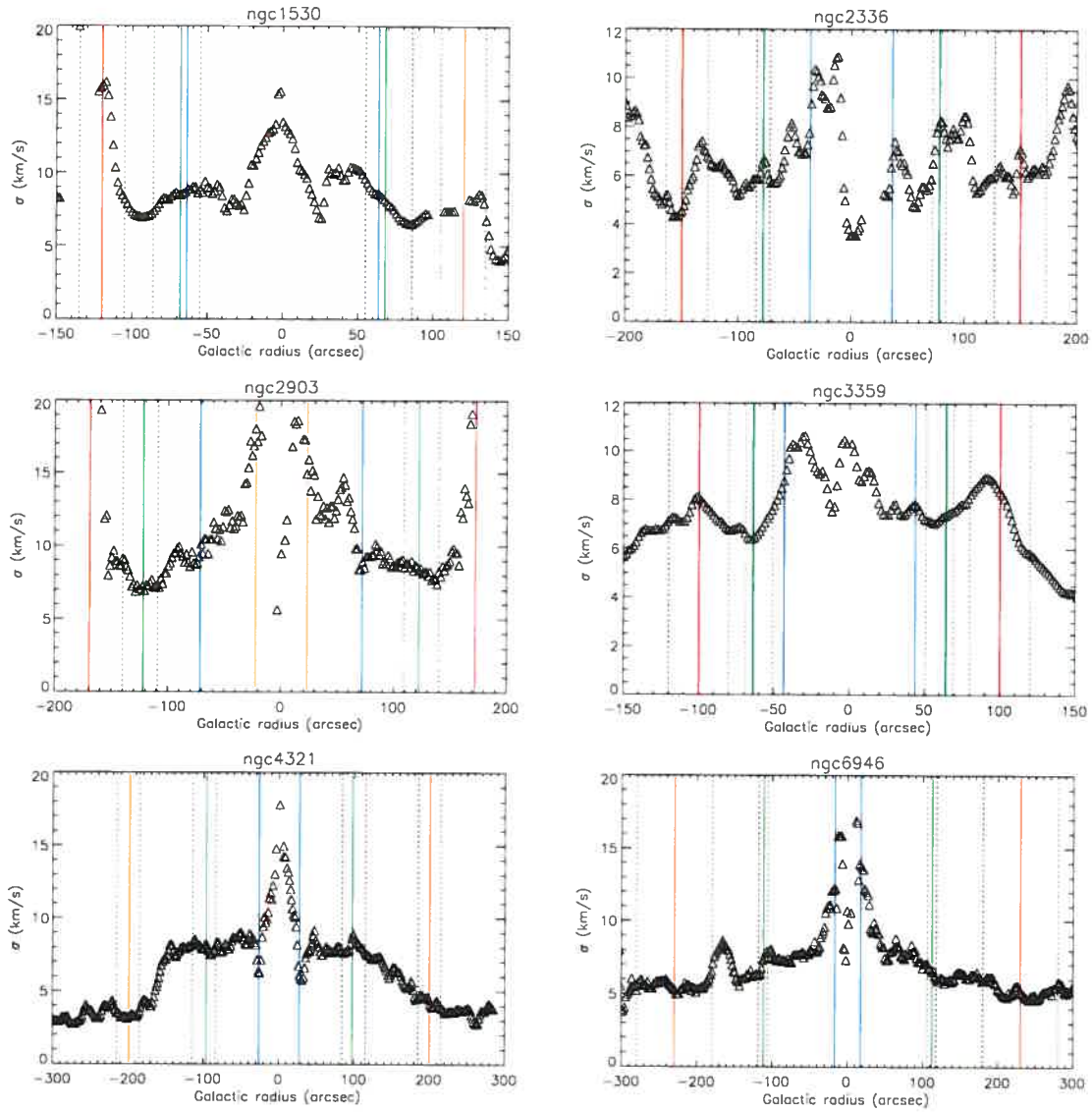

Fig. 59: Velocity dispersions as a function of the radius. The dots represent the mean at each point of the sector for each side of the galaxies. The vertical continuous lines represent the location of the resonance of the bar pattern derived from the TW method. The green line is the corotation radius surrounded by two dotted lines representing the errors associated. The red line is the position of the outer Linblad resonance (OLR). The blue line is the deprojected bar length.

model for such a potential can be tested by simulating the gas flow within the potential, and comparing the resulting morphology and kinematics to observations. The earliest efforts to apply such a method used general forms for the potential derived either from N-body simulations (Huntley, 1978) or from analytic considerations (Sanders & Tubbs, 1980). Subsequent efforts to constrain disc galaxy potentials via hydrodynamical simulations have focused on deriving galactic potentials from specific galaxies rather than assuming a general form for the potential (England, 1989 ; Garcia-Burillo, Combes & Gerin, 1993 ; Sempere et al., 1995 ; Sempere, Combes & Casoli, 1995 ; Lindblad, Lindblad & Athanassoula, 1996 ; Lindblad & Kristen, 1996 ; Sempere & Rozas, 1997). In barred galaxies, where gas motion in the inner region is strongly non-circular, Weiner, Sellwood & Williams (2001), Kranz et al. (2001, 2003), Slyz et al. (2004) argued that model fits to the observed velocity fields could unequivocally differentiate between maximal and submaximal discs.

In addition to those already cited in the previous paragraph, numerous specific studies exist in the literature comparing simulations to observations : Rautiainen et al. (2004) determined the gravitational potential using NIR photometry and the gas dynamics by inelastically colliding particles. Block et al. (2004) obtained deep near-infrared images of 15 nearby spiral galaxies having a range of Hubble types and apparent bar strengths and converted them into gravitational potentials to estimate the maximum relative gravitational torques due to the bars and the spirals. Wilke et al. (1999) paid special attention at matching the simulations to the observed gaseous velocity fields. Cepa & Beckman (1990) restrict themselves to the arm/interarm comparison and did not examine self-consistent models with respect to the observed gas velocity field. Hunter et al. (1988) used hydrodynamic SPH models. Kaufmann & Contopoulos (1996) put special emphasis on a good reproduction of the spiral arms and not so much on the kinematics of the regions within the CR. Sempere et al. (1995) evaluated non-self-gravitating models for the molecular gas component which are based on CO data. Laine et al. (1998) used a tree SPH code, where the potential is based on NIR images and put special emphasis on a good fit of the dust lane structure along the bar and the form and pitch angle of the spiral arms. They encountered problems for fitting the model kinematics to the observations.

Using the same framework, our plan is to construct (three-dimensional) morphological and kinematical models for the whole *BHαBAR* sample from the observed NIR surface brightness distributions. The aim is to explain the Hα 2D gaseous velocity fields of the different type of galaxies, especially in the regions dominated by the non-axisymmetric bar

potential component. Two major factors affecting the simulated morphology and kinematics are the strength of the non-axisymmetric perturbation and the pattern speed of the bar (Rautiainen et al., 2004), provided here by the TW method.

Three components (bulge, bar, disk) will be determined from the stellar mass distribution and a weak realistic dark halo component will be added. The disk will be modelled by an exponential Freeman distribution, the bulge by generalized Hernquist functions (Dehnen, 1993) and the non-axisymmetric component will be computed by deriving the potential from NIR images. The resulting potentials will be implemented numerically in GADGET. The gas clouds will serve as test particles in the potential and be used for the examination of the construction of simulated gas rotation curves. The model parameters of bulge disk bar and halo will br adjusted by iteractively computing and evaluating a number of different models until an optimal fit will be obtained that reproduces well the observations. The parameters will be adjusted to minimize the residuals remaining after the subtraction of the model from the observed luminosity distribution. Then, the simulated rotation curves will be compared to the observed Hα rotation curves.

Weinberg (1985) studied the dynamical friction between bar and halo analytically and by a semi-restricted N-body simulation, and found that it causes the bar to loose most of its angular momentum in just a few bar rotations. Little & Carlberg (1991) studied bar slowdown by self-gravitating N-body models where both the disc and halo were two-dimensional. The bar deceleration in their model was considerably lower, only by a factor of 2 during 10 Gyr, half of which was due to the interaction with the outer disc. Alternatively, Hernquist & Weinberg (1992) who used an analytical bar with a self-gravitating halo, found a high slowdown rate. Interaction between the bar and the dark halo can introduce bar slowdown that cannot be compensated by bar growth. This is also in accordance with estimates of the disc mass contribution by dynamical modeling (e.g. Weiner, Sellwood & Williams, 2001), but disagrees with cold dark matter cosmological N-body simulations which produce cuspy haloes (e.g. Navarro, Frenk & White, 1996).

Finally, this kind of approach has been used by Pérez et al. (2004). However, our study will differ in two major aspects. First, their comparison was relative to a small sample, whereas *BHαBAR* is homogeneous and well distributed over the Hubble sequence. Second, they only used long-slit data, whereas Hα velocity fields and Hα monochromatic images will be used to provide more accurate results avoiding, for example, the uncertainties on *P.A.* and

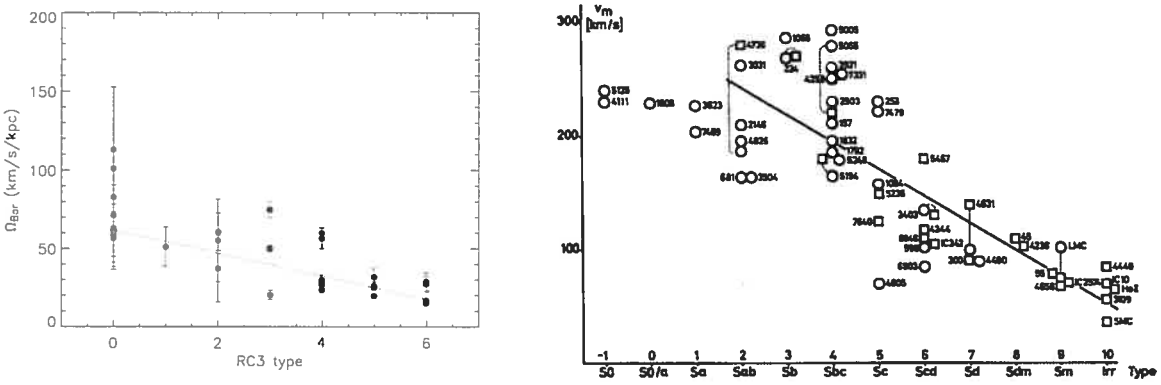

Fig. 60: **Left :** Bar pattern speeds as a function of the morphological type; the blue dots come from this study. **Right :** maximum rotational velocity $V_{\max}$ vs. morphological type (Brosche, 1971)

i present in 1D data.

Moreover, a moderate halo component will be included. Indeed, from the comparison done between modeled (Athanassoula & Misiriotis, 2002) and observed velocity fields (Hernandez et al., 2005a), a dominating halo can be ruled out. Similar conclusions can be found in the literature, e.g. by Rautiainen et al. (2004) studying carefully two barred galaxies (included in the *BHαBAR* sample). Thus, the contribution of the luminous matter dominates the rotation curve inside the whole region of the optical disc.

5.5 Discussion and Conclusions.

The TW method allowed to determine multiple pattern speeds for 20 out of the 21 galaxies in the *BHαBAR* sample. The richness of the sample provides means to study the evolution of the bar pattern speeds in correlation with many parameters. This study only stresses the morphological type dependence of the Ω_p^{Bar}. The left part of figure 60 is a mix between published data and Hα data. Red dots are data obtained with the TW method using CO velocity maps. Green dots are data obtained from stellar kinematics and photometry, and blue dots come from this study. The black dot represents the galaxy NGC 7079 done with FP in absorption.

The agreement between the CO and the Hα data is very good. The errors on the parameters derived from the gaseous components are much smaller than on those derived

using the stellar kinematics. This is mainly due to the incorrect determination of the PA of the galaxy studied and to the width of the absorption profile. The error position of the slit must be taken into account in the source of errors and a misalignment occurs frequently. This is not the case with CO and especially with Hα data because the determination of the PA and the inclination is much more accurate in 2D fields.

The mean results of this study can be summarize as follows :

- The TW method is a powerful tool to measure patterns in spiral galaxies.
- The TW method can be applied to Hα emission velocity and monochromatic maps under special conditions.
- The TW method can clearly indicate if multiple pattern speeds are present.
- The high Signal to Noise Ratio and the robustness of the Hα velocity and monochromatic maps obtained from FP help to minimize the systematic errors from long slit spectroscopy (PA errors, uncertainty on the systemic velocity, slit parallelism with respect to the major axis....)
- The location of resonance radii has been derived for 20 of the 21 galaxies of the *BHαBAR* sample. The information has been used to check if there is a correlation between a feature of the $\sigma(r)$ curve and the location of a resonance. The results are not obvious even if, near a resonance radius, the global form of the $\sigma(r)$ curve changes.
- Finally, a global relation is drawn between Ω_p^B and the morphological type in full agreement with previous studies of the maximum of the radial velocities.

Conclusion

La plus sensible caméra à comptage de photons couplée à un interféromètre de Fabry-Perot constituent maintenant FANTOMM, un des meilleurs instruments au monde pour l'étude du gaz ionisé Hα dans les galaxies spirales proches. Cette thèse a permis l'amélioration de cet instrument et son utilisation. Pas moins de 30 missions ont utilisé à ce jour cette caméra.

Les données tridimensionnelles des galaxies de *BHαBAR*, issues des observations avec FANTOMM, constituent un échantillon de galaxies spirales barrées homogène. Ces données ont été analysées rigoureusement avec une méthodologie robuste et reproductible. Un nouveau lissage adaptatif révolutionnaire a été développé pour obtenir un rapport signal sur bruit uniforme sur tout le champ de vue. Des champs de vitesses et des images monochromatiques Hα ont été produits pour toutes les galaxies de l'échantillon. La signature de la barre est visible dans les champs résiduels et les diagrammes Position-Vitesse (PV) qui révèlent, pour la plupart des galaxies de *BHαBAR*, de fortes non-axisymétries.

Les angles de position (PA) et les inclinaisons des disques des galaxies ont été calculés avec une très grande précision. Les paramètres cinématiques ont été déterminés par des modèles "tilted-ring" en ne tenant compte que de la partie axisymétrique du disque pour éviter toute contamination par des mouvements non circulaires dus à la barre (parties centrales) ou au gauchissement du plan (parties externes des disques). L'analyse de l'échantillon a montré que les PAs et les inclinaisons cinématiques et photométriques sont globalement en accord, sauf pour les galaxies de type tardif.

D'autre part, les champs de vitesses des données FP se distinguent des observations longues fentes car ils ont permis de mettre en évidence le décallage qu'il existe entre le centre photométrique et le centre cinématique des spirales barrées. Enfin, une première analyse des champs de vitesses a montré que les halos de matière sombre semblent être plutôt moins

concentrés que très concentrés dans les parties centrales des spirales barrées.

La méthode de Tremaine-Weinberg (TW), qui permet le calcul direct de la fréquence de rotation des barres à l'aide d'observations cinématiques et photométriques, a été ensuite testée et confrontée aux données Hα. D'abord, sous forme de modèles numériques de type SPH et N-Corps, la méthode de TW a pu être appliquée à du gaz sous certaines conditions : (a) que les régions de chocs soient évitées, (b) que les mesures soient effectuées dans les régions où la barre est bien formée et (c) qu'une sélection rigoureuse et précise des points de mesure soit effectuée. Les simulations numériques ont aussi montré que l'addition d'un halo de matière non lumineuse ne changeait pas le résultat des mesures. Enfin, les mesures doivent absolument éviter les régions d'intense formation d'étoiles, la source principale d'erreurs étant principalement les régions de fort gradient de vitesses dans les champs de vitesses associés au gaz.

Par la suite, M100 a été étudiée dans le but de trouver la fréquence de rotation de la barre en appliquant la méthode de TW. Le succès fut total car la méthode a permis d'avoir accès aux fréquences de rotation des trois ondes présentes dans la galaxie (structure nucléaire, barre & structure spirale). De plus, la méthode a permis de mettre en évidence des couplages entre les résonances associées à chacune de ondes comme prédit par la théorie non-linéaire de couplage.

Cette méthode a donc été répétée et appliquée à toute les galaxies de l'échantillon. Les positions des résonances associées à la barre et à la spirale des galaxies ont été trouvées. Ces données ont permis de tracer l'évolution de la fréquence de rotation des barres en fonction du type morphologique des galaxies. La relation déduite est en parfait accord avec la tendance attendue. La décroissance de la fréquence de rotation de la barre en fonction du type morphologique va, en effet, dans le même sens que celle de la vitesse de rotation maximum. Enfin, une étude sur la dispersion des vitesses $\sigma(r)$, le long des barres, permet de mettre en évidence que les résonances correspondent à des extrema remarquables dans les courbes '$\sigma(r)$ vs r'.

Cette thèse se veut donc le point de départ de plusieurs projets tant instrumentaux, observationnels que théoriques.

Instrumentation. Même si FANTOMM est la caméra la plus sensible, elle a été dévelopée pour des télescopes de diamètre 2 à 4 m. L'avènement des grands télescopes (diamètre $\geqslant$ 8 m) nécessite de dépenser le maximum d'effort pour la recherche dans les domaines

suivants :

- Caméra L3CCD : les L3CCDs (pour Low Light Level CCD), sont des CCDs dont l'amplification se fait après la conversion du photon en électron. Elles sont en développement actuellement au LAE et au LAM et offriront la possibilité de comptage de photons à des efficacités quantiques proches de 90% et avec une plage dynamique beaucoup plus grande que les tubes amplificateurs.
- Nouveaux Tubes AsGa. Les développements dans ce domaine suggèrent que l'efficacité quantique (point faible de ces systèmes) doit augmenter avec les nouveaux modèles. La taille physique du pixel doit diminuer et la taille totale (champ de vue) doit augmenter.
- Design et conception de nouveaux revêtements de haute reflexion pour obtenir des étalons FP de meilleure qualité, plus adaptés au domaine scientifique recherché.
- Développement de nouvelles technologies pour le contrôle des FP.
- Mise en place de FP ajustables (filtres accordables).

Observation. Les observations et leur analyse constituent la base fondamentale pour la compréhension des phénomènes physiques. Il est donc important d'avoir les meilleures observations possibles et que leur analyse soit la plus fine possible. Cela passe par :

- la mise en place de la technique FP en absorption à l'OmM, pour une validation supplémentaire de la méthode TW. Comparaison possible entre les champs de vitesses stellaires et gazeux.
- la décomposition en composante de Fourier (Schoenmakers et al., 1997) des champs de vitesses 2D
- la décomposition multiple en gaussiennes des profils doubles, triples des champs de vitesses 2D
- l'analyse de la dispersion des vitesses
- la mise en place d'étude bidimensionnelle donc de diagrammes de type θ vs R de la vitesse de rotation, de la dispersion des vitesses...
- la prise en compte des vitesses d'expansion et des vitesses dans le plan z comme composante de la vitesse observée.

Simulations numériques. Les simulations numériques 3D N-Body/SPH avec GADGET vont servir à mieux comprendre les observations et cerner la problématique des mouvements non circulaires. Trois grandes étapes sont prévues :

- Étape 1 : comprendre les mouvements non circulaires et reproduire les champs 2D issus des observations dans toutes sortes de configuration (ligne de visée, PA et inclinaison diverses et variées). Construction des courbes de rotation uniquement à partir de la partie axisymétrique. Enfin, cela passe par une bonne connaissance des images IR pour la détermination du potentiel de la barre et de la minimisation des paramètres libres, comme le Ω_p^B par exemple.
- Étape 2 : construire une grille de correction des courbes de rotation en fonction de paramètres de la galaxie, i.e., type morphologique, luminosité, masse, etc...
- Étape 3 : étudier les profils de dispersion des vitesses et les comparer aux observations.

Modélisation de masse. Enfin, le but ultime est de déterminer la masse des galaxies spirales. Ce projet se décomposera suivants deux grands axes principaux :

- la modélisation de la masse via la vitesse circulaire corrigée des mouvements non-axisymétriques sur la grille précédemment définie. Il conviendra alors de tester différents modèles de halo et de vérifier l'hypothèse de disque maximum.
- le développement de modèles de masse en deux (trois) dimensions afin d'utiliser directement les champs de vitesses 2D.

Nous avons maintenant les clés pour comprendre beaucoup de problèmes physiques liés aux galaxies spirales. À nous de nous en servir correctement pour tenter de mieux élucider les mystères de notre Univers.

Références

Aguerri, J. A. L., Debattista, V. P., & Corsini, E. M. 2003, MNRAS, 338, 465

Amram, P. 1991, PhD thesis, Université de Provence

Amram, P. & Östlin, G. 2001, The Messenger, 103, 31

Amram, P., Le Coarer, E., Marcelin, M., Balkowski, C., Sullivan, W. T., I., & Cayatte, V. 1992, A&AS, 94, 175

Amram, P., Mendes de Oliveira, C., Boulesteix, J., & Balkowski, C. 1998, A&A, 330, 881

Arsenault, R., Roy, J.-R., & Boulesteix, J. 1990, A&A, 234, 23

Artamonov, B. P., Badan, Y. Y., Bruyevich, V. V., & Gusev, A. S. 1999, Astronomy Reports, 43, 377

Athanassoula, E. 1992a, MNRAS, 259, 328

—. 1992b, MNRAS, 259, 345

Athanassoula, E. 2003, in Revista Mexicana de Astronomia y Astrofisica Conference Series, 28–29

Athanassoula, E., Fady, E., Lambert, J. C., & Bosma, A. 2000, MNRAS, 314, 475

Athanassoula, E. & Misiriotis, A. 2002, MNRAS, 330, 35

Atherton, P. D., Taylor, K., Pike, C. D., Harmer, C. F. W., Parker, N. M., & Hook, R. N. 1982, MNRAS, 201, 661

Ball, R. 1986, ApJ, 307, 453

Barnes, J. & Hut, P. 1986, Nature, 324, 446

Bates, B., Bradley, D. J., Kohno, T., & Yates, H. W. 1966, Journal of Scientific Instruments, 43, 476

Begeman, K. G. 1987, Ph.D. Thesis

—. 1989a, A&A, 223, 47

—. 1989b, A&A, 223, 47

Binney, J. & Tremaine, S. 1987, Galactic dynamics (Princeton, NJ, Princeton University Press, 1987, 747 p.)

Blais-Ouellette, S. 2000, Ph.D. Thesis

Blais-Ouellette, S., Amram, P., & Carignan, C. 2001, AJ, 121, 1952

Blais-Ouellette, S., Amram, P., Carignan, C., & Swaters, R. 2004, A&A, 420, 147

Blais-Ouellette, S., Carignan, C., Amram, P., & Côté, S. 1999a, AJ, 118, 2123

Blais-Ouellette, S., Carignan, C., Amram, P., & Côté, S. 1999b, AJ, 118, 2123

Bland, J. & Tully, R. B. 1989a, AJ, 98, 723

—. 1989b, AJ, 98, 723

Blazit, A. 1985, in ESA SP-226 : Kilometric Optical Arrays in Space, 155–156

Blazit, A., Bonneau, D., Koechlin, L., & Labeyrie, A. 1977, ApJL, 214, L79

Block, D. L., Bournaud, F., Combes, F., Puerari, I., & Buta, R. 2002, A&A, 394, L35

Block, D. L., Buta, R., Knapen, J. H., Elmegreen, D. M., Elmegreen, B. G., & Puerari, I. 2004, AJ, 128, 183

Boksenberg, A. 1977, in IAU Colloq. 40 : Astronomical Applications of Image Detectors with Linear Response, 13

Bosma, A. 1981a, AJ, 86, 1791

—. 1981b, AJ, 86, 1825

Bottema, R. & Verheijen, M. A. W. 2002, A&A, 388, 793

Boulesteix, J. 2004, www.oamp.fr/interferometrie/adhoc.html

Boulesteix, J., Georgelin, Y., Marcelin, M., & Monnet, G. 1984, in Instrumentation in astronomy V; Proceedings of the Fifth Meeting, London, England, September 7-9, 1983 (A85-25360 10-89). Bellingham, WA, SPIE - The International Society for Optical Engineering, 1984, p. 37-41. Research supported by the Institut National d'Astronomie et de Geophysique., 37–41

Boulesteix, J. & Marcelin, M. 1980, in Two Dimensional Photometry, 119

Bournaud, F. & Combes, F. 2002, A&A, 392, 83

Brosche, P. 1971, A&A, 13, 293

Bureau, M. & Freeman, K. C. 1999, AJ, 118, 126

Bureau, M., Freeman, K. C., Pfitzner, D. W., & Meurer, G. R. 1999, AJ, 118, 2158

Buta, R. 1986, ApJS, 61, 609

—. 1995, ApJS, 96, 39

Buta, R. & Combes, F. 1996, Fundamentals of Cosmic Physics, 17, 95

Buta, R. & Crocker, D. A. 1993, AJ, 105, 1344

Canzian, B. 1993, ApJ, 414, 487

Canzian, B. & Allen, R. J. 1997, ApJ, 479, 723

Canzian, B. J. 1990, Ph.D. Thesis

Cappellari, M. & Copin, Y. 2002, in ASP Conf. Ser. 282 : Galaxies : the Third Dimension, 515

Carignan, C., Charbonneau, P., Boulanger, F., & Viallefond, F. 1990, A&A, 234, 43

Carignan, C., Fontaine, G., Wesemael, F., & Lamontagne, R. 2003, Notes de cours d'astronomie générale - PHY1971

Carignan, C. & Freeman, K. C. 1988, ApJ, 332, L33

Cayatte, V., van Gorkom, J. H., Balkowski, C., & Kotanyi, C. 1990, AJ, 100, 604

Cecil, G., Greenhill, L. J., DePree, C. G., Nagar, N., Wilson, A. S., Dopita, M. A., Pérez-Fournon, I., Argon, A. L., & Moran, J. M. 2000, ApJ, 536, 675

Cepa, J. & Beckman, J. E. 1990, A&AS, 83, 211

Charmandaris, V., Combes, F., & van der Hulst, J. M. 2000, A&A, 356, L1

Chary, R. & Becklin, E. E. 1997, ApJL, 485, L75+

Chemin, L. 2003, Ph.D. Thesis

Combes, F., Boisse, P., Mazure, A., Blanchard, A., & Seymour, M. 1995, Galaxies and Cosmology (Galaxies and Cosmology, XVI, 407 pp. 192 figs.. Springer-Verlag Berlin Heidelberg New York. Also Astronomy and Astrophysics Library)

Combes, F., Debbasch, F., Friedli, D., & Pfenniger, D. 1990, A&A, 233, 82

Combes, F. & Elmegreen, B. G. 1993, A&A, 271, 391

Combes, F. & Gerin, M. 1985, A&A, 150, 327

Contopoulos, G. 1980, A&A, 81, 198

Contopoulos, G. & Papayannopoulos, T. 1980, A&A, 92, 33

Corradi, R. L. M., Boulesteix, J., Bosma, A., Amram, P., & Capaccioli, M. 1991, A&A, 244, 27

Corsini, E. M., Debattista, V. P., & Aguerri, J. A. L. 2003, ApJL, 599, L29

Courtes, G. & Cruvellier, P. 1961, Publications of the Observatoire Haute-Provence, 5

Crosthwaite, L. P., Turner, J. L., & Ho, P. T. P. 2000, AJ, 119, 1720

Curtis, H. D. 1918, Publ. Lick. Obs.; Vol. 13; Page 45-54, 13, 45

Daigle, O., Carginan, C., & Hernandez, O. 2005, in preparation

de Vaucouleurs, G. 1963, ApJS, 8, 31

de Vaucouleurs, G., de Vaucouleurs, A., & Corwin, H. G. 1976, 2nd reference catalogue of bright galaxies containing information on 4364 galaxies with reference to papers published between 1964 and 1975 (University of Texas Monographs in Astronomy, Austin : University of Texas Press, 1976)

De Vaucouleurs, G., De Vaucouleurs, A., Corwin, Herold G., J., Buta, R. J., Paturel, G., & Fouque, P. 1991, Third Reference Catalogue of Bright Galaxies (Volume 1-3, XII, 2069 pp. 7 figs.. Springer-Verlag Berlin Heidelberg New York)

Debattista, V. P. 2003, MNRAS, 342, 1194

Debattista, V. P., Corsini, E. M., & Aguerri, J. A. L. 2002, MNRAS, 332, 65

Debattista, V. P. & Sellwood, J. A. 1998, ApJL, 493, L5

Debattista, V. P. & Williams, T. B. 2004, ApJ, 605, 714

Dehnen, W. 1993, MNRAS, 265, 250

Dupraz, C. & Combes, F. 1986, A&A, 166, 53

Elmegreen, B. G. & Elmegreen, D. M. 1989, ApJ, 342, 677

Elmegreen, B. G., Elmegreen, D. M., Chromey, F. R., Hasselbacher, D. A., & Bissell, B. A. 1996, AJ, 111, 2233

Elmegreen, B. G., Elmegreen, D. M., & Hirst, A. C. 2004, ApJ, 612, 191

Elmegreen, B. G., Elmegreen, D. M., & Montenegro, L. 1992, ApJS, 79, 37

Elmegreen, B. G., Wilcots, E., & Pisano, D. J. 1998, ApJL, 494, L37

Elmegreen, D. M. 1998, Galaxies and galactic structure (Galaxies and galactic structure /Debra Meloy Elmegreen. New Jersey : Prentice Hall, c1998. QB 857 E455 1998.)

Elmegreen, D. M. & Elmegreen, B. G. 1995, ApJ, 445, 591

England, M. N. 1989, ApJ, 344, 669

Eskridge, P. B., Frogel, J. A., Pogge, R. W., Quillen, A. C., Davies, R. L., DePoy, D. L., Houdashelt, M. L., Kuchinski, L. E., Ramírez, S. V., Sellgren, K., Terndrup, D. M., & Tiede, G. P. 2000, AJ, 119, 536

Ferrarese, L., Freedman, W. L., Hill, R. J., Saha, A., Madore, B. F., Kennicutt, R. C., Stetson, P. B., Ford, H. C., Graham, J. A., Hoessel, J. G., Han, M., Huchra, J., Hughes, S. M., Illingworth, G. D., Kelson, D., Mould, J. R., Phelps, R., Silbermann, N. A., Sakai, S., Turner, A., Harding, P., & Bresolin, F. 1996, ApJ, 464, 568

Foy, R. 1988, in Instrumentation for Ground-Based Optical Astronomy, Present and Future. The Ninth Santa Cruz Summer Workshop in Astronomy and Astrophysics, July 13- 24, 1987, Lick Observatory. Editor, L.B. Robinson; Publisher, Springer-Verlag, New York, NY, 1988. LC # QB856 .S26 1987. ISBN # 0-387-96730-3. P.589, 1988, 589

Fraternali, F., Oosterloo, T., Sancisi, R., & van Moorsel, G. 2001, ApJL, 562, L47

Freedman, W. L. & Madore, B. F. 1988, ApJ, 332, L63

Freeman, K. C. 1970, ApJ, 160, 811

Friedli, D. 1996, A&A, 312, 761

Friedli, D. & Benz, W. 1993, A&A, 268, 65

—. 1995, A&A, 301, 649

Friedli, D. & Martinet, L. 1993, A&A, 277, 27

Friedli, D., Wozniak, H., Rieke, M., Martinet, L., & Bratschi, P. 1996, A&AS, 118, 461

Gach, J.-L., Hernandez, O., Boulesteix, J., Amram, P., Boissin, O., Carignan, C., Garrido, O., Marcelin, M., Östlin, G., Plana, H., & Rampazzo, R. 2002, PASP, 114, 1043

Garcia-Burillo, S., Combes, F., & Gerin, M. 1993, A&A, 274, 148

García-Burillo, S., Combes, F., & Neri, R. 1999, A&A, 343, 740

Garcia-Burillo, S., Sempere, M. J., & Combes, F. 1994, A&A, 287, 419

Garcia-Burillo, S., Sempere, M. J., Combes, F., & Neri, R. 1998, A&A, 333, 864

Garrido, O., Marcelin, M., Amram, P., & Boissin, O. 2003, A&A, 399, 51

Garrido, O., Marcelin, M., Amram, P., & Boulesteix, J. 2002, A&A, 387, 821

Gerssen, J., Kuijken, K., & Merrifield, M. R. 1999, MNRAS, 306, 926

—. 2003, MNRAS, 345, 261

Gnedin, O. Y., Goodman, J., & Frei, Z. 1995, AJ, 110, 1105

Gooch, R. 1996, in ASP Conf. Ser. 101 : Astronomical Data Analysis Software and Systems V, 80

Gottesman, S. T. 1982, AJ, 87, 751

Grosbøl, P., Patsis, P. A., & Pompei, E. 2004, A&A, 423, 849

Hackwell, J. A. & Schweizer, F. 1983, ApJ, 265, 643

Helfer, T. T., Thornley, M. D., Regan, M. W., Wong, T., Sheth, K., Vogel, S. N., Blitz, L., & Bock, D. C.-J. 2003, ApJS, 145, 259

Heller, C., Shlosman, I., & Englmaier, P. 2001, ApJ, 553, 661

Hernandez, G. 1986, Fabry-Perot interferometers (Cambridge Studies in Modern Optics, Cambridge : University Press, 1986)

Hernandez, O., Carignan, C., Amram, P., Chemin, L., & Daigle, O. 2005a, submitted to MNRAS

Hernandez, O., Carignan, C., Amram, P., & Daigle, O. 2004, ArXiv Astrophysics e-prints

Hernandez, O., Gach, J., Carignan, C., & Boulesteix, J. 2003, in Instrument Design and Performance for Optical/Infrared Ground-based Telescopes. Edited by Iye, Masanori; Moorwood, Alan F. M. Proceedings of the SPIE, Volume 4841, 1472–1479

Hernandez, O., Wozniak, H., Carignan, C., Amram, P., Chemin, L., & Daigle, O. 2005b, submitted to ApJ

Hernquist, L. & Katz, N. 1989, ApJS, 70, 419

Hernquist, L. & Weinberg, M. D. 1992, ApJ, 400, 80

Hubble, E. P. 1926, ApJ, 64, 321

Huntley, J. M. 1978, ApJL, 225, L101

Joye, W. & Mandel, E. 1999, in ASP Conf. Ser. 172 : Astronomical Data Analysis Software and Systems VIII, 429

Kelson, D. D., Illingworth, G. D., Freedman, W. F., Graham, J. A., Hill, R., Madore, B. F., Saha, A., Stetson, P. B., Kennicutt, R. C., Mould, J. R., Hughes, S. M., Ferrarese, L., Phelps, R., Turner, A., Cook, K. H., Ford, H., Hoessel, J. G., & Huchra, J. 1996, ApJ, 463, 26

Kelson, D. D., Illingworth, G. D., Saha, A., Graham, J. A., Stetson, P. B., Freedman, W. L., Kennicutt, R. C., Mould, J. R., Ferrarese, L., Huchra, J. P., Madore, B. F., Prosser, C. F., Bresolin, F., Ford, H. C., Gibson, B. K., Hoessel, J. G., Hughes, S. M. G., Macri, L. M., Sakai, S., & Silbermann, N. A. 1999, ApJ, 514, 614

Kennicutt, R. C. 1998, ARA&A, 36, 189

Kent, S. M. 1987, AJ, 93, 1062

Kent, S. M. & Glaudell, G. 1989, AJ, 98, 1588

Kicks, T. R., Reay, N. K., Ring, J., & Scaddan, R. J. 1975, MNRAS, 172, 53P

Knapen, J. H., Cepa, J., Beckman, J. E., Soledad del Rio, M., & Pedlar, A. 1993, ApJ, 416, 563

Knapen, J. H., Shlosman, I., Heller, C. H., Rand, R. J., Beckman, J. E., & Rozas, M. 2000a, ApJ, 528, 219

Knapen, J. H., Shlosman, I., & Peletier, R. F. 2000b, ApJ, 529, 93

Kormendy, J. 1982, ApJ, 257, 75

—. 1983, ApJ, 275, 529

Kormendy, J. 1993, in IAU Symp. 153 : Galactic Bulges, 209

Kranz, T., Slyz, A., & Rix, H. 2001, ApJ, 562, 164

—. 2003, ApJ, 586, 143

Lütticke, R., Dettmar, R.-J., & Pohlen, M. 2000, A&A, 362, 435

Laine, S. & Gottesman, S. T. 1998, MNRAS, 297, 1041

Laine, S., Shlosman, I., & Heller, C. H. 1998, MNRAS, 297, 1052

Le Coarer, E., Bensammar, S., Comte, G., Gach, J. L., & Georgelin, Y. 1995, A&AS, 111, 359

Lin, C. C. & Shu, F. H. 1964, ApJ, 140, 646

Lindblad, B. 1963, Stockholms Observatoriums Annaler, 5

Lindblad, P. A. B. & Kristen, H. 1996, A&A, 313, 733

Lindblad, P. A. B., Lindblad, P. O., & Athanassoula, E. 1996, A&A, 313, 65

Little, B. & Carlberg, R. G. 1991, MNRAS, 251, 227

Lucy, L. B. 1977, AJ, 82, 1013

Macri, L. M., Huchra, J. P., Stetson, P. B., Silbermann, N. A., Freedman, W. L., Kennicutt, R. C., Mould, J. R., Madore, B. F., Bresolin, F., Ferrarese, L., Ford, H. C., Graham, J. A., Gibson, B. K., Han, M., Harding, P., Hill, R. J., Hoessel, J. G., Hughes, S. M. G., Kelson, D. D., Illingworth, G. D., Phelps, R. L., Prosser, C. F., Rawson, D. M., Saha, A., Sakai, S., & Turner, A. 1999, ApJ, 521, 155

Maillard, J. P. & Simons, D. 1992, First results of an imaging FTS with a NICMOS camera, Tech. rep.

Malin, D. F. & Carter, D. 1983, ApJ, 274, 534

Marcelin, M., Boulesteix, J., & Courtes, G. 1982, A&A, 108, 134

Marcelin, M., Boulesteix, J., & Georgelin, Y. 1983, A&A, 128, 140

Martin, P. 1995, AJ, 109, 2428

Martin, P. & Roy, J. 1995, ApJ, 445, 161

Masset, F. & Tagger, M. 1997, A&A, 322, 442

Massey, P. & Foltz, C. B. 2000, PASP, 112, 566

Mendes de Oliveira, C., Plana, H., Amram, P., Balkowski, C., & Bolte, M. 2001, AJ, 121, 2524

Mendes de Oliveira, C., Plana, H., Amram, P., Bolte, M., & Boulesteix, J. 1998, ApJ, 507, 691

Merrifield, M. R. & Kuijken, K. 1995, MNRAS, 274, 933

Michel-Dansac, L. & Wozniak, H. 2004, A&A, 421, 863

Milgrom, M. 1983, ApJ, 270, 365

Miyamoto, M. & Nagai, R. 1975, PASJ, 27, 533

Navarro, J. F., Frenk, C. S., & White, S. D. M. 1996, ApJ, 462, 563

—. 1997, ApJ, 490, 493

O'dell, C. R. & Townsley, L. K. 1988, A&A, 198, 283

Osterbrock, D. E. 1989, Astrophysics of gaseous nebulae and active galactic nuclei (Research supported by the University of California, John Simon Guggenheim Memorial Foundation, University of Minnesota, et al. Mill Valley, CA, University Science Books, 1989, 422 p.)

Ostlin, G., Amram, P., Bergvall, N., Masegosa, J., Boulesteix, J., & Márquez, I. 2001, A&A, 374, 800

Ostlin, G., Amram, P., Masegosa, J., Bergvall, N., & Boulesteix, J. 1999, A&AS, 137, 419

Ostriker, J. & Peebles, P. 1973, ApJ, 467

Pérez, I., Fux, R., & Freeman, K. 2004, A&A, 424, 799

Patsis, P. A. & Athanassoula, E. 2000, A&A, 358, 45

Peterson, C. J., Thonnard, N., Rubin, V. C., & Ford, W. K. 1978, ApJ, 219, 31

Pfenniger, D. & Norman, C. 1990, ApJ, 363, 391

Pisano, D. J., Wilcots, E. M., & Elmegreen, B. G. 1998, AJ, 115, 975

Pizzella, A., dalla Bontà, E., Corsini, E. M., Coccato, L., & Bertola, F. 2004, in IAU Symposium, 339

Plana, H. 1996, PhD thesis, Université de Provence

Plana, H., Amram, P., de Oliveira, C. M., & Balkowski, C. 2000, AJ, 120, 621

Plana, H., Mendes de Oliveira, C., Amram, P., Bolte, M., Balkowski, C., & Boulesteix, J. 1999, ApJL, 516, L69

Quillen, A. C. & Frogel, J. A. 1997, ApJ, 487, 603

Quinn, P. J. 1984, ApJ, 279, 596

Rand, R. J. 1995, AJ, 109, 2444

Rand, R. J. & Wallin, J. F. 2004, ApJ, 614, 142

Rautiainen, P. & Salo, H. 1999, A&A, 348, 737

Rautiainen, P., Salo, H., & Buta, R. 2004, MNRAS, 349, 933

Rozas, M., Zurita, A., & Beckman, J. E. 2000a, A&A, 354, 823

Rozas, M., Zurita, A., Beckman, J. E., & Pérez, D. 2000b, A&AS, 142, 259

Sérsic, J. L. 1973, PASP, 85, 103

Sakamoto, K., Okumura, S., Minezaki, T., Kobayashi, Y., & Wada, K. 1995, AJ, 110, 2075

Sanders, R. H. & Huntley, J. M. 1976, ApJ, 209, 53

Sanders, R. H. & Tubbs, A. D. 1980, ApJ, 235, 803

Schaap, W. E., Sancisi, R., & Swaters, R. A. 2000, A&A, 356, L49

Schiminovich, D., van Gorkom, J. H., van der Hulst, J. M., & Malin, D. F. 1995, ApJL, 444, L77

Schoenmakers, R. H. M., Franx, M., & de Zeeuw, P. T. 1997, MNRAS, 292, 349

Sellwood, J. A. 1985, MNRAS, 217, 127

—. 1993, PASP, 105, 648

Sellwood, J. A. & Sparke, L. S. 1988, MNRAS, 231, 25P

Sellwood, J. A. & Wilkinson, A. 1993, Reports of Progress in Physics, 56, 173

Sempere, M. J., Combes, F., & Casoli, F. 1995a, A&A, 299, 371

Sempere, M. J., Garcia-Burillo, S., Combes, F., & Knapen, J. H. 1995b, A&A, 296, 45

Sempere, M. J. & Rozas, M. 1997, A&A, 317, 405

Shaw, M. A., Combes, F., Axon, D. J., & Wright, G. S. 1993, A&A, 273, 31

Sheth, K., Regan, M. W., Scoville, N. Z., & Strubbe, L. E. 2003, ApJL, 592, L13

Shostak, G. S. 1973, A&A, 24, 411

Siegmund, O. H. W., Everman, E., Vallerga, J. V., & Lampton, M. 1988, in Optoelectronic technologies for remote sensing from space; Proceedings of the Meeting, Cannes, France, Nov. 19, 20, 1987 (A88-42526 17-19). Bellingham, WA, Society of Photo-Optical Instrumentation Engineers., 18–24

Silbermann, N. A., Madore, B. F., Ferrarese, L., Ford, H., Saha, A., Freedman, W. L., Hill, R. J., Graham, J. A., Hoessel, J. G., Huchra, J. P., Hughes, S. M., Illingworth, G. D., Kennicutt, R. C., Mould, J. R., & Stetson, P. B. 1994, Bulletin of the American Astronomical Society, 26, 1353

Slyz, A. D., Devriendt, J. E. G., Bryan, G., & Silk, J. 2004, MNRAS, 665

Sofue, Y., Tomita, A., Tutui, Y., Honma, M., & Takeda, Y. 1998, PASJ, 50, 427

Springel, V., Yoshida, N., & White, S. D. M. 2001, New Astronomy, 6, 79

Swaters, R. A., Madore, B. F., van den Bosch, F. C., & Balcells, M. 2003, ApJ, 583, 732

Sygnet, J. F., Tagger, M., Athanassoula, E., & Pellat, R. 1988, MNRAS, 232, 733

Tagger, M., Sygnet, J. F., Athanassoula, E., & Pellat, R. 1987, ApJL, 318, L43

Teuben, P. J. 2002, in ASP Conf. Ser. 275 : Disks of Galaxies : Kinematics, Dynamics and Peturbations, 217–228

Thomson, R. C. 1991, MNRAS, 253, 256

Thomson, R. C. & Wright, A. E. 1990, MNRAS, 247, 122

Toomre, A. 1964, ApJ, 139, 1217

—. 1969, ApJ, 158, 899

Tremaine, S. & Weinberg, M. D. 1984, ApJL, 282, L5

Tully, R. B. 1988, Journal of the British Astronomical Association, 98, 316

van Albada, T. S. & Sanders, R. H. 1982, MNRAS, 201, 303

van Driel, W. & Buta, R. J. 1991, A&A, 245, 7

van Moorsel, G. A. 1983, A&AS, 54, 19

Verheijen, M. A. W. & Sancisi, R. 2001, A&A, 370, 765

Vogt, N. P., Haynes, M. P., Herter, T., & Giovanelli, R. 2004, AJ, 127, 3273

Wada, K., Sakamoto, K., & Minezaki, T. 1998, ApJ, 494, 236

Weil, M. L. & Hernquist, L. 1993, ApJ, 405, 142

Weinberg, M. D. 1985, MNRAS, 213, 451

Weiner, B. J., Sellwood, J. A., & Williams, T. B. 2001, ApJ, 546, 931

Westpfahl, D. J. 1998, ApJS, 115, 203

Wilke, K., Möllenhoff, C., & Matthias, M. 1999, A&A, 344, 787

Wozniak, H. 1991, Ph.D. Thesis

—. 2001, Notes de cours de gravitation classique

Wozniak, H., Combes, F., Emsellem, E., & Friedli, D. 2003, A&A, 409, 469

Wozniak, H., Friedli, D., Martinet, L., Martin, P., & Bratschi, P. 1995, A&AS, 111, 115

Wynn-Williams, C. G. & Becklin, E. E. 1985, ApJ, 290, 108

Zimmer, P., Rand, R. J., & McGraw, J. T. 2004, ApJ, 607, 285

Zurita, A., Relaño, M., Beckman, J. E., & Knapen, J. H. 2004, A&A, 413, 73

Zwicky, F. 1933, Helv.Phys.Acta, 6, 110

Annexe A

Organigrame de réduction de données Fabry-Perot pour galaxies barrées

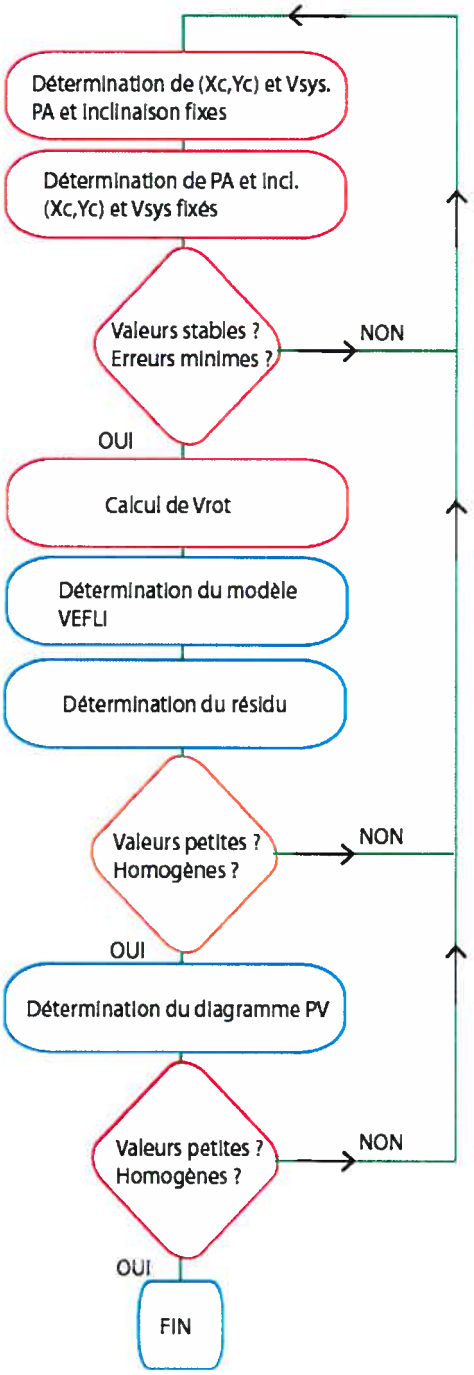

Fig. 61: Organigramme de réduction des données. Les blocs rouges indiquent que seules les parties considérées comme axisymétriques sont prises en compte pour la recherche des paramètres.

Annexe B

Tableau des routines de génération de Conditions Initiales et de potentiel pour Gadget

Table XIV: Routines propres à GADGET

Génération du Potentiel	
Nom de la Routine	*Fonction*
XOTE.PRO	Enlève les étoiles du champs
XDEPROJECTION.PRO	Déprojection de la galaxie
XETEND.PRO	Transformation 2D $\rightarrow$ 3D
XGENEPOT.PRO	Génération du potentiel
XDERIVE.PRO	Calcul des forces
Utilitaires pour Gadget	
SHOW_GALAXY.PRO	Visionnement des snapshots
SHOW_ENERGIE.PRO	Trace l'évolution temporelle de l'énergie
CONSTRUCTIONCIGADGET.PRO	Construction des Conditions Initiales
TIRMIYAMOTO.F	Tirage d'une distribution de Miyamoto & Nagai (1975)

Table XV: Exemple de paramètres d'entrée pour GADGET - Partie I/II

Fichiers d'E/S	
InitCondFile	/home/gadget/Gadget-1.1/ICs/gaz20kdisk20khalo40k.dat.intel
OutputDir	/home/gadget/Exemples/PSPNB2/
EnergyFile	energy.txt
InfoFile	info.txt
TimingsFile	timings.txt
CpuFile	cpu2.txt
RestartFile	restart
SnapshotFileBase	snapshot
OutputListFilename	parameterfiles/output_list.txt
Limites de temps CPU	
TimeLimitCPU	360000 (= 10 hours)
ResubmitOn	0
ResubmitCommand	my-scriptfile
Options du code	
ICFormat	1
ComovingIntegrationOn	0
CoolingOn	0
TypeOfTimestepCriterion	3
OutputListOn	0
PeriodicBoundariesOn	0
Carctéristiques d'une simulation	
TimeBegin	0.0
TimeMax	0.01
Omega0	0
OmegaLambda	0
OmegaBaryon	0
HubbleParam	1.0
BoxSize	0
Fréquence de sortie des fichiers	
TimeBetSnapshot	0.001
TimeOfFirstSnapshot	0
CpuTimeBetRestartFile	3600.0
TimeBetStatistics	0.001
NumFilesPerSnapshot	1
NumFilesWrittenInParallel	2
Précision pour l'intégration temporelle	
ErrTolIntAccuracy	0.1
ErrTolVelScale	0.1
CourantFac	0.1
MaxSizeTimestep	0.01
MinSizeTimestep	0

Table XVI: Exemple de paramètres d'entrée pour GADGET - Partie II/II

Code en arbre, décompostion du domaine	
ErrTolTheta	0.4
TypeOfOpeningCriterion	1
ErrTolForceAcc	0.002
MaxNodeMove	0.05
TreeUpdateFrequency	0.1
DomainUpdateFrequency	0.2
Paramètres du SPH	
DesNumNgb	40
MaxNumNgbDeviation	5
ArtBulkViscConst	0.75
InitGasTemp	0
MinGasTemp	0
Allocation de la mémoire	
PartAllocFactor	2.0
TreeAllocFactor	0.8
BufferSize	35 (en MBytes)
Système d'unités	
UnitLength_in_cm	3.085678e21 (1.0 kpc)
UnitMass_in_g	1.989e43 (1.0e10$\mathcal{M}_\odot$)
UnitVelocity_in_cm_per_s	1e5 (1 km s^{-1})
GravityConstantInternal	0
Paramètres de lissage	
MinGasHsmlFractional	0.04
SofteningGas	0.04
SofteningHalo	1.0
SofteningDisk	1.0
SofteningBulge	0
SofteningStars	0
SofteningGasMaxPhys	0.04
SofteningHaloMaxPhys	1.0
SofteningDiskMaxPhys	1.0
SofteningBulgeMaxPhys	0
SofteningStarsMaxPhys	0
Dyn. et Ciné. pour les barres	
BarredGalaxyOn	0
Omegap	20.0

Annexe C

FaNTOmM : Fabry Perot Observations using a new GaAs Photon Counting System

FaNTOmM : Fabry Perot Observations using a new GaAs Photon Counting System

OLIVIER HERNANDEZ

Département de physique and Observatoire du mont Mégantic, Université de Montréal, C.P. 6128, Succ. centre ville, Montréal, Québec, Canada. H3C 3J7 and

Observatoire de Marseille, 2 Place Le Verrier, F–13248 Marseille Cedex 04, France

e–mail : [redacted]

JEAN-LUC GACH

Observatoire de Marseille, 2 Place Le Verrier, F–13248 Marseille Cedex 04, France

JACQUES BOULESTEIX

Observatoire de Marseille, 2 Place Le Verrier, F–13248 Marseille Cedex 04, France

CLAUDE CARIGNAN

Département de physique and Observatoire du mont Mégantic, Université de Montréal, C.P. 6128, Succ. centre ville, Montréal, Québec, Canada. H3C 3J7

e–mail : [redacted]

Published in Galaxies : The Third Dimension, ASP Conference Proceedings, Vol. 282. Edited by Margarita Rosado, Luc Binette, and Lorena Arias. ISBN : 1-58381-125-7. San Francisco : Astronomical Society of the Pacific, 2002., p.477

Abstract

We present a third generation photon counting camera (IPCS) based on a GaAs photocathode that can achieve quantum efficiency up to 23 %, comparable to a thick CCD, but without readout noise. This system is 10 times more sensitive at Hα wavelength than previous photon counting cameras. In terms of S/N ratio, the system outperforms CCD for extremely faint fluxes, included AR coated low-noise thin CCDs. This system offers up to 1k $\times$ 1k pixels, which is the largest monolithic IPCS. An original cooling system is used with this camera settled by a Ranque-Hilsh vortex tube. The real-time centering is done by a scalable DSP board. Preliminary results obtained with this new camera coupled with a scanning Fabry-Perot at the Cassegrain focus of the 3.6m ESO telescope, the 1.93m Obser-

vatoire de Haute Provence (OHP) telescope, and 1.6m mont Mégantic (OmM) telescope are presented.

C.1 Introduction

In the last two decades, several multiplex scanning instruments, e.g Fourier Transform Spectrographs FTS (Maillard & Simons 1992), scanning Fabry-Perot integral field spectrometers such as TAURUS (Atherton et al. 1982), CIGALE (Boulesteix et al. 1984), HIFI (Bland et al. 1989), PYTHEAS (Le Coarer et al. 1995), have been developed and tested at the foci of 2 -6 m class telescopes . At the same time, since the last development achieved in the 80's (see e.g. Boulesteix & Marcelin 1980, Blazit 1985, Foy 1988), it's only recently that image photon counting systems (IPCS) have opened new perspectives for the full exploitation of multiplex scanning instruments. Indeed, a new generation of GaAs and GaAsP photocadodes has appeared, with high quantum efficiency (QE) and proximity-focused image intensifier without image distortion, associated to high frame rate and large format CCDs that can be used as detectors behind the image intensifier leading to large format IPCS.

The paper presents the study and the application of a third generation of IPCS based on a GaAs photocathode that can achieve a quantum efficiency up to 23 %, comparable to a thick CCD, but without read-out noise. The paper is organized as follows. Section 2 presents the new GaAs photocathode. Section 3 develops basic considerations about the comparison between IPCS and CCD in multiplex scanning mode. Section 4 presents an overview of this new IPCS system. Preliminary results obtained at different observatories during recent observing runs are briefly shown in Section 5. Future applications are sketched in Section 6.

C.2 New GaAs Photocathode

The new generation of image intensifier tubes employs proximity-focus microchannel plate intensifiers (see Figure 62 for an overview) with Gallium-Arsenide photocathodes (GaAs Electron Tube). These kinds of devices have a very compact design with their length (10mm long) smaller than their diameter (18mm). They are also free of geometric distortion. A potential difference is made to accelerate electrons from the cathode to the anode (phos-

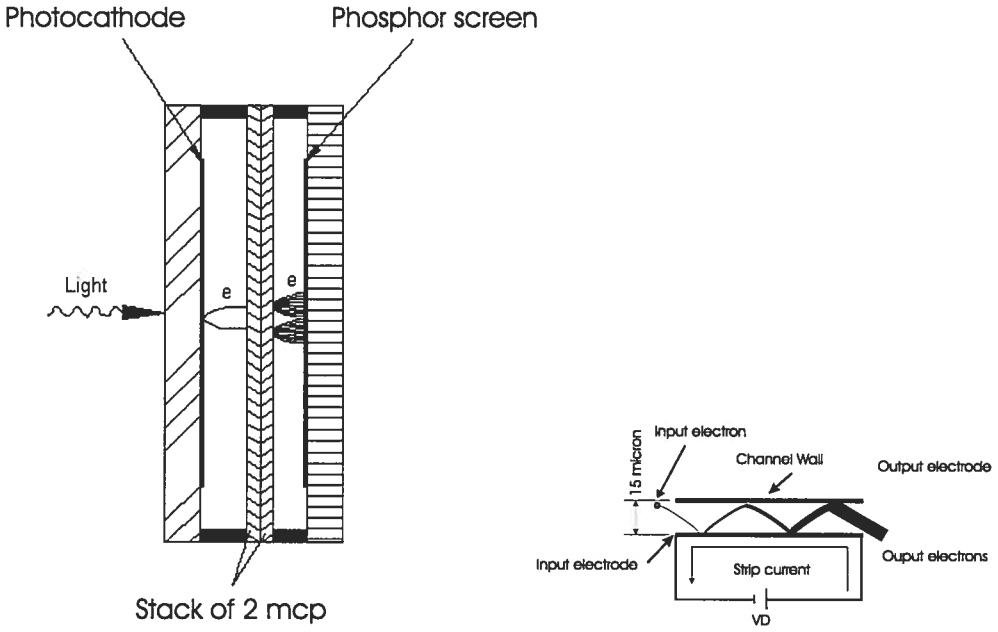

Fig. 62: **(left)** : GaAs Electron Tube - **(right)** : Operating principle of GaAs Micro Channel Plate (MCP)

phor screen). Electron multiplication is done, between the anode and the cathode, using a device called microchannel plate (MCP). In this plate, made of conductive glass, very small holes of 15μm diameter are used to make the multiplication of electrons. When 2 MCPs are used in cascade, the amplification factor can reach 10^7.

C.3 CCD vs IPCS

One of remarkable line of progress with this new generation of GaAs electron tubes (GaAs photocathode, 2 MCPs and the phosphor screen) is their quantum efficiency, 5 times higher than previous. 23 % of RQE are now achieved over a broadband range of wavelength (500 to 850 nm, see Figure 63). IPCS do not have readout noise and are less affected by cosmic rays since one event is seen as one photon only, a decisive advantage with respect to CCDs when long exposures are required as in the case of faint object investigations. Although first generation IPCSs offer a poorer quantum efficiency with respect to CCDs and are affected by image distortion, they are still competitive with CCDs in multiplex instruments or in speckle interferometry.

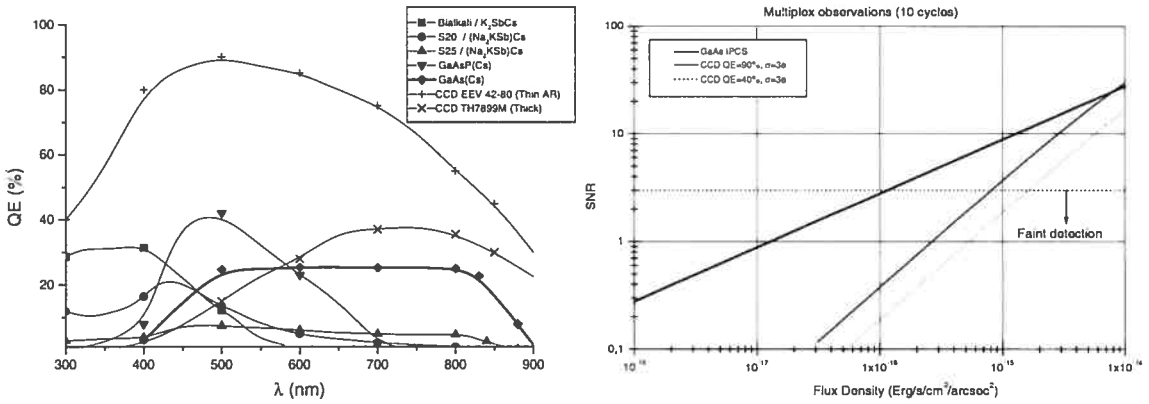

Fig. 63: **(left)** : Quantum efficiency of different types of photocathodes compared to CCDs. **(right)** : SNR obtained by different detectors using a scanning Fabry Perot with a 48-channel observation and 10 cycles to average night sky variations

Because of the very small readout time (25 ms in our case) for an IPCS, it is possible to observe each channel several times during the multiplex observation, then averaging all these variations. Typically, each channel is observed 5 to 15 seconds, and when the last channel has been integrated, the first is observed again. Each set of n channels is called a cycle whose duration is typically 3 to 10 minutes (depending on the exposure time per channel and the number of channels) and the total observation consists of several cycles. Technically, it is possible to make one whole cycle within a few seconds, taking only one 25ms exposure per channel, but we found that unnecessary and preferred instrument stability instead. Since there is no readout noise, it is then possible to sum up each i^{th} channel of all the cycles without losing any SNR. Obviously, adapting this observing technique to CCDs would degrade considerably the SNR due to the large number of images produced.

Figure 63 (right) shows the SNR obtained with an 8m telescope in a 1-hour observation of multiplex 48 channels each with 10 cycles 25x0.25 arcsec^2 pixels.

C.4 GaAs system overview

(Note : A movie was shown during this section. Contact Olivier Hernandez to have a copy of it : olivier@astro.umontreal.ca. A complete description of the system can be found on the following web site : www.astro.umontreal.ca/fantomm)

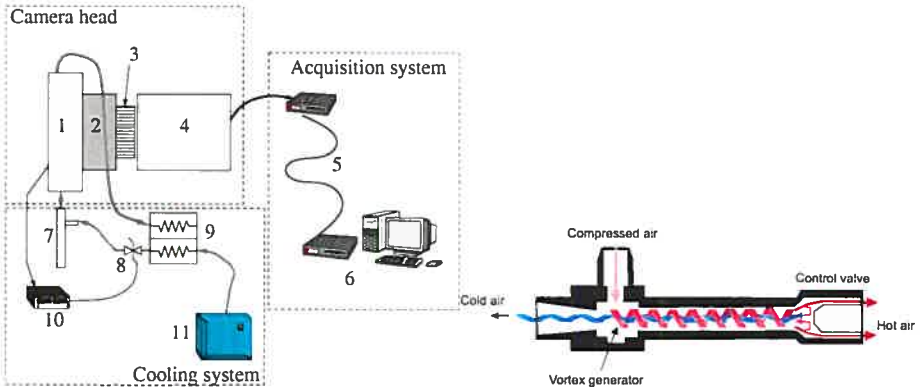

Fig. 64: (left) : Overview of the system, **(right)** : Principle of a vortex tube

C.4.1 Camera head

The camera head is composed of a GaAs proximity-focused 2-stage MCP image intensifier tube fiber-coupled to a 1k×1k 40-frame per second (fps) CCD. The cathode is cooled down to -25 ^{o}C with a cold air flow in the cold finger. A vacuum is created between the cathode and the input window, which is isolated with a thermal non conductive ceramic to avoid thermal losses or condensation and ice on the window. The CCD can work in 1k×1k mode (12 μm pixel) at 40 fps or in hard binned mode 512×512 pixels at 80 fps (24 μm pixel). Each photon interacting with the photocathode is amplified up to 10^6 to 10^7 times by the image intensifier producing a signal much larger than the internal noise of the CCD.

C.4.2 Acquisition

The acquisition system is completely different from those used for classical CCD systems. The philosophy is not to accumulate flux on pixels but to detect events that correspond to the arrival of each photon. Each event is then accumulated in one computer memory forming the final image. The main difference with this new IPCS camera compared to older ones is the centering system. In previous IPCS, the centering of the spot produced by amplified photons was done by a hardwired system. Here, the camera is connected to a scalable DSP board based on a TMS 320C80 MVP chip consisting of 4 DSP cores working in Multiple Instruction Multiple Data scheme (MIMD). This board acquires data from the camera into a buffer and centers each spot. This allows more versatility and would even permit centering events at a better resolution than the physical pixel of the readout CCD

by fitting a gaussian on the event spot. The centering task is done in real time at the frame readout rate. The computing power is of prime importance here since the ability to acquire all frames is directly connected to it. With one TMS320C80 the system is limited to 1.6×10^4 photons/s. If the number of photons is bigger, some frames would be lost since the DSP is still computing the centering of events in the previous frame when the new frame arrives. This is equivalent to a RQE loss directly proportional to the number of frames missed. The way around this is to use a parallelized DSP system (up to 14 DSP in our case). Parallelization of tasks is very easy : the game is to allocate one incoming frame to one DSP processor core, up to the maximal amount of cores present on the system. In our case, the gain adding processors is fully linear, leading to a maximal flux of 2.24×10^5 photons/s when the 56 cores (14 DSP) are present. The acquisition and centering of the events is done in real time by the ©ADHOCw software developed by Jacques Boulesteix (for more information : http ://www-obs.cnrs-mrs.fr/adhoc/adhoc.html).

C.4.3 New cooling system

A new cooling system has been developed based on a Ranque-Hilsh vortex tube (see Figure 64 right). A vortex tube uses compressed air as a power source and produces hot air from one end and cold air from the other with no moving parts. The flow and temperature of the two airstreams are adjustable with a valve and a sleeve. Differential temperatures close to -70^oC are possible between compressed air and cold air. Compressed air (7 Bars), is injected tangentially through a generator into the vortex spin chamber. At up to 1,000,000 rounds per minute, this air stream revolves toward the hot end where some escapes through the control valve. The remaining air, still spinning, is forced back through the center of this outer vortex (see Figure 64 right). The inner stream gives off kinetic energy in the form of heat to the outer stream (due to the principle of conservation of angular momentum) and exits from the vortex tube as cold air. The outer stream exits at the opposite end as hot air. Hence, the flow of cold air passes through the cryostat chamber, in front of the GaAs proximity focused image intensifier tube. The calories not used are directed towards a heat exchanger to cool down compressed air before it goes through the vortex tube.

We use a compressor and an auto regenerative dryer to avoid frost formation. The flow of cold air is regulated with an electronically controlled proportioning valve and a temperature process meter. Temperature is set to -25^oC in order to have thermal noise

close to 3 events per frame, to assure good quantum efficiency and to protect the GaAs tube from thermal shocks. This system is very stable and requires no maintenance.

C.5 Results

C.5.1 First results on various telescopes

The new IPCS camera has been tested coupled with the scanning Fabry-Perot *CIGALE* at the Cassegrain focus of the 3.6m ESO telescope (La Silla : September 2000), and of the 1.93m OHP telescope (October 2000 and May 2001), and with the scanning Fabry-Perot *PANORAMIX* of the 1.6m OmM telescope (March 2001). The observations are parts of different scientific projects addressed to studies ranging from gas rich, late-type galaxies (GHASP project : Garrido et al., 2002) to gas poor ($\approx 10^6$ $M_\odot$) early-type systems (Rampazzo et al. 2001). Figure 65 gives two examples of velocity fields obtained on two different telescopes using the new IPCS.

C.5.2 Raw comparison IPCS vs CCD

Figure 66 shows raw comparison between a CCD and the new IPCS system. The CCD data were obtained at the 3.6m Canada France Hawaii telescope (CFHT) with an exposure of 3 hours. The IPCS data were obtained on the 1.6m Observatoire du mont Mégantic telescope with only a one hour exposure. Note that OmM data are raw data and a further paper will compare correctly the two velocity fields but the final result is the same.

C.6 Further developments

Current developments on GaAs tubes should make available up to 35% RQE tubes with flat response in the 500-800 nm domain in the very near future, reducing the difference with backside AR coated CCDs and making them even more competitive when used in scanning instruments. Another interesting path to explore, which will be done in the near future, consists of centering the events at a better resolution than the readout CCD resolution as described above, increasing then the virtual size of the array and keeping a reasonable size for the detector itself. Finally this kind of system could find interesting applications on

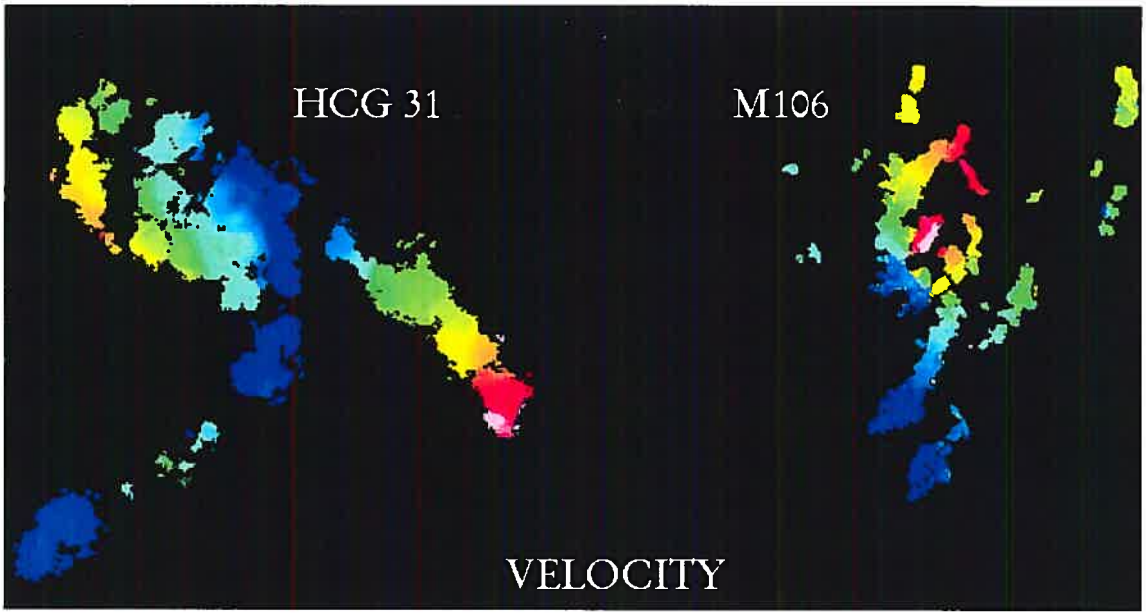

Fig. 65: **(left)** : Radial velocity field of the compact group of galaxies HCG 31. The field of view of the image is 104" square. The pixel size is ~0.4 arcsec. The velocity range is from 3840 km/s to 4160 km/s. This group contains 3 galaxies overlapping in projection in the velocity field, which looks strongly perturbed. **(right)** : Hα emission-line map of NGC 4258 (M 106). The field of view is 12.5′ square. The pixel size is ~1.5 arcsec. The velocitiy range is from 260 km/s to 755 km/s. The optical jet has been highlighted.

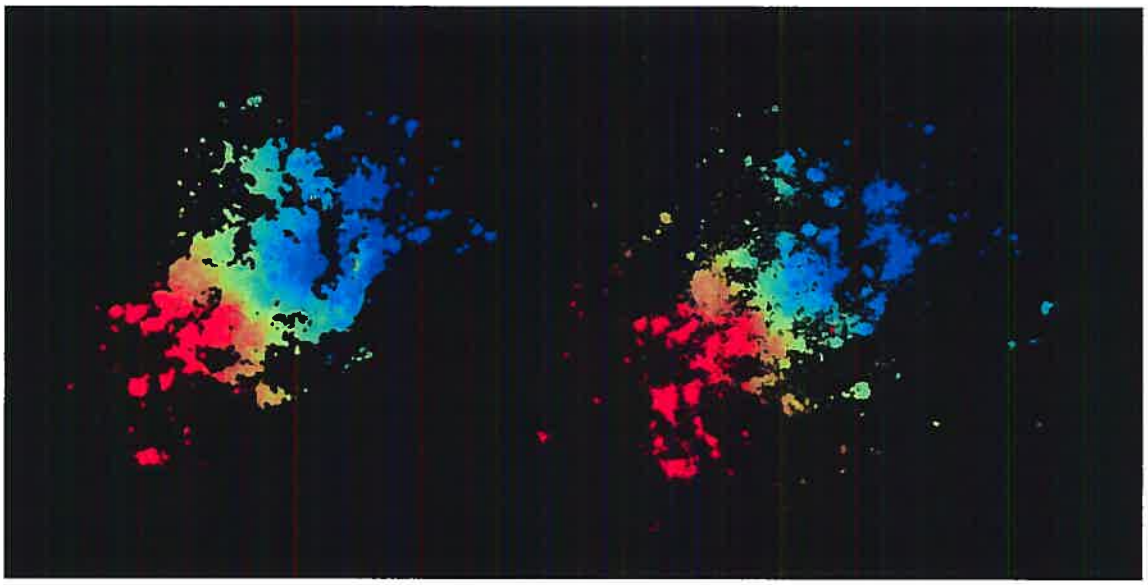

Fig. 66: **(left)** : NGC 2403 velocity field using the MOS/FP at CFHT **(right)** : NGC 2403 velocity field using FaNTOmM IPCS at OmM

bioluminescence and all other fields where time resolution and high sensitivity are needed at the same time.

Acknowledgements

We would like to thank the ESO (La Silla), the OHP, and the OmM staff for their assistance during the commissionning of the new camera, Olivier Boissin for his technical help and Mathieu Ouellet for the mechanical design. Many thanks also to our collaborators Chantal Balkowski, Nils Bergvall, Sébastien Blais-Ouellette, Isabel Marquez, Josefa Masegosa, Claudia Mendes de Oliveira. Special thanks to Philippe Amram, Olivia Garrido, Michel Marcelin, Goran Östlin, Henri Plana and Roberto Rampazzo for their reduced data.

References

Atherton, P.D., Taylor, K., Pike, C.D., Harmer, C.F.W., Parker, N.M., Hook, R.N. 1982, MNRAS, 201, 661

Blazit, A. 1985, ESA Colloq. on Kilometric Opt. Arrays in Space,155

Boulesteix, J., Georgelin, Y.P., Marcelin, M., Monnet, G. 1984, SPIE, 445, 37

Boulesteix, J., Marcelin, M. 1980, ESO : Two-dimens. Photom., 119

Foy, R. 1988 9th Santa Cruz Summer Workshop in Astronomy and Astrophysics, 589

Garrido, O., Marcelin, M., Amram, P., Boulesteix, J. 2002, A& A, 387,381

Gach J.L., Hernandez O., Boulesteix J., Amram P., Boissin O., Carignan C., Garrido O., Marcelin M., Ostlin G., Plana H., Rampazzo R., 2002, PASP, 114, 1043 .

Le Coarer, E., Bensammar, S., Comte, G., Gach, J.L., Georgelin, Y. 1995, A& AS, 111, 359

Maillard, J.P., Simons, D. 1992 ESO conf. on Progress in Telescope and Instrumentation Technologies, 733

Östlin, G., Amram, P. , Masegosa, J., Bergvall, N., Boulesteix, J., M árquez, I. 2001, A& A, 374, 800

Rampazzo, R. et al. 2003, MNRAS, 343, 819

Annexe D

Coupleur FaNTOmM-MOS pour le CFHT

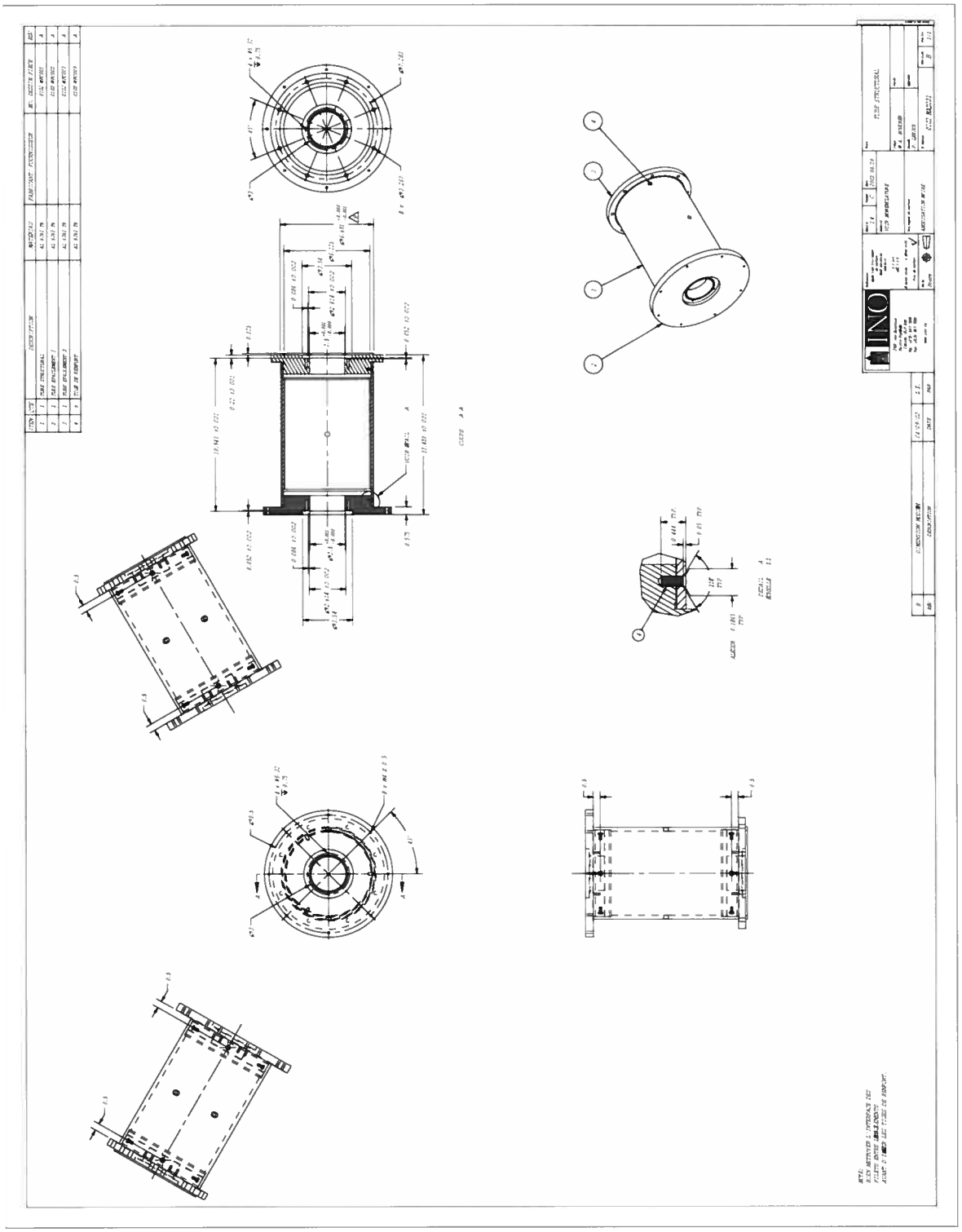

Annexe E

GIRAFFE multiple integral field units at VLT : a unique tool to recover velocity fields of distant galaxies

GIRAFFE multiple integral field units at VLT : a unique tool to recover velocity fields of distant galaxies.

HECTOR FLORES,

GEPI, Observatoire de Paris Meudon, 92190 Meudon, France

MATHIEU PUECH,

GEPI, Observatoire de Paris Meudon, 92190 Meudon, France

FRANÇOIS HAMMER

GEPI, Observatoire de Paris Meudon, 92190 Meudon, France

OLIVIA GARRIDO

GEPI, Observatoire de Paris Meudon, 92190 Meudon, France

OLIVIER HERNANDEZ

Département de physique and Observatoire du mont Mégantic, Université de Montréal, C.P. 6128, Succ. centre ville, Montréal, Québec, Canada. H3C 3J7 and

Observatoire de Marseille, 2 Place Le Verrier, F–13248 Marseille Cedex 04, France

e–mail : [redacted]

Published in Astronomy and Astrophysics, v.420, p.L31-L34 (2004)

Abstract

The GIRAFFE spectrograph is unique in providing the integral field spectroscopy of fifteen distant galaxies at the same time. It has been successfully implemented at the second VLT unit within the FLAMES facility. We present GIRAFFE observations acquired during the Guaranteed Time Observation of the Paris Observatory, using total exposure times ranging from 6 to 12 hours. The reduced 3D cube of each galaxy has been deconvolved using our new package DisGal3D. This software has been written using the only assumption that UV light traces the emission line regions. The comparison between GIRAFFE spectra and HST imagery allows us to recover details on velocity fields as small as $0.3 - 0.4$ arcsec. It has been successfully tested using Fabry Perot observations of nearby galaxies purposely redshifted to large distances. We present here preliminary results for three distant galaxies at $0.45 < z < 0.65$, whose velocity fields have been derived with exquisite spectral ($R = 10000$)

and spatial resolutions. Observed velocity fields range from disturbed fields expected in major merger events to those of regular spirals with minor perturbations. For the latter, one could accurately derive the dynamical major axis and the maximal rotational velocity. We conclude that dynamical properties of a large number of distant galaxies can be routinely derived at VLT. This opens a new avenue towards the understanding of the galaxy formation and evolution during the last 8 Gyr.

Keywords : galaxy formation – velocity field – star formation rate – 3D spectroscopy

E.1 Introduction

Studies of galaxies at intermediate redshift ($0.4 < z < 1.2$) have revealed large changes of galaxy properties during the last 8 Gyr, which follow the strong declines in cosmic star-formation density (Lilly et al., 1996 ; Flores et al., 1999) and of the merging rate (Le Fèvre et al., 2000). Indeed, galaxies at intermediate redshift have complex morphologies and colors different from those of the Hubble sequence and they show metal abundances lower than those of present day galaxies (Hammer et al., 2004). Major contributors for this evolution have been identified to be luminous IR galaxies (LIRGs) and luminous compact galaxies (Flores et al., 1999 ; Hammer et al., 2001). Besides the numerous studies of their photometric and chemical properties, very little is known about the dynamical properties of galaxies beyond $z = 0.1$.

The Tully-Fisher relation is hard to reproduce in simulations (Steinmetz & Navarro 1999), and it is of prime importance to study its evolution up to $z = 1$. Significant changes of the slope of the Tully-Fisher relation are expected in the distant Universe ($z \sim 1$, Ferreras and Silk, 2001) and this would be the best observable quantity to explore the star formation process in disk galaxies. The TF relation at high redshift has been investigated by several studies using slit spectroscopy (Simard & Pritchet 1998 ; Bershady et al., 1999 ; Vogt et al., 2000 ; Barden et al., 2003 ; Boehm et al., 2003). Most of them have revealed a brightening of the rest frame B-band, but its magnitude (from 0.2 to 1.1 mag) as well as the constraints on the TF slope (see Fig. 10 in Ferreras & Silk) are far from being predictive up to now. Kinematic studies using 3D spectroscopy appear to be a pre-requisite to sample the whole Velocity Field (hereafter VF) of individual galaxies to distinguish between interacting and non-interacting galaxies (Mendes de Oliveira et al., 2003), and to limit uncertainties related

to the major axis determination. Such effects have been already tested for nearby spirals by comparing Fabry-Perot (hereafter FP) observations with long-slit spectroscopy. The latter can easily provide under- or over-estimates of the maximum velocity by factors reaching 50% (Amram et al., 1995). Could slit spectroscopy be appropriate for distant galaxies which are actively forming stars (up to rates larger than 100 $M_{\odot}$/yr) and where the frequency of interactions is very common ? It seems that our present knowledge of the dynamics of distant galaxies is very poor, maybe comparable to that provided from long slit spectroscopy of local galaxies in the beginning of the last century (Wolf, 1914). During the last 20 years, 2D velocity fields obtained from scanning FP interferometers (and more recently also from integral field and long slit spectroscopy) have proved to be powerful kinematic tools to investigate the properties of nearby galaxies (Veilleux et al., 2001 ; Kosugi et al., 1995 ; Swinbank et al., 2003 ; Mendes de Oliveira et al., 2003 ; Garrido et al., 2004 ; Ostlin et al., 2001).

To observe VF of distant galaxies, the integral mode IFU of FLAMES/GIRAFFE at VLT seems particularly well suited. Compared to available integral field instruments (e.g. GEMINI/GMOS, Swinbank et al., 2003), the FLAMES/GIRAFFE instrument and its IFU mode provide 3D spectroscopy of fifteen distant galaxies at the same time on a 20 arcmin FoV, thus this instrument optimizes the long exposure time needed to observe faint objects. Moreover, with IFUs, spectra are directly observed within each pixel and no further analysis is needed, contrary to FP data.

In this paper, we present the preliminary analysis of three (among 50) distant galaxies up to $z = 0.7$ which have been observed with GIRAFFE/IFU (section 2). In section 3 we present our new package **DisGal3D** which has been purposely developed to derive galaxy VF using the combination of GIRAFFE/IFU spectroscopy and HST/F606W imagery. A major purpose of this paper is to derive the accuracy of our method determining the maximal velocity as well as distinguishing disturbed VF from more regular, typical spiral galaxies. In section 4 we present our first results on distant galaxies.

E.2 Observations

As part of Guaranteed Time Observation programs of the Paris Observatory (P.I : F. Hammer) more than 50 distant galaxies have been observed, using the ESO VLT/FLAMES facility, IFU mode ($3'' \times 2''$ array of 20 square $0.52''$ width microlenses) with setups L04

Table XVII: Observational and deduced parameters of the three distant galaxies.

CFRS	z	I	M_B	f^a_λ	$(f_\lambda/A)^a$	S/N^b	Morph^c	VF^d	D.P.A^e	O.P.A.^{f}	i^f	V^e_{max}
03.0508	0.464	21.9	−20.01	31.0	11.2	446	Sp	Sp	119±5	143±2	39±3	70
03.1309	0.617	20.6	−21.76	14.9	8.0	182	Merger	Merger	N.A.	N.A.	N.A.	N.A.
03.9003	0.619	20.8	−21.51	21.3	1.5	310	Sp/Ir	Warp Sp	296±5	326±2	52±3	190

a - [OII] integrated from VLT/FORS spectroscopy and [OII] per arcsec^2. Fluxes in units of $\times 10^{-16}$ ergs/s/cm^2/Å and $\times 10^{-16}$ ergs/s/cm^2/Å/arcsec^2 using HST images to measure the surface of the object. b -Total S/N from the reconstructed spectrum using the 20 IFU channel spectra. c - From HST images (Brinchman et al., 1998; Zheng et al., 2004). d - Dynamical morphology from the reconstructed velocity field. e - Principal axis and maximum velocity deduced using the ADHOCw package (http ://www-obs.cnrs-mrs.fr/adhoc/adhoc.html). f - Optical principal axis and inclination deduced from HST I-band images.

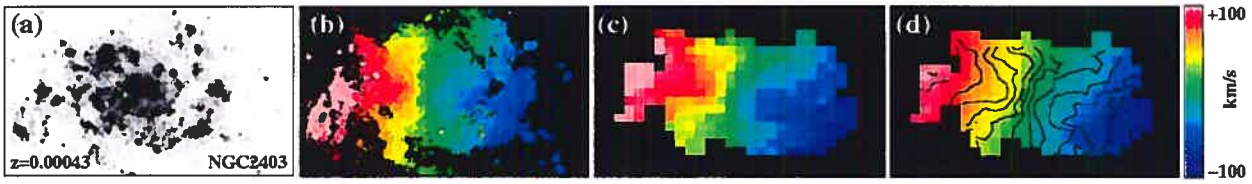

Fig. 67: Example of performed DisGal3D tests with nearby galaxies (here NGC 2403, observed with FaNTOmM $R = 27000$, Hernandez et al., 2004 et Gach et al., 2003). (a) : Hα map used during the deconvolution process (see text). (b) : VF obtained by FP observation at the mont Megantic Observatory (1.6 arcsec/pix) with FaNTOmM. (c) : same VF obtained with the galaxy redshifted to $z \sim 0.22$ (0.1 arcsec/pix corresponding to the HST/WFPC2 sampling). (d) : deconvolved VF obtained by DisGal3D after convolution of the redshifted galaxy by 0.6 arcsec seeing (see text). Superimposed isovelocities are those from (c).

($R = 0.55$ Å – 30 km/s) and L05 ($R = 0.45$ Å – 22 km/s), and integration times from 4 to 12 hours (ESO runs No 71.A-0322(A) and 72.A-0169(A)). Observational seeing during 1hr × n exposures ranged from 0.4 to 0.8 arcsec. Data reduction was done using the dedicated software BLDRS developed at the Geneva Observatory (http ://girbldrs.sourceforge.netweb). Sky subtraction was made using standard IRAF and written purpose IDL tools. The three galaxies presented here was selected from their morphological properties, ranging from an apparently well formed disk (03.0508) to an extreme case of merging (03.1309). Table XVII summarizes the observational strategy and deduced parameters of the three distant galaxies presented in this paper.

E.3 Analysis

VF of galaxies have been reconstructed using a dedicated IDL package named DisGal3D. DisGal3D includes a guided microscanning algorithm and a standard deconvolution method to reconstruct VF using 3D observations. It will be detailed in a forthcoming paper (Puech et al., 2004 in preparation, hereafter P04). Our method has been validated using ten FP cubes of nearby galaxies observed at the mont Megantic (Hernandez et al., 2004 in prep) and Haute Provence Observatories (Garrido et al., 2004). Galaxies have been redshifted in order to simulate GIRAFFE IFU spatial observational conditions but no specific spectral treatment has been done. Several simulated GIRAFFE data cubes at different seeings values (from 0.6 to 1) have been produced.

Our deconvolution method proceeds in a two-main-steps algorithm. The first step consists of interpolating the GIRAFFE data cube through a guided microscanning, thanks to HST/F606W images (Chemin et al., 2003). Here is the single assumption of our method, that is, the emission line regions are traced by the UV light. Indeed both UV and [OII] are directly or indirectly associated to hot star emissions and their luminosities correlates well (Swinbank et al., 2003 ; Hammer & Flores, 1998). Notice that the [OII] line fall in the F606 filter at $z = 0.4 - 0.8$. At this stage, only the spatial sampling has been increased and the spatial resolution remains still unchanged. The second step consists of a standard Maximum Entropy deconvolution method of each spatial slice of the interpolated cube. Spatial resolution is then improved down to approximatively one half a GIRAFFE pixel ($0.52''$). Thus, no kinematical assumption has been made, since our method is not model-dependent. We then do background subtraction, line symmetrisation and central wavelength

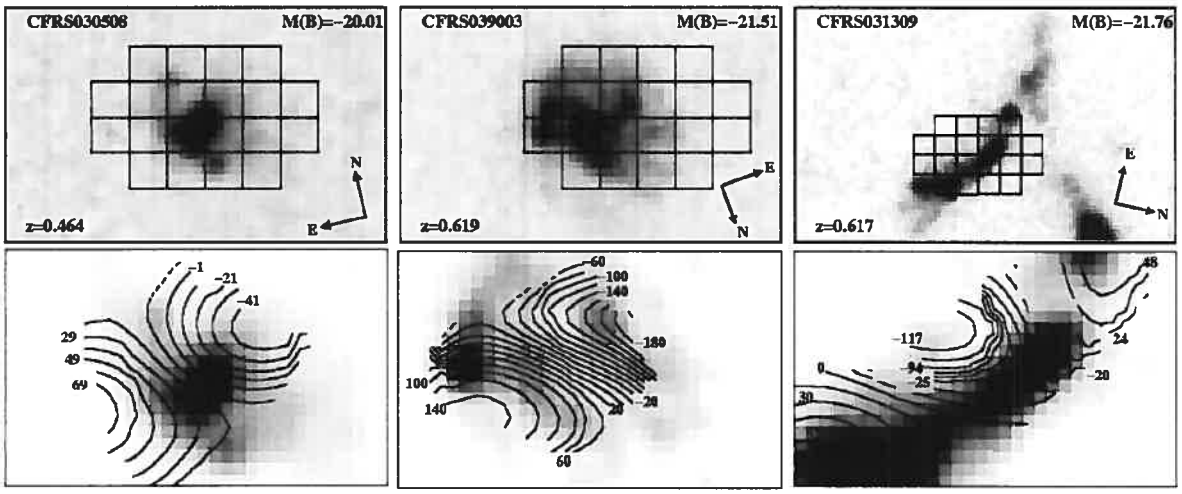

Fig. 68: Top : positions of the 3 × 2 arcsec^2 IFU bundle on sky, superimposed on HST I-band images. Bottom : 3 × 2 arcsec isovelocities of observed galaxies derived with DisGal3D. Each velocity field has been previously cleaned spatially by a sky level thresholding and spectrally by a S/N line thresholding. All features identified as possible extrapolation/deconvolution artifacts are removed before computing isovelocites within ADHOCw. Photometry in background is HST V-band, used during the deconvolution process (see text). The dynamical axis is much better defined than the optical axis, which is color dependent and may be affected by many irregularities.

estimation by a barycenter method (Garrido et al., 2002). Our software includes classical box smoothing or a filtering process based on wavelet decomposition (P04).

Simulated deconvolved GIRAFFE cubes have then been compared to original FP observations (Figure 67). Our analysis demonstrates that GIRAFFE VF are equivalent to smoothed FP observations. This method allows us to discriminate between disturbed and spiral-like galaxies. Figure 67 shows one of the nearby galaxies used to test our software. A preliminary analysis of residuals between Figure 67c and Figure 67d indicates that structures with sizes $> 0.3 - 0.5$ arcsec are recovered (P04). A preliminary study of deduced rotation curves shows that ΔV should be recovered within a 10% error (P04).

E.4 Results

To derive the VF of each galaxy we have used the well resolved [OII][3726.2, 3728.9]Å doublet emission lines. Figure 68 displays the three optical I-band images (upper panel) superimposed on the IFU bundle and the respective reconstructed isovelocities (lower panel) superimposed on high resolution HST images in the rest frame

UV-band. CFRS03.0508 presents a regular VF with isovelocity lines which suggest a possible warp of the E-N side of the disk, probably due to the companion at the same redshift, 60 kpc off and opposite to it. CFRS03.9003 was classified by Brinchmann et al. (1998) as a spiral galaxy. However after analysing its colormap, Zheng et al. (2004) classify it as an irregular. It is forming stars at a very high rate, $\sim$ 75 $M_{\odot}$/yr (Flores et al., 2004). At $z = 0.619$, CFRS03.9003 present a symetric VF with a peculiar pattern of the isovelocity lines. For the two above galaxies we have been able to derive their rotation curves using the ADHOCw package (http ://www-obs.cnrs-mrs.fr/adhoc/adhoc.html, see Table XVII and Figure 69). To derive a rotation curve from a VF, one needs to correct for projection effects on the plane of the sky. The simplest way to do this is to first estimate the kinematical parameters i (inclination angle of the galaxy), PA (Position Angle of the dynamical major axis), (X_C, Y_C) (dynamical center) and $V_{\rm sys}$ (systemic velocity). Afterwards, these parameters are visually optimized within ADHOCw until the rotation curve reaches a sufficient degree of symmetry (at least in the rise of the curve if asymmetries occur in the VF). In our case, estimates are based on photometric PA, center and inclination (outer isophot determined by Sextractor). The most spectacular galaxy is a giant merger, CFRS031309 at $z = 0.617$ (Flores et al, 2004). The VF is extremely irregular and somewhat chaotic as revealed by sharp variations of the velocity along this "chain" galaxy. These can be taken as evidence for strong interactions, meaning that this system is evolving rapidly as proved also by its very high star formation rate ($\sim$ 200 $M_{\odot}$/yr, Flores et al., 2004).

E.5 Conclusion

From a preliminary analysis of three isolated field galaxies observed with the FLAMES facility (GIRAFFE/IFU mode), we show its efficiency in producing VF of distant galaxies. Our main conclusions are :

– 3D spectroscopy with GIRAFFE IFUs is able to distinguish disturbed VF from those of regular spirals;

– the maximal velocity of distant regular spirals can be estimated within $\Delta V = 10\%$, an accuracy which can be only obtained with 3D spectroscopy;

– with its 15 deployable IFUs, VLT/GIRAFFE is the best tool to establish a robust Tully Fischer relation up to $z = 1.2$, which is independent of galaxy interactions or of crude assumptions on the VF (major axis, inclination, barycenter).

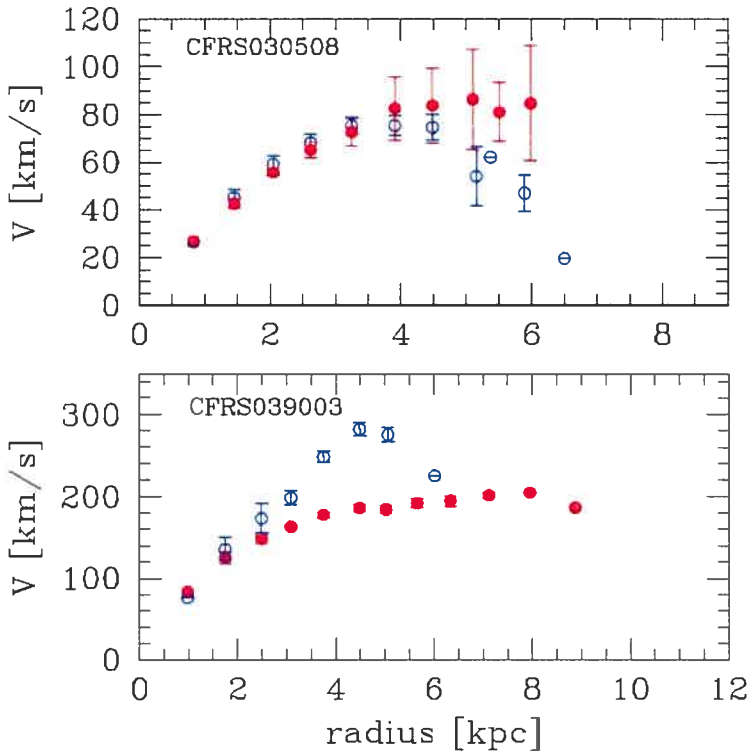

Fig. 69: Preliminary rotational velocity curves (corrected from projection effects) of CFRS03.0508 (top) and CFRS03.9003 (bottom) deduced using ADHOCw (preceding sides are in blue/empty circles). Both reveal a perturbed side due to possible perturbations in the VF. Each point/error bar represents the average/scatter obtained on a 1 pixel crown ($\sim$ 0.1 arcsec) spreading over a given angular sector centered on PA (40 and 36 degrees, respectively). In the case of CFRS03.0508, the decreasing side is likely due to an interaction with a nearby companion.

Further tests must be done on the capability to distinguish finer dynamical details such as minor merger, bars and warps. This is related to the spatial accuracy of our observations and of our deconvolution techniques. We will also investigate whether (heavy) extinction can affect our results. Establishing the VF of several hundreds of distant galaxies is now within the capabilities of the VLT and this is a new tool to investigate how the Hubble sequence was formed. A preliminary public release of DisGal3D will be soon available.

Acknowledgements

We are especially indebted to P. Amram and C. Carignan who provide us with several datacubes of velocity fields of nearby galaxies, including those from the GHASP project. We thank I. Fuentes-Carrera and C. Balkowski for useful discussions and advices. We wish to thank the excellent work of the GIRAFFE team at Paris-Meudon Obseervatory as well as at ESO and Geneva Observatory (the FLAMES consortium). H.F. and M.P. wish to thank the ESO Paranal staff for their reception and very useful advices.

References

Amram P., Boulesteix J., Marcelin M. et al., 1995, A&AS113, 35

Barden G., Lehnert M., Tacconi L.et al., 2003, submitted to ApJL,astro-ph/0302392

Bershady, M. A., Haynes, M. P., Giovanelli, R., & Andersen, D. R. 1999, Astronomical Society of the Pacific Conference Series, 182, 499

Böhm, A., et al. 2004, A&A, 420, 97

Brinchmann, J., et al. 1998, ApJ, 499, 112

Chemin, L., Cayatte, V., Balkowski, C., & Flores, H. 2002, Astronomical Society of the Pacific Conference Series, 275, 101

Ferreras, I., & Silk, J. 2001, ApJ, 557, 165

Flores, H., Hammer, F., Elbaz, D., Cesarsky, C. J., Liang, Y. C., Fadda, D., & Gruel, N. 2004, A&A, 415, 885

Flores, H., et al. 1999, ApJ, 517, 148

Gach, J.-L., et al. 2002, PASP, 114, 1043

Garrido, O., Marcelin, M., & Amram, P. 2004, MNRAS, 349, 225

Hammer, F., Gruel, N., Thuan, T. X., Flores, H., & Infante, L. 2001, ApJ, 550, 570 F

Hammer, Gruel, Thuan et al., 2001, ApJ, 550, 570.

Hernandez, O., Gach, J., Carignan, C., & Boulesteix, J. 2003, SPIE, 4841, 1472.

Kosugi, G., et al. 1995, PASP, 107, 474

Le Fèvre, O., et al. 2000, MNRAS, 311, 565 O. Le Fevre, R. Abraham, S. Lilly et al., 2000, MNRAS, 311, 565.

Lilly, S. J., Le Fevre, O., Hammer, F., & Crampton, D. 1996, ApJL, 460, L1

Mendes de Oliveira, C., Amram, P., Plana, H., & Balkowski, C. 2003, AJ, 126, 263

Östlin, G., Amram, P., Bergvall, N., Masegosa, J., Boulesteix, J., & Márquez, I. 2001, A&A, 374, 800

Simard, L., & Pritchet, C. J. 1998, ApJ, 505, 96

Steinmetz, M., & Navarro, J. F. 1999, ApJ, 513, 555

Swinbank, A. M., et al. 2003, ApJ, 598, 162

Tully, R. B., & Fisher, J. R. 1977, A&A, 54, 661

Veilleux, S., Shopbell, P. L., & Miller, S. T. 2001, AJ, 121, 198

Vogt, N. P. 2001, Astronomical Society of the Pacific Conference Series, 240, 89

Wolf, M., 1914, Vierteljahresschift Astron Gessel, 49 :112

Zheng, X. Z., Hammer, F., Flores, H., Assémat, F., & Pelat, D. 2004, A&A, 421, 847

Annexe F

The Compact Group of Galaxies HCG 31 is in an early phase of merging

The Compact Group of Galaxies HCG 31 is in an early phase of merging.

P. AMRAM

Observatoire de Marseille, 2 Place Le Verrier, F–13248 Marseille Cedex 04, France

C. MENDES DE OLIVIERA

IAG, São Paulo, Brazil and

Ludwig-Maximilians-Universität, München, Germany

H. PLANA

Universidade Estadual de Santa Cruz, Ilhéus, Brazil

C. BALKOWSKI

GEPI, Observatoire de Paris Meudon, 92190 Meudon, France

O. HERNANDEZ

Département de physique and Observatoire du mont Mégantic, Université de Montréal, C.P. 6128, Succ. centre ville, Montréal, Québec, Canada. H3C 3J7 and

Observatoire de Marseille, 2 Place Le Verrier, F–13248 Marseille Cedex 04, France

C. CARIGNAN

Département de physique and Observatoire du mont Mégantic, Université de Montréal, C.P. 6128, Succ. centre ville, Montréal, Québec, Canada. H3C 3J7

e–mail : [redacted]

E.S. CYPRIANO

Laboratório Nacional de Astrofísica, Itajubá, Brazil and

Southern Astrophys. Research Telescope, La Serena, Chile

L. SODRE Jr

IAG, São Paulo, Brazil

J.L. GACH

Observatoire de Marseille, 2 Place Le Verrier, F–13248 Marseille Cedex 04, France

J. BOULESTEIX

Observatoire de Marseille, 2 Place Le Verrier, F–13248 Marseille Cedex 04, France

Plublished in The Astrophysical Journal, 2004, Volume 612, Issue 1, pp. L5-L8.

Abstract

We have obtained high spectral resolution (R = 45900) Fabry-Perot velocity maps of the Hickson Compact Group HCG 31 in order to revisit the important problem of the merger nature of the central object A+C and to derive the internal kinematics of the candidate tidal dwarf galaxies in this group. Our main findings are : (1) double kinematic components are present throughout the main body of A+C, which strongly suggests that this complex is an ongoing merger, (2) regions *A*2 and E, to the east and south of complex A+C, present rotation patterns with velocity amplitudes of $\sim$ 25 $km\ s^{-1}$ and they counterrotate with respect to A+C, (3) region F, which was previously thought to be the best example of a tidal dwarf galaxy in HCG 31, presents no rotation and negligible internal velocity dispersion, as is also the case for region *A*1. HCG 31 presents an undergoing merger in its center (A+C) and it is likely that it has suffered additional perturbations due to interactions with the nearby galaxies B, G and Q.

keywords : galaxies : individual (HCG 31) — galaxies : kinematics and dynamics — galaxies : evolution — galaxies : interactions — galaxies : formation — instrumentation : interferometers

F.1 Introduction

The spectacular Hickson Compact Group 31 (Hickson 1982) shows a wide range of indicators of galaxy interaction and merging : tidal tails, irregular morphology, complex kinematics, vigourous star bursting (e.g. Rubin et al. 1990) and possible formation of tidal dwarf galaxies (e.g. Hunberger et al. 1996). All the objects belonging to the group are embedded in a common large HI envelope (Williams et al. 1991). The group is formed by members A+C, B, E, F, G, Q (Rubin et al. 1990).

Two scenarios have been put forward to explain the nature of the central system A+C : it is either two systems that are about to merge (e.g. Rubin et al. 1990) or a single interacting galaxy (Richer et al. 2003). In this Letter we use our new Fabry-Perot maps and

deep imaging from Gemini-N to revisit the important problem of the merger nature of the central object of the group, A+C, and, in addition, we investigate the internal kinematics of the tidal dwarf galaxies, in an attempt to identify if they are self gravitating objects or not. We adopt a distance of 54.8 Mpc, from the redshift z=0.0137 (Hickson et al. 1992) and using H_o=75 km s^{-1} Mpc^{-1}, hence 1" $\sim$ 0.27 kpc.

F.2 Observations

Observations were carried out with the Fabry-Perot instrument CIGALE (Gach et al. 2002) attached to the ESO 3.6m telescope in August 2000. Interferograms were obtained with a high order (p=1938) Fabry-Perot scanning interferometer, giving a free spectral range of 155 $km\ s^{-1}$ with a *Finesse F=24* leading to a spectral resolution of $R = 45\ 900$. The pixel size is 0.405 arcsec ; the total exposure time was 72 min (6 cycles of 12 min each, 48 scanning steps per cycle) and the FWHM of the interference filter centered around 6651 $\AA$ was 20 $\AA$. The velocity sampling was 3 $km\ s^{-1}$ and the relative velocity accuracy is $\sim$ 1 $km\ s^{-1}$ over the whole field where the S/N is greater than 3. Reduction of the data cubes was performed using the CIGALE/ADHOCw software (Boulesteix, 2002). The data reduction procedure has been described e.g. in Blais-Ouellette et al. (1999) and Garrido et al. (2002). For the adopted distance of the group, one pixel corresponds to $\sim$ 0.11 kpc.

In August 2003, we obtained two images with GMOS at Gemini-N in g' and r' with exposure times of 1200 and 900 seconds, respectively. These images have a pixel size of 0.14" and typical seeing of 0.75".

F.3 Results

A color map of the group is presented in Figs. 70a. It shows a wealth of star forming regions and the large extent of the optical diffuse light which envelopes the group. For the first time, regions *A1* and *A2*, to the east of complex A+C, are seen in great detail and depth.

Fig. 70b–d show the Hα monochromatic map of the group, the velocity map and several zoom panels showing the typical velocity profiles in selected regions of the group. The velocity field was corrected from free spectral range ambiguity using previous kinematic

observations. At first look, galaxies A and C appear to be a single kinematic entity, as their velocity fields show no discontinuity. Under this assumption, we can infer a rough mass for the A+C complex, within a radius of $\sim$ 18 arcsec ($\sim$ 4.9 kpc) of $M \sim 4.5 \times 10^9 M_\odot$. The following parameters and assumptions were used for this mass determination : a maximum rotational velocity of 70±10 $km\ s^{-1}$ (only from the NW side of the system given that the SE side is too disturbed), a kinematic inclination and position angle of 51±5 and 130±3 degrees, respectively, and the assumption that the measured motions are due to disk rotation. Nevertheless, multiple profiles (see Fig. 70d), evident almost everywhere in the main body of A+C, strongly suggests that A+C is not a single entity and therefore this rough determination provides only an order of magnitude for the mass.

Fig. 71 shows the velocity gradients of the objects *A*1, *A*2, E and F, situated around the pair A+C (see Fig 70a) and which have been thought to be candidate tidal dwarf galaxies (Hunsberger et al. 1996, Iglesias-Páramo & Vílchez 2001 and Richer et al. 2003). The curves are not corrected for inclination and the central position and velocity were chosen such that the curves were as symmetric as possible, with both sides matching, when possible. The object with the highest velocity gradient is E, with ordered velocities which range from 3950 $km\ s^{-1}$ to 4000 $km\ s^{-1}$. Object *A*2 also shows ordered motion, with velocities going from 4125 to 4175 $km\ s^{-1}$. Surprisingly, object F, thought to be the best tidal dwarf galaxy candidate in the group, shows a completely flat rotation curve, as does also the smaller object to the northeast of A+C, fragment *A*1. In addition, *A*1 and F have low gaseous velocity dispersions. These results will be discussed in the next section.

We obtained the map of the gaseous velocity dispersion at each pixel of the image (Amram et al. 2004, in preparation) assuming the profiles are well represented by a single gaussian. The value for the velocity dispersion ranges from 10 to 30 $\mathrm{km\,s^{-1}}$ throughout the group. In particular, objects *A*1, *A*2, E and F show typical velocity dispersions of 15 $\mathrm{km\,s^{-1}}$, which in some isolated regions can reach up to 25 $\mathrm{km\,s^{-1}}$. The highest values for the velocity dispersion lie in the overlapping region between A and C, mainly due to double components. It is noticeable that these highest values do not match the most intense star forming regions everywhere in the galaxies but particularly where disk A and C overlap, implying that the line broadening and the multiple components are not directly linked to star formation triggered by interaction with another galaxy but specifically by the merging of A+C. Hickson & Menon (1985) reached a similar conclusion, analyzing a radio continuum map of the group. They found that the 20 cm peak of emission comes from the overlapping

regions of A and C, indicating additional evidence of recent excessive starburst activity in this region.

F.4 Discussion

F.4.1 The ongoing merger A+C

Richer et al. (2003) also presented Fabry-Perot velocity maps of HCG 31. There is fairly good general agreement between their velocity field and ours. The spectral resolution of our maps is nevertheless six times higher (7900 vs 45900) and the detection limit several magnitudes fainter. Several authors supported that A and C are separate entities in an ongoing merging phase (e.g. Vorontsov-Velyaminov and Arhipova, 1963 ; Rubin et al., 1990) while Richer et al. (2003) supported the scenario that A+C is a single interacting spiral galaxy. The new piece of evidence in support of the merging scenario reported in this paper is the presence of double velocity components throughout the system A+C. In fact, our higher resolution velocity field shows kinematic structures which are not naturally explained by a single disk but by the merging of two disks.

Although Sc galaxies are, in general, transparent objects (Bosma 1995), moderate amounts of molecular gas (as traced by the CO) and cold dust may make some regions opaque. The CO emission is weak in HCG 31 but the brightest CO peak occurs in the overlapping region between galaxies A and C (Yun et al. 1997) where the broader Hα profiles are observed. If the CO belongs to the foreground galaxy, multiple components are observed in regions optically thick and then could not be observed if disk A and C are two separate galaxies seen in projection, i.e. chance alignment. Multiple gaseous components are observed in the same disk plane when they are not in equilibrium (e.g. Östlin et al. 2001). This occurs when two different entities merge, or when the feedback gas due to star formation interacts with the ISM. We observe in HCG 31 the signature of both mechanisms, the second one being probably a consequence of the first one.

The general pattern of the velocity field of HCG31 A+C is somewhat similar to that of NGC 4038/9 (the Antennae, Amram et al., 1992) in which a continuity in the isovelocities between both galaxies is also observed in the overlapping region. The merging stage of the Antennae is slightly less advanced than that for A+C. In the Antennae, the two galaxies are clearly separate entities and their bodies, which are not yet overlapping, each display

an increasing velocity gradient, which is roughly parallel and run from the NE to the SW (Amram et al. 1992). It is likely that when the disks of NGC 4038 and of NGC 4039 overlap, the velocity field will also present total continuity, as observed in A+C.

Galaxy C (Mrk 1089) has been classified as a double nucleus Markarian galaxy, the two nuclei being separated by 3.4 arcsec (Mazzarella & Boroson, 1993) and it is difficult to explain the existence of the two nuclei without invoking a merging scenario, as shown by numerical simulations (e.g. Barnes & Hernquist 1992). To reproduce the double line profile in NGC 4848, Vollmer et al (2001) have used numerical simulations. They interpret them as the consequence of infalling gas which collides with the ISM within the galaxy. This gives rise to an enhanced star formation observed in the Hα and in the 20 cm continuum map.

HCG 31 is most probably a group in an early phase of merger, growing through slow and continuous acquisition of galaxies from the associated environment. Moreover, several pieces of evidence for interaction with the other galaxy components of the group, namely B, Q and G (e.g. the group is completely embedded in a large HI envelope showing a local maximum on G to the SW and another one around Q to the NE) indicate that the complex A+C is most probably accreting the surrounding galaxies.

F.4.2 Tidal Fragments

Several papers in the past (Hunsberger et al. 1996, Johnson and Conti 2000, Richer et al. 2003 and Iglesias-Páramo & Vílchez 2001) have mentionned the possibility that tidal dwarf galaxies in HCG 31 were formed. The best candidates are objects E and F, for which metallicities were measured and they were determined to be similar to that of the complex A+C, suggesting a tidal origin for these objects (Richer et al., 2003).

As shown in Fig. 71, we detect ordered motions only for objects $A2$ and E and not for $A1$ but F. It might be suspected that the internal velocity motions measured in $A2$ and E could be due to streaming motions in incipient tidal tails in formation (see Fig. 70a). This is, however, not the case because these objects are counterrotating with respect to the main body of A+C. The discontinuity of the isovelocities can be clearly seen from Fig. 70c : the velocities go from high (northeast) to low (southwest) in A+C, towards object E. Then, along the body of E they go in the opposite sense. Similarly, for object $A2$, it presents counterrotation with respect to its immediate neighbor to the west : galaxy A. These objects may fall back onto their progenitor. In fact, from their velocity differences with respect to the

A+C complex (+115 $km\ s^{-1}$ and -60 $km\ s^{-1}$ respectively) and from their relative projected distances (6.7 kpc and 5.4 kpc respectively) and assuming a total mass for the A+C complex of $M \sim 4.5 \times 10^9\ M_\odot$, we could determine that these two objects will indeed, most probably, fall back onto A+C. The same is true for object F, which although more distant from A+C, has a very small radial velocity difference of $\sim 60 km\ s^{-1}$. We note, however, that given the fact that we measure radial velocities (and not the velocity component in the plane of the sky), the observed internal velocities of the tidal fragments are lower limits.

Region F, which was previously thought to be the best example of a tidal dwarf galaxy in HCG 31, is indeed part of the main merger, following the same kinematic pattern of the parent galaxy and presenting no rotation nor significant internal velocity dispersion. Region F was found to have a low or inexistent old stellar population by Johnson and Conti (2000). If there is no old stellar population the velocity dispersion of the gas is mainly indicating the dynamics of the cloud. The range of values derived for the internal velocity dispersion of F, 15-25 $km\ s^{-1}$, is too close to the natural turbulence of the gas and/or the expanding velocity due to starburst winds. The lack of rotation and the continuity of the kinematics between the main body of the merger and object F suggest it is simply tidal debris, although, considering its projected distance from A+C (16 kpc) and the large amount of fuel available in the whole area of the merger ($2.1 \times 10^{10}\ M_\odot$ of HI gas), it could perhaps develop into a tidal dwarf galaxy in the future, by accretion of infalling material.

There is also the possibility that regions $A1$ and F present no velocity gradient due to their rotation pattern being along the line of sight. Although this could be a possibility for the smaller and rounder region $A1$, it is less likely the case for region F, given its elongated morphology.

F.5 Conclusions

Our two main results are : 1) We measure multiple kinematic components throughout the body of A+C which we interpret as a strong indication that this complex is an ongoing merger. The double photometric nucleus has been identified in several previous images of HCG 31 including the spectacular HST image published by Johnson and Conti (2000) and in Fig. 70a. The double kinematic component is shown here for the first time in Fig. 70d. 2) F and $A1$ present flat rotation velocity profiles and insignificant velocity dispersions. In

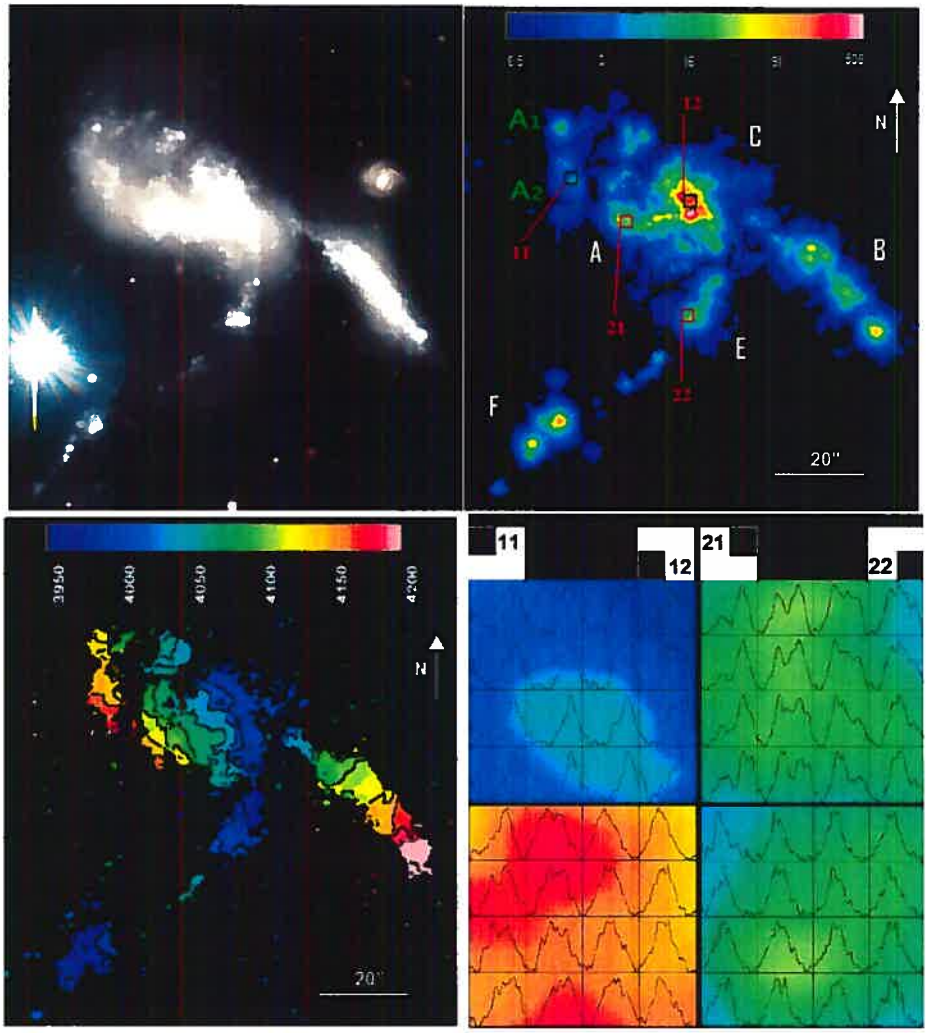

Fig. 70: *HCG 31.* **Upper Left, Fig. a :** Composite g' and r' color image of the central region of the group. **Upper Right, Fig. b :** net-Hα map. The flux is given in a logarithmic scale, in units of 10^{-16} $erg\ s^{-1}\ arcsec^{-2}\ cm^{-2}$, the calibration has been done with the Hα image from Iglesias-Páramo & Vílchez (2001). The four small open squares labeled 11, 12, 21, 22 are the windows within which the profiles shown in Fig. d have been extracted. Their size are 8×8 pixels. (~3.2"×3.2" or ~0.9 kpc×0.9 kpc). **Bottom Left, Fig. c :** Hα velocity field; the scale is labeled in $km\ s^{-1}$ and the black isocontours are separated by 25 $km\ s^{-1}$. **Bottom Right, Fig. d :** Examples of velocity profiles corresponding to the windows displayed on the Hα image (Fig. b). Each small box represents 2×2 pixels (~0.8"×0.8" or ~0.22 kpc×0.22 kpc) on the sky. The origin of the X-axis corresponds to 6648 $\mathring{A}$ (3917 $km\ s^{-1}$) and the amplitude of the *x-axis* represents the ~ 3.5$\mathring{A}$ free spectral range of the interferometer (~ 155 $km\ s^{-1}$). The profiles are plotted without correction for possible free spectral range jump : velocity differences between various components may be the value plotted in the figure plus n × 155 $km\ s^{-1}$ (n being an integer, positive or negative). The intensities of the profiles have been normalized to the brightest one. The color background pixels correspond to the intensities displayed on the Hα image.

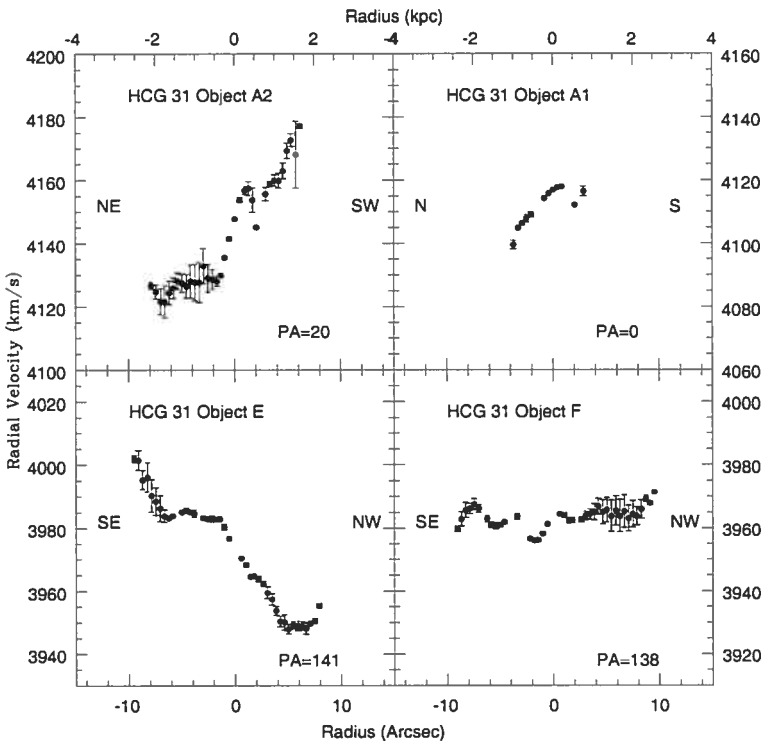

Fig. 71: Velocity gradients for the tidal dwarf galaxy candidates

contrast, *A*2 and E are structures counterrotating with respect to the parent A+C complex.

We conclude that HCG 31 is a merging group which is probably going to soon end up as a field elliptical galaxy. It would be very valuable to compare our new, high spectral resolution maps to simulations of groups to investigate which interaction and merger parameters fit these data.

Acknowledgments

The authors thank Olivier Boissin for help during the observations, Jorge Iglesias-Páramo for kindly providing the calibrated Hα image and to acknowledge financial support from the French-Brazilian PICS program. CMdO, LS and ESC would like to thank the Brazilian PRONEX program, FAPESP, CNPq. CMdO deeply acknowledges the funding and hospitality of the MPE Institut in Garching, where this work was finalized. CC and OH acknowledge support from FQRNT, Québec and NSERC, Canada.

References

Amram P., Marcelin M., Boulesteix J. et al. 1992, A&A, 266, 106

Amram P., Mendes de Oliveira C., Boulesteix J. et al. 1998, A&A, 330, 881

Blais-Ouellette S.; Carignan C., Amram P. et al. 1999, AJ, 118, 2123

Boulesteix J., 2002, ADHOCw Red.Package, www.oamp.fr/adhoc/

Bosma A., 1995 in NATO Advanced Science Inst. Ser. C, 469, 317

Gach J.-L., Hernandez O., Boulesteix J. et al. 2002, PASP, 114, 1043

Garrido O., Marcelin M., Amram P. et al. 2002, A&A, 387, 821

Hickson P. 1982, ApJ, 255, 382

Hickson P., Mendes de Oliveira C., Huchra J.P. et al. 1992, ApJ 399,353

Hickson P. & Menon T.K. 1985, ApJ 296, 60

Hunsberger S.D., Charlton J.C. & Zaritsky D. 1996, ApJ 462, 50

Iglesias-Páramo J. & Vílchez J.M. 2001, ApJ 550, 204

Johnson K.E. & Conti P.S. 2000, AJ 119, 2146

Östlin G., Amram P., Bergvall N. et al. 2001, A&A 374, 800

Richer M.G., Georgiev L., Rosado M. et al. 2003, A&A, 397, 99

Rubin V.C., Hunter D.A., Ford W.K.Jr. 1990, ApJ, 365, 86

Vollmer B., Braine J., Balkowski C. et al. 2001, A&A,374,824

Vorontsov-Velyaminov B.A. & Arhipova, Trudy G., 1963, Astron. Inst. Sht., 33, 1

Williams B.A., McMahon P.M., van Gorkom J.H., 1991, AJ, 101, 1957

Yun M.S., Verdes-Montenegro L., del Olmo A. et al. 1997, ApJ, 475L,21.